All-two-dimensional van der Waals heterostructures for spin injection and detection

DISSERTATION ZUR ERLANGUNG DES
DOKTORGRADES DER NATURWISSENSCHAFTEN
(DR. RER. NAT.) DER FAKULTÄT FÜR PHYSIK

DER UNIVERSITÄT REGENSBURG

vorgelegt von

Jan Bärenfänger

aus Burglengenfeld

im Jahr 2024

Promotionsgesuch eingereicht am: 30.10.2024

Die Arbeit wurde angeleitet von: Prof. Dr. Mariusz Ciorga

Prüfungsausschuss:

Vorsitzender:	Prof. Dr. Jaroslav Fabian
Erstgutachter:	Prof. Dr. Mariusz Ciorga
Zweitgutachter:	Prof. Dr. Dominique Bougeard
Weiterer Prüfer:	Prof. Dr. Milena Grifoni

Datum Promotionskolloquium: 10.02.2025

Contents

1. Introduction

1.1. The element of life

Carbon is truly the element of life. It is the primary component of all known life on Earth. Carbon forms in stars by the fusion of three ^{4}He nuclei (the so-called triple-alpha process) [1], and is spread across the whole universe via supernovas, the end of a star's life. The abundance of carbon here on Earth has enabled the formation of a multitude of chemical compounds. Carbon is so special as it is able to form a variety of chemical compounds, collectively referred to as organic compounds. Molecules based on carbon constitute the building blocks of a vast array of biological macromolecules, including proteins, ribonucleic acid (RNA), deoxyribonucleic acid (DNA), carbohydrates, peptides, lipids, and the list goes on [2]. Consequently, life here on Earth is shaped by the properties of this chemical element. The ability of carbon to form stable yet reactive bonds is what makes it a key building block in the construction of living organisms. Moreover, in contrast to other oxides in the carbon group, such as SiO_2 or GeO_2, which are solid under Earth's conditions, carbon's fully oxidised compound CO_2 is gaseous. This is significant as it enables the intricate carbon cycle here on earth [3]. In the fast carbon cycle, gaseous CO_2 in the atmosphere can easily be absorbed by plant cells and allows for the formation of sugar with the help of water and the energy from the sun, a process known as photosynthesis. CO_2 is then emitted through several mechanisms. Plants break down sugar in order to grow, animals or bacteria obtain energy from consuming the plants and their fruits, essentially breaking down the carbon compounds, and fire oxidizes the plants. This carbon cycle enabled the evolution of complex life here on Earth. When carbon-rich sediments accumulate over millions of years, the carbon atoms are exposed to increasingly greater pressures in the absence of oxygen. Under the right circumstances (high temperatures), this allows for carbon to form crystal structures like diamond and graphite [4], both having precious properties. Diamond, with its distinctive lustre, is employed in a variety of contexts, including the manufacture of jewellery and in applications that require the use of highly robust materials. This is due to the fact that diamond is the hardest known naturally occurring material [5]. Graphite, on the other hand, is most commonly associated with graphite pens. Graphite is a crystalline material composed of single layers of carbon atoms. The carbon atoms within these layers are held together by strong covalent bonds. However, the layers themselves are only bound via relatively weak van der Waals forces. When writing with a graphite pen, one effectively

peels the layers of graphite on to the surface of the paper. A single layer of these graphite crystals is called graphene. The question of whether a single sheet of carbon atoms is thermodynamically stable under ambient conditions has been a topic of discussion for some time [6]. However, the isolation of graphene in 2004 by Novoselov and Geim using only sticky tape provided the answer [7]. This discovery was awarded the Nobel Prize in Physics in 2010. Given its thickness of only one atom, graphene represents the thinnest solid possible, exhibiting a range of extraordinary properties. It is a semimetal with electronic properties that require a description based on relativistic theories for massless particles, it exhibits bipolar conduction, which means that it can utilize electrons and holes for charge transfer [8]. The isolation of graphene prompted research into other layered materials, which are held together by van der Waals forces, also known as van der Waals materials. This focused research on these materials led to the expansion of the van der Waals materials family to encompass metals, semiconductors, and insulators, and are future candidates to replace conventional materials currently utilized in electronic devices.

This thesis investigates all-van der Waals spin transport devices based on graphene acting as the transport channel, in combination with insulating hexagonal boron nitride (hBN) and the ferromagnetic Fe_3GeTe_2. This investigation forms the basis for further research into other spintronic devices based on van der Waals materials. In the following, the concepts of spintronics and spintronic devices are introduced.

1.2. Introduction into spintronics

Moore's law states that the number of transistors in integrated circuits will double approximately every two years [9]. This prediction was made in 1965 and remains accurate to this day. Integrated circuits, which are predominantly based on silicon, are indispensable components of the electronic devices we use everyday. As a consequence of Moore's law, the dimensions of the transistors are becoming increasingly reduced. Nevertheless, this process of miniaturization necessitates the development of sophisticated lithographic techniques, and is ultimately constrained by the natural limit of gate sizes reaching atomic scale [10]. Consequently, novel concepts must be developed in order to keep up with Moore's law in future. One concept is to utilize not only the charge of the electron, as is the case with conventional transistors, but instead to employ the electron's spin for information transport. This field of study is also referred to as *spintronics*, and it is already possible to find spintronic devices in use in our everyday lives, e.g. magnetic random access memory and magnetic read heads in hard-disk drives [11].

The two most fundamental spintronic effects are the tunnelling magnetoresistance (TMR) and the giant magnetoresistance (GMR) effect. The TMR was first observed by Jullière in 1975 in a Fe/Ge/Co heterostructure [12], wherein a tunnel current was measured through

the junction at a constant applied bias voltage. It was observed that the resistance of the junction depends on the relative magnetization orientation of the two ferromagnetic electrodes. Later, the GMR was discovered in 1988 by Grünberg [13] and Fert [14], in a Fe/Cr/Fe heterostructure comprising a thin non-magnetic conductor sandwiched between two ferromagnetic layers. Once more, the resistance of the junction depends on the relative magnetization orientation of the two Fe-electrodes. This resulted in the first commercial spintronic hard drive storage utilizing the GMR introduced only a couple of years after its discovery in 1997, and in the Nobel Prize in Physics in 2007 [11].

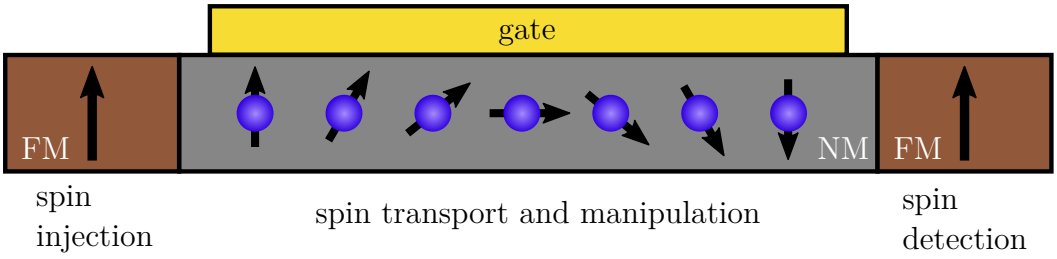

Fig. 1.1: Schematics of a spin field-effect transistor (spin-FET). Spins are injected from a ferromagnetic (FM) electrode (brown) on the left into the non-magnetic conducting (NM) channel (grey). The application of a voltage at the gate (yellow) enables the manipulation of spins within the NM. Subsequently, the spins are detected at the second FM electrode. The arrows in the FM indicate their magnetization direction, whereas the arrows in the NM indicate the spin orientation of the injected spin ensemble. As spins reach the NM/detecting FM interface anti-parallel to the detector's magnetization direction, the spin-FET is in the off-state. Turning off the gate voltage, also turns off the spin manipulation. Consequently, spins reaching the detector are parallel to its magnetization direction, which results in the on-state of the spin-FET. Adapted from [15].

In contrast to data storage spintronic devices, spintronic devices which allow for data manipulation have not been realized commercially yet. An analogue to the traditional field-effect transistor, which could fill in the gap, is the spin field-effect transistor (spin-FET), as proposed by S. Datta and B. Das in 1989 [16]. A spin-FET comprises two ferromagnets (FM) and a non-magnetic conductor (NM), which is positioned in-between, as illustrated in Fig. 1.1. Spins are injected from one of the FM into the NM. In analogy to the conventional field-effect transistor, where the gate controls the flow of charge, the orientation of the spins in the NM can be manipulated by a gate. Subsequently, the spin signal is detected by the second ferromagnetic electrode. The orientation of the spins at the NM/FM interface at the detecting electrode and the magnetization direction of the detecting ferromagnet determine whether the spin-FET is in an on- or off-state, which corresponds to a parallel and anti-parallel alignment, respectively. The electrical injection of spins from a FM into a NM is an intricate task, that highly depends on the conductivities of both materials, as will be discussed in more detail later on [17]. Additionally, the electrical manipulation of spins in the NM channel requires electrically tunable spin-orbit coupling.

All electrical spin injection and detection devices have already been realized in various conventional semiconductor materials [18–20]. These semiconductors are usually synthesized through molecular beam epitaxy, chemical vapor deposition, or liquid phase epitaxy. However, when combining different materials, the lattice constants of these materials must be similar, to ensure defect-free growth and, consequently, the desired properties of the heterostructure [15]. This considerably constrains the potential material combinations. Van der Waals materials offer a means of circumventing this limitation, as they can be mechanically stacked on top of each other, layer by layer. This enables the fabrication of novel heterostructures with a variety of properties. Since the initial reports of graphene by Geim and Novoselov *et al.* [7], the development of new two-dimensional (2D) crystals has been rapidly expanding to include metals ($NbSe_2$, VS_2, Fe_3GeTe_2), semiconductors (MoS_2, $MoSe_2$, WS_2, WSe_2, PdS_2) and insulators (hBN, CrI_3) [21]. In many cases the properties of the 2D layers differ from those of their bulk crystals. Furthermore, when two van der Waals materials are stacked on top of each other, it is possible to control the electric properties in the resulting heterostructure by adjusting the twist angle of these two adjacent layers. This phenomenon has led to the emergence of the research field of *twistronics* [22].

Graphene is predestined for spin transport, given its weak intrinsic spin-orbit coupling, which leads to theoretical predictions of large spin lifetimes [23]. Moreover, induced spin orbit coupling via proximity effects [24, 25], spin lifetime anisotropies [26, 27], and gate tunable spin absorption [28, 29] have introduced novel methods for modulating spins in graphene. The first demonstration of spin transport in graphene was conducted in 2007 [30] and employed conventional Al_2O_3 tunnel barriers and Cobalt for the spin-aligning electrodes. However, a leap towards all-van der Waals spin-FETs was taken in 2023, where spin injection and detection utilizing the van der Waals ferromagnet Fe_3GeTe_2 was demonstrated [31]. However, the absence of a tunnel barrier resulted in inefficient spin injection so that spin precession experiments remained elusive.

1.3. Thesis outline

This thesis presents all-two-dimensional van der Waals devices that facilitate efficient spin injection from a ferromagnetic Fe_3GeTe_2 (FGT) electrode into a conducting monolayer graphene channel. The injected spin signal is detected at a second FGT electrode. To ensure efficient spin injection, a thin hBN layer between the FGT and graphene serves as a tunnel barrier. Such a heterostructure allows for the investigation of spin transport and precession in non-local spin valve and Hanle measurements. Prior to the spin experiments, a detailed characterization of each building block is conducted. The spin injection efficiency P and spin transport parameters, such as the spin lifetime τ_s and the spin diffusion constant D_s, are determined from the Hanle experiments by fitting the experimental data to an analytical fitting function. The obtained values of P of up to

$P \approx 40\,\%$ demonstrate highly efficient spin injection and detection. The spin lifetimes range from $\tau_s = 0.1$ to $1.3\,\text{ns}$ and spin diffusion constants D_s span from $D_s = 0.0046\,\text{m}^2\text{s}^{-1}$ up to $0.037\,\text{m}^2\text{s}^{-1}$. These values are in good agreement with those obtained in other spin transport experiments in graphene utilizing conventional tunnel barriers and spin aligning electrodes [27, 30, 32, 33]. Interestingly, the extracted values of D_s do not match the extracted values of the charge diffusion constant D_c in both presented spin transport samples, which is an unexpected finding [33, 34]. In order to evaluate this discrepancy, simulations were conducted using *COMSOL Multiphysics*. Hints of magnetic moments were found in one of the two samples, although their origin remains unknown. The results presented in this thesis successfully demonstrate efficient spin transport in all-van der Waals heterostructures, paving the way for future all-2D spintronic applications.

The thesis is organised as follows:

- **Chapter 2** introduces the van der Waals materials employed in this thesis. It provides a concise overview of the key aspects of magnetic order in 2D van der Waals materials, together with an account of the theoretical physics which is associated with FGT, graphene, and hBN.

- **Chapter 3** continues with a theoretical description of spin transport, which is essential for understanding the experiments and their outcomes. The non-local spin valve and Hanle effect are discussed, followed by a brief overview of the most relevant spin-relaxation mechanisms in graphene. Finally, the chapter outlines how these spin transport experiments can be modelled using *COMSOL Multiphysics*.

- **Chapter 4** introduces the experimental methods employed for device fabrication and measurement of the previously introduced spin experiments. It provides a comprehensive description of the exfoliation process for each material, the stacking process, and the processing of the van der Waals heterostructure. Additionally, it outlines the measurement setup layout for the non-local spin valve and Hanle experiments.

- **Chapter 5** presents the characterization of the ferromagnetic material Fe_3GeTe_2, which is employed as the spin-aligning electrodes in the spin transport samples. From these experiments, an estimation of the Curie temperature T_C is derived. Moreover, an antisymmetric magnetoresistance in FGT/FGT homojunctions is reported.

- **Chapter 6** characterizes the transport properties of the graphene and determines the height of the hBN tunnel barriers of the two spin transport samples presented in this thesis.

- **Chapter 7** presents the main results of this thesis. Firstly, the results of the non-local spin valve measurements are presented for Samples A and B successively,

demonstrating successful spin transport in all-van der Waals heterostructures. Subsequently, the findings of the non-local Hanle experiments of both samples are presented, and the results of the spin injection efficiency P and the spin transport properties τ_s and D_s are discussed. The objective of the COMSOL simulations is to ascertain the potential causes for the discrepancy in the values of D_s and D_c.

- **Chapter 8** provides a conclusion to the thesis and summarizes the results. Additionally, it offers a brief outlook on the future of spintronics in van der Waals-based devices.

2. Theoretical background on van der Waals materials

Since the discovery of graphene in 2004 [7], van der Waals (vdW) materials have emerged as a new research field due to their unique structural and electronic properties. Unlike traditional materials with strong covalent, ionic or metallic bonds, van der Waals materials exhibit strong covalent bonds within, but weak van der Waals forces between layers, enabling the formation of layered structures. The emergence of clean interfaces between layers is due to the absence of any dangling bonds or surface charges. Van der Waals materials exhibit a diverse range of electric and magnetic properties, spanning from metals, semiconductors or insulators, and from para- and diamagnets to (anti-)ferromagnets [21, 35]. These properties allow for forming heterostructures with tailored functionalities, rendering vdW materials promising for diverse applications. The versatility of van der Waals materials, therefore, bears potential for applications ranging from electronics to optics, and even spintronics [21, 35]. It was previously believed that magnetic order would not exist in these materials, because of the Mermin-Wagner theorem [36]. This chapter gives an introduction in how magnetism can be materialized by anisotropy in these materials (Sec. 2.1), with a focus on the ferromagnetic metal Fe_3GeTe_2 (FGT) in Sec. 2.2. Subsequently, a brief overview of graphene and hexagonal boron nitride (hBN), which are two fundamental materials in the field of 2D van der Waals systems, is presented in Sec. 2.3 and 2.4, respectively.

2.1. Magnetic order in 2D van der Waals materials

Magnetism in thin metallic films has been extensively investigated over the last few decades [37–39]. The magnetic properties of these films usually grown by molecular beam epitaxy are sensitive to the substrate and resulting interface. However, mechanical exfoliation of layered two-dimensional (2D) van der Waals crystals avoids these issues, allowing for the stacking of different van der Waals materials without constraints. The first exfoliated van der Waals magnets, $Cr_2Ge_2Te_6$ [40] and CrI_3 [41], were investigated in 2017. Since then, the family of 2D vdW magnets has grown ever since, ranging from insulators and semiconductors to metals [42–48]. This section gives a short introduction on how magnetic order establishes in these van der Waals materials.

2.1.1. Heisenberg model

In magnetic materials, the magnetic moments due to spin angular momentum are aligned over a macroscopic length scale. This magnetic order is driven by an exchange interaction of neighbouring spins. Once the temperature exceeds the critical Curie temperature T_{C}, thermal energy causes misalignment of the magnetic moments, which can induce a phase transition to a non-magnetic state. In 1966 Mermin and Wagner [36] demonstrated that long-range magnetic order in ideal Heisenberg 2D magnetic systems is strongly suppressed by thermal fluctuations. However, magnetic anisotropy can counteract the effect of thermal fluctuations, enabling long-range order in 2D materials. The exchange interaction between nearest neighbouring spins is described by a generalized Heisenberg Hamiltonian [35]

$$H = -2\sum_{i<j}\left[J_x S_{ix} S_{jx} + J_y S_{iy} S_{jy} + J_z S_{iz} S_{jz}\right] - D_{\mathrm{on}}\sum_i S_{iz}^2, \tag{2.1}$$

where $S_{ix,iy,iz}$ and $S_{jx,jy,jz}$ are the x-, y-, and z-components of the neighbouring spins $\vec{S}_i$ and $\vec{S}_j$ that interact via the exchange couplings $J_{x,y,z}$ in the x-, y-, and z-direction. In a 2D system, isotropy in the xy-plane can be assumed [49]. Consequently, J_z and D_{on} can be considered as the "inter-site" and "on-site" magnetic anisotropies, respectively [35, 50]. The anisotropy in the nearest neighbour exchange couplings $J_{x,y} \neq J_z$ and the on-site anisotropy are essential to break the spin-rotational symmetry to allow magnetic order in 2D [49]. To ensure ferromagnetic order $J_{x,y,z}$ have to be positive [51].

The presence of long-range magnetic order is influenced by the dimensionality of the system [50]. In 3D systems, magnetic order can always persist at finite temperatures, while in 1D systems, it can only persist at $T = 0\,\mathrm{K}$ [50, 52]. In 2D systems, such as 2D vdW magnets, the existence of long-range magnetic order depends heavily on the spin dimensionality $\mathcal{N}$ and the strength of magnetic anisotropy [50]. The spin dimensionality $\mathcal{N}$ determines whether the spins are constrained to one, two or three dimensions. Fig. 2.1 a) shows a sketch of a 2D Ising model with $\mathcal{N} = 1$. Here, spins are oriented either parallel or anti-parallel along the given direction perpendicular to the plane. This uniaxial anisotropy is shown to withstand thermal fluctuations [53]. For $\mathcal{N} = 2$, spins are oriented in a given plane. In such a system, Berezinskii, Kosterlitz and Thouless demonstrated, a quasi-long-range topological magnetic order below a critical Berezenskii-Kosterlitz-Thouless temperature T_{BKT} [54, 55]. However, in an isotropic Heisenberg model, where spins can be oriented in any direction ($\mathcal{N} = 3$), coherent spin excitations are easily excited, destroying any magnetic order. This then prevents long-range magnetic order in 2D [36].

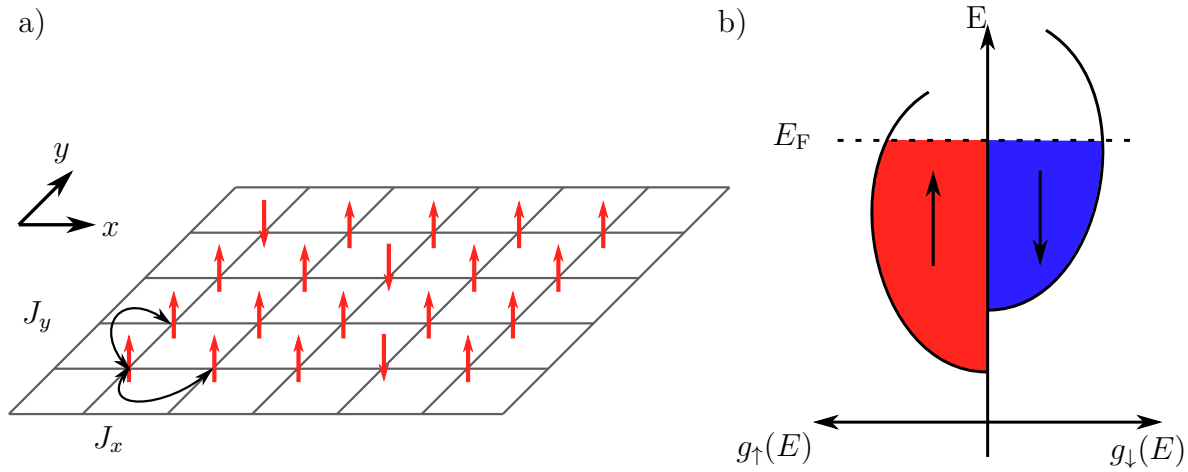

Fig. 2.1: a) 2D Ising model with spin dimensionality $\mathcal{N} = 1$. The spins are aligned in a 2D lattice with their spins constrained in one dimension, such that they are either oriented upwards or downwards. The exchange couplings J_x and J_y couple neighbouring spins. b) The density of states $g(E)$ is spin-split for a ferromagnetic metal due to the exchange. Majority spins (spin up) have a larger electronic density compared to the minority spin (spin down). The density of states at the Fermi level, however, is higher for the minority spin carrier. Adapted from [17].

2.1.2. Stoner criterion

As given by Eq. (2.1), magnetic order is driven by the exchange interaction of electron spins. In semiconductors or insulators, these spins are assumed to be localized. In metals, however, conduction electrons are fully delocalized, and the magnetic order in this itinerant regime is described by the band magnetism where magnetic order is discussed in the Pauli paramagnetism picture [56]. Here, applying an external magnetic field B shifts the energy of spin-up and spin-down electrons with respect to each other. This results in a spin-split density of states as long as the external magnetic field is applied.

In itinerant ferromagnets, this spin-split density of states establishes spontaneously without the applied magnetic field, as depicted in Fig. 2.1 b). For this, an exchange of spin is considered [51]. Electrons from the spin-down band are put in the spin-up band by flipping their spins resulting in a magnetized electron gas, which induces a molecular field. The exchange of spins results in an increase of the total energy. However, the interaction of the magnetization with the molecular field reduces the total energy again. The system establishes spontaneous ferromagnetism if the total change of energy is negative, so that the total energy is minimized by forming this magnetic order. The change of the total energy considering the spin exchange and the interaction of the resulting magnetization with the molecular field is determined by the Stoner criterion. For $U \cdot g(E_F) > 1$ the system establishes spontaneous ferromagnetism. Here, U is a measure of the Coulomb energy and $g(E_F)$ is the density of states at the Fermi level [51]. This spontaneous

ferromagnetism only arises when the Coulomb energy is strong and the density of states at the Fermi energy is large.

2.1.3. Temperature dependence of the magnetization

The spins in a material are always exposed to a finite temperature, which can excite spin waves and thus limit the magnetic order. Understanding the temperature dependence of the magnetization helps to discriminate between different theoretical models and determine the Curie temperature of ferromagnets. The Ising model was found to be unsuitable for modelling the temperature-dependent properties of 2D magnetic materials, as it leads to the prediction of excessively large Curie temperatures [35]. Consequently, the temperature dependence of magnetic ordering in 2D magnets is most accurately described by the Heisenberg model with $\mathcal{N} = 3$. The temperature dependent magnetization $m(T)$ is described by the critical power law [35, 57, 58]

$$m(T) \propto \left(1 - \frac{T}{T_\mathrm{C}}\right)^{\beta}, \tag{2.2}$$

where $m(T) = M(T)/M(0\,\mathrm{K})$ with $M(T)$ being the magnetization at a temperature T. The critical exponent β distinguishes between different classes of models and can be obtained by fitting, together with T_C. For a 3D Heisenberg model, $\beta = 0.33$, while for the 2D Heisenberg model $\beta = 0.125$ [57]. For example, a two-dimensional ferromagnet Fe_3GeTe_2 (FGT), which is of interest in this thesis, is reported to undergo a transition from the 3D to the 2D Ising ferromagnetism when its thickness is less than four layers, where β decreases from $\beta = 0.25 - 0.27$ in flakes thicker than 9 nm to $\beta = 0.14$ in the monolayer [57]. However, the reported values for the critical exponent β in FGT (β=0.25-0.327 [57, 59])) are lower than the expected value of 0.33 for the 3D Heisenberg model.

This discrepancy between the model and the experimental data can be attributed to the distinct nature of the thermal fluctuations. In the Heisenberg model, the magnetization varies linearly with temperature as $T \to 0$, while the spin fluctuations due to the underlying heat bath are of a quantum mechanical nature [35]. At low temperatures, the magnetization follows the Bloch $T^{3/2}$-law, while at temperatures close to the Curie temperature, it follows a power law [51, 58, 60]. The Curie-Bloch equation interpolates between the Bloch-law for $T \to 0$ and the Curie behaviour of $T \to T_\mathrm{C}$ and is given by [35, 58]

$$m(T) = \left(1 - \left(\frac{T}{T_\mathrm{C}}\right)^{\alpha}\right)^{\beta}, \tag{2.3}$$

where α is the Bloch exponent. This accurately describes the temperature dependence of the magnetization of 3D and 2D magnets for all temperatures.

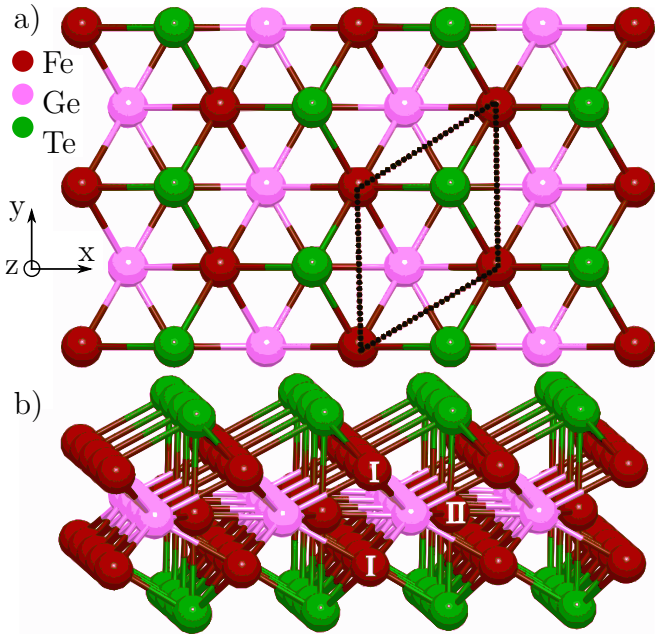

Fig. 2.2: a) Top and b) side view of the lattice structure of FGT. The dotted lines mark the unit cell. The inequivalent Fe_I^{3+} and Fe_{II}^{2+} sites are indicated in b). Adapted from [64].

2.2. Fe_3GeTe_2

Fe_3GeTe_2 is the metallic van der Waals ferromagnet that is utilized as the spin aligning electrode in the spin transport samples in this thesis. It was first synthesized in 2006 and exhibits magnetic order down to the monolayer limit [57, 61]. FGT is composed of Fe_3Ge slabs sandwiched between layers of Te atoms. Its crystal structure is illustrated in Fig. 2.2. The substructure of the Fe_3Ge slabs consists of three atomic layers, comprising Fe, Fe or Ge, and Fe atoms, which leads to two inequivalent Fe-sites, Fe_I^{3+} and Fe_{II}^{2+}. Both sites have partially filled 3d-orbitals, which induce different magnetic properties. The former induces a local magnetic moment, while the latter induces itinerant ferromagnetic order [62–64]. FGT satisfies the Stoner's criterion, which takes the competition between the exchange of spin and the magnetized electron gas into account, as discussed in Sec. 2.1.2 [64]. The gap between two adjacent FGT layers is reported to be 374 pm [61]. Due to the weak van der Waals forces between the layers, FGT can be mechanically exfoliated with the Scotch tape method [7]. However, it is not air stable and its surface oxidizes, when exposed to the environment [65–67]. It has been reported that oxidized FGT-layers couple anti-ferromagnetically to pristine FGT-layers [67]. Therefore, FGT needs to be exfoliated in inert environments, as provided by gloveboxes or in vacuum, and encapsulated, e.g. with hBN, to ensure high quality crystals and clean interfaces with other vdW materials [68].

FGT exhibits a large out-of-plane magnetic anisotropy ($J_{x,y} \neq J_z$) [48, 57], and a strong magnetrocrystalline anisotropy D_{on} which is due to the reduced crystal symmetry [64]. Both anisotropies stabilize the long-range ferromagnetic order in the monolayers against thermal fluctuations. The Curie temperature T_C depends on the number of

layers and ranges from 220-230 K in the bulk [61] to 130 K in the monolayer limit [57]. This is accompanied by a transition from 3D to 2D Ising ferromagnetic behaviour for thicknesses below 4 nm [48, 57]. For low temperatures and thicknesses smaller than 200 nm the magnetic behaviour can be described by one domain [57]. FGT exhibits a large anomalous Hall response, which is reflected in the material's anomalous Hall coefficients [69]. This makes anomalous Hall effect measurements an ideal approach for investigating the magnetization of FGT.

FGT displays electrically tunable magnetic properties, rendering it a highly promising candidate for potential future applications in electrically controlled spintronic devices. T_C was reported to be enhanced up to room temperature with liquid ionic gating [70]. This also tunes the coercive fields. Both properties are also reported to be modified by Fe-intercalation into the van der Waals gaps between the monolayer sheets [62]. Furthermore, it has been shown that the magnetization can be switched electrically by a spin-orbit torque originated from currents flowing in an additional Pt layer on top [71, 72] or via the Edelstein effect, when FGT is in contact to the topological insulator $(Bi_{1-x}Sb_x)_2Te_3$ [73].

FGT in spintronic devices

FGT has been utilized in many different spintronic devices. Magnetic tunnel junction devices consisting of FGT/hBN/FGT heterostructures result in a tunnelling magnetoresistance, defined as $(R_P - R_{AP})/R_P$, of up to 160% at 4.2 K [74]. Here, R_{AP} and R_P denote the resistance of the device in the antiparallel and parallel magnetization configuration of both FGT electrodes. This is two orders of magnitude larger than for tunnelling spin valve devices based on conventional ferromagnetic metallic films separated by van der Waals materials [75–80]. From these tunnelling spin valve measurements, the spin polarization of FGT of 0.66 could be deduced, corresponding to a percentage of majority and minority spins of 83 % and 17 %, respectively [74]. Vertical spin valve devices with a MoS_2 spacer layer between FGT electrodes only show a magnetoresistance of 12 % at 1.5 K [81, 82]. Here, the MoS_2 layer works as a conducting layer rather than a tunnelling layer [82]. Spin valve signals have even been observed in FGT/FGT homojunctions without an additional spacer layer exhibiting a magnetoresistance of 1.37 % at 10 K [83]. In this case, independent switching of the electrodes is maintained due to the increased van der Waals gap between both crystals due to the lattice misalignment.

Unlike in conventional giant magnetoresistance devices, a FGT/graphite/FGT heterostructure shows an antisymmetric magnetoresistance with respect to the external magnetic field with three distinct resistance states which is attributed to spin momentum locking induced by the spin polarized current at the graphite/FGT interface [84]. Here, a magnetoresistance of 1.3 % is observed at 2 K. Antisymmetric magnetoresistance signals have also been observed in single FGT flakes of inhomogeneous thickness [85]. An

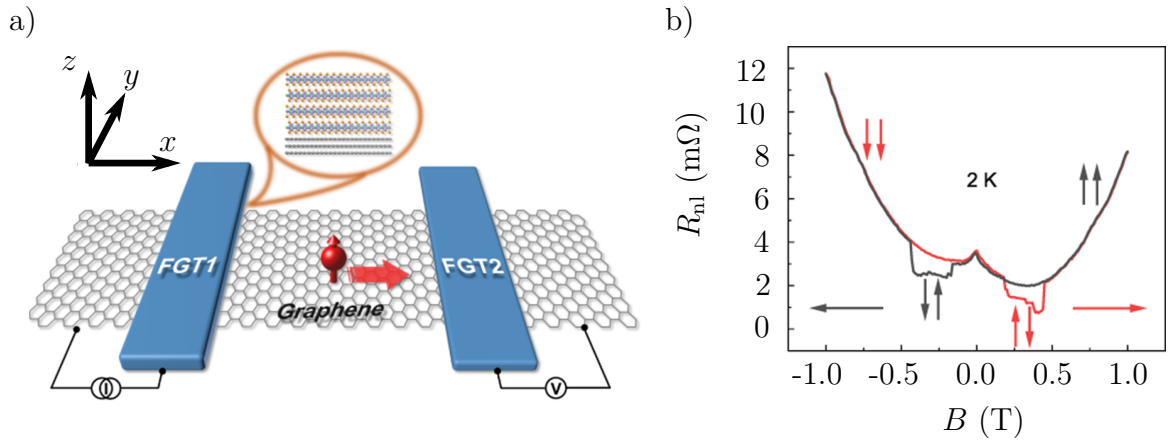

Fig. 2.3: a) Schematic of a fabricated non-local spin valve device from Ref. [31] consisting of a graphene channel and two Fe_3GeTe_2 flakes on top. A spin-polarized current is injected from the left FGT into the left side of the graphene flake. This results in a spin-accumulation in the graphene which also diffuses towards the right FGT electrode. A spin signal can then be measured as a non-local voltage. b) Spin valve measurement presented at a temperature of $T = 2\,\mathrm{K}$ and an applied bias of $I = 0.8\,\mathrm{mA}$ resulting in a spin valve height of $\Delta R_{\mathrm{nl}} \approx 1.5\,\mathrm{m\Omega}$. The red and grey arrows indicate the magnetization configuration of both FGT electrodes. Taken from [31].

unsynchronized switching of the magnetic domains at each FGT thickness results in a sign change of the anomalous Hall effect. Therefore, the measured resistance across the step terrace is sensitive to the exact magnetization direction of each domain. This can also be measured in a FGT/FGT homojunction as is described in Sec. 5.3.

The first reported lateral non-local spin valve devices utilizing FGT as spin injecting and detecting electrodes were reported in 2023 [31]. The sample schematic of these experiments is presented in Fig. 2.3 a). In this all-van der Waals based device, multilayer graphene is used for the spin transport channel. Independent switching of the FGT electrodes is ensured by their different thicknesses (16 and 23 nm) and geometry. The edge-to-edge distance of both FGT electrodes is 3 µm. As no tunnel barrier between the ferromagnetic FGT flakes and the graphene spin transport channel is present, both contact resistances are lower than 200 Ω. These transparent contacts lead to low spin injection and detection efficiencies as will be described in Sec. 3.2. As a consequence, the reported spin valve height ΔR_{nl} is only 1.5 mΩ, as illustrated in Fig. 2.3 b). From this, a spin injection efficiency of only 1 % is estimated. Due to the low spin injection efficiency and wide FGT electrodes, no Hanle spin precession signal could be observed. Therefore, an extraction of spin transport parameters was not possible. An introduction to the theory describing the non-local spin injection, detection, and transport can be found in Sec. 3.2. The non-local spin valve and Hanle experiments are described in Sec. 3.3 and 3.4, accordingly. The takeaway message is, that even though all-van der Waals based non-local spin valve devices using FGT have already been realized, the spin signals are

low due to the transparent FGT/graphene contacts. Therefore, also no spin precession experiments have been reported in such devices.

2.3. Graphene

The excitement surrounding 2D materials can be traced back to the first exfoliation of graphene in 2004 [7]. It is the thinnest possible material, being only one atom thick, which exhibits a wide range of remarkable properties. The following section will provide a detailed explanation of the crystallography and band structure of graphene, which will serve as a foundation for understanding the properties of this novel material. For this purpose, the theory presented in Sec. 2.3.2 is based on Katsnelson's book "Graphene: Carbon in Two Dimensions", which provides a comprehensive insight into graphene's properties [8]. This is followed by a brief introduction to the charge transport properties and the ambipolar electric field effect in graphene in Sec. 2.3.3.

2.3.1. Crystal lattice

Graphene is a two-dimensional layer of carbon atoms arranged in a hexagonal lattice, also known as a honeycomb lattice. Carbon is the sixth element in the periodic table, with an orbital configuration of $1s^2 2s^2 2p^2$, when naively filling the orbitals. However, in graphene, the $2s$ orbital mixes with the $2p_x$ and $2p_y$ orbitals, forming hybridized sp^2 orbitals, as can be seen in Fig. 2.4 a) [8, 86]. This hybridization requires energy which is provided by the lattice formation of carbon atoms. A maximization of the electron wave function overlap results in minimizing the total energy, which is sufficient to form this sp^2 hybridization [8]. In graphene, three out of the four valence electrons create sp^2 hybrid orbitals that form strong σ-bonds with their in-plane neighbours, separated by 120°, as shown in Fig. 2.4 a) [8]. This results in the hexagonal structure of the graphene lattice and its mechanical stability is mainly attributed to these bonds [86]. The fourth valence electron is located in the p_z orbital, perpendicular to the lattice plane, forming delocalized π-bonds. The electrical properties of graphene are mainly attributed to these π-bonds. The σ- and π-bonds result in a lattice with an atom-to-atom distance of $a = 1.42\,\text{Å}$ [86, 87]. The lattice is described by a basis of two atoms with equivalent sites A and B, each with separate triangular Bravais lattices, as depicted in Fig. 2.4 b). The corresponding reciprocal lattice with the special $\vec{K}$ and $\vec{K}'$ points in the Brillouin zone are shown in Fig. 2.4 c).

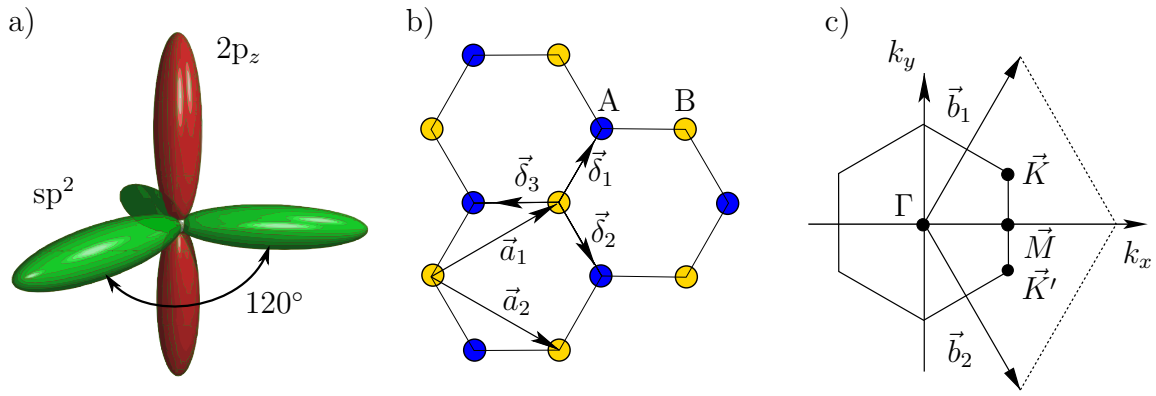

Fig. 2.4: a) Sketch of the three sp^2 orbitals (green) and the 2p$_z$ orbital (red) of a single carbon atom. The sp^2 orbitals are in a plane separated by an angle of 120° to each other. Adapted from [88]. b) Hexagonal crystal lattice with sublattices A and B shown in blue and yellow, respectively. The lattice vectors $\vec{a}_1$ and $\vec{a}_2$ span the triangular Bravais lattice, $\vec{\delta}_1$, $\vec{\delta}_2$, and $\vec{\delta}_3$ are the vectors to the nearest neighbours. Adapted from [86]. c) Brillouin zone of graphene with the lattice vectors $\vec{b}_1$ and $\vec{b}_2$. In the special $\vec{K}$ and $\vec{K}'$ points the energy bands touch. Adapted from [86].

2.3.2. Band structure

The band structure of graphene can be seen in Fig. 2.5 a). It was first calculated by Wallace in 1947 [87], using a tight binding model to describe the band structure of graphite. In this model, the wave function is a linear combination of two Bloch-functions $\Psi_{A,B}$ that originate from the two atomic p_z orbitals $X(\vec{r})$ at the sublattices A and B [5, 86]

$$\begin{aligned}\Psi_{\vec{k}}(\vec{r}) &= \Psi_A + \lambda\Psi_B \\ &= \sum_A \exp\left(i\vec{k}\cdot\vec{R}_\mathrm{A}\right) X\left(\vec{r}-\vec{R}_\mathrm{A}\right) + \lambda\sum_B \exp\left(i\vec{k}\cdot\vec{R}_\mathrm{B}\right) X\left(\vec{r}-\vec{R}_\mathrm{B}\right),\end{aligned} \tag{2.4}$$

where the sum over A or B is taken over all lattice points of sublattice A and B, respectively. Furthermore, $\vec{r}$ is the coordinate of the atom in real space, $\vec{R}_\mathrm{A}$ and $\vec{R}_\mathrm{B}$ are the positions of the atoms in each sublattice, $\vec{k}$ is the Bloch wavevector, and $\lambda = \pm 1$ [5]. Using the nearest-neighbour approximation with t_hopping as the hopping parameter, only hopping to the nearest neighbour from sublattice A to B is considered [8, 87]. Hopping within a sublattice is neglected. The tight-binding Hamiltonian in this approximation is written as [8]

$$H(\vec{k}) = \begin{pmatrix} 0 & t_\mathrm{hopping} S(\vec{k}) \\ t_\mathrm{hopping} S^*(\vec{k}) & 0 \end{pmatrix}. \tag{2.5}$$

The values for the hopping parameter vary in the literature from $t_\mathrm{hopping} \approx 2.7 - 3.1\,\mathrm{eV}$ [8, 86, 89]. Furthermore,

$$S(\vec{k}) = \sum_{\vec{\delta}} \exp\left(i\vec{k}\vec{\delta}\right) = 2\exp\left(\frac{ik_x a}{2}\right)\cos\left(\frac{k_y a\sqrt{3}}{2}\right) + \exp\left(-ik_x a\right), \tag{2.6}$$

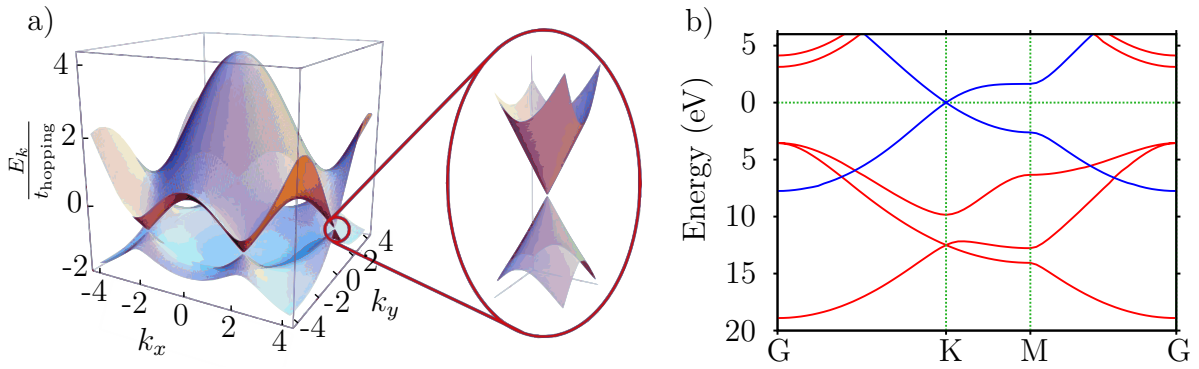

Fig. 2.5: a) Band structure of graphene with a zoom to the dispersion close to the $\vec{K}$ and $\vec{K}'$ points. The energy scale is divided by the hopping parameter t_{hopping}. Adapted from [86]. b) Band structure of graphene with energy bands arising from the σ- and π-bonds in red and blue, respectively. The π-bands touch each other at the $\vec{K}$ point. Adapted from [90].

where the summation is over the nearest neighbours $\vec{\delta}$ (see Fig. 2.4 b)) [8]. The energy dispersion can be obtained by finding the eigenvalues of this Hamiltonian. One finds [8]:

$$E(\vec{k}) = \pm t_{\text{hopping}} \left|S(\vec{k})\right| = \pm t_{\text{hopping}} \sqrt{3 + 2\cos\left(\sqrt{3}k_y a\right) + 4\cos\left(\frac{\sqrt{3}}{2}k_y a\right)\cos\left(\frac{3}{2}k_x a\right)}. \tag{2.7}$$

The conduction and valence band correspond to the positive (+) and negative (-) prefactor of Eq. (2.7), respectively. It can be seen that there are points $\vec{K}$ and $\vec{K}'$ in the Brillouin zone where $S(\vec{K}) = S(\vec{K}') = 0$, and thus $E(\vec{K}) = E(\vec{K}') = 0$. These are high-symmetry points with the wavevectors [86]

$$\vec{K} = \left(\frac{2\pi}{3a}, -\frac{2\pi}{3\sqrt{3}a}\right), \vec{K}' = \left(\frac{2\pi}{3a}, \frac{2\pi}{3\sqrt{3}a}\right). \tag{2.8}$$

As illustrated in Fig. 2.5 a) and b), the valence and conduction bands touch at these special points in the Brillouin zone. By expanding the Hamiltonian around these points with $\vec{q} = \vec{k} - \vec{K}$, $\vec{q} = \vec{k} - \vec{K}'$, and $|\vec{q}| \ll |\vec{K}|, |\vec{K}'|$, one gets [8]

$$H_{K,K'}(\vec{q}) = \hbar v_{\text{F}} \begin{pmatrix} 0 & q_x \mp i q_y \\ q_x \pm i q_y & 0 \end{pmatrix}, \tag{2.9}$$

where $v_{\text{F}} = \frac{3a|t_{\text{hopping}}|}{2\hbar} \approx 1 \cdot 10^6 \frac{\text{m}}{\text{s}}$ is the Fermi velocity, with $\hbar$ being the reduced Planck's constant [89]. The dispersion relation near $\vec{K}$ and $\vec{K}'$ is dependent on the Fermi velocity v_{F} and is given by [86]

$$E(\vec{q}) \approx \pm \hbar v_{\text{F}} |\vec{q}|. \tag{2.10}$$

This linear dispersion relation is equivalent to the Dirac equation for relativistic particles with zero mass. Consequently, electrons close to the $\vec{K}$ and $\vec{K}'$ points, which are also

referred to as Dirac points, behave like such particles. However, it should be noted that these relativistic particles are subject to a finite cyclotron mass, as will be described in the following section.

2.3.3. Charge transport in graphene

The charge carrier transport in graphene can be described by the Drude model. This model employs the kinetic gas theory to describe charge carriers as free particles moving with a thermal velocity v_{th} that scatter with the atoms in the lattice. The electrical conductivity is described as [91]

$$\sigma = \frac{ne^2\tau}{m^*} = ne\mu_{\mathrm{m}}, \tag{2.11}$$

where $\mu_{\mathrm{m}} = \frac{e\tau}{m^*}$ is the mobility, n is the charge carrier density, e is the electron charge, τ is the mean relaxation time, and m^* is the effective mass of the carriers. Although the linear energy dispersion in graphene suggests zero mass, as it is inversely proportional to the curvature, the cyclotron (effective) mass m_{c} of charge carriers scales with the Fermi wavevector $k_{\mathrm{F}} = \sqrt{\pi n}$ and is $m^* = m_{\mathrm{c}} = \hbar k_{\mathrm{F}}/v_{\mathrm{F}}^2$ [15, 92].

Ambipolar electric field effect of graphene

Graphene's transport properties can be widely tuned by applying a voltage V_{g} at a gate electrode. This allows for the manipulation of the type of charge carriers from electrons to holes and modifies the charge carrier density and, consequently, the conductivity. This phenomenon is known as the ambipolar electric field effect of graphene, as illustrated in Fig. 2.6 a) and b). Here, the resistivity and conductivity are plotted as a function of the gate voltage V_{g}, respectively. The Fermi energy of intrinsic graphene lies at the intersection of the valence and conduction bands, resulting in maximum resistivity. By applying a negative (positive) gate voltage, the Fermi energy is shifted into the valence (conduction) band leading to charge transport governed by holes (electrons).

This effect can be derived using a simple plate capacitor model. The samples presented in this thesis have graphene placed onto a highly doped p^{++} Si substrate with a 285 nm thick dielectric SiO_2-layer on top. In the capacitor model, the doped Si substrate and graphene correspond to the plates of the capacitor, while the SiO_2 serves as the gate dielectric. The capacitance is $C = \frac{Q}{V_{\mathrm{g}}} = \epsilon_0\epsilon_r\frac{A}{d}$, with Q and V_{g} being the charge and the applied voltage at the gate. A and d are the area and the distance of the capacitor plates. ϵ_0 and ϵ_r denote the vacuum permittivity and relative permittivity of the dielectric material, respectively. From this ansatz one obtains

$$n = \epsilon_0\epsilon_r\frac{V_{\mathrm{g}}}{ed} = C_g\frac{V_{\mathrm{g}}}{e}, \tag{2.12}$$

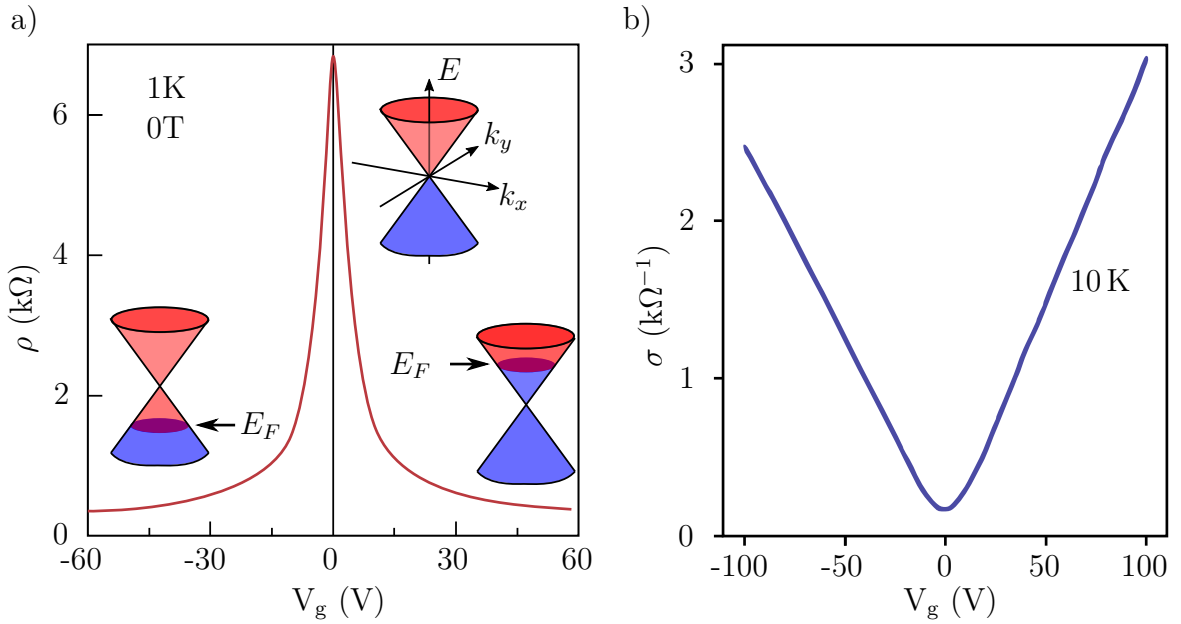

Fig. 2.6: Ambipolar electric field effect of graphene. a) The resistivity ρ decreases with V_g^{-1}. V_g changes the charge carrier density n and induces holes (electrons) at negative (positive) V_g. The insets show the corresponding positions of the Fermi energy. Blue (red) color indicates occupied (empty) states. Adapted from [92]. b) Conductivity σ as a function of V_g. σ scales linearly with the applied V_g, as expected by Eq. (2.13). At $V_g = 0\,\mathrm{V}$ the Fermi energy lies in the intersection of valence and conduction band, showing a finite resistivity and conductivity due to electron-hole puddles. Adapted from [93]. It has to be noted that panels a) and b) do not correspond to the same measurement.

with $C_g = \frac{\epsilon_0 \epsilon_r}{d}$ being the gate coupling constant. When there are multiple dielectrics, i.e. insulating layers with varying thicknesses between the doped Si substrate and the graphene, the total gate coupling constant is calculated as the sum of the individual inverse gate coupling constants, similar to a series circuit of capacitors. With a SiO_2 thickness of $d = 285\,\mathrm{nm}$ and a relative permittivity of $\epsilon_{r,\mathrm{SiO_2}} = 3.9$ [94] the gate coupling constant is then calculated to be $C_g = 1.2 \cdot 10^{-4}\,\frac{\mathrm{As}}{\mathrm{Vm}^2}$. By inserting Eq. (2.12) into Eq. (2.11), one obtains the conductivity in dependence of the applied gate voltage V_g

$$\sigma = ne\mu_m = \frac{\epsilon_0 \epsilon_r}{d} V_g \mu_m = C_g V_g \mu_m. \tag{2.13}$$

Unintentional doping of the graphene, e.g. by absorbed water or adsorbates from the environment, can introduce an initial charge carrier density and can be observed as a voltage shift V_{CNP} of the minimum of the conductivity, while sweeping the gate voltage [7, 92]. To account for this voltage shift V_{CNP}, V_g needs to be exchanged with $(V_g - V_{\mathrm{CNP}})$ in Eq. (2.12) and Eq. (2.13).

Fig. 2.6 a) and b) show a gate sweep of the resistivity $\rho = \sigma^{-1}$ and conductivity σ, which exhibit the expected dependencies according to Eq. (2.13). σ scales linearly with V_g. At

$V_g = 0\,\mathrm{V}$, the conductivity is finite even though the charge carrier density vanishes. This can be attributed to the rough SiO_2 surface, which introduces an inhomogeneous potential across the graphene due to charged impurities trapped at the surface. As a result, the charge carrier density is unevenly distributed, leading to localized areas with electrons and holes, known as electron-hole puddles [95, 96]. Gate-dependent measurements of graphene's resistivity are also known as Dirac measurements. As the gate voltage tunes the Fermi energy across the Dirac cone, the density of states (DOS) and, consequently, the resistivity changes. The point of highest resistivity reflects the point where the valence and conduction bands touch, as indicated by the inset of Fig. 2.6 a). This special point is also referred to as charge neutrality point (CNP), as at this point the hole and electron densities are equal.

Charge diffusion constant D_c

The charge carrier transport in graphene can be described by a diffusion process characterized by the charge diffusion constant D_c. Applying a gate voltage V_g shifts the Fermi energy E_F through the electronic band structure of graphene. In electrical transport measurements this can be seen in the gate response of the conductivity σ, which is a measure of the density of states at the Fermi energy $g(E_F)$. The Einstein relation $\sigma = e^2 g(E) D_c$ links the conductivity σ to the DOS $g(E)$ and the charge diffusion constant D_c. The DOS of graphene is given by [97]

$$g(E) = \frac{g_v g_s 2\pi |E|}{h^2 v_F^2}, \tag{2.14}$$

with the valley and spin degeneracies $g_v = 2$ and $g_s = 2$ and the Planck's constant h. The charge carrier density $n(E_F)$ at the Fermi energy can be derived by integrating the energy from 0 to E_F. One obtains

$$n(E_F) = \frac{g_v g_s \pi E_F^2}{h^2 v_F^2}. \tag{2.15}$$

The DOS at the Fermi energy can be calculated by rearranging Eq. (2.15) and substituting the result into Eq. (2.14)

$$g(E_F) = \frac{2}{h v_F} \sqrt{g_v g_s \pi n(E_F)}. \tag{2.16}$$

Applying the Einstein relation allows to calculate the charge diffusion constant D_c at the Fermi energy E_F with Eq. (2.16)

$$D_c = \frac{\sigma}{e^2 g(E_F)} = \frac{h v_F}{2e^2 \sqrt{g_v g_s \pi}} \frac{\sigma}{\sqrt{n(E_F)}}. \tag{2.17}$$

With a vanishing charge carrier density $n(E_F)$ at $E_F = 0$, this introduces a singularity in the charge diffusion constant D_c. In real experiments, however, it is found that the

carrier density and consequently the DOS are finite at $E_\mathrm{F} = 0$ due to finite temperature and electron-hole puddles [97]. To account for these effects, a Gaussian broadening of the density of states is introduced in the form of [97]

$$\begin{aligned} g^*(E_\mathrm{F}) &= \frac{1}{\sqrt{2\pi}\xi} \int_{-\infty}^{\infty} \exp\left(-\frac{(\epsilon - E_\mathrm{F})^2}{2\xi^2}\right) g(\epsilon)\, d\epsilon \\ &= \frac{g_v g_s 2\pi}{h^2 v_\mathrm{F}^2} \left[\frac{2\xi}{\sqrt{2\pi}} \exp\left(-\frac{E_\mathrm{F}^2}{2\xi^2}\right) + E_\mathrm{F} \operatorname{erf}\left(\frac{E_\mathrm{F}}{\sqrt{2}\xi}\right)\right], \end{aligned} \tag{2.18}$$

with the Gaussian error function erf and the broadening energy ξ. Using this modified DOS and the Fermi energy E_F from Eq. (2.15), one obtains a modified charge diffusion constant. This modified charge diffusion constant can later be compared to the spin diffusion constant D_s, which is extracted from spin precession experiments.

2.4. Hexagonal Boron Nitride hBN

Hexagonal boron nitride (hBN) is a layered van der Waals polymorph of the boron nitride compounds. It is commonly used as a substrate, gate dielectric, tunnelling barrier, as well as a protective layer in van der Waals heterostructures [68, 98–101]. The hexagonal structure of hBN results from the sp^2-hybridisation similar to graphene, forming a two-dimensional hexagonal lattice with alternating boron and nitrogen atoms [102–104]. Boron and nitrogen form strong covalent bonds in plane, with weak van der Waals forces between the layers. As a consequence, bulk crystals can easily be exfoliated by the scotch tape method. In bulk hBN crystals, the boron and nitrogen atoms of the individual sheets are stacked directly on top of each other in an alternating manner, as can be seen in Fig. 2.7 a). The lattice constant of hBN is quite similar to that of graphene with a nearest neighbour distance of $a_\mathrm{hBN} = 1.44\,\text{Å}$ [105]. This results in a small lattice mismatch to graphene of only 1.7 %. Despite the same sp^2 orbital hybridisation, the electrical properties of hBN are quite different compared to graphene. With an indirect band gap of 5.95 eV [103, 106, 107], bulk hBN is electrically insulating. The band structure of monolayer hBN can be seen in Fig. 2.7 b).

When graphene is exfoliated onto a commonly utilized $\mathrm{Si/SiO_2}$ substrate, it adheres to the rough surface. However, exfoliating hBN results in atomically flat crystals that do not have any dangling bonds or trapped charges [108], which could negatively affect the transport properties of graphene when hBN is used as a substrate [21]. Furthermore, the atomic smoothness of hBN can mask the roughness of an underlying substrate, resulting in almost perfectly flat graphene layers. Together with the small lattice mismatch to graphene, this makes hBN an ideal substrate candidate for graphene devices [98, 99]. Placing hBN on top of graphene protects it from environmental influences [68]. Therefore, sandwiching graphene between two hBN layers isolates it from the environment, resulting

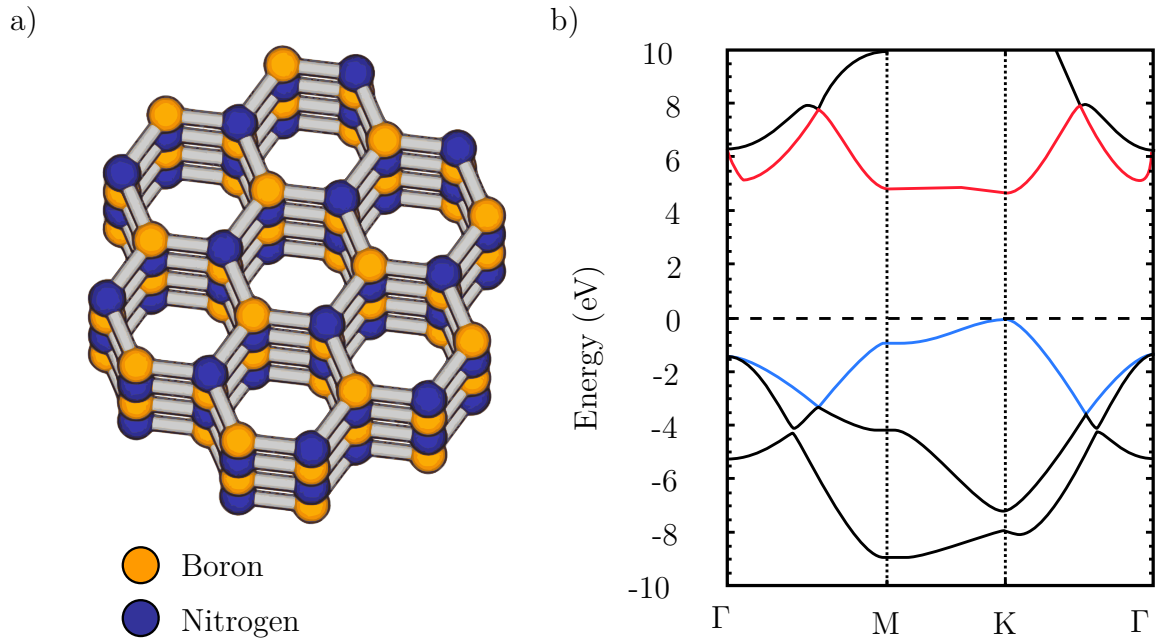

Fig. 2.7: a) Lattice structure of hBN. In the covalent bonds, boron and nitrogen atoms are alternating. hBN favours an alternating stacking with a boron atom on top of a nitrogen atom and vice versa. Adapted from [104]. b) Band structure of monolayer hBN calculated using density functional theory with the PBE-D3 method. The band gap of 4.69 eV at the K point is visible. The calculated band gap varies with respect to included corrections in the model from 4.69 eV to 7.92 eV. Adapted from [102].

in excellent transport properties and mobilities in fully encapsulated graphene samples [100]. In this thesis, hBN is used as a tunnel barrier and protection layer. This ensures an efficient spin injection between the ferromagnetic FGT and graphene as will be explained in Sec. 3.2. Furthermore, the hBN encapsulation on top of FGT prevents oxidation of these ferromagnetic contacts [68].

3. Theoretical background on spin transport

Spin injection is the process of generating a non-equilibrium spin accumulation in materials, such as metals and semiconductors. This can be achieved electrically, optically, and by other mechanisms like spin pumping. Sending a current consisting of spin-polarized electrons from one material to another to produce a spin accumulation is called electrical spin injection. Typically, these spin-polarized currents are obtained by means of ferromagnetic metals, which have a different density of states for spin up and down electrons, as depicted in Fig. 2.1 b). A detailed theoretical explanation of spin injection is beyond the scope of this thesis. However, a brief theoretical framework is presented here to help understand the experimental results of this thesis. The following sections Sec. 3.1 and Sec. 3.2 describe the electrical injection, transport, and detection of such a spin accumulation, based on the comprehensive description of J. Fabian *et al.* [17] and Žutić *et al.* [109]. The notation adheres to the established standard model of spin injection [110]. This is followed by the description of the non-local spin valve and the non-local Hanle effect in Sec. 3.3 and Sec. 3.4, respectively. Subsequently, the most prevalent spin-relaxation mechanisms discussed in the literature for graphene are presented in Sec. 3.5, followed by a description of the *COMSOL Multiphysics* simulations in Sec. 3.6.

3.1. Spin transport

Spin transport is described by separately defining quantities for majority and minority spins. The transport is treated as occurring in a parallel circuit of two spin channels, following the two-current model introduced by N. Mott [111]. For example, the total carrier density n is described as the sum of the carrier densities of spin-up $n_\uparrow$ and spin-down $n_\downarrow$ charge carriers, while the difference between the two densities gives the spin density s:

$$\begin{aligned} n &= n_\uparrow + n_\downarrow, \\ s &= n_\uparrow - n_\downarrow. \end{aligned} \tag{3.1}$$

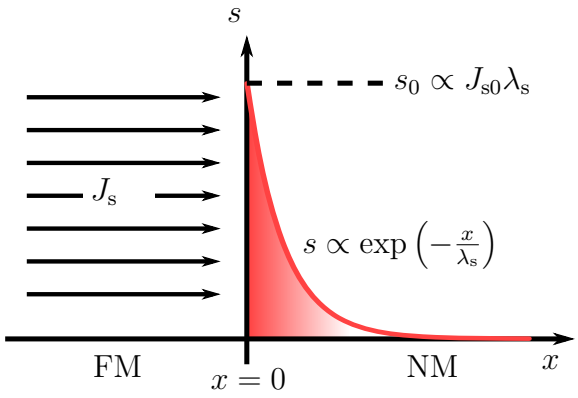

Fig. 3.1: Schematic of the spin injection from a FM ($x < 0$) into a NM ($x > 0$). A constant spin current from a FM leads to a finite spin density at the FM/NM interface which diffuses exponentially with the corresponding diffusion length λ_s in the NM. Adapted from [17].

The drift and diffusion of the spin density s can be derived from a random walk model of electrons that change direction after a mean free path l. This results in the spin drift-diffusion equation [17]

$$\frac{\partial s}{\partial t} = D_s \frac{\partial^2 s}{\partial x^2} + \mu_m E \frac{\partial s}{\partial x} - \frac{s}{\tau_s}, \tag{3.2}$$

where D_s is the spin diffusion constant, E is the electric field, and τ_s is the spin relaxation time. The equation is made up of three terms on the right-hand side: the first describes the diffusion, while the second and third describe the drift and relaxation of the spin density s, respectively. In the following, an interface of a ferromagnetic conductor (FM) at $x < 0$ and a non-magnetic conductor (NM) at $x > 0$ is analysed. Assuming a constant spin current $J_s(0) = J_{s0} = -D_s \partial s/\partial x|_{x=0}$ at this interface leads to an accumulation of spin at the interface. The spatial distribution of the spin density s, as shown in Fig. 3.1, can be obtained by solving the steady-state solution of the spin drift-diffusion equation when no electric field is applied (E=0):

$$s(x) = s(0) \exp\left(-\frac{x}{\lambda_s}\right) = J_{s0} \frac{\lambda_s}{D_s} \exp\left(-\frac{x}{\lambda_s}\right), \tag{3.3}$$

where $\lambda_s = \sqrt{D_s \tau_s}$ is the spin diffusion length over which the spin density diffuses exponentially from the interface at $x = 0$ in the non-magnetic conductor. The accumulated spin density at the interface due to the constant spin current is given by

$$s_0 \equiv s(0) = J_{s0} \frac{\lambda_s}{D_s}. \tag{3.4}$$

Instead of using continuous drift-diffusion equations for charge and spin currents, the spin-transport can also be described by considering a quasi-chemical potential $\mu(x)$. In the presence of an electrostatic potential $\phi(x)$, the chemical potential η of the electronic system is no longer in equilibrium. Therefore, the chemical potential in the non-equilibrium situation is described by $\eta + e\mu(x)$. Assuming that charges do not accumulate inside the conductor (also referred to as local charge neutrality), the quasi-chemical potential μ fully balances the electrostatic potential ϕ so that $\mu(x) = -\phi(x)$. By introducing the

quasi-chemical potential for both spin species, the total quasi-chemical potential μ and the spin quasi-chemical potential μ_s are defined as

$$\begin{aligned} \mu &= \frac{1}{2}\left(\mu_\uparrow + \mu_\downarrow\right), \\ \mu_\mathrm{s} &= \frac{1}{2}\left(\mu_\uparrow - \mu_\downarrow\right). \end{aligned} \tag{3.5}$$

The introduction of the quasi-chemical potential generalizes the electric current $j = \sigma E$ to also include diffusive transport. The generalized current for each spin species is written as

$$j_{\uparrow/\downarrow} = \sigma_{\uparrow/\downarrow} \nabla \mu_{\uparrow/\downarrow}, \tag{3.6}$$

with the corresponding conductivities $\sigma_{\uparrow/\downarrow}$ of spin-up and -down charge carriers, respectively. The gradient of $\mu_{\uparrow/\downarrow}$ describes drift and diffusive currents. With Eq. (3.6) the total current carried by both spin species j and the spin current j_s, which corresponds to the difference of the currents of both spin species, is calculated as

$$j = j_\uparrow + j_\downarrow = \sigma \nabla \mu + \sigma_\mathrm{s} \nabla \mu_\mathrm{s}, \tag{3.7}$$

$$j_s = j_\uparrow - j_\downarrow = \sigma_\mathrm{s} \nabla \mu + \sigma \nabla \mu_\mathrm{s}, \tag{3.8}$$

with $\sigma = \sigma_\uparrow + \sigma_\downarrow$ and $\sigma_\mathrm{s} = \sigma_\uparrow - \sigma_\downarrow$. These two equations have the following implications: In a non-magnetic conductor, with $\sigma_\mathrm{s} = 0$, a charge current is generated solely as a consequence of a gradient in the total quasi-chemical potential μ. Furthermore, a spin current only arises due to a gradient in the spin quasi-chemical potential μ_s, which can only be caused by a spin accumulation. In contrast, in ferromagnetic conductors, where $\sigma_\mathrm{s} \neq 0$, a charge current can arise due to both, a gradient in the total quasi-chemical potential μ and a gradient in the spin quasi-chemical potential μ_s. The same is true for spin currents in ferromagnetic conductors. Consequently, in contrast to non-magnetic conductors, charge currents can be generated due to a gradient in the spin quasi-chemical potential μ_s, while spin currents can also arise as a consequence of a gradient in the total quasi-chemical potential μ in ferromagnetic conductors. This is crucial for both spin injection and detection.

The spin quasi-chemical potential μ_s is often referred to as the spin accumulation since it is directly proportional to the non-equilibrium spin density δs. Calculating the spin density using charge neutrality, one obtains:

$$s = s_0 + 4e\mu_\mathrm{s}\frac{g_\uparrow g_\downarrow}{g} = s_0 + \delta s, \tag{3.9}$$

where $g_{\uparrow/\downarrow}$ is the corresponding density of states for spin-up and spin-down charge carriers, g is the total density of states, and δs is the accumulated non-equilibrium spin. Since δs is linear in μ_s, from now on μ_s will be referred to as spin accumulation. Assuming a finite spin accumulation at the interface of the ferromagnetic and non-magnetic conductor, the diffusion of the spin accumulation is then described by the following diffusion equation:

$$\nabla^2 \mu_\mathrm{s} = \frac{\mu_\mathrm{s}}{L_\mathrm{s}}. \tag{3.10}$$

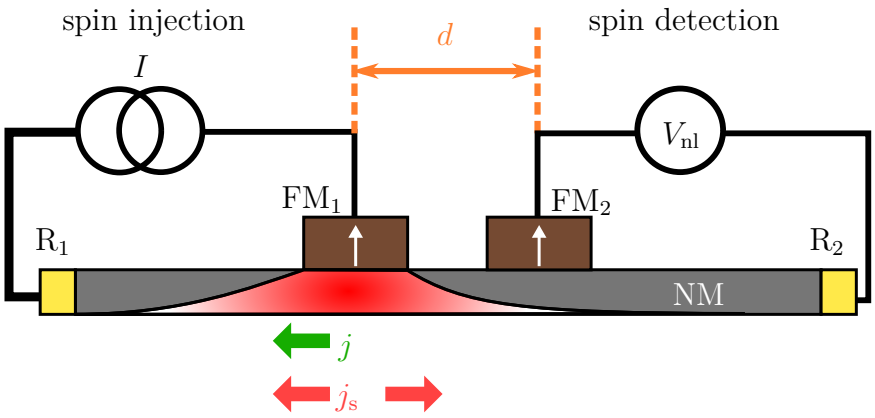

Fig. 3.2: Non-local spin injection geometry. A constant spin polarized current j (green) is applied between FM_1 and the reference contact R_1 on the left side. No charge current is present between FM_1 and FM_2. The injected spin current j_s (red) diffuses in all directions, so that underneath the FM_2 electrode at a distance d a finite non-equilibrium spin accumulation is still present that can be measured as a non-local voltage V_{nl}. It is to be noted, that at the injecting circuit, the spin current is accompanied by an electric field which influences the spin accumulation according to Eq. (3.2). Therefore, the spin accumulation is not symmetric on the left and right side of the injector.

Here, L_s is the diffusion length of the spin accumulation related to the generalized diffusivity $\overline{D}$:

$$\begin{aligned} L_s &= \sqrt{\overline{D}\tau_s}, \\ \overline{D} &= \frac{g}{\frac{g_\uparrow}{D_\downarrow} + \frac{g_\downarrow}{D_\uparrow}}. \end{aligned} \tag{3.11}$$

In non-magnetic conductors $g_\uparrow = g_\downarrow$ and $D_\uparrow = D_\downarrow$. In this case, $\overline{D} = D_s$ so that the diffusion lengths of the spin accumulation and of the spin density are identical ($L_s = \lambda_s$).

3.2. Electrical spin injection and detection

So far, spin transport has been discussed under the introduction of a quasi-chemical potential at a single ferromagnet/non-magnet interface. The following section describes the electrical injection and detection of spins using the non-local spin-injection geometry introduced by M. Johnson and R. Silsbee [112, 113]. This geometry consists of two ferromagnetic contacts on top of a non-magnetic channel, as shown in Fig. 3.2. A charge current is passed from FM_1 to the NM reference contact R_1 on the left, resulting in a constant spin-polarized current in the NM channel, as indicated by the green arrow.

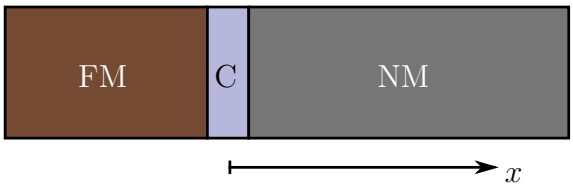

Fig. 3.3: Schematics of the FM/C/NM junction that is considered for the theoretical description of the electrical spin injection. Adapted from [17].

No charge current flows between both FM electrodes FM_1 and FM_2 or in the detection circuit on the right. This separation of the charge and the spin flow gives the non-local geometry its name. The spin accumulation in the NM due to the spin-polarized current diffuses exponentially in all directions, as indicated by the red arrows and the red shading in the NM channel. For sufficiently large spin diffusion lengths, a finite non-equilibrium spin accumulation is established below the detecting FM_2. The magnitude of this spin accumulation underneath this FM_2 electrode can be measured as a non-local voltage drop V_{nl} between the detecting FM_2 and a NM reference contact R_2 on the right. As FM_1 and FM_2 are responsible for injecting and detecting the spin accumulation, they are also referred to as injector and detector, respectively. This non-local geometry is the underlying basis of the spin transport and precession experiments and prevents the measurement of spurious voltage signals such as an additional voltage drop due to contact resistances as well as anisotropic magnetoresistance as a result of the separation of the charge and spin currents [15, 114].

Spin injection

In the following, we consider the injection of a spin accumulation from a FM located at $x < 0$ into a NM at $x > 0$ through a contact region C at $x = 0$, as shown in Fig. 3.3. The spin polarization of the electric current P_j is the ratio of the spin current j_s and the charge current j. By rearranging Eq. (3.7) to $\nabla\mu$ and substituting the result into Eq. (3.8), one obtains the spin polarization of the electric current P_j

$$P_j = \frac{j_{\mathrm{s}}}{j} = P_\sigma + \frac{4}{j}\frac{\sigma_\uparrow\sigma_\downarrow}{\sigma}\nabla\mu_{\mathrm{s}}, \tag{3.12}$$

where $P_\sigma = \sigma_{\mathrm{s}}/\sigma$ is the conductivity spin polarization. Eq. (3.12) can be used to calculate the spin injection efficiency, which quantifies how efficiently spins are injected from the FM into the NM. To calculate the spin injection efficiency, a FM/C/NM junction at $x = 0$ is considered. Solving the spin diffusion equation Eq. (3.10) at $x = 0$ for the FM and NM regions gives

$$\mu_{\mathrm{sF}}(x) = \mu_{\mathrm{sF}}(0)\exp\left(\frac{x}{L_{\mathrm{sF}}}\right), \qquad \text{(FM region)} \tag{3.13}$$

$$\mu_{\mathrm{sN}}(x) = \mu_{\mathrm{sN}}(0)\exp\left(-\frac{x}{L_{\mathrm{sN}}}\right), \qquad \text{(NM region)} \tag{3.14}$$

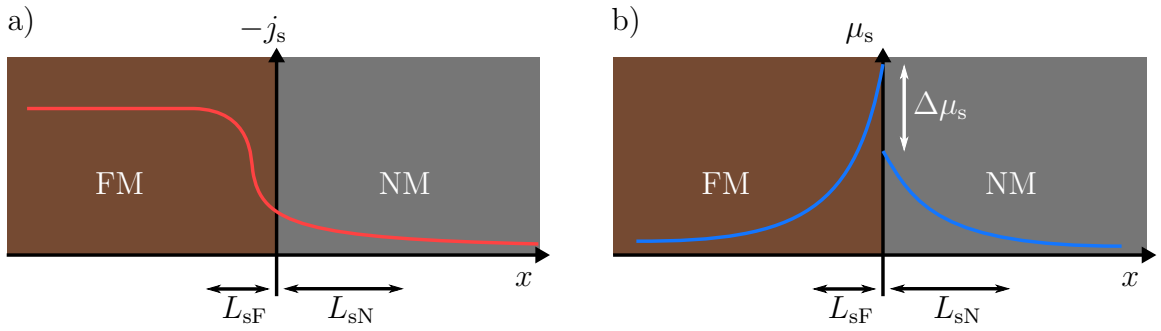

Fig. 3.4: Spatial profile of a) the continuous spin current j_s and b) the discontinuous non-equilibrium spin accumulation μ_s at the contact C at a FM/C/NM interface. Adapted from [17].

for the spin quasi-chemical potentials μ_{sF} and μ_{sN} with the corresponding spin diffusion lengths L_{sF} and L_{sN} in the FM and NM region, respectively. Here, a vanishing spin accumulation was assumed at $\mu_{sF}(-\infty) = 0$ and $\mu_{sN}(\infty) = 0$, which is well satisfied if the lengths of the FM and NM regions are larger than their corresponding spin diffusion lengths L_{sF} and L_{sN}. By forming the gradients of Eqs. (3.13) and (3.14) at $x = 0$ and inserting the result into Eq. (3.12), the current spin polarizations in the FM and NM are obtained as

$$P_{jF}(0) = P_{\sigma F} + \frac{1}{j}\frac{\mu_{sF}(0)}{R_F}, \qquad \text{(FM region)} \tag{3.15}$$

$$P_{jN}(0) = -\frac{1}{j}\frac{\mu_{sN}(0)}{R_N}, \qquad \text{(NM region)} \tag{3.16}$$

where $P_{\sigma F}$ is the conductivity spin polarization of the FM and

$$R_F = \frac{\sigma_F}{4\sigma_{F\uparrow}\sigma_{F\downarrow}} L_{sF} \qquad \text{(FM region)} \tag{3.17}$$

$$R_N = \frac{L_{sN}}{\sigma_N} \qquad \text{(NM region)} \tag{3.18}$$

denote the effective resistances of the FM and NM region, respectively. In a similar manner, the current spin polarization at the contact C ($x = 0$) can be derived, resulting in

$$P_{jC} = P_\Sigma + \frac{1}{j}\frac{\mu_{sN}(0) - \mu_{sF}(0)}{R_C}, \tag{3.19}$$

where Σ is the contact conductance and $P_\Sigma = \Sigma_s/\Sigma$ is its corresponding spin polarization, with the effective contact resistance $R_C = \Sigma/4\Sigma_\uparrow\Sigma_\downarrow$. Note, that at the contact the spin quasi-chemical potential is discontinuous, as can be seen in Fig. 3.4 b). Assuming that the spin current is continuous and, therefore, conserved across the contact, as illustrated in Fig. 3.4 a), the current spin polarizations must be identical at $x = 0$, so that $P_j \equiv P_{jF}(0) = P_{jN}(0) = P_{jC}$. Solving this algebraic problem gives the current spin

polarization P_j, also known as the spin injection efficiency:

$$P_j = \frac{R_\mathrm{F} P_{\sigma F} + R_\mathrm{C} P_\Sigma}{R_\mathrm{F} + R_\mathrm{C} + R_\mathrm{N}}. \tag{3.20}$$

This is one of the key results of the standard model of spin injection and explains the so-called conductivity mismatch problem. If the conductivities of the NM and FM region differ significantly from each other, a high contact resistance is required for efficient spin injection. In the case of transparent contacts, the effective contact resistance is negligible ($R_\mathrm{C} \to 0$). The effective resistances in the NM region R_N are typically larger than those in the FM region R_F, as $L_\mathrm{sN} \gg L_\mathrm{sF}$. If the NM region is also a semiconductor and the FM region is a metal, then $\sigma_\mathrm{F} \gg \sigma_\mathrm{N}$, so that $R_\mathrm{N} \gg R_\mathrm{F}$. In this case, the spin injection efficiency is greatly reduced as the conductivities of the two regions are very different. However, by adding a tunnel contact in between the FM and NM regions with $R_\mathrm{C} \gg (R_\mathrm{N}, R_\mathrm{F})$, the spin injection efficiency is dominated by the conductivity spin polarization of the contact P_Σ. In this scenario, the mismatch of the conductivities in the FM and NM is negligible and spin injection can be highly efficient. Therefore, the conductivity mismatch problem motivates the use of a tunnel barrier to ensure efficient spin injection.

The injected spin accumulation in the NM can be calculated with the spin injection efficiency from Eq. (3.16), such that

$$\mu_\mathrm{sN}(0) = -jP_j R_\mathrm{N}. \tag{3.21}$$

The spin accumulation is directly proportional to the current. If the current in the NM is carried by electrons, spins from the FM are injected into the NM for $j < 0$ and extracted from the NM for $j > 0$. However, if the current is carried by holes, spins are injected for $j > 0$ and extracted for $j < 0$. Both processes, known as spin injection and spin extraction, result in a non-equilibrium spin accumulation in the NM region.

Spin bottleneck

As can be seen in Fig. 3.4 b), the spin accumulation in the FM region builds up at the FM/C/NM interface. This leads to a non-vanishing gradient of the spin accumulation μ_s, that results in a charge current in the FM according to Eq. (3.7), flowing back into the FM in the opposite direction to the applied current. This creates an additional resistance δR, known as the spin bottleneck effect. The total series resistance of the FM/C/NM junction can then be written as $\hat{R}_\mathrm{F} + 1/\Sigma + \hat{R}_\mathrm{N} + \delta R$, where $\hat{R}_\mathrm{F}$ and $\hat{R}_\mathrm{N}$ are the actual resistances of the FM and NM regions normalized to their cross-sectional area, respectively. If $\Sigma_\uparrow = \Sigma_\downarrow$, then $1/\Sigma$ corresponds to the electrical resistance of the contact R_C. The additional resistance δR due to the non-equilibrium spin accumulation in the FM at the interface is given by

$$\delta R = \frac{R_\mathrm{N}(P_\Sigma^2 R_\mathrm{C} + P_{\sigma F}^2 R_\mathrm{F}) + R_\mathrm{F} R_\mathrm{C}(P_{\sigma F} - P_\Sigma)^2}{R_\mathrm{F} + R_\mathrm{C} + R_\mathrm{N}} > 0. \tag{3.22}$$

This additional resistance is always positive, resulting in an increase in the total junction resistance in the presence of a non-equilibrium spin accumulation in the FM.

Spin detection

When a spin-polarized electric current is driven from a FM to a NM, a non-equilibrium spin density accumulates in the NM region. To detect this spin accumulation, the inverse effect, also known as the Silsbee-Johnson spin-charge coupling, can be used. Here, a spin accumulation in the NM region, which is in proximity to a FM, induces a current flow in the FM in a closed circuit. In an open circuit, an electromotive force (emf) builds up, which can be measured as a non-local voltage V_{nl}, as depicted by the spin detection circuit on the right in Fig. 3.2. This inverse effect was proposed by Silsbee [112] in 1980 and experimentally demonstrated five years later by Johnson and Silsbee [113].

The Silsbee-Johnson spin-charge coupling is analysed in a FM/C/NM junction. The spin accumulation in the FM region ($x < 0$) vanishes for $\mu_{\mathrm{sF}}(-\infty) = 0$, while a finite spin accumulation in the NM region ($x > 0$) at $x = \infty$, $\mu_{\mathrm{sN}}(\infty) \neq 0$, is present. This results in a finite spin accumulation at the contact ($x = 0$) that generates an emf in the open circuit ($j = 0$). The emf is the drop of the quasi-chemical potentials across the junction. Assuming local charge neutrality, the emf can be calculated,

$$\mathrm{emf} = \mu_{\mathrm{N}}(\infty) - \mu_{\mathrm{F}}(-\infty) = \Delta\mu(0) - P_{\sigma\mathrm{F}}\mu_{\mathrm{sF}}(0), \tag{3.23}$$

where the drop of the quasi-chemical potential at the contact is

$$\Delta\mu(0) = -R_{\mathrm{C}}P_{\Sigma}j_{\mathrm{s}}(0). \tag{3.24}$$

To calculate the emf, it is necessary to determine the spin quasi-chemical potential $\mu_{\mathrm{sF}}(0)$ and the spin current $j_{\mathrm{s}}(0)$. Assuming a conserved spin current across the interface at $x = 0$ yields

$$\mu_{\mathrm{sF}}(0) = \frac{R_{\mathrm{F}}}{R_{\mathrm{F}} + R_{\mathrm{C}} + R_{\mathrm{N}}}\mu_{\mathrm{sN}}(\infty), \tag{3.25}$$

with $j_{\mathrm{s}}(0) = 1/R_{\mathrm{F}}\mu_{\mathrm{sF}}(0)$, as can be calculated from Eq. (3.7), (3.8), and (3.13) in the FM region. The emf is summarized as

$$\mathrm{emf} = -\frac{R_{\mathrm{F}}P_{\sigma\mathrm{F}} + R_{\mathrm{C}}P_{\Sigma}}{R_{\mathrm{F}} + R_{\mathrm{C}} + R_{\mathrm{N}}}\mu_{\mathrm{sN}}(\infty) = -P_j\mu_{\mathrm{sN}}(\infty). \tag{3.26}$$

The emf allows for the experimental detection of the non-equilibrium spin accumulation in the NM in proximity to a detecting FM as a non-local voltage. To achieve efficient spin detection, the spin injection efficiency P_j introduced in Eq. (3.20) must be sufficiently large. Therefore, the same contact resistance requirements ($R_{\mathrm{C}} \gg R_{\mathrm{N}}, R_{\mathrm{F}}$) apply to both spin injection and detection. This motivates utilizing tunnel barriers between the FM

and NM not only at the injecting, but also at the detecting FM electrode to ensure a large contact resistance R_C. In addition, the emf changes sign when either P_j or $\mu_{sN}(\infty)$ reverse sign. This can be achieved by reversing the magnetization direction of either the injector (which reverses the sign of the spin quasi-chemical potential $\mu_{sN}(\infty)$) or the detector (which reverses the sign of P_j).

Combining the spin injection with the detection circuit enables the realization of the non-local spin injection geometry. Here, spins are injected from a FM electrode into the NM ($x = 0$). This creates a non-equilibrium spin accumulation in the NM underneath the injector. Notably, there is no charge current between the injecting and detecting FM electrodes. As a result, spin transport between both electrodes is purely diffusive. The spin accumulation relaxes exponentially with L_s and can be detected at a second FM electrode ($x = d$) as a non-local voltage V_{nl}.

3.3. Non-local spin valve effect

The non-local spin-injection geometry, as depicted in Fig. 3.2, enables the experimental realization of spin injection and detection across a distance d. A spin-polarized current is driven from an injecting ferromagnetic contact FM_1 to a reference contact R_1 through a tunnel barrier C. This creates a non-equilibrium spin accumulation in the NM underneath FM_1, which diffuses in all directions. The transport between FM_1 and FM_2 is considered purely diffusive, as there is no voltage drop, and thus no electric field in this region. As spins are not conserved, spin relaxation occurs during diffusion, leading to an exponential decrease in spin accumulation as distance increases. A non-equilibrium spin accumulation is still present at a distance d at the detecting ferromagnetic electrode FM_2, when the spin diffusion length L_s of the NM is sufficiently large. Due to the tunnel barrier between the NM and FM_2 a sizeable emf can be measured as a non-local voltage drop V_{nl} between the FM_2 and a reference contact R_2 on the right side. The magnitude of this signal can be derived from the spatial distribution of the spin quasi-chemical potential. The associated non-local voltage drop V_{nl} measured at the detector at a distance d is given by [110, 115]

$$V_{nl}(d) = \frac{P_{inj} P_{det} R_s I L_s}{2w} \exp\left(-\frac{d}{L_s}\right), \tag{3.27}$$

where P_{inj} and P_{det} are the spin injection and detection efficiencies of the corresponding electrodes and correspond to the P_j used in Eq. (3.20) and Eq. (3.26), respectively. I is the applied current and R_s and w are the sheet resistance and the width of the NM channel. It is important to note that $V_{nl}(d)$ is either positive in a parallel or negative in an anti-parallel magnetization configuration. Inverting the magnetization direction of the injector (detector) inverts P_{inj} (P_{det}). In experiments, the difference of the parallel and anti-parallel signals normalized by the applied current I is evaluated as the spin

valve height ΔR_{nl} defined as

$$\Delta R_{\mathrm{nl}}(d) = \frac{P_{\mathrm{inj}} P_{\mathrm{det}} R_{\mathrm{s}} L_{\mathrm{s}}}{w} \exp\left(-\frac{d}{L_{\mathrm{s}}}\right). \tag{3.28}$$

3.4. Non-local Hanle effect

When applying an external magnetic field perpendicular to the magnetization direction of both FM electrodes, and therefore perpendicular to the injected spin direction, the magnetic field exerts a torque on the spin. The spins begin to rotate. In order to incorporate the precession of the spin $\vec{s}$, the spin drift-diffusion equation (Eq. (3.2)) has to be modified to [17]

$$\frac{\partial \vec{s}}{\partial t} = \vec{s} \times \vec{\omega}_0 + D_{\mathrm{s}} \nabla^2 \vec{s} + \mu_{\mathrm{m}} \vec{E} \nabla \vec{s} - \frac{\vec{s}}{\tau_{\mathrm{s}}}, \tag{3.29}$$

where $\vec{\omega}_0 = \frac{g_{\mathrm{L}} \mu_{\mathrm{B}}}{\hbar} \vec{B}$ is the Larmor frequency with the g-factor $g_{\mathrm{L}} = 2$, the Bohr's magneton μ_{B}, and the external perpendicular magnetic field $\vec{B}$. The additional term $\vec{s} \times \vec{\omega}_0$ describes the precession of the spins in the applied magnetic field. It is important to note that the spin $\vec{s}$ now has to be written as a vector due to finite x-, y- and z-components of $\vec{s}$ caused by the precession.

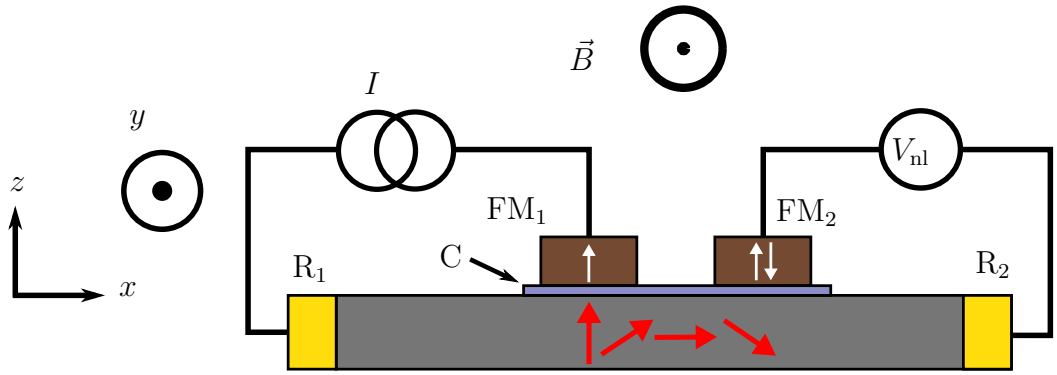

Fig. 3.5: Schematic of the non-local geometry for the Hanle effect. The external magnetic field is applied in y-direction, perpendicular to the magnetization direction of the FM electrodes. The injected spins (red arrows) precess in the x-z-plane. The tunnel barrier (C) ensures efficient spin injection into the NM.

When an external magnetic field is applied in y-direction, as shown in Fig. 3.5, the spins precess in the x-z-plane, as illustrated by the red arrows. The spins diffuse from the injector to the detector in a random walk. Therefore, the spins arriving at the detector travel along different paths, resulting in varying transit times t for each spin. As a result, spins arrive at the detector with different spin precession angles $\omega_0 t$. The detector probes

the average spin beneath the FM in the magnetization direction as a non-local voltage. In the presence of an external magnetic field perpendicular to the magnetization direction of the injector, the non-local voltage is then an integral over all transit times t given by [17]

$$V_{\mathrm{nl}}(\omega_0) = V_{\mathrm{nl}}(0) \int_0^\infty \mathrm{d}t \frac{1}{\sqrt{4\pi D_{\mathrm{s}} t}} \exp\left(-\frac{d^2}{4D_{\mathrm{s}} t}\right) \exp\left(-\frac{t}{\tau_{\mathrm{s}}}\right) \cos\left(\omega_0 t\right), \tag{3.30}$$

where the prefactor $V_{\mathrm{nl}}(0)$ is the non-local voltage signal at a distance $x = 0$ and $\vec{B} = 0$, as defined in Eq. (3.27). The first term in the integral - $\frac{1}{\sqrt{4\pi D_{\mathrm{s}} t}} \exp\left(-\frac{d^2}{4D_{\mathrm{s}} t}\right)$ - represents the spin diffusion, the second term - $\exp\left(-\frac{t}{\tau_{\mathrm{s}}}\right)$ - accounts for the spin relaxation, and the third term - $\cos\left(\omega_0 t\right)$ - corresponds to the projection of the precessed spin onto the magnetization axis of the detector. It is important to note that the spin relaxation may vary depending on the spin direction, resulting in different values of τ_{s} for spins aligned in different directions. Additionally, the size of the spin injector and detector have been disregarded in Eq. (3.30). In order to compare Eq. (3.30) with experimental measurements, it has to be integrated over the injector and detector widths w_{in} and w_{det}, respectively. The exact integration of Eq. (3.30) is presented in the Appendix Sec. A.4.1 and results in Eq. (A.6).

For spin precession experiments, the width of the ferromagnetic electrodes should be minimized. In wide injectors (detectors), spins are injected (detected) at different points of the FM. Consequently, the spins must travel different path lengths in the NM until they are detected, and thereby acquire disparate phases. This results in a reduction of the spin signal, which is circumvented by using narrow spin aligning electrodes. The Hanle effect allows to determine the spin relaxation time τ_{s}, spin diffusion constant D_{s}, and spin injection efficiency P by fitting the experimental data with Eq. (A.6), which takes the extended sizes of the injector and detector into account. Therefore, Hanle measurements give insights into the spin transport properties of the NM channel. It has to be noted that from fits, the product $P = \sqrt{P_{\mathrm{inj}} \cdot P_{\mathrm{det}}}$ is determined. However, for homogeneous tunnel barriers and small applied currents one can assume that $P_{\mathrm{inj}} = P_{\mathrm{det}}$. Consequently, P is also referred to as spin injection efficiency.

3.5. Spin-relaxation mechanisms in graphene

Hanle measurements provide access to the spin lifetime τ_{s}, often referred to as spin relaxation time or spin diffusion time. It is the time over which a non-equilibrium spin polarization decays. In graphene, several possible mechanisms that lead to spin relaxation have been considered [116–124]. This section presents the most common relaxation mechanisms discussed in the literature for graphene. The two most prominent representatives of spin-relaxation mechanisms are the Elliott-Yafet (EY) [125, 126] and Dyakonov-Perel (DP) [127] mechanisms, which originated in metal and semiconductor

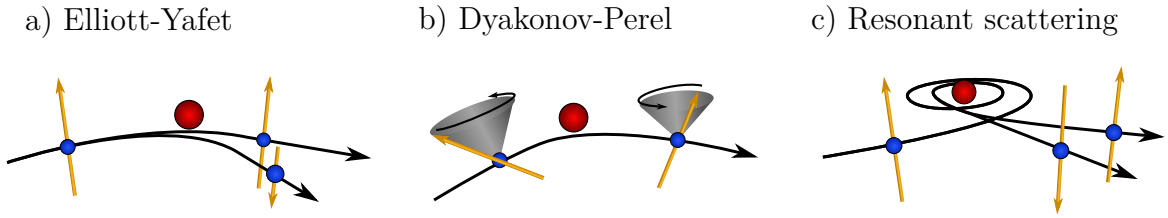

Fig. 3.6: The most frequently discussed spin relaxation mechanisms in graphene. a) In the Elliot-Yafet mechanism a charge carrier (blue) flips its spin (yellow arrow) due to momentum scattering at a scattering centre (red) in the presence of SOC. b) The Dyakonov-Perel mechanism describes the precession of the spin, indicated by the grey cone, in-between momentum scattering events in an effective magnetic field due to SOC. c) Resonant scattering at magnetic impurities leads to spin relaxation due to their finite magnetic moment. Adapted from [23].

spintronics. Both rely on spin-orbit coupling (SOC) and momentum scattering. The SOC is a relativistic effect that arises from electrons moving in the electric field of positively charged nuclei. In the electron's frame of reference, the nuclei are in motion, thereby producing a magnetic field that interacts with the spins. The strength of the SOC scales with the nuclei charge. The SOC in graphene is relatively weak, due to the sp^2 hybridization which leads to a reduced mixing of electrons with different spin directions [25]. This results in theoretical predictions of large spin relaxation times of up to 1 µs [23]. However, experiments have shown spin relaxation times of only several hundred picoseconds [27, 30, 32, 119], indicating an extrinsic origin of spin-relaxation. In real world graphene samples, multiple spin-relaxation mechanisms are present, resulting in an observable total spin relaxation time obtained from the Hanle fits. Therefore, identifying the dominant spin-relaxation mechanism in experiments is a non-trivial task.

3.5.1. Elliott-Yafet mechanism

The Elliott-Yafet mechanism [125, 126], as shown in Fig. 3.6 a), describes how spin flip can occur as a result of momentum scattering on impurities, lattice defects, or by phonons. These scattering mechanisms typically are spin-conserving. However, due to the presence of intrinsic SOC, the spin-up and spin-down states are no longer eigenstates of the complete Hamiltonian that describes the system. As a result, the charge carrier wave functions are described by a linear combination of states of opposing spin directions, which transforms the spin-conserving momentum-scattering into a mechanism that no longer conserves spin. As the SOC is introduced as a small perturbation, the spin states can still be identified as spin-up and spin-down along the initial axis. Each scattering event now has a finite probability to flip the spin. As a consequence, the momentum-scattering time τ_p and spin-relaxation time τ_s are coupled by [23, 120]

$$\tau_\mathrm{s} = \frac{\tau_\mathrm{p}}{\alpha_\mathrm{sf}} \approx \frac{E_\mathrm{F}^2}{\Delta_I^2}\tau_\mathrm{p}, \tag{3.31}$$

where α_{sf} can be interpreted as the spin-flip probability during a momentum-scattering event. E_{F} and Δ_I denote the Fermi energy and the intrinsic SOC strength. As the intrinsic SOC in graphene is relatively weak, an electron scatters up to a million times before its spin is flipped [23]. It has to be noted that the intrinsic spin-orbit interaction does not affect spins perpendicular to the surface, and therefore, they are not relaxed. This results in an anisotropy of spin relaxation times for in- and out-of-plane spins [121]. The EY mechanism can also be caused by Rashba type SOC due to gating electric fields or ripples [121]. Assuming realistic values for $E_{\mathrm{F}} = 100\,\mathrm{meV}$, $\Delta_I = 10\,\mu\mathrm{eV}$ [128, 129], and $\tau_{\mathrm{p}} = 10\,\mathrm{fs}$, one obtains large spin relaxation times of $\tau_{\mathrm{s}} = 1\,\mu\mathrm{s}$ [23] which is more than two orders of magnitude larger than experimentally observed [34]. To identify whether the EY mechanism is the dominant spin-scattering mechanism, the direct proportionality of τ_{s} to τ_{p} is investigated (as suggested by Eq. (3.31)). However, the ratio $\tau_{\mathrm{s}}/\tau_{\mathrm{p}}$ depends on the Fermi energy, which also tunes the charge carrier density in graphene (Eq. (2.15)). Therefore, a linear scaling between τ_{s} and τ_{p} which is independent of the carrier concentration cannot be attributed to the Elliot-Yafet mechanism [120].

3.5.2. Dyakonov-Perel mechanism

The Dyakonov-Perel mechanism [127], shown in Fig. 3.6 b), describes the precession of spins between two momentum scattering events. This precession can be caused by effective internal magnetic fields induced by Rashba type SOC. The direction of these fields depends on the momentum of the charge carrier. Spins that are at a finite angle to this effective magnetic field start to precess between two momentum-scattering events. After scattering, the momentum of the charge carrier is altered, resulting in a change of the effective magnetic field direction in which the spins precess. As charge carriers move in a random walk, their spins precess in different effective magnetic fields of varying directions and strengths. Therefore, each spin collects different phase angles, leading to destructive interference of the spin directions. The spin accumulation relaxes. To minimize this acquired phase angle, the momentum-scattering time τ_{p} should be kept short to minimize the mean free path in which the spins precess. This maximizes the spin relaxation time τ_{s}. The more the charge carrier's momentum scatters, the less its spin relaxes. As a consequence, τ_{s} scales inversely with the momentum-scattering time τ_{p} as [121]

$$\tau_{\mathrm{s}} = \frac{\hbar^2}{\Delta_R^2}\frac{1}{\tau_{\mathrm{p}}}, \tag{3.32}$$

where Δ_R corresponds to the Rashba SOC strength. Rashba SOC can be induced by breaking the space-inversion symmetry. This can be achieved by placing graphene on a substrate, but also by ripples in the graphene, adatoms, or gating electric fields [121, 130]. The SOC of graphene can also be enhanced when in proximity to a transition metal dichalcogenide (TMDC) which induces a large spin relaxation time anisotropy of in-plane and out-of-plane spins [26, 117]. Assuming $\Delta_R \approx 1\,\mu\mathrm{eV}$ with $\tau_{\mathrm{p}} = 10\,\mathrm{fs}$ for pristine

graphene gives a relaxation time of $\tau_s = 1\,\mu s$, again overestimating the spin relaxation time as in the case of the EY mechanism [23]. Introducing a Rashba field produced by the substrate in the presence of electron-hole puddles results in more realistic values ranging from 50 ps to several nanoseconds, where longer spin relaxation times are calculated for higher impurity concentrations, which is consistent with the DP mechanism [131].

3.5.3. Resonant scattering by magnetic impurities

Another spin relaxation mechanism is resonant scattering at magnetic impurities, as depicted in Fig. 3.6 c). Spins that scatter at magnetic impurities precess around the impurity's associated magnetic fields. The spin collects a phase angle which destructively interferes with other spins. Therefore, the spin accumulation relaxes. In pristine graphene samples, the concentration of these point-like defects that introduce magnetic moments, e.g. vacancies or covalently bonded hydrogen adatoms [123, 132, 133], is on the order of a few parts per million (ppm). Therefore, the effect would be expected to play a small role in spin-relaxation. However, in the case of resonant scattering at these sites, charge carriers spend more time in the vicinity of those magnetic moments. This increases the acquired phase angle of the spin, leading to a faster relaxation of the spin accumulation [123]. Calculations show that already a concentration of 1 ppm of these defects is able to produce a realistic spin relaxation time of $\tau_s = 100\,ps$ [123].

In the case of covalently bonded hydrogen adatoms in the graphene lattice, resonance peaks in the spin relaxation rate $1/\tau_s$ appear near the charge neutrality point, corresponding to singlet and triplet states shifted in energy with respect to each other, as shown in Fig. 3.7 a) [123]. If the Fermi energy matches the energy of these states, spin relaxation is enhanced. In realistic samples, at finite temperatures, charge neutrality point fluctuations due to electron-hole puddles, and different magnetic impurities, resulting in different peak positions and widths, lead to a broadening of the spin-relaxation rate [123]. The peaks of the singlet- and triplet-state cannot be distinguished anymore, resulting in a large spin-relaxation rate in the vicinity of the charge neutrality point that decreases towards larger Fermi energies. The temperature dependence is rather weak and given by a Fermi broadening of the resonance structure, as shown in Fig. 3.7 b). This results in an increased spin-relaxation rate at 77 K, an intermediate rate at 4 K and a low rate at 300 K for the case of resonant scattering at magnetic impurities. Experimental results of hydrogenated graphene samples [134] agree well with the theoretical calculations, as seen in Fig. 3.7 c) [123].

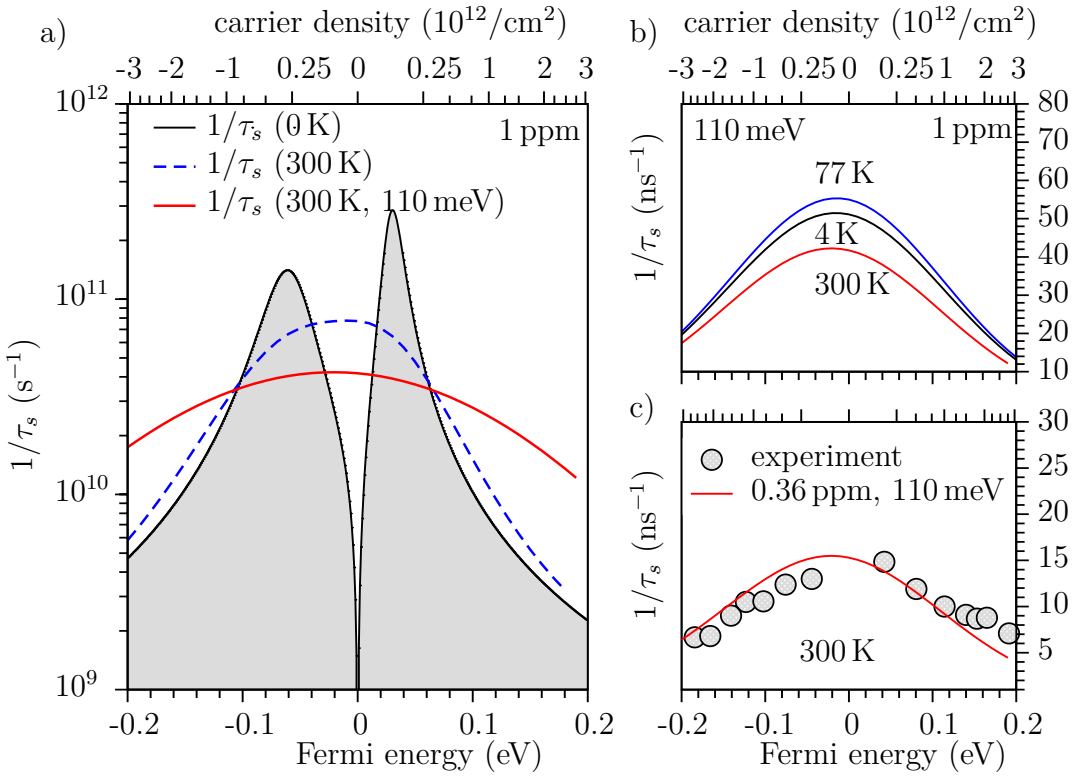

Fig. 3.7: a) Singlet- and triplet-state at a hydrogen adatom concentration of 1 ppm, visible as resonance peaks in the spin-relaxation rate at 0 K (black line). At finite temperature (blue dashed line), these resonance peaks exhibit broadening. Furthermore, additional Gaussian broadening due to electron-hole puddles and other magnetic impurities (red line) results in a spin-relaxation rate that is even more broadened. Consequently, the distinction between the singlet- and triplet-states is no longer possible. b) Spin-relaxation rate plotted for various temperatures. It has to be noted that the spin-relaxation rate tends to decrease with increasing temperature. c) Comparison of experimental data from Ref. [134] and theoretical calculations. Adapted from [123].

3.5.4. Contact-induced spin relaxation

The contact resistance plays an important role for efficient spin injection, as described by Eq. (3.20). In the typical scenario, the effective resistance of the FM R_F is smaller than that of the NM R_N. The conductivity mismatch of both materials, together with small contact resistances R_C, lead to small spin injection efficiencies P_j. In this situation, spins are able to flow back from the NM into the FM, as depicted in Fig. 3.8 a). This results in a small spin accumulation $\mu_\mathrm{sN}(0)$ in the NM underneath the FM. Small spin injection efficiencies can be prevented by inserting a tunnel barrier between both materials that introduces a large contact resistance R_C (see Fig. 3.8 b)). Technically speaking, this backflow of spins into the FM does not relax spins. However, it acts as a spin sink and affects the shape of the Hanle measurements similar to increased spin relaxation,

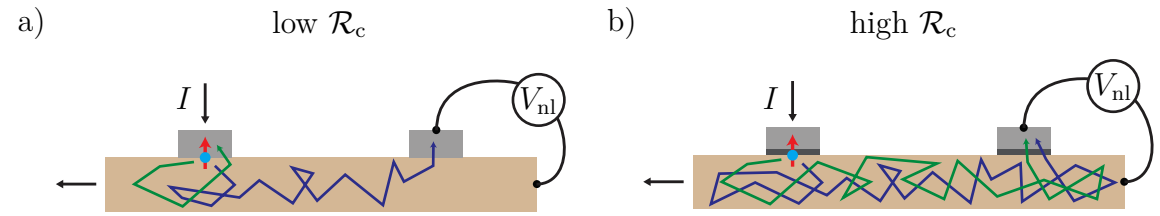

Fig. 3.8: Depiction of the conductivity mismatch for a) low contact resistances and b) high contact resistances. The added tunnel barriers between the FM and the NM prevent the spins from flowing back into the FM contacts. Adapted from [124].

resulting in incorrect spin relaxation times τ_s extracted from fits [124].

Maassen *et al.* [124] studied the effect of the conductivity mismatch on non-local Hanle measurements. The influence of the contacts is described by the ratio of the contact resistance $\mathcal{R}_c$ and the spin resistance of the channel R^s_{ch}. This ratio affects the shape and height of the Hanle curves and reflects the ratio of spins diffusing through the channel versus those that are reabsorbed by the contacts [124]. The spin resistance is defined as $R^s_{ch} = R_s L_s/w$, with R_s, L_s and w being the sheet resistivity, spin-relaxation length, and width of the transport channel, respectively. Note, that $\mathcal{R}_c$ denotes the electrical resistance of the contact and is not to be confused with the effective contact resistance R_C, as defined in Sec. 3.2. Typically, a homogeneous barrier at the injector and detector is assumed. In the case of a different barrier thickness at the injector and detector, the contact resistances at those electrodes are different from each other. In the case of an inhomogeneous barrier thickness, an effective contact resistance, approximated as $1/\mathcal{R}_{c,\,eff} = (1/\mathcal{R}_{c,\,inj} + 1/\mathcal{R}_{c,\,det})/2$, is considered [124].

In order to ascertain whether the fit parameters corresponded to the simulation parameters, a series of simulated Hanle curves were fitted. Maassen and co-workers observed that when $\mathcal{R}_c/R^s_{ch} \ll 1$, the extracted spin relaxation time is significantly smaller than the lifetime used for the simulation. They also observed that the injector-detector spacing d influences the Hanle curves. Therefore, they considered the ratio d/L_s, observing that ratios $d/L_s \gg 1$ lead to correct measured spin relaxation times even for small values of $\mathcal{R}_c/R^s_{ch}$. To conclude, for ratios of $\mathcal{R}_c/R^s_{ch} > 1$ and $d/L_s \geq 10$ the extracted spin transport properties from fits coincide with the values used in the simulations. As a consequence, fit results extracted in this regime result in correctly extracted values.

3.5.5. Further mechanisms

The mechanisms presented above are only the most relevant relaxation mechanisms in graphene. But there are also other mechanisms that can introduce spin relaxation. One involves stray fields from the FM, which can penetrate the graphene transport channel.

Spins exposed to this inhomogeneous magnetic field, will precess as long as there is a perpendicular component of the field direction. This introduces a local relaxation of spins in the graphene channel, especially at the edges of the FM injector and detector. Furthermore, SOC is greatly increased when graphene is proximitized by a TMDC and can even be tuned by a gate in bilayer graphene devices [135] or by the twist angle [136, 137]. The increased SOC due to the proximity effect can introduce an anisotropy of the spin relaxation times for in-plane and out-of-plane spins [26]. Larger SOC can even result in a much more efficient Dyakonov-Perel mechanism [26]. Another source of spin relaxation is the coupling of the spin to the pseudospin. The pseudospin in graphene is a sublattice degree of freedom and corresponds to the quantum number that describes the distribution of electrons in sublattices A and B [8]. In the presence of SOC, the spin couples to the pseudospin and the two quantities cannot be treated independently from each other anymore [122]. Here, SOC is introduced by adatoms that don't contribute to intervalley scattering. This leads to fast spin relaxation ranging from 0.1 to 200 ps at adatom densities of 0.05 %, which drastically overestimates the adatom concentration in pristine graphene samples.

Identifying the dominant spin-relaxation mechanisms remains an important task to maximize the spin relaxation time in real graphene samples. The EY mechanism overestimates the spin relaxation times of pristine graphene samples by two orders of magnitude due to the weak intrinsic SOC [23, 34]. The DP mechanism produces more realistic spin relaxation times when a Rashba field originating from the substrate in the presence of electron-hole puddles is introduced [131]. Investigating whether τ_s scales directly or indirectly with τ_p could help distinguishing between EY- and DP-type mechanisms. However, a linear scaling of τ_s with τ_p does not necessarily imply the EY mechanism, as mentioned above. So far, this approach of finding the proportionality of τ_s and τ_p did not produce any conclusive results [23]. Another method to distinguish between scattering mechanisms is to investigate the lifetime anisotropy of in- and out-of-plane spins [27, 138]. This can give insights into the prevailing spin-orbit mechanisms. Theoretical calculations of scattering at magnetic impurities, as described in Sec. 3.5.3, are able to reproduce experimental results at low impurity concentrations [123]. These impurities can be introduced for example by intentionally hydrogenated graphene samples. However, experimental results differ due to the different applied hydrogenation processes [132, 134, 139]. The influence of the contact resistance on the spin relaxation was studied in [32], resulting in a conclusion that spin relaxation time decreases with decreasing contact resistance. In order to eliminate the influence of the contacts, the injector-detector distance has to be increased.

3.6. *COMSOL Multiphysics* simulations

COMSOL Multiphysics enables the simulation of diverse physical phenomena through the numerical solution of partial differential equations (PDEs) using the finite element method. This approach involves dividing a modelled geometry into a mesh of finite elements. The solutions to the PDEs that describe the system are then calculated in each element. The general solution of the problem is obtained by accounting for the continuity conditions of the solutions in neighbouring elements [140]. The spin transport simulations are based on a template, which was developed by Stefan Hartl and has already been used in several publications by our research group in order to validate experimental results [27, 141, 142].

In order to simulate spin precession experiments, the coefficient form PDE in the form of

$$e_{\mathrm{a}}\frac{\partial^2\vec{u}}{\partial t^2}+d_{\mathrm{a}}\frac{\partial\vec{u}}{\partial t}+\nabla\cdot(-c\nabla\vec{u}-\alpha\vec{u}+\gamma)+\beta\cdot\nabla\vec{u}+A\vec{u}=f, \tag{3.33}$$

integrated in *COMSOL* is utilized, with $\vec{u}=[s_x,s_y,s_z]^T$ being the spin vector with its corresponding x-, y-, and z-components and the partial derivatives vector $\nabla=[\frac{\partial}{\partial x},\frac{\partial}{\partial y}]$. By comparing Eq. (3.33) to the modified spin-drift-diffusion Eq. (3.29), Eq. (3.33) is reduced to

$$d_{\mathrm{a}}\frac{\partial\vec{u}}{\partial t}=\nabla\cdot(c\nabla\vec{u})-\beta\cdot\nabla\vec{u}-A\vec{u}. \tag{3.34}$$

The coefficients of the PDE can be identified with the parameters from the spin-drift-diffusion equation. The damping or mass coefficient $d_a=\mathbb{1}$ is identified with the 3×3 unit matrix. The diffusion coefficient c is a 3×3 matrix containing the spin diffusion constant as

$$c=\begin{pmatrix}D_{\mathrm{s}}&0&0\\0&D_{\mathrm{s}}&0\\0&0&D_{\mathrm{s}}\end{pmatrix}, \tag{3.35}$$

where an isotropic diffusion is assumed. The spin precession and absorption is summarized in the absorption coefficient A as

$$A=\begin{pmatrix}1/\tau_{\mathrm{s},x}&-\omega_{0,z}&\omega_{0,y}\\\omega_{0,z}&1/\tau_{\mathrm{s},y}&-\omega_{0,x}\\-\omega_{0,y}&\omega_{0,x}&1/\tau_{\mathrm{s},z}\end{pmatrix}, \tag{3.36}$$

where $\omega_{0,x/y/z}$ and $\tau_{\mathrm{s},x/y/z}$ are the corresponding x-, y-, and z-components of the Larmor frequency $\vec{\omega}_0$ and spin relaxation time τ_{s}, respectively. The external applied field $\vec{B}=(B_x,B_y,B_z)^T$ is introduced in the Larmor frequency as $\vec{\omega}_0=\frac{g^*\mu_{\mathrm{B}}}{\hbar}\vec{B}$. The convection

coefficient β is then

$$\beta = \begin{pmatrix} \mu_{\mathrm{m}} \begin{pmatrix} E_x \\ E_y \end{pmatrix} & \begin{pmatrix} 0 \\ 0 \end{pmatrix} & \begin{pmatrix} 0 \\ 0 \end{pmatrix} \\ \begin{pmatrix} 0 \\ 0 \end{pmatrix} & \mu_{\mathrm{m}} \begin{pmatrix} E_x \\ E_y \end{pmatrix} & \begin{pmatrix} 0 \\ 0 \end{pmatrix} \\ \begin{pmatrix} 0 \\ 0 \end{pmatrix} & \begin{pmatrix} 0 \\ 0 \end{pmatrix} & \mu_{\mathrm{m}} \begin{pmatrix} E_x \\ E_y \end{pmatrix} \end{pmatrix}, \tag{3.37}$$

where $E_{x/y}$ are the x- and y-components of the electric field $\vec{E}$. Spin injection is implemented by via the boundary condition on the injector line

$$-\vec{n} \cdot (-c\nabla\vec{u}) = \vec{\tilde{g}}, \tag{3.38}$$

and ensures a constant flux of spins into the geometry along the x-direction. The vector $\vec{n} = (1, 0)^T$ is the normal vector on the defined boundary of injection. Consequently, Eq. (3.38) can be rewritten as

$$D_{\mathrm{s}} \frac{\partial \vec{u}}{\partial x} = \vec{\tilde{g}}. \tag{3.39}$$

The boundary flux $\vec{\tilde{g}}$ determines the orientation and magnitude of the injected spin density. In general, the spin orientation can be chosen arbitrarily. As FGT is utilized as the spin aligning electrodes with an out-of-plane magnetization, an injected spin orientation in the z-direction is assumed. Therefore, in the following $\vec{\tilde{g}}$ consists of only a z-component. The magnitude of $|\vec{\tilde{g}}|$ can be obtained by comparison with the definition of the injected spin current [110]

$$j_{\mathrm{s}} = eD_{\mathrm{s}} \frac{\partial s}{\partial x} = P_j \cdot j. \tag{3.40}$$

Consequently, $|\vec{\tilde{g}}|$ is obtained as

$$|\vec{\tilde{g}}| = \frac{j_{\mathrm{s}}}{e} = \frac{P_j \cdot j}{e}, \tag{3.41}$$

and is determined by the spin injection efficiency P_j, the charge current j and the elementary charge e. This allows for the simulation of a spin density $\vec{s}$, injected in an out-of-plane direction at the injector subjected to an external magnetic field of arbitrary orientation. In order to facilitate a comparison between the simulations and experiments, the simulated spin density $\vec{s}$ has to be converted into a voltage signal. The spin density generates an emf that is measured as voltage. The injected spin density at $x = 0$ can be calculated with [110]

$$s(0) = e\mu_{\mathrm{sN}}(0) \cdot g. \tag{3.42}$$

Combining Eq.(3.26) with Eq. (3.42) then gives

$$\mathrm{emf} = -\frac{P_j}{e \cdot g} s(0), \tag{3.43}$$

with the prefactor $-\frac{P_j}{e \cdot g}$ converting a calculated spin density to a voltage signal. Consequently, to simulate a voltage generated by the spin density, the magnitude of the spin signal has to be multiplied by this prefactor. It follows

$$|\vec{\tilde{g}}| = \frac{-P_j^2}{e^2 \cdot g} j, \tag{3.44}$$

and assumes the spin injection and detection efficiencies to be identical. As the FGT detecting electrode is also magnetized out-of-plane, the simulated spin signal in the z-direction is then read out at a distance d from the injector, integrated along the detector. It is possible to omit this integration and detect the signal at a single point, as the integration only rescales the signal.

COMSOL facilitates the incorporation of intricate interactions, some of which are challenging to integrate into analytical fit functions. For instance, it is straightforward to integrate anisotropy in spin relaxation, define different transport parameters across distinct regions, and magnetic stray fields into the simulation, and, if necessary, simulate all of these simultaneously. The simulated spin signal can also be fitted to experimental data via the Optimization Module utilizing a global least-squares objective. This enables the determination of parameters associated with the introduced effects.

4. Experimental methods

This chapter provides a comprehensive overview of the sample fabrication process of the fabricated spin transport samples and of the measurement setup. In Sec. 4.1.1, the exfoliation of graphene, hBN and FGT is explained. The subsequent processing of the materials involves their stacking and further processing of the stack to obtain the finished sample which is outlined in Sec. 4.1.2 and Sec. 4.1.3, respectively. The sample fabrication section concludes with a brief overview of the challenges encountered during the fabrication process in Sec. 4.1.4. Following this, the fabricated spin transport samples and the measurement setup are introduced in Sec. 4.2 and Sec. 4.3, respectively. Sec. 4.4 elucidates the correspondence between the measured signals and the theoretical framework, as introduced in the previous chapter.

4.1. Sample fabrication

Recent efforts in growing van der Waals materials have managed to synthesize graphene at a large scale via Chemical Vapour Deposition (CVD) [143]. This technique has been refined to produce adlayer-free, large-scale single crystals on single-crystal Cu(111) foils [144] and even improved to be fold free on single-crystal Cu-Ni(111) foils [145]. More recently, insulating sapphire substrates have also been identified as potential substrates for graphene growth [146]. Such advancements are crucial for integrating graphene into industrial applications, where wafer-scale growth of graphene and other van der Waals materials is essential.

Despite these significant improvements in synthesis techniques, the simplicity and high quality of exfoliated graphene continue to make the mechanical exfoliation method, famously known as the "Scotch tape method", highly relevant. This manual exfoliation process, which led to the first isolation of graphene by Novoselov and Geim in 2004 [7], remains a low-barrier entry point for obtaining pristine van der Waals materials. As a consequence, all materials have been manually exfoliated in this thesis. By placing a van der Waals crystal onto adhesive tape and folding the sticky sides onto each other, the layers of the crystal are separated upon peeling. Since the raw crystals have different properties depending on the compound, each one needs to be exfoliated differently. The amount of pressure applied during exfoliation and how the source material is applied

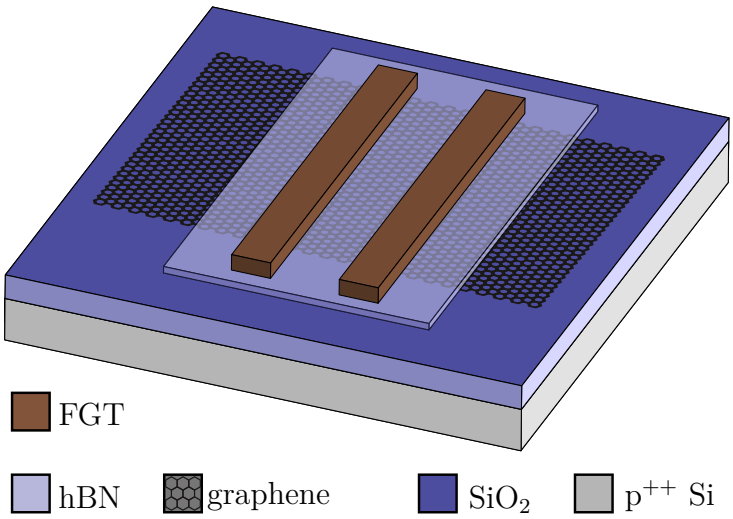

Fig. 4.1: Sample schematics of the finished samples. Two FGT flakes are positioned on top of a thin hBN tunnel barrier, which separates them from the underlying monolayer graphene. The stack is placed on a Si/SiO_2 substrate. The hBN on top, that encapsulates all vdW materials underneath, is not shown for improved visual clarity.

on the cleavage-tape is varied. Furthermore, some crystals require being exfoliated in a glovebox to prevent oxidation during processing.

For the samples in this thesis, the quality of the interfaces between the individual flakes is crucial and must be as clean as possible. For this reason, exfoliation with Polydimethylsiloxane (PDMS) films, which is quite popular for exfoliating TMDC's, is avoided as it contaminates the surface of flakes with polymer residues [147] and removing these can be quite challenging. There are reports on annealing [148], using organic solvents [149] or mechanically cleaning flakes with an atomic force microscope (AFM) in contact-mode [150–152] to get rid of residues. However, there is still a risk of damaging the flakes in these steps. Mechanical cleaning can rip the flake and causes a build-up of polymers at the edge of the "broomed" area. To avoid any contaminations on the surface of the cleaved materials, all crystals were exfoliated onto clean chips of Si/SiO_2. Consequently, only residues from the cleavage-tape need to be addressed which are typically on the substrate rather than on the freshly cleaved material. Thus, this technique minimizes the residues on flakes and, therefore, at the interfaces.

4.1.1. Exfoliation of the different materials

The samples presented in this thesis are fabricated using only three different van der Waals materials: Fe_3GeTe_2 (FGT), monolayer graphene and hexagonal boron nitride (hBN). In spin transport experiments, graphene functions as the spin transport channel. hBN acts as the tunnel barrier between FGT and graphene and also serves as a capping layer to prevent sample degradation and oxidation of FGT. FGT is utilized as a ferromagnetic spin aligner for spin injection and detection. All these materials were exfoliated onto p^{++} Si/SiO_2 substrates. The schematic layout of the stack can be seen in Fig. 4.1, but without the encapsulating hBN layer for improved visual clarity. To create such a stack,

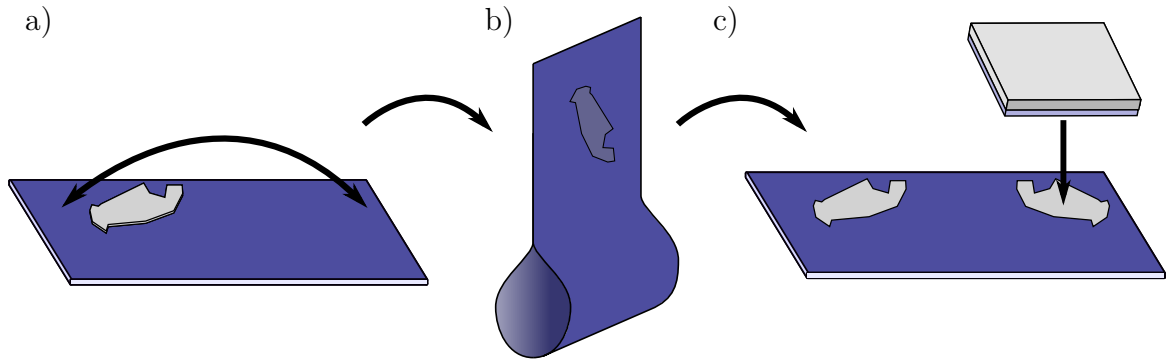

Fig. 4.2: Schematic of the Scotch tape exfoliation method. a) A crystal is placed onto the sticky side of a tape. b) Both sticky sides are glued to each other. c) Separating the tape again results in a copy of the original crystal. By pressing a cleaned Si/SiO_2 chip upside down onto the tape, the crystal is transferred to the substrate. This results in various thicknesses of flakes on the chip which can be identified under an optical microscope.

first small chips, typically measuring 1 cm by 1 cm, are cut from p^{++} Si/SiO_2 (90 nm) wafers and then cleaned in an ultrasonic acetone bath, followed by an oxygen plasma cleaning process. As each material exfoliates in a distinct manner, in the following, the handling of each material is described separately. For exfoliation of these materials the same tape (ELP BT-150E-CM), commercially obtained from *Nitto*, is employed.

Exfoliation of graphene

Graphene was exfoliated under ambient conditions in the cleanroom from purchased "Flaggy Flakes", natural graphite from *NGS Naturgraphit GmbH*. To obtain sizeable monolayers of graphene, a graphite crystal with an already clean surface was placed onto the tape. The graphite crystal was then cautiously lifted, so that the area of the cleaved material on the tape was already large in size, as illustrated in Fig. 4.2 a). The material on the tape was subsequently stamped onto other parts of the tape by folding and pulling, as depicted in Fig. 4.2 b) and c). This process was performed multiple times, resulting in a total of five copies of the cleaved material. After the Si/SiO_2 chips have been cleaned in an oxygen plasma cleaner, they are placed on the cleaved material on the tape while still hot, as illustrated in Fig. 4.2 c). Subsequently, each chip is pressed against the tape with the thumb for 30 s, with as much force as it is possible to apply manually. The tape is then slowly lifted from the chips. Monolayer graphene is identified under the microscope through optical contrast. Given that the exfoliation process is conducted under ambient conditions within a cleanroom, it is important that subsequent processing is carried out as quickly as possible to minimise the accumulation of adsorbates on the surface. Otherwise, it is recommended that exfoliated graphene is stored in a desiccator.

Exfoliation of hBN

hBN was exfoliated using material provided by T. Taniguchi and K. Watanabe [1] . To exfoliate the hBN tunnel barriers, a hBN crystal is placed onto the *Nitto* tape, which is then folded and pulled apart a couple of times until vast areas of the tape are covered with hBN. Here, it is important to use a sufficient amount of the source material to increase the probability of discovering a thin hBN flake consisting of only few layers. After cleaning the p^{++} Si/SiO_2 (90 nm) chips in the oxygen plasma cleaner, they are delicately placed onto the tape surfaces that hold the most amount of hBN. The temperature of the Si/SiO_2 chips is not important here. However, no pressure should be applied during this process to prevent the hBN from breaking into small pieces. Afterwards, the tape is lifted from the chips slowly. Tunnel barrier candidates are identified through optical contrast under the microscope. It is crucial to exfoliate hBN on Si substrates with 90 nm SiO_2 layer on top, as this improves the optical contrast of thin hBN on the Si/SiO_2 chip [108]. To determine, whether the exfoliated hBN flakes are thin enough, their thicknesses were measured using an AFM. As a reference, these should be one to four layers thick [101], which leads to measured AFM thicknesses of 0.3 - 1.3 nm [101]. However, in case of non-annealed hBN flakes, larger thicknesses can be measured, depending on how well the flake adheres to the substrate and the presence of water adsorbates on the surface. In this exfoliation step, also thicker (thicknesses of up to 30 nm), large area hBN flakes can be found and used for encapsulation purposes.

Exfoliation of FGT

FGT was purchased from *HQ Graphene*. It is exfoliated in a glovebox with an oxygen concentration of less than 0.1 ppm to avoid oxidation. Similar to the exfoliation of hBN, a crystal is placed onto the *Nitto* tape and cleaved until the tape is covered with thin FGT flakes. The cold but cleaned Si/SiO_2 chips are then pressed with the thumb onto the tape with as much force as possible for 30 seconds. Slowly, the tape is removed from the chips. For FGT, our goal is to exfoliate long strips of the material rather than large area flakes, to obtain well-defined electrodes for spin injection and detection. For this application, the thickness of the obtained long FGT strips is not of importance, as it is only their ferromagnetic properties that are of interest.

4.1.2. Stacking of the materials

After the exfoliation of all materials, the obtained flakes must be stacked to create the heterostructure, consisting of monolayer graphene on the bottom, a thin hBN tunnel

[1] both are from the National Institute for Materials Science, Tsukuba, Japan

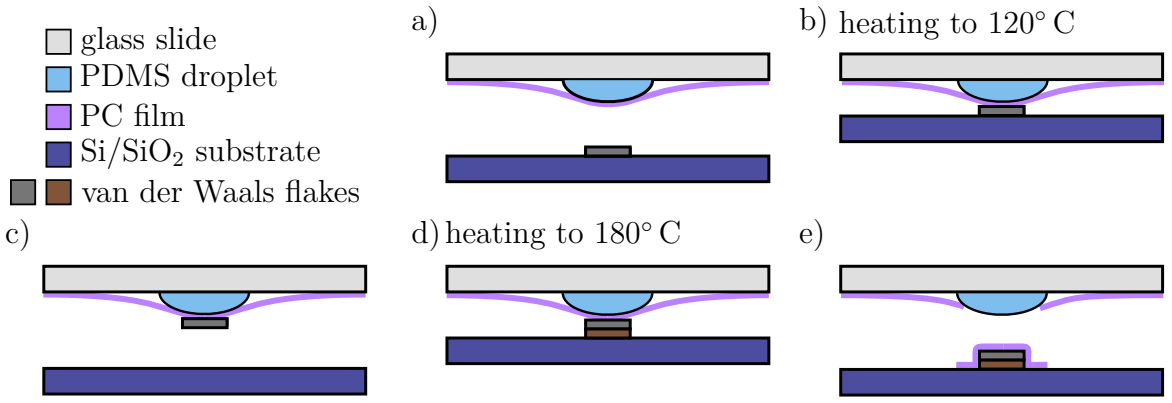

Fig. 4.3: Schematics for the stacking of the materials. a) Glass slide with a PDMS droplet with a thin PC-film stretched over it. Underneath, there is the flake on the substrate. b) After contact, the substrate with the flake is heated to 120° C. c) The contact is loosened carefully and the flake is picked up by the PC. This process from a) to c) can be repeated multiple times in order to pick up and place multiple flakes on top of each other. d) When the desired heterostructure is stacked, the PC is burned onto a new cleaned Si/SiO_2 chip at 180° C. e) After heating and loosening the contact, the PC rips and sticks with the heterostructure onto the substrate. The PC on top of the heterostructure can subsequently be dissolved in chloroform.

barrier above, and FGT electrodes on top of the tunnel barrier, not touching the graphene, as depicted in Fig. 4.1. This heterostructure is encapsulated with a large area hBN flake on top, to prevent the entire stack from degradation. To put all of the cleaved materials together, a dry-transfer stacking technique is applied, employing a thin polycarbonate (PC) film stretched over a PDMS-drop on a microscope slide, as depicted in Fig. 4.3 a) [153]. This top-down stacking process was carried out at a customized microscope. The chips with the exfoliated materials are put on a manipulator underneath the stage where usually the condenser of the microscope sits. The glass slide with the stretched PC-film is fixed on top of the microscope stage with the PC-film facing downwards.

To pick up an exfoliated flake, the PC-film is carefully brought in contact with the Si/SiO_2 chip next to the flake that is about to be picked up. When in contact, the chip is heated up to a temperature of 120°C, as illustrated in Fig. 4.3 b). While heating, the polycarbonate film expands and the contact area increases until the desired flake is in complete contact with the PC-film. The contact of the polycarbonate film and the chip is constantly observed under the microscope and can be seen as an expanding circle. At 120°C the contact is loosened carefully and the flake sticks to the PC-film (see Fig. 4.3 c)). This can then be repeated multiple times to pick up other flakes to create the desired heterostructure.

It has to be noted, that the stacking process was carried out in a glovebox with an oxygen concentration of less than 0.1 ppm. This is necessary to prevent the oxidation of FGT, which would affect the surface of this material. It has been reported that oxidized FGT-layers couple anti-ferromagnetically to pristine FGT-layers [67]. Therefore, stacking

in an inert atmosphere is crucial to ensure clean interfaces between FGT and the tunnel barrier.

As this stacking process is a top-down process, materials which should end up on top of the final heterostructure are picked up first. Thus, the first flake to be picked up is the encapsulating hBN flake, which must then enclose each subsequent flake completely. The two FGT flakes are then picked up separately. Subsequently, the hBN tunnel barrier will be picked up, which is the crucial part in the sample fabrication and simultaneously one of the most challenging. On the one hand, the hBN tunnel barrier is only a few layers thick, therefore, barely visible on the 90 nm SiO_2 substrate itself. On the other hand, it is very important that the tunnel barrier stacking is very precise. The thin hBN must cover the entirety of both FGT strips to prevent any parallel currents shortcutting the barrier. Finally, a graphene flake is picked up precisely. It is crucial that the FGT strips stick out from one side of the graphene flake to avoid electrical edge-contacts to graphene, as will be discussed in detail in Sec. 4.1.4. Once everything is picked up, the stack is consolidated by melting the PC-film onto a cleaned p^{++} Si / 285 nm SiO_2 chip with Cr/Au markers on top, at a temperature of 180°C, as illustrated in Fig. 4.3 d). The consolidated PC-film encapsulating the stack can be seen in Fig. 4.3 e). The PC-film is subsequently dissolved in a chloroform bath and the finished stack is obtained. During the entire stacking process it is crucial not to apply too much force between the substrate and the glass slide as the flakes can easily break.

4.1.3. Processing the stack and finishing the sample

Since the processed graphene is of arbitrary shape, it is necessary to define the transport channel into a Hall bar in order to establish a well-defined geometric ratio. Thus, the stack needs to be etched, which can be accomplished via reactive ion etching (RIE). Firstly, the etch mask is defined by electron beam lithography (EBL) using a double positive Poly-(methyl methacrylate) (PMMA) resist system, as can be seen in Fig. 4.4 a). This comprises PMMA 200K 9% and 950K 5% resists, which were successively spin coated onto the chip. The shape of the etch mask was defined in the *eDraw* software and written using the *eLitho* software, employing the *Zeiss AURIGA* scanning electron microscope (SEM).

As PMMA is a positive resist, the areas to be etched are illuminated by the electron beam. After lithography, the resist is developed in a solution of deionized water and isopropanol (IPA) in a ratio of 3:7 at room temperature [154, 155]. This dissolves the resist in the irradiated areas, as depicted in Fig. 4.4 b). Areas that were not illuminated during lithography are still covered by the resist. The H_2O:IPA solution was used instead of a Methyl isobutyl ketone (MIBK):IPA (1:3) solution to prevent swelling of the resist, which can cause cracks [156, 157]. Subsequent to defining the etch mask, the exposed areas of the stack are etched with RIE in an O_2/SF_6 plasma. In this fabrication step,

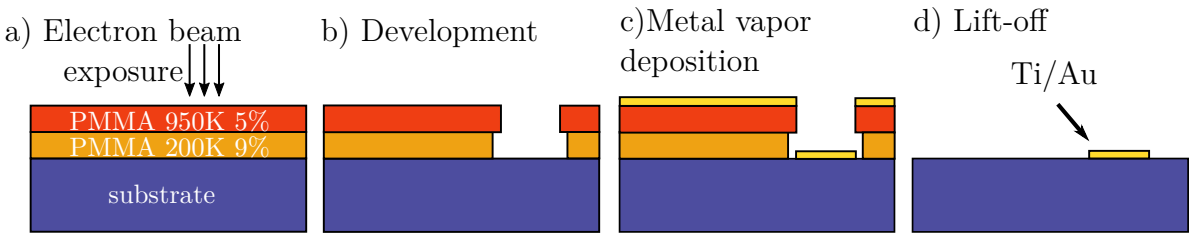

Fig. 4.4: EBL lithography process. a) The double resist structure is exposed by the electron beam. b) During the development step, the resist is removed in the exposed areas resulting in a T-shaped undercut. c) The metal for wiring and bond pads is evaporated. d) The resist with the evaporated metal on top are removed, leaving the final structure on the sample.

every material except FGT is etched. Consequently, FGT also acts as an etching mask, preserving underlying layers, e.g. graphene or hBN. Following this etching process, there will be exposed areas of FGT, thus requiring further fabrication of the sample to be carried out immediately afterwards.

The wiring and bond pads are also fabricated using EBL. Again, the double resist system is used, as described above. After lithography, the resist is developed using the H_2O:IPA (3:7) solution. To ensure optimal edge-contacts to graphene, a brief RIE etching step with O_2-plasma was performed [100, 158, 159]. Immediately afterwards, the samples were transferred into a metal evaporation chamber (Univex A) for Ti and Au deposition, as illustrated in Fig. 4.4 c). An Argon pre-sputtering process of 4 min (2 kV, 20 mA) was performed prior to the in-situ evaporation of 10 nm Ti and 150 nm Au. The in-situ pre-sputtering procedure guarantees reliable electrical contact to FGT. In order to lift off the thin metal film, the samples are deposited into a closed lift-off vial filled with acetone, resting on a 60° C warm hot-plate overnight. The following day, the thin metal film is rinsed away with warm acetone using a syringe in close proximity to the surface. During the lift-off procedure it is essential that the samples are fully covered by either acetone or IPA, otherwhise excess gold sticks to the surface when dried. The defined structure is now etched and contacted by the Ti/Au wiring, as can be seen in Fig. 4.4 d). Micrographs of finished samples are shown in Fig. 4.6 b) and c).

In order to be able to perform transport measurements on these samples, it is necessary to wire-bond them. Prior to this, the samples are glued into a chip carrier with a gold coating on its surface. This enables the p^{++} Si at the bottom of the sample to be contacted. To achieve this, the edges of the chips are scraped to reveal the conducting p^{++} Si beneath the surface. The samples are glued onto the chip carriers using a conducting two-component silver epoxy which contacts the exposed Si so that it can be used as a global back gate. Subsequently, the sample is wire-bonded with an Al-wire-bonding machine. At this point, the samples are ready to be measured and should be stored in either a glovebox or desiccator to prevent oxidation and degradation.

4.1.4. Fabricational challenges

During the device fabrication, numerous challenges arose. The alignment of the various flakes is particularly challenging, as the microscope used for stacking is operated manually in the glovebox and the individual flakes are only a few micrometers in size. It is crucial that the tunnel barrier prevents any direct contact between FGT and graphene. Furthermore, FGT must extend beyond the graphene layer to prevent electric side contacts to the graphene, as depicted in Fig. 4.5. It is only when the individual alignment of these flakes is correct that an efficient spin injection and detection is ensured. Consequently, stacking must be carried out with great precision. This can be particularly challenging as monolayer graphene and few-layer hBN are barely visible on the substrate. In addition to the low contrast of the flakes, the materials are observed through the microscope slide, PDMS droplet, and the PC-film during stacking. This lowers the contrast of the flakes on the substrate that are about to be picked up even more. Especially the round PDMS droplet distorts the image. Therefore, it is important to memorise the exact shape of each flake. This can be achieved by taking micrographs of the flakes prior to stacking or by utilising software (e.g. epicPen (open source software)) to mark the outlines of the flakes on the computer screen during the stacking process. The latter proved to be very helpful during alignment. In cases when a thicker hBN or graphene is attached to the thin flake, the thicker section can serve as a reference, as thick crystals are clearly visible through all the layers.

Furthermore, the distance between the FGT flakes should be minimal, on the order of a few micrometers, to maximize the spin signal that will be measured. However, to pick up the flakes the PC-film must be heated, causing the PC-film to expand. This can result in FGT flakes moving during stacking, making a precise positioning of the flakes difficult. Therefore, a compromise must be reached between maintaining a minimal distance and ensuring that both FGT flakes are not in direct contact after pick-up. For the devices investigated in this thesis the FGT strips are spaced at a distance $d \approx 5\,\mu m$ from center-to-center which corresponds to an edge-to-edge distance of $\approx 3.5\,\mu m$.

In addition, some FGT flakes were unable to be picked up by the PC-film. This, however, can potentially be prevented by the "polymer gripper arm" method, first realized by Robin Huber [160] and further developed in the Bachelor's thesis of Alexander Nachtnebel under the supervision of Stefan Peterhans and Jonathan Eroms, to pick up $CrGeTe_3$ (CGT) [161], a semiconducting vdW ferromagnet. CGT also proved to be unable to be stacked via the hot pick-up technique already described. The "polymer gripper arm" method employs the same PDMS droplet covered by a thin PC-film. Upon contact with the target flake, the substrate is heated up to higher temperatures of 130-150° C, which softens the PC-film. The film adheres to the flake, fully enclosing it, establishing contact not only on the surface but also on the sides. After heating, the substrate is cooled down to 85° C while in contact with the PC-film, which then hardens and acts as a gripper arm. Subsequently, the PC-film can be removed from the substrate, with the flake picked up.

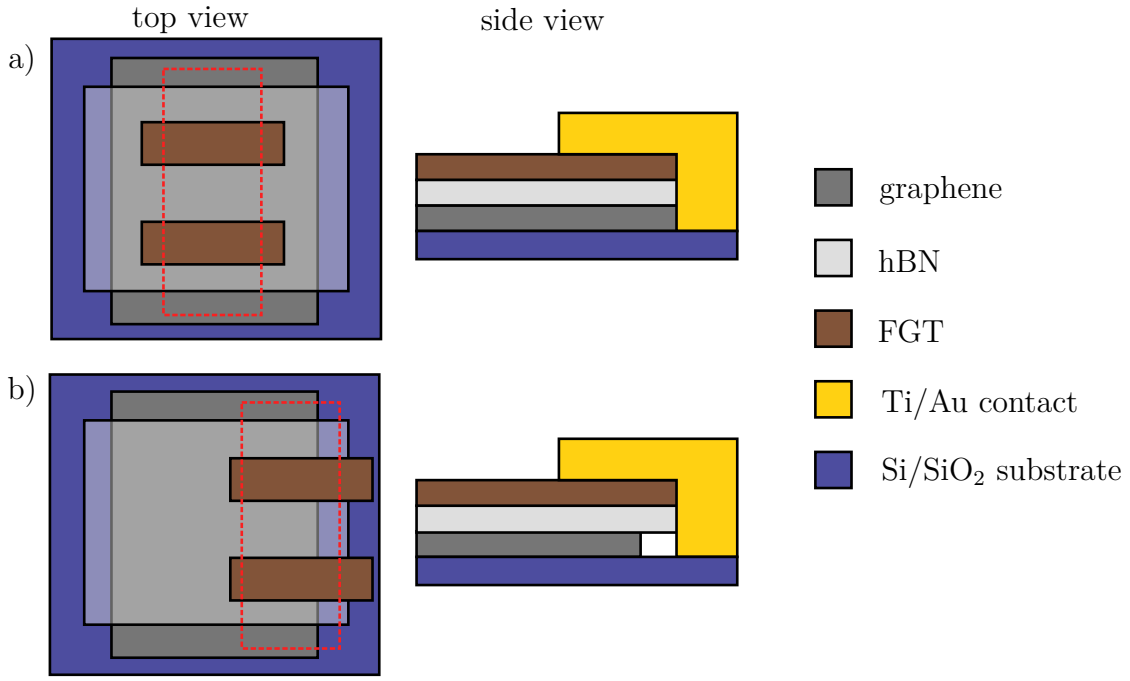

Fig. 4.5: Schematic of the alignment of the FGT, tunnel hBN, and graphene flake shown in top view and side view. The encapsulating hBN is not shown for improved visualization. a) When the three materials are aligned towards the centre and the stack is etched along the red dotted rectangle, graphene is distributed throughout the region beneath the FGT. Consequently, the evaporation of metal contacts results in a side contact to graphene shortcutting the hBN tunnel barrier. b) Conversely, when FGT is aligned in a way that the flakes extend beyond the graphene, side contacts to graphene are prevented. As there is no graphene underneath the right side of the FGT flakes, etching along the red dotted line and evaporating metal contacts results in an electrical contact only to FGT. Following the etching process, the encapsulating hBN is confined to the area of the red rectangle, thereby exposing FGT beyond the boundaries of the rectangle.

Furthermore, there have been instances where the PC adhered too firmly to the substrate, causing the PC to detach from the PDMS droplet when loosening the contact during the pick-up process. This leads to significant stretching of the PC-film and can even damage the already picked-up flakes. As a consequence, further stacking is prevented. Under the microscope this adhesion and stretching of the PC-film can be observed by the emergence of two contact fronts: one corresponding to the PC/substrate contact and the other to the PDMS/substrate contact.

4.2. Fabricated spin transport samples

During this thesis, many samples were fabricated. However, due to the difficult sample fabrication only two devices allowed for spin transport measurements, which are referred to as Sample A and Sample B in the following. Fig. 4.6 a) shows a micrograph of the finished monolayer graphene/hBN/FGT/hBN stack of Sample A prior to etching. The contours of each flake are marked by coloured solid outlines. Fig. 4.6 b) and c) show the finished spin transport samples A and B, respectively. The FGT electrodes, the evaporated Ti/Au leads and the encapsulated graphene Hall bar are indicated by the arrows. Sample A and B were fabricated in parallel following the same order of the flakes, starting with the graphene on the bottom, followed by the tunnel barrier hBN, FGT electrodes, and an encapsulating hBN layer, as described above. The width of the graphene Hall bar is 3.5 µm for both samples. The widths of the FGT flakes in Sample A are 2.6 µm and 1.6 µm, with measured thicknesses of 144.5 nm and 84.5 nm, respectively. In Sample B, the FGT flakes are 2.3 µm and 1.6 µm wide, with a height of 66 nm and 112.9 nm, respectively. The center-to-center distances of both FGT electrodes are $d = 5\,\mu\text{m}$ (Sample A) and $d = 5.6\,\mu\text{m}$ (Sample B). This proved to be a good compromise between maintaining a small distance for a large spin signal and ensuring a sufficient distance to prevent contact between both electrodes during the stacking process. Each FGT electrode is contacted by four Ti/Au leads, which enables the measurement of the anomalous Hall effect on each FGT flake. The graphene Hall bar areas serve as reference areas where the transport properties of the graphene itself were investigated.

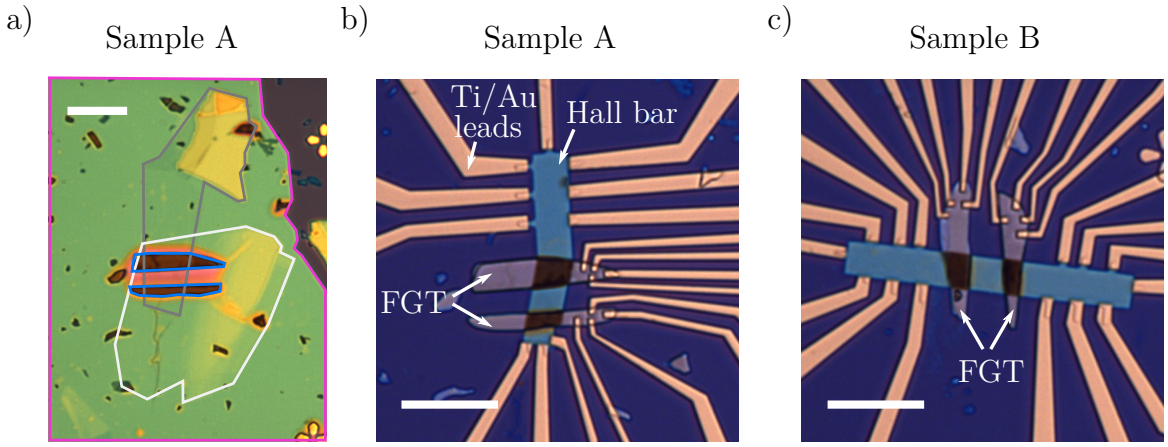

Fig. 4.6: a) Optical micrograph of the finished stack of all materials of Sample A before etching and evaporating contacts. The grey, blue, white, and pink outlines mark the contours of the graphene, FGT, tunnel hBN, and encapsulating hBN flakes of arbitrary shape, respectively. b) and c) show optical micrographs of the finished spin transport Samples A and B. The white bar in all images indicates 10 µm.

4.3. Measurement setup

All measurements in this thesis were conducted at *Oxford Instruments* cryostats reaching down to temperatures as low as 1.5 K. These cryogenic temperatures are essential, to ensure magnetic switching of FGT in one domain as its Curie temperature is $T_C \approx 220\,K$ [61]. Spin injection measurements were performed in the standard non-local configuration to separate the measured spin current from the charge current. The measurement setup is illustrated in Fig. 4.7. A constant direct current (DC) was applied from FGT_1 to a non-magnetic reference contact at the left end of the graphene mesa using a *Yokogawa 7651* programmable DC source. This current was measured as a voltage V_I by converting it into a voltage via an *Ithaco* current-to-voltage-converter. The non-local voltage V_{nl} between the second FGT_2 electrode and the other end of the graphene mesa was amplified by a *FEMTO DLPVA-101* voltage amplifier connected to a *Synktek MCL1-540* multi-channel data acquisition system. Additionally, the transverse voltage V_{AHE} on the injecting FGT_1 electrode and the three-terminal voltage V_{3T} between the same electrode and graphene are measured with the data acquisition system. The back gate voltage V_g was supplied by a *Keithley 2400* DC voltage source. Given that the direction of the external magnetic field is fixed with respect to the cryostat, the samples were mounted on a rotating holder. This allows the angle between the sample and applied external magnetic field to be varied. FGT's easy-axis is out-of-plane. Therefore, non-local spin valve measurements are conducted sweeping the external magnetic field along the easy-axis. To measure the non-local spin dynamics, an in-plane field was applied.

In order to characterize the transport properties of graphene, transport measurements have been conducted employing a four-point measurement technique as depicted in Fig. 4.8. Separating the contacts where the current is applied and the voltage is measured eliminates the cable and contact resistances from the measurement. Therefore, the measured voltage corresponds to the voltage drop in the graphene. Again, a constant DC current I was applied and measured as a voltage V_I, utilizing the *Ithaco* current-to-voltage-converter. The back gate voltage V_g was supplied by a *Keithley 2400* sourcemeter. The longitudinal voltage V_{xx} was measured using the *Synktek MCL1-540* multi-channel data acquisition system. Additionally, AC lock-in measurements of the transport properties were conducted with Sample A, and yielded results that were in good agreement with the DC measurements. However, these results are not presented in this thesis.

4.4. Non-local measurements

With the fabricated samples introduced in Sec. 4.2, non-local spin transport experiments can be conducted. The device design resembles the non-local geometry introduced in Sec. 3.2, consisting of two ferromagnetic FGT contacts FM_1 and FM_2 for injection and

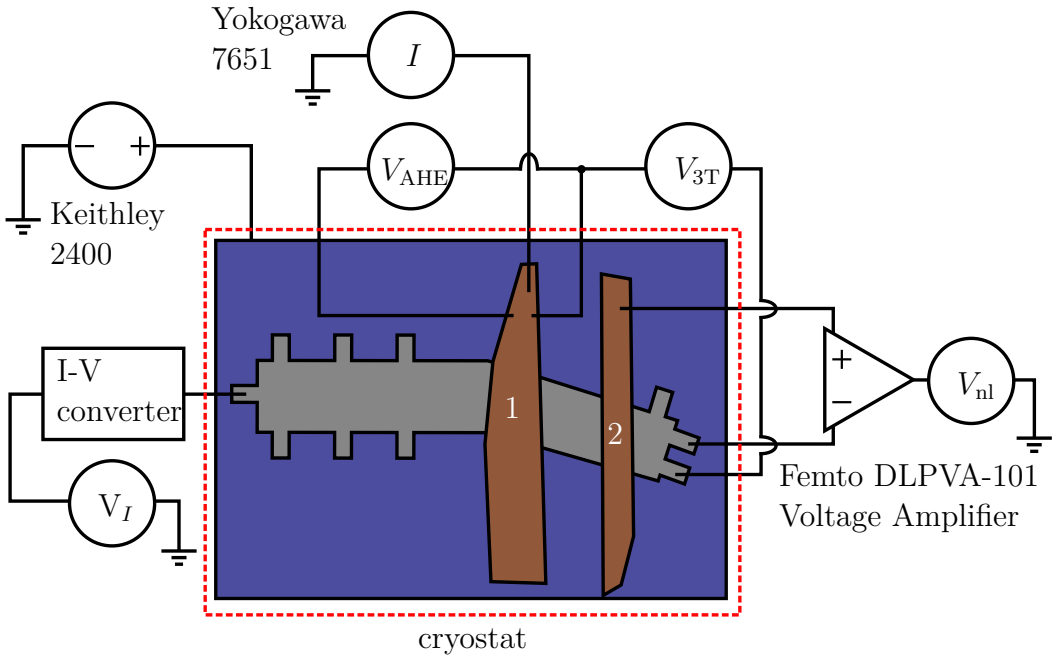

Fig. 4.7: Schematic of the non-local measurement setup. The red dotted and dark blue rectangles indicate the cryostat and the Si/SiO_2 substrate, respectively. Graphene and FGT flakes are indicated by the grey and brown areas, respectively. The gate voltage provided by the Keithley 2400 is applied at the p^{++} Si underneath the insulating SiO_2 layer which is illustrated as a blue rectangle.

detection of spins. In order to obtain different coercive fields, both FGT strips are of different thickness and shape. Beneath the FGT flakes, there is the hBN flake acting as a tunnel barrier for efficient spin injection from the FGT into the non-magnetic conducting graphene channel below. Spin injection is realized by applying a charge current between the injecting FM_1 and a non-magnetic reference contact R_1 on the left-hand side of the NM graphene channel, as illustrated in Fig. 4.9 a). As a result of the spin-split density of states of FGT, this charge current is spin-polarized. This leads to a spin accumulation in the NM channel, which diffusively spreads in all directions. As no charge current flows between both FM_1 and FM_2 electrodes, the spin transport in this region is considered purely diffusive. For sufficiently large spin diffusion lengths L_s, a finite spin accumulation is still present in the NM underneath the FM_2 which can be measured as a non-local voltage V_{nl}. The height of this signal is governed by Eq. (3.27).

4.4.1. Non-local spin valve measurements

In the non-local spin valve measurements, a constant current is applied between the ferromagnetic injector FM_1 and the NM reference contact R_1. The non-local voltage is

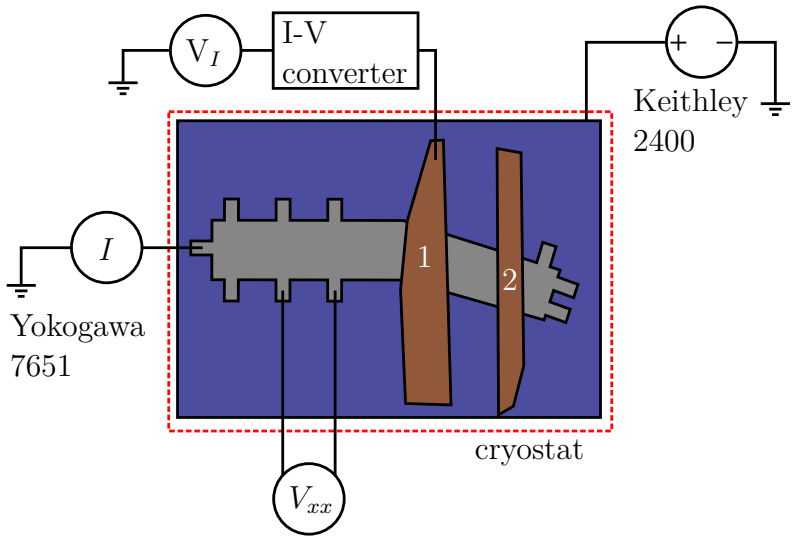

Fig. 4.8: Schematic of the four-point measurement setup used to measure the longitudinal resistance of graphene. This method is employed to avoid measuring the resistance of the contacts and cables.

measured as a function of an external magnetic field applied along the easy-axis of the FM electrodes. As a result of the different coercive fields of the injector and detector, a parallel and anti-parallel magnetization configuration can be realized by sweeping the external magnetic field. The spin-polarized current results in a spin accumulation in the NM channel, and therefore a splitting of the quasi-chemical potential for majority and minority spins as depicted in Fig. 4.9 b). In the following it is assumed that when the magnetization direction of the injecting electrode is in the up-direction, the majority spins are $\mu_\uparrow$ and the minority spins are $\mu_\downarrow$. The quasi-chemical potentials of both spin species converge to the total quasi-chemical potential μ with the spin diffusion length L_s. For $x < 0$, this total quasi-chemical potential μ has a slope due to the applied current in this region, whereas for $x > 0$ it vanishes. Fig. 4.9 b), c) and d) illustrate a down-sweep of the external magnetic field from positive to negative values. In the parallel configuration of both FGT electrodes (Fig. 4.9 b)), both FM are magnetized in the positive out-of-plane direction pointing upwards. The detecting electrode FM_2 is sensitive to the majority spins $\mu_\uparrow$, whereas the reference electrode R_2 is not spin selective and probes the total chemical potential. Measuring the non-local voltage V_{nl} probes the difference of these potentials resulting in a positive signal, as can be seen in the inset. In Fig. 4.9 c), the detector switches its magnetization direction abruptly by sweeping the external magnetic field past its coercive field. The magnetization direction of the injector remains unaffected. In this anti-parallel configuration, the detector probes the minority spin $\mu_\downarrow$ in the graphene, resulting in a negative V_{nl}. In Fig. 4.9 d), the magnetization direction of the injector is inverted, restoring the parallel magnetization configuration. Now, the majority spins are $\mu_\downarrow$ to which the detector is sensitive to and a positive signal V_{nl} is measured. This magnetic field sweep results in the sharp spin valve signal as indicated by the red curve in the inset of Fig. 4.9 d). The spin valve is usually measured for magnetic up- and down-sweeps resulting in a mirror-symmetrical curve around $B = 0$. However, due to exchange bias in FGT, as will be described in Sec. 5.1.2, the coercive fields can vary for up- and down-sweeps, leading to a non-mirror-symmetrical

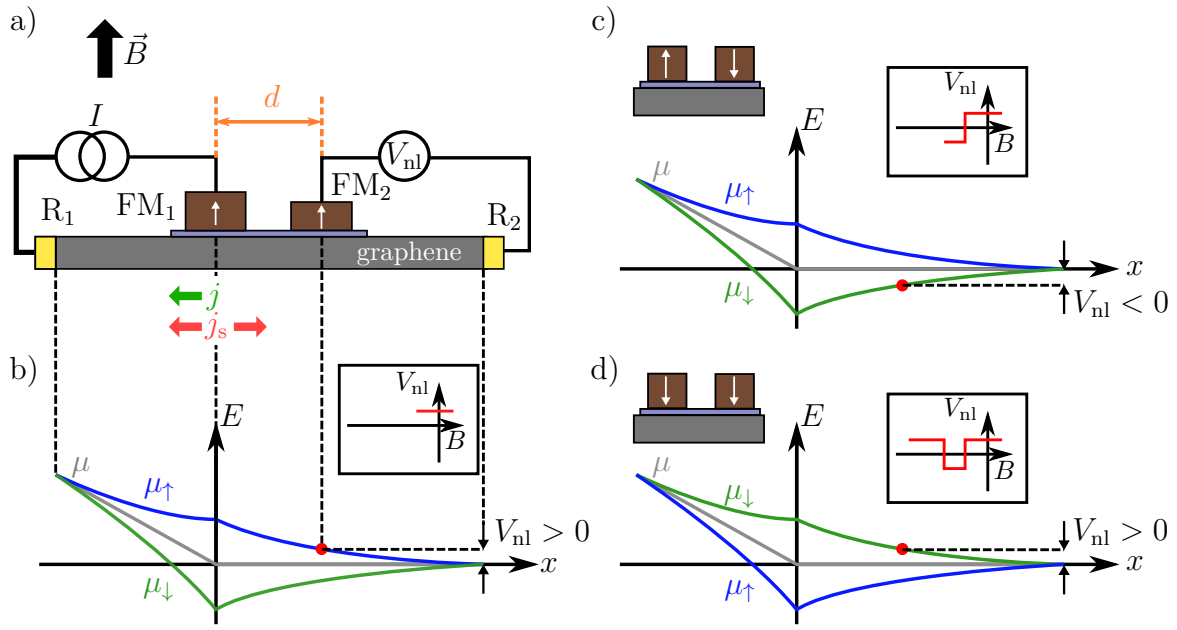

Fig. 4.9: Magnetic down-sweep of the non-local spin valve experiment. a) Non-local geometry consisting of two FM FGT electrodes (brown) FM_1 and FM_2 separated by a distance d used for spin injection and detection, respectively, a hBN tunnel barrier (light purple), and the graphene transport channel with the NM reference contacts R_1 and R_2. A constant current is applied between FM_1 and R_1 resulting in a spin polarized current j (green arrow) for $x < 0$. This current leads to a spin accumulation in the graphene that diffuses in all directions as indicated by the spin current j_s in red. A non-local voltage V_{nl} is measured as the out-of-plane magnetic field is varied. b) Spatial distribution of the total quasi-chemical potential μ (grey) and quasi-chemical potential of the majority and minority spins, $\mu_\uparrow$ (blue) and $\mu_\downarrow$ (green), respectively, in the graphene channel. In the parallel configuration of both FM electrodes, FM_2 is sensitive to the majority spins in the graphene channel as indicated by the red dot. The resulting non-local signal V_{nl} is positive, as shown in the inset in the box. c) The detector switches its magnetization direction as a result of sweeping the magnetic field past its coercive field. In the anti-parallel configuration, the detecting electrode is sensitive to the minority spin accumulation $\mu_\downarrow$, resulting in a negative signal. d) After sweeping the magnetic field past the coercive fields of both FGT electrodes, the magnetization vectors of both FGT electrodes point downwards. $\mu_\downarrow$ is now the quasi-chemical potential of the majority spins, i.e. the detector is again sensitive to the majority spin accumulation. A positive signal V_{nl} is measured. This results in the sharp spin-valve curve as indicated by the red curve in the inset. Adapted from [15]

curve. It has to be noted that if the injector switches prior to the detector, the same spin-valve signal is measured. The majority spin type in the FM generally depends on its density of states at the Fermi energy and can point in the opposite direction to the magnetization vector. Consequently, different ferromagnetic materials can exhibit opposite spin polarizations, as was shown for Fe_5GeTe_2 and Co electrodes [162].

The non-local signal V_{nl} is a measure of the quasi-chemical potential of the spin species $\mu_{\uparrow/\downarrow}$ at a distance d from the injector. Therefore, the difference of V_{nl} in the parallel and anti-parallel configuration ΔV_{nl}, is a measure of the spin accumulation μ_s as introduced in Eq. (3.5). ΔV_{nl} is usually normalized by the applied current I and is referred to as the spin-valve height ΔR_{nl} as introduced in Sec. 3.3. Therefore, the spin valve measurement enables the detection of a spin accumulation μ_s in the NM and clearly indicates successful spin injection.

4.4.2. Non-local Hanle measurements

The Hanle effect refers to the phenomenon where a spin accumulation is subjected to a torque induced by a perpendicular applied magnetic field, leading to a precession of the spins as described in Sec. 3.4. Here, the experimental setup is the same as for the spin-valve experiments, but the external magnetic field is now applied perpendicular to the direction of magnetization. In experiments, the external magnetic field is swept from small to large fields while measuring the non-local voltage V_{nl} at a constant applied current I. The magnetization of both FM electrodes remains constant and oriented out-of-plane in z-direction while the external magnetic field is applied. When the FM electrodes are in the parallel configuration, as depicted in the upper left inset of Fig. 4.10, and $B_\perp = 0\,\mathrm{T}$, the detecting FM measures the same V_{nl} as in the spin valve measurements. Then Eq. (3.30) is identical to Eq. (3.27), resulting in a large non-local signal. As the magnetic field increases, the spins accumulate an increasing precession angle $\omega_0 t$. When spins arrive perpendicular to the magnetization direction of the detector, the detecting FM is not able to detect those spins, resulting in a vanishing non-local voltage, as shown in the top right inset of Fig. 4.10. Further increasing the external magnetic field results in spins arriving anti-parallel to the detector's magnetization. A negative non-local signal V_{nl} is measured, similar to the anti-parallel configuration of the spin valve geometry. However, the signal is not as large as it is at $B_\perp = 0\,\mathrm{T}$ due to dephasing of spins in an external magnetic field. At higher magnetic fields, the non-local signal even vanishes due to this dephasing, as spins reaching the detector acquire random precession angles which add up to a vanishing spin signal. The magnetic field sweep described above results in the characteristic Hanle curve shown in Fig. 4.10 by the red solid and grey dashed lines for the parallel and anti-parallel configurations of the FM electrodes, respectively. The anti-parallel configuration results in the same curve with opposite polarity of the signal. The difference of the parallel and anti-parallel signal at $B_\perp = 0\,\mathrm{T}$ ideally corresponds to the height of the non-local spin valve signal.

The assumption of a fixed magnetization direction of the FM electrodes is valid for FGT at temperatures significantly below its Curie temperature $T_{\mathrm{C}} = 200\,\mathrm{K}$, as coercive fields are typically in the range of 0.2 - 0.6 T. As the magnetic field is applied perpendicular to its easy-axis, it would take even larger magnetic fields to affect the magnetization direction significantly. However, there are some factors that affect the shape of the Hanle

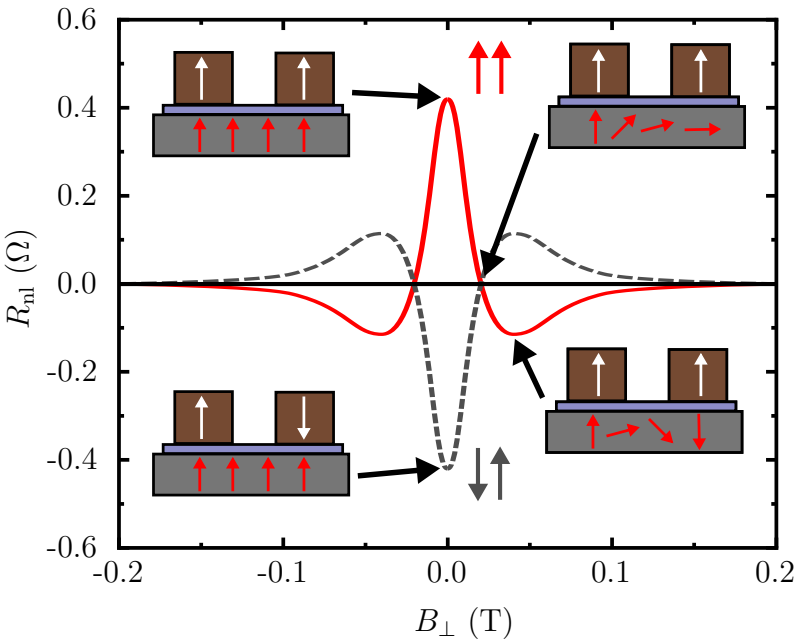

Fig. 4.10: Sweeping the external magnetic field results in the characteristic Hanle curve. The insets show specific configurations of the spins at various magnetic fields. The red solid and grey dotted curves show Hanle curves calculated from Eq. (3.30), considering a finite injector and detector width in a parallel and anti-parallel configuration of the injector and detector, respectively.

curve. When the injector and detector are magnetized at an angle to each other, the Hanle curve will exhibit an anti-symmetric component. However, this anti-symmetric component will vanish at large magnetic field values. Furthermore, when the external magnetic field is not perfectly perpendicular to the FGT magnetization direction, the Hanle curve will broaden as only the perpendicular component of the external magnetic field leads to the spin precession. Therefore, larger magnetic fields are necessary to obtain the same spin precession angle in this scenario.

4.4.3. Spurious voltage signals in non-local spin transport measurements

As can be seen from Eq. (3.27), the non-local spin signal is symmetric around $V_{nl} = 0$. However, in real samples spurious signals can arise that result in a shift of the non-local signal V_{nl}. Volmer *et al.* summarized various charge-induced artefacts in non-local spin-transport measurements [114]. As the experiments in this thesis have been conducted using a DC setup, only the most relevant mechanisms for these spurious signals are introduced here, skipping artefacts of AC measurement setups. For a more detailed description, the reader is referred to Ref. [114].

One possible source for spurious voltage signals is an inhomogeneous, non-uniform injection of the spin current due to an inhomogeneous tunnel barrier which leads to a non-uniform potential landscape in the non-local spin detection region. This results in a potential difference in the detection circuit which depends on an out-of-plane

magnetic field and the charge carrier density similar to a Hall-like effect [114, 141]. This contribution can be minimized by reducing the width of the transport channel. Furthermore, thermoelectric or magnetothermoelectric effects can also lead to spurious signals [114]. Applying large injection currents generates a temperature gradient in the detection circuit. As the detection electrode can act as a heat sink, the temperature gradient results in a voltage signal due to the Seebeck or Nernst effect, for example [114, 163–165]. Another possible source for spurious signals is the input bias current from operational amplifiers. Here, currents are flowing into or out of the inputs of a voltage amplifier even when the injection electrodes are grounded, resulting in a voltage signal [114, 166, 167]. The source of spurious signals can even be the measurement setup itself [114]. In cryogenic measurements, the samples are placed on a sample rod, where the signals are passed on through various unshielded cables placed closely together over distances of a couple meters. This can result in capacitive coupling between wires. Furthermore, damage to their insulation results in direct leakage currents between the cables. This can be checked by measuring the impedances between each line, before starting the measurements on the samples.

5. Characterization of FGT

5.1. Single FGT flake characterization

This thesis focuses on the use of FGT ferromagnetic electrodes for injecting and detecting spins in a non-local geometry. As a preliminary step, the magnetic behaviour of a single FGT flake is investigated. For this, a sample with a 66 nm thick FGT flake was encapsulated with hBN on the standard p^{++} Si/SiO_2 (285 nm) substrate. An etch mask for the contacts was defined via EBL. The hBN on top of the FGT was then etched using a standard SF_6-RIE recipe. Afterwards, Cr/Au (15nm/150nm) was evaporated to establish an electric contact to the FGT. An optical image of the sample can be seen in Fig. 5.1 a).

Electrical measurements were conducted using standard lock-in technique at a frequency of $f = 17\,\mathrm{Hz}$. To measure the anomalous Hall effect of FGT, a constant current of $I_{\mathrm{AC}} = 1.5\,\mu\mathrm{A}$ was applied between contacts 1 and 5 and the transverse voltage V_{AHE} was measured between contacts 3 and 7. Due to the perpendicular magnetic anisotropy of FGT [48, 57], the external magnetic field was swept in the out-of-plane direction from 1 T to -1 T and vice versa. The transverse resistance, defined as $R_{xy} = V_{\mathrm{AHE}}/I_{\mathrm{AC}}$, can be seen in Fig. 5.1 b) for magnetic up and down sweeps at various temperatures. Here, we notice a few things: first, the hysteresis loops exhibit a sharp single domain switching of the FGT magnetization at temperatures far from the Curie temperature. In this case, the coercive field H_{C} can be identified with the saturation field and corresponds to the value of the external magnetic field, where the magnetic domain in FGT switches its magnetization direction. At temperatures $T \geq 175\,\mathrm{K}$, close to the Curie temperature T_{C}, this single domain switching is lost. This behaviour at those elevated temperatures can be explained by multiple magnetic domains instead [51]. One domain switches its magnetization immediately, while the other domains slowly align their magnetization along the external magnetic field. Secondly, both the height of the signal ΔR_{xy} and the coercive fields H_{C} decrease with increasing temperature. Furthermore, the hysteresis loop measured at $T = 1.65\,\mathrm{K}$ is not symmetric around 0 T but is shifted by an offset. These features will be addressed in the following.

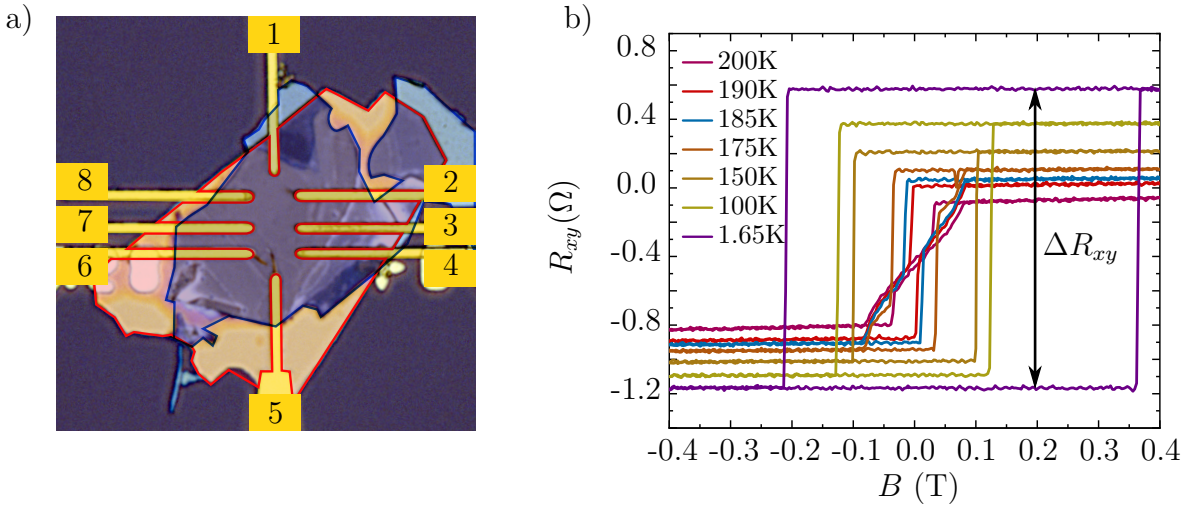

Fig. 5.1: a) Optical image of the encapsulated FGT sample. The FGT is colored in blue, the top hBN in red, and the contacts in yellow. The electrical contacts are labelled from 1 to 8. b) Temperature dependence of the magnetic hysteresis loops of the FGT flake at a constant current of $I = 1.5\,\mu\text{A}$. For comparison, the FGT flake exhibits a 2-point resistance of approximately $R_{xx} \approx 260\,\Omega$ across contacts 1 to 5.

5.1.1. Estimation of the Curie temperature

First, the Curie temperature of this sample is estimated from the measured hysteresis loops of Fig. 5.1 b). The transverse Hall resistivity of a ferromagnet is composed of the normal Hall effect and an anomalous contribution that scales with the magnetization in z-direction and is described as [48, 67, 168]

$$\rho_{xy} = \mu_\text{B}(R_\text{H}H_z + R_\text{AH}M_z), \tag{5.1}$$

with μ_B being the Bohr's magneton, H_z and M_z being the z-component of the magnetic field strength and the magnetization of the ferromagnet, respectively. R_H and R_AH are the ordinary Hall and anomalous Hall resistivities, respectively. Therefore, measuring the transverse voltage gives us information about the magnetization in z-direction of the ferromagnet. Since FGT is metallic, the charge carrier density is so high, that the ordinary Hall effect can be neglected. In Fig. 5.1 b) the raw data are shown with no visible slope in the Hall resistance. Only a sharp switching is observed. Assuming that the saturated magnetization in z-direction $M_{z,\text{sat}}$ is equal when fully saturated at positive and negative magnetic fields, the height of the hysteresis loop can be approximated as

$$\Delta R_{xy} = 2\mu_\text{B}R_\text{AH}M_{z,\text{sat}}. \tag{5.2}$$

We see that ΔR_{xy} directly scales with the saturated magnetization in z-direction $M_{z,\text{sat}}$. This is only valid if the prefactor R_AH is independent of temperature. R_AH is found to subtly depend on a variety of material specific parameters and in particular on the

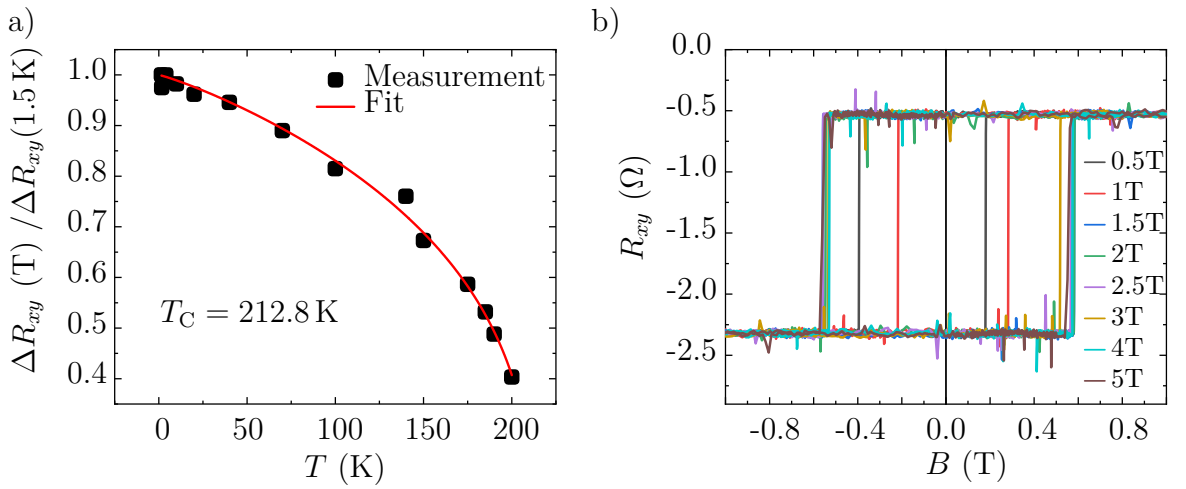

Fig. 5.2: a) $\Delta R_{xy}(T)/\Delta R_{xy}(1.5\,\mathrm{K})$ as a function of temperature. From the fit according to Eq. (2.3), a Curie temperature of $T_C = 212.8\,\mathrm{K}$ and $\alpha = 1.12696$ is determined. b) Magnetic field sweeps where the magnetic field was swept from various starting fields at $T = 4\,\mathrm{K}$. The FGT switches at different fields for different sweeps. To better visualize the symmetry, there is a solid line at $B = 0\,\mathrm{T}$.

longitudinal resistivity ρ_{xx} [168]. Given the thickness of 66 nm, FGT exhibits a metallic-like resistivity, increasing by a factor of only 1.15 when increasing the temperature from 2 K to 300 K [169]. Consequently, the temperature dependence of the prefactor R_{AH} is neglected in the following. Normalizing the signal height ΔR_{xy} to the value measured at the lowest temperature $\Delta R_{xy}(1.5\,\mathrm{K})$ plotted against the temperature results in Fig. 5.2 a). From this, the Curie temperature can be estimated. Since ΔR_{xy} scales with the magnetization, Eq. (2.3) is used to fit the experimental data in Fig. 5.2 a). As the FGT flake is 66 nm thick, we assume a 3D Ising model by fixing the critical exponent β of Eq. (2.3) to $\beta = 0.33$. This results in an estimate of the Curie temperature of $T_C = 212.8\,\mathrm{K}$ which is in agreement to the literature values ranging from 150 K to 220 K [57, 61, 62].

5.1.2. Exchange bias effect

As a next step, the asymmetry of the hysteresis loops is examined. As shown in Fig. 5.1 b), the magnetization loop is not symmetrical with respect to the applied magnetic field at 1.65 K. To investigate this feature, magnetization loops were recorded at $T = 4\,\mathrm{K}$, with the sample cooled down at zero field. To study the effect of the magnetic field strength on the hysteresis, several loops with increasing magnetic field strength were recorded, so that the hysteresis was recorded sweeping from $\pm 0.5\,\mathrm{T}$ up to sweeping from $\pm 5\,\mathrm{T}$. First, the down-sweep and then the up-sweep were performed. The Hall resistance hysteresis loops can be seen in Fig. 5.2 b). The magnetization reversal occurs

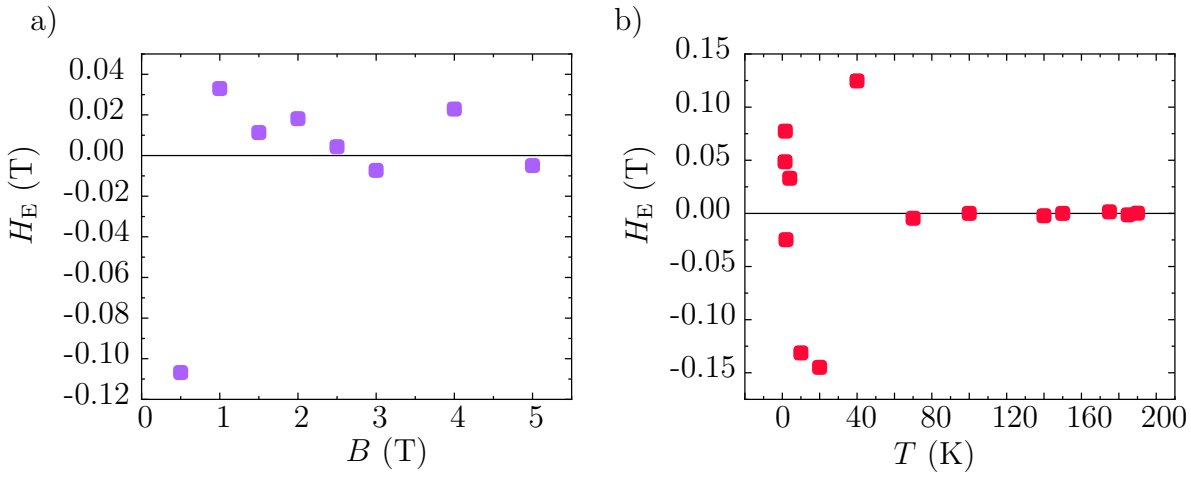

Fig. 5.3: a) Exchange bias from hysteresis loops with different starting magnetic field strengths on the x-axis at 4 K. b) Temperature dependence of the exchange bias from the 1 T-hysteresis loops shown in Fig. 5.1 b). The exchange bias vanishes between 40 K and 70 K. Therefore, the critical temperature T_N of this anti-ferromagnetic coupling is within this temperature range.

at different coercive fields, designated H_{C1} (at positive field values) and H_{C2} (at negative field values), which both vary per loop. H_{C1} varies from 0.18 T to 0.58 T and appears to stabilize at a value of 0.55 T. However, the values of H_{C1} are only occasionally identical to coercive fields H_{C1} from other loops. A similar phenomenon is observed for H_{C2}, which varies from -0.22 T to -0.56 T and seems to stabilize around -0.54 T. This asymmetric hysteresis can be interpreted as the hysteresis loop being shifted from zero field by a certain additional field, called exchange bias H_E, as illustrated in Fig. 5.4. It is a typical feature of the exchange bias effect, where a ferromagnetic layer couples to an adjacent anti-ferromagnetic layer [62, 170, 171].

In Fig. 5.3 a), H_E was evaluated from each sweep. H_E fluctuates between -0.11 T and 0.03 T and even changes sign between the sweeps from large magnetic field values. This is consistent with Wu *et al.* [62], who reported a varying H_E for zero-field-cooled samples. H_E could be fixed by field cooling at ± 14 T to negative (positive) values, respectively, as illustrated in Fig. 5.4. The temperature dependence of the exchange bias was determined from the hysteresis loops shown in Fig. 5.1 b). The exchange bias is only dominant at $T \leq 40$ K and vanishes for higher temperatures. The anti-ferromagnetic coupling seems to get destroyed by the thermal energy at higher temperatures. Consequently, its critical temperature T_N is between 40 K to 70 K.

The exchange bias effect can be intuitively understood by introducing an exchange interaction at an anti-ferromagnetic (A-FM)-ferromagnetic (FM) interface [170] and is illustrated for negative- and positive-field cooled samples in Fig. 5.4 a) and b), respectively. Let us suppose that the critical Néel temperature T_N of the A-FM is lower than the Curie temperature T_C of the FM. When the temperature is between T_N and T_C, the spins in the FM are aligned in an initial direction, while the spins of the A-FM are still

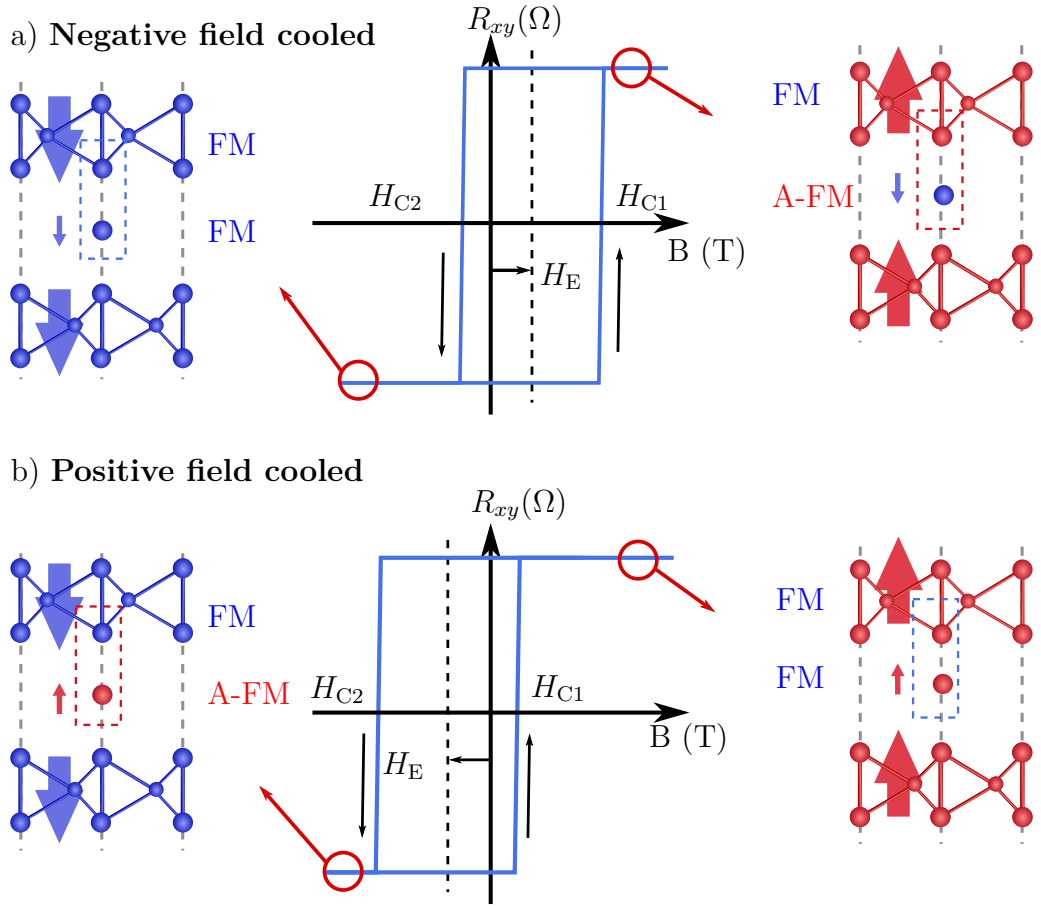

Fig. 5.4: Schematic hysteresis loops for a) negative- and b) positive-cooled device. The schematics to the left and right illustrate the magnetization configuration of the FGT layers and the intercalated Fe at the red circles. Locally intercalated Fe between the FGT layers induce the exchange bias effect by coupling anti-ferromagnetically to the ferromagnetic layers at positive (negative) saturating magnetic fields in the negative (positive) field cooled devices. The red and blue arrows represent the magnetic moment of the corresponding Fe-atoms. Adapted from [62].

unoriented. Cooling the A-FM-FM interface below T_N, aligns the spins of the A-FM along the magnetization of the FM. The orientation of the spins of the A-FM layer is robust against external fields. Applying an external field in the opposite direction of the FM magnetization, the spins in the FM are rotated, while the spins of the A-FM remain unaffected for a sufficiently large A-FM anisotropy. As a result, the spins of the A-FM at the interface aim to align the FM spins at the interface ferromagnetically in the initial direction and exert a microscopic torque. Hence, the field required to reverse the magnetization of the FM is larger, as this additional microscopic torque must be overcome. In order to switch the FM magnetization back to the initial direction, a lower field is already sufficient due to the interaction of the spins of the FM and A-FM at the interface. Now, the spins of the A-FM exert a torque in the same direction as the external

field. The hysteresis loop appears as if an additional internal bias field is applied, by which the hysteresis curve is shifted. This bias field H_{E} points in the opposite direction of the initial FM magnetization. When the material is cooled in an applied magnetic field, the exchange bias H_{E} also shows in opposite direction, as illustrated in Fig. 5.4.

For FGT crystals with a $T_c \approx 210\,\mathrm{K}$ (which is in agreement to our FGT device) it was shown from scanning transmission electron microscopy (STEM) measurements, that Fe-atoms are intercalated in the van der Waals gap between the sheets of FGT [62]. This was already suggested in the first reports on FGT [61]. In Fig. 5.4 a) it can be seen that for a positive H_{E} the intercalated Fe-atoms couple anti-ferromagnetically (ferromagnetically) to the adjacent FGT sheets at high positive (negative) external magnetic fields since the magnetization of the intercalated Fe-atoms is fixed. For negative H_{E} it is the other way round (see Fig. 5.4 b)). The direction of H_{E} can be fixed by cooling the sample in high negative or positive fields [62]. This anti-ferromagnetic layer between the ferromagnetic sheets can introduce an exchange bias of up to 0.16 T [62]. Additionally, the coercive fields H_{C1} and H_{C2} were found to be elevated in FGT samples with this anti-ferromagnetic coupling [62]. However, intercalated Fe is not the only possible origin for exchange bias in FGT. An anti-ferromagnetic coupling can also be introduced by an oxidized FGT surface on top of the pristine ferromagnetic FGT layers [67, 171]. Gweon *et al.* attribute the exchange bias to this oxidation layer, since freshly cleaved samples did not show any exchange bias in their experiments [171]. They found an exchange bias up to 0.05 T persisting up to 180 K. In our samples, an oxidation of the FGT surface cannot be excluded, since the FGT flake is partially exposed to the environment. However, the magnitude and the lower thermal stability of the exchange bias in our samples suggest that it is rather due to intercalated Fe than an oxidized FGT surface.

5.2. Characterization of the spin injecting electrodes

During the spin injection measurements, the anomalous Hall voltage at the injector was simultaneously measured. In the following section, the magnetic properties of the injector of Sample A will be analysed. The characterization of the injecting FGT electrode of Sample B can be found in the Appendix A.1. Fig. 5.5 a) shows the hysteresis loop for the injecting FGT electrode at a constant DC current of $I = -250\,\mu\mathrm{A}$, at various temperatures showing sharp switching of the magnetization for all investigated temperatures similar to those of the single FGT flake discussed in Sec. 5.1. As spin injection experiments were carried out only up to 150 K, to ensure sharp magnetic switching, measurements close to the Curie temperature T_{C} are missing. The signal height ΔR_{xy} and coercive fields $H_{\mathrm{C1,2}}$ decrease with increasing temperature. The hysteresis loops are symmetric around B=0 T, with small exchange bias H_{E} ranging from -3 mT to 12 mT. Such small exchange bias values indicate a pristine FGT electrode that was not subjected to any oxidation,

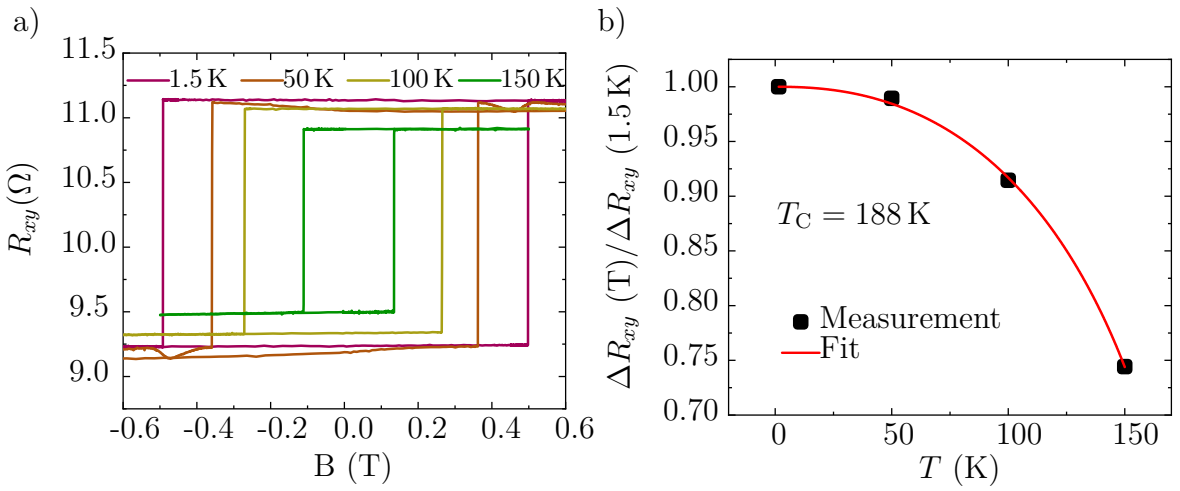

Fig. 5.5: a) Anomalous Hall measurements of Sample A for various temperatures with an applied DC current of $I = -250\,\mu A$. The anomalous Hall signal was recorded simultaneously with the spin injection experiments. b) Determination of the Curie temperature by fitting $\Delta R_{xy}(T)/\Delta R_{xy}(1.5\,K)$ (black dots) with Eq. (2.3). The fit (red line) results in $T_C = 188\,K$. The Curie temperature is drastically reduced due to Joule heating.

as previously stated [171]. The Curie temperature for the injector was estimated by fitting $\Delta R_{xy}(T)/\Delta R_{xy}(1.5\,K)$ with Eq. (2.3), as can be seen in Fig. 5.5 b). Since the injector's thickness is 144.5 nm, we assume a 3D Ising model to be the best to describe the magnetism in the injector. Therefore, the critical exponent was fixed at $\beta = 0.33$. The fit results in a Curie temperature of $T_C = 188\,K$. The reduced Curie temperature of the injector compared to $T_C = 212.8\,K$ of the single FGT flake presented Sec. 5.1 is attributed to Joule heating due to large applied currents and the finite resistance of the FGT flake itself. The electrical energy is converted to thermal energy via the resistance R with the corresponding power $P = I^2R$ heating the FGT locally. This is also confirmed by calculating the Curie temperature with data recorded at $I = 100\,\mu A$ that resulted in a higher $T_C = 192\,K$. However, such high currents already heat the sample and reduce the Curie temperature noticably. Since FGT is a metallic ferromagnet, no influence on the anomalous Hall signal with respect to the back gate voltage was observed.

To further investigate the influence of the Joule heating on parameters of FGT, a current dependence of the FGT magnetization was investigated. In Fig. 5.6 the current dependence of the anomalous Hall signal and the coercive fields can be seen in the current range from -250 to +250 µA. Both signals decrease as larger currents are applied. The anomalous Hall signal height ΔR_{xy} reduces from 1.99 Ω to 1.89 Ω when decreasing the current from -25 to -300 µA, which is a reduction of 5%. In the same current range, the coercive field reduces even more drastically, from an average $H_C = 0.68\,T$ to 0.49 T, which equals a reduction of 29%. The reduction of both parameters with increasing current is expected due to Joule heating. It was also attributed to be the major contribution in reducing the coercive field in other 2D FGT heterostructures [172]. The drastic reduction

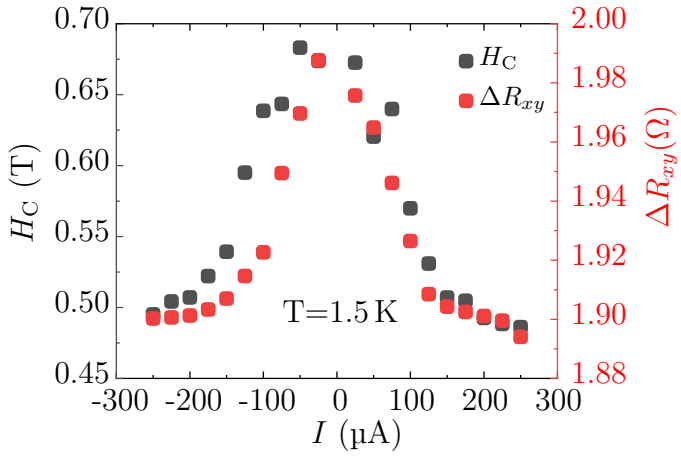

Fig. 5.6: Current dependence of the coercive field H_C and the anomalous Hall signal height ΔR_{xy} at a temperature of 1.5 K.

of H_C also agrees with Shao *et al.* [172], where a reduction of H_C of up to 28.5% was reported in the current regime from 5 to 250 µA.

5.3. Antisymmetric magnetoresistance in FGT/FGT homojunctions

Additionally, FGT/FGT homojunctions were investigated, revealing an antisymmetric magnetoresistance caused by the anomalous Hall effect. For this experiment, FGT was exfoliated as described in Sec. 4.1.1. Two FGT flakes were then stacked on top of each other, overlapping only in a limited area, covered with hBN. The stack was prepared on the standard p^{++} Si/SiO_2 (285 nm) substrate utilizing the dry transfer method using Polycarbonate as described in Sec. 4.1.2. Contacts were fabricated with standard EBL and RIE etching techniques as previously described in Sec. 4.1.3. The reported sample consists of two FGT flakes, FGT1 and FGT2, with thicknesses of 5.3 nm (lower H_C) and 6.56 nm (higher H_C), respectively. Fig. 5.7 a) shows an optical micrograph with numbered contacts, while Fig. 5.7 b) displays the schematic of the sample.

For the measurements carried out on these FGT/FGT homojunctions, a constant DC current was applied across both FGT flakes from contact 1 to 7 using a *Yokogawa 7651* current supply. The anomalous Hall voltages were measured on both FGT1 (contacts 3-13) and FGT2 (contacts 6-10) flakes, as well as the local voltage V_L (contacts 2-6) from one FGT flake to the other, using *Agilent 34410A* digital multimeters, while sweeping an external out-of-plane magnetic field. By applying a current across both flakes, the magnetization hysteresis loops of both flakes can be measured simultaneously, as shown in Fig. 5.8 a). The external magnetic field was swept from 1 to -1 T (down-sweep), and

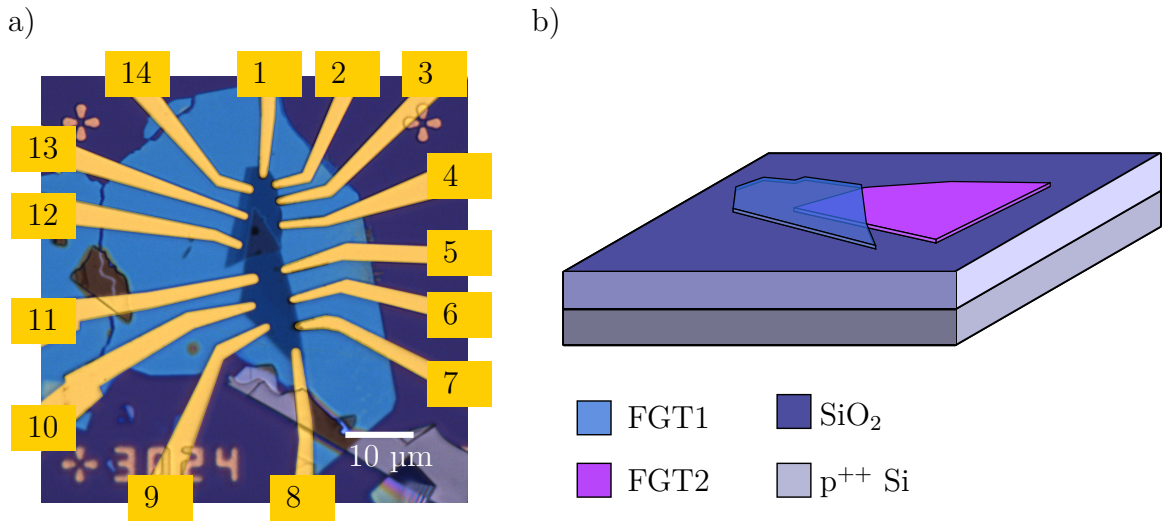

Fig. 5.7: a) Micrograph with colored contacts to the FGT flakes. The scale bar indicates 10 µm. b) Schematic of the two overlapping FGT flakes. The thicknesses are 5.3 nm and 6.56 nm for the FGT1 and FGT2 flake, respectively. The encapsulating hBN layer on top is not illustrated for better visualisation.

then from -1 to 1 T (up-sweep). The coercive fields of both flakes are unsynchronized and the magnetization is only partially coupled as evidenced by the anomalous Hall signals $R_{xy,\mathrm{FGT1}}$ and $R_{xy,\mathrm{FGT2}}$. The magnetization of FGT1 can be described by two domains. One switches at lower coercive fields, while the second is magnetically coupled to the FGT2 magnetization. This second domain reverses its magnetization simultaneously with FGT2, which reverses its magnetization in one domain. The switching behaviour of all magnetic domains is sharp.

The magnetic sweeps of the local resistance $R_\mathrm{L} = V_\mathrm{L}/I$ measured across both flakes in Fig. 5.8 b) show a high and low resistance state in the magnetic up- and down-sweeps, respectively, when the magnetizations of both flakes are antiparallel. In the parallel configuration, an intermediate resistance state is observed. The high and low resistance states are also sensitive to the exact magnetization alignment of each FGT flake. The high resistance state can only be observed in the $\downarrow\uparrow$ configuration, while the low state is only observed in the reversed $\uparrow\downarrow$ configuration. Here, the first and second arrow correspond to the magnetization direction of the FGT1 and FGT2 flake, respectively. Up and down magnetization directions are defined in the reference system of the sample. As the sample is built in the cryostat upside-down, the magnetization points down (up) at high positive (negative) external magnetic fields. The magnetization configuration of FGT1 and FGT2 is shown in Fig. 5.8 b) by the blue and purple arrows, respectively.

When a negative magnetic field of -1 T is applied, both FGT flakes are magnetized in the up-direction. As the external magnetic field increases, R_L also increases with a constant slope. This is a common characteristic of longitudinal resistances in most ferromagnetic

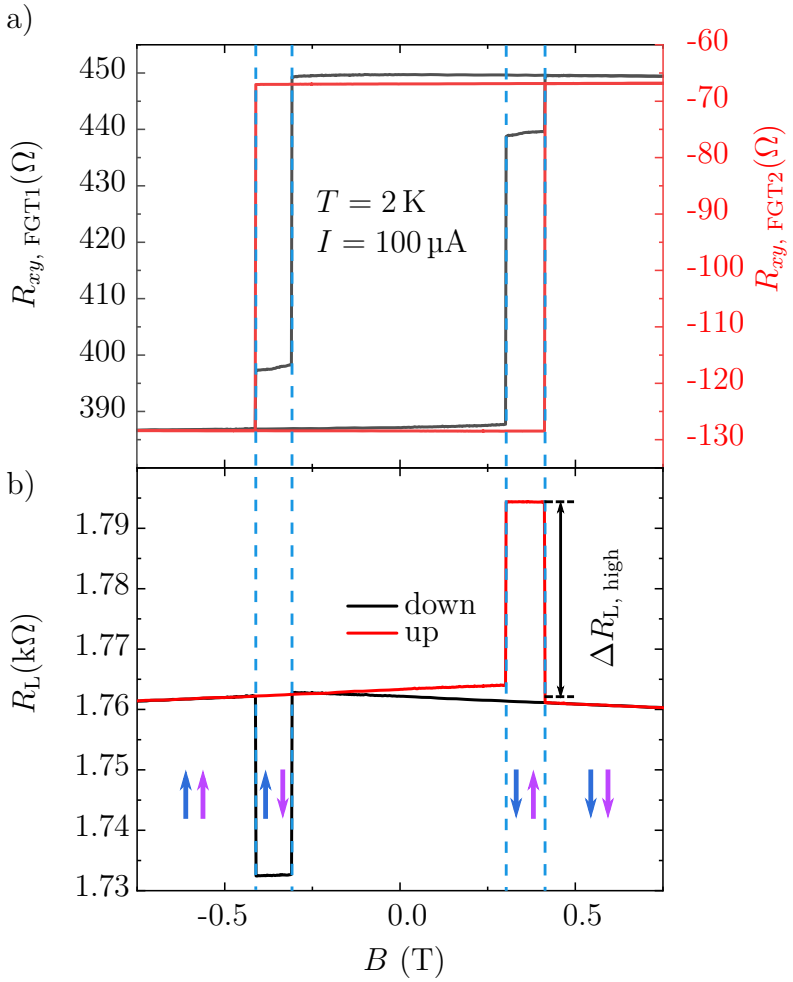

Fig. 5.8: a) Hysteresis loops of both FGT flakes. The anomalous Hall signal for the FGT1 (FGT2) is shown in grey (red). b) Magnetic up- and down-sweeps of the local resistance R_{L} across the FGT/FGT homojunction on one side. The signal depends on the exact magnetization configuration showing a plateau (positive magnetic fields) and dip (negative magnetic fields) in the anti-parallel magnetization configuration of both FGT flakes. Blue (purple) arrows show the exact magnetization direction for the FGT1 (FGT2) flake.

systems, resulting in a symmetric butterfly-shaped longitudinal hysteresis [143, 173] (see Fig. A.3 in the appendix). By increasing the magnetic field above the coercive field of FGT1, the first domain reverses its magnetization direction, as shown in the anomalous Hall signal in Fig. 5.8 a). R_{L} abruptly increases from the intermediate to a high resistance state. Since FGT2 has a larger coercive field, it remains magnetized in the up-direction. When the magnetic field is increased above the coercive field of FGT2, both flakes are magnetized parallel in the down-direction. Here, the magnetization reversal of the second domain of FGT1 occurs simultaneously with FGT2 due to coupling. R_{L} abruptly decreases again to the intermediate state. Upon further increasing the magnetic field, R_{L} decreases with a constant negative slope, similar to the longitudinal resistances

of single FGT flakes. When decreasing the magnetic field from 1 to -1 T, the slope in the parallel configuration and the unsynchronized switching of FGT1 and FGT2 is observed again. This time resulting in a low resistance state in R_L in the antiparallel ↑↓ configuration.

Origin of the antisymmetric magnetoresistance

Antisymmetric magnetoresistance has been observed in FGT heterostructures and other ferromagnetic metals with a perpendicular magnetic anisotropy [84, 85, 173, 174]. In Ref. [173], this signal was measured in a single FGT flake with inhomogeneous thickness. The magnetizations of the thicker and thinner parts of the flake were decoupled from each other due to its inhomogeneous thickness. The antisymmetric magnetoresistance was attributed to opposite signs of the anomalous Hall effect in both regions and the current continuity close to the boundary of the magnetic domains [173]. The unsynchronized switching of both FGT regions is identified as the natural cause of this antisymmetric magnetoresistance. Furthermore, a similar behaviour was observed in FGT/graphite/FGT-trilayer heterostructures [84]. At the graphite/FGT interface, spin momentum locking induces spin-polarized currents that cause an antisymmetric magnetoresistance in these heterostructures. The spin momentum locking originates from a Rashba-split 2D electron gas in the FGT, induced by spin orbit coupling.

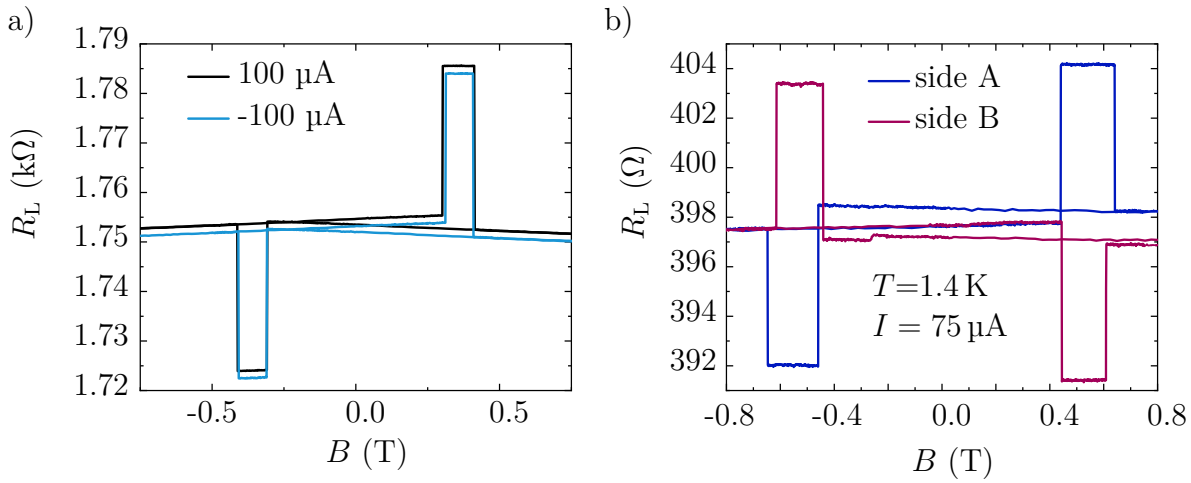

Fig. 5.9: a) Reversing the sign of the current results in the same R_L thus ruling out spin momentum locking as a cause for the antisymmetric magnetoresistance. b) Measuring R_L at opposite sides A and B of the sample inverts the signal. This is in agreement with the picture sketched in Fig. 5.10. The measurements on side A and B are carried out after one another. This explains the different coercive fields. This measurement was conducted on a second sample that showed the exact same antisymmetric magnetoresistance.

If spin momentum locking was the origin of the antisymmetric magnetoresistance in our samples, R_L would reverse sign for opposite current directions. However, this is not the

case in our samples as shown in Fig. 5.9 a). The up- and down-sweeps of R_L are identical, when the current direction is changed, except for a small offset. Therefore, we can exclude spin momentum locking as the cause of this antisymmetric magnetoresistance. Rather, this observation is consistent with the anomalous Hall effect being the origin. If this is the case, the signal should also reverse polarity when measured on opposite sides of the sample, as illustrated in Fig. 5.10. Up- and down-sweeps of R_L measured at opposite sides of a second sample (see Fig. A.2 a) in the appendix for an optical micrograph) are shown in Fig. 5.9 b), demonstrating inverse behaviour of R_L. The measurements on each side were recorded sequentially, which explains the different coercive fields when comparing the corresponding sweeps. As presented in Fig. 5.2 b), the coercive fields are not necessarily fixed and can vary from sweep to sweep.

Therefore, the control measurements suggest that the observed antisymmetric magnetoresistance arises due to the independent anomalous Hall effect of both FGT flakes. As depicted in Fig. 5.10, the voltage across both flakes on one side is a measure of the potential difference between the flakes. Due to the anomalous Hall effect, the charge carriers are deflected to the sides of the flakes due to the magnetization, similar to the ordinary Hall effect. The direction of deflection depends on the magnetization direction. Electrons accumulate on one edge of the FGT while a lack of electrons arises on the opposite edge. This creates an electrical field, resulting in the anomalous Hall voltage. As the magnetizations of both flakes are decoupled, this leads to the four magnetization scenarios sketched in Fig. 5.8 b) ($\uparrow\uparrow, \uparrow\downarrow, \downarrow\uparrow$ and $\downarrow\downarrow$). In each scenario, the potential difference measured by the voltmeter is unique, as illustrated in Fig. 5.10, where both anti-parallel configurations are shown. In Fig. 5.10 a) the magnetization configuration $\downarrow\uparrow$ yields a positive voltage while the $\uparrow\downarrow$ configuration yields a negative voltage. This results in an antisymmetric magnetoresistance signal. The measured signal is reversed on opposite sides of the sample. However, the polarity of R_L is not affected by the direction of the current.

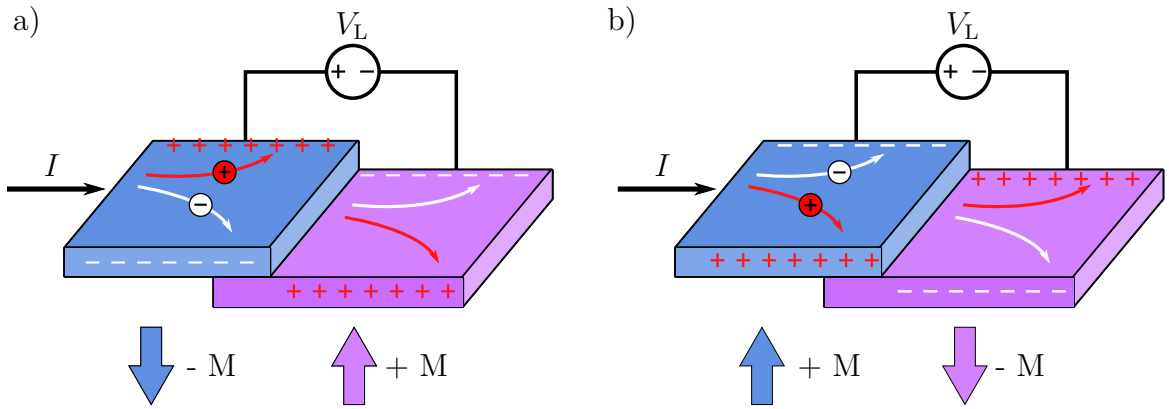

Fig. 5.10: Schematic of the anomalous Hall effect in both FGT flakes. Due to the anomalous Hall effect, charge carriers are deflected to the edges of the flakes. The direction of deflection is dependent on the magnetization. a) and b) are showing both anti-parallel alignment configurations which leads to a high V_L signal in a) and a low signal in b).

To confirm that the antisymmetric magnetoresistance is linked to the ferromagnetic ordering of FGT and, consequently, to the nature of the anomalous Hall effect, we examine the temperature and current dependence of both R_{L} and $R_{xy,\mathrm{FGT1/FGT2}}$ signals. As the signal of R_{L} exhibits a slight slope (see Fig. 5.8 b)), the heights of the high and low resistance states $\Delta R_{\mathrm{L,\,high/low}}$ are determined by calculating the mean value of R_{L} from points in the parallel configuration near both coercive fields. This mean parallel value is then subtracted from the mean value of the corresponding antiparallel configuration, resulting in the height of the antisymmetric magnetoresistance $\Delta R_{\mathrm{L,\,high/low}} = R_{\mathrm{L,\,AP,\,high/low}} - R_{\mathrm{L,\,P,\,high/low}}$ for the high and low resistance states. The absolute value of the magnetoresistance $|\Delta R_{\mathrm{L,\,high/low}}|$ is almost identical for the high and low resistance state (see Fig. A.2 b) in the Appendix). For this reason, a mean value $\Delta R_{\mathrm{L,\,mean}} = (|\Delta R_{\mathrm{L,\,high}}| + |\Delta R_{\mathrm{L,\,low}}|)/2$ is calculated and compared to the height of the magnetization loops $\Delta R_{xy,\mathrm{FGT2}}$ of the FGT2 flake. Fig. 5.11 a) displays the current dependence of the antisymmetric magnetoresistance $\Delta R_{\mathrm{L,\,mean}}$ at $T = 50\,\mathrm{K}$ in blue, while red shows the height of the anomalous Hall effect $\Delta R_{xy,\mathrm{FGT2}}$ of FGT2. Both signals exhibit identical qualitative behaviour in terms of current dependence. The same can be observed when examining the temperature dependence of both signals in Fig. 5.11 b). Here, $\Delta R_{\mathrm{L,\,mean}}$ and $\Delta R_{xy,\mathrm{FGT2}}$ signals were measured at a current of $I = 100\,\mu\mathrm{A}$. The Curie temperature of FGT1 and FGT2 was extracted from the temperature dependence of the anomalous Hall effects, resulting in $T_{\mathrm{C,\,FGT1}} = 189\,\mathrm{K}$ and $T_{\mathrm{C,\,FGT2}} = 188\,\mathrm{K}$, respectively.

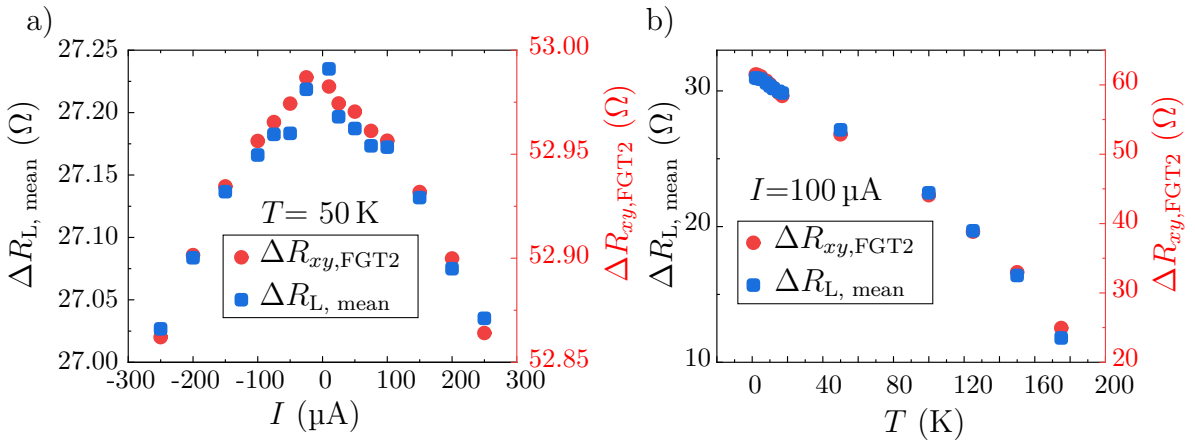

Fig. 5.11: a) ΔR_{L} and $\Delta R_{xy,\mathrm{FGT2}}$ as a function of applied current I. b) ΔR_{L} and $\Delta R_{xy,\mathrm{FGT2}}$ as a function of temperature T. Both signals show similar qualitative behaviour with respect to the current and temperature dependence.

The antisymmetric magnetoresistance can even be obtained manually by when subtracting the anomalous Hall voltages, separately measured at each flake. The result can be seen in Fig. 5.12 a), where R_{L} is the measured antisymmetric magnetoresistance, while $R_{\Delta\mathrm{AHE}} = \frac{V_{xy,\mathrm{FGT1}} - V_{xy,\mathrm{FGT2}}}{I}$ is the difference of both anomalous Hall resistances. $R_{\Delta\mathrm{AHE}}$ resembles the antisymmetric magnetoresistance R_{L} qualitatively except for the slope. As the anomalous Hall effect and the antisymmetric magnetoresistance exhibit a similar

qualitative scaling with temperature, it is evident that also $\Delta R_{\Delta\mathrm{AHE}}$ does, as can be seen in Fig. 5.12 b). Here, $\Delta R_{\Delta\mathrm{AHE,\,mean}}$ is the mean height of the $R_{\Delta\mathrm{AHE}}$ magnetoresistance and is calculated the same way as $\Delta R_{\mathrm{L,\,mean}}$.

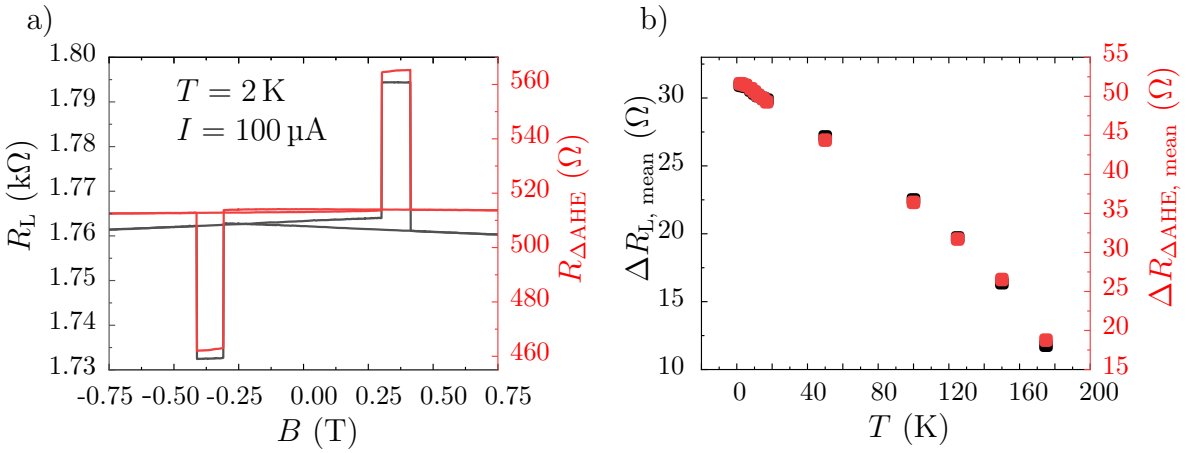

Fig. 5.12: a) Measured (R_L) and artificially generated ($R_{\Delta\mathrm{AHE}}$) antisymmetric magnetoresistance at $I = 100\,\mu\mathrm{A}$ and $T = 2\,\mathrm{K}$. Both signals show the exact same behaviour with respect to the magnetization configuration of both FGT flakes b) Temperature dependence of the measured (ΔR_L) and artificially generated ($\Delta R_{\Delta\mathrm{AHE}}$) antisymmetric magnetoresistance height. Both signals scale qualitatively the same.

Summary

In summary, an antisymmetric magnetoresistance was measured in decoupled FGT/FGT homojunctions. The sign of this magnetoresistance is sensitive to the exact magnetization configuration of both FGT flakes. The signal remains invariant when the current direction is reversed. However, it changes polarity when measured on opposite sides of the sample. This rules out spin momentum locking as a possible cause of this antisymmetric magnetoresistance. Instead, it can be explained by the anomalous Hall effect. Indeed, the scaling of ΔR_L with temperature and current is qualitatively the same as for the anomalous Hall signal. Antisymmetric magnetoresistance can be artificially created by subtracting the anomalous Hall voltages. The current and temperature dependence of the signal height of the artificially generated signal and the individual anomalous Hall signals are qualitatively the same. Overall, this suggests that the origin of this antisymmetric magnetoresistance is due to the decoupled magnetization of the two FGT flakes resulting in different anomalous Hall signals. This antisymmetric magnetoresistance clearly demonstrates that the longitudinal signal R_L contains information of both transverse Hall voltages, so that the coercive fields of both flakes can be determined by measuring only one signal.

6. Charge transport and tunnel barrier characterization

The previous chapter provided a detailed characterization of FGT, with a special focus on its magnetic properties. This chapter focusses on the comprehensive characterization of the two missing building blocks of the non-local spin transport Samples A and B, namely the graphene and hBN tunnel barrier. The chapter begins with a thorough examination of the graphene channel properties in Sec. 6.1, followed by a detailed analysis of the hBN tunnel barriers in Sec. 6.2. This systematic characterization serves as the foundation for the subsequent measurements and findings.

6.1. Characterization of graphene

6.1.1. Mobility

One important quantity characterizing the transport properties is the charge carrier mobility. It is determined experimentally by measuring the resistivity of the graphene sheet in dependence of an applied back gate voltage or via Hall measurements. Fig. 6.1 a) shows the schematics of Sample A. The four-point resistivity measurements were carried out as described in Fig. 4.8, so that a constant DC current I is applied at the reference region (from contact 19 to contact 6) and the longitudinal voltage V_{xx} was measured between contacts 17 and 16, while the gate voltage V_g was varied (contact 12). The resistivity ρ is then calculated with $\rho = \frac{V_{xx}}{I}\frac{W}{L}$, where W and L are the width of the Hall-bar and the edge-to-edge distance of the voltage probes, respectively. In Fig. 6.1 b), the resistivity as a function of the applied back gate voltage is depicted. It exhibits almost no temperature dependence in the examined temperature range from 1.5 K to 150 K. The charge neutrality point is at $V_\mathrm{CNP} = -4\,\mathrm{V}$ which indicates a slight n-type-doping.

The mobility of the graphene can be determined by the slope of the linear gate voltage dependence of the conductivity σ. Eq. (2.13) gives the linear dependence between σ and V_g with $a = C_\mathrm{g} \cdot \mu_\mathrm{m}$ being the slope of this dependence, with the gate coupling constant C_g. Therefore, the mobility can be calculated by a linear fit to the conductivity measurement

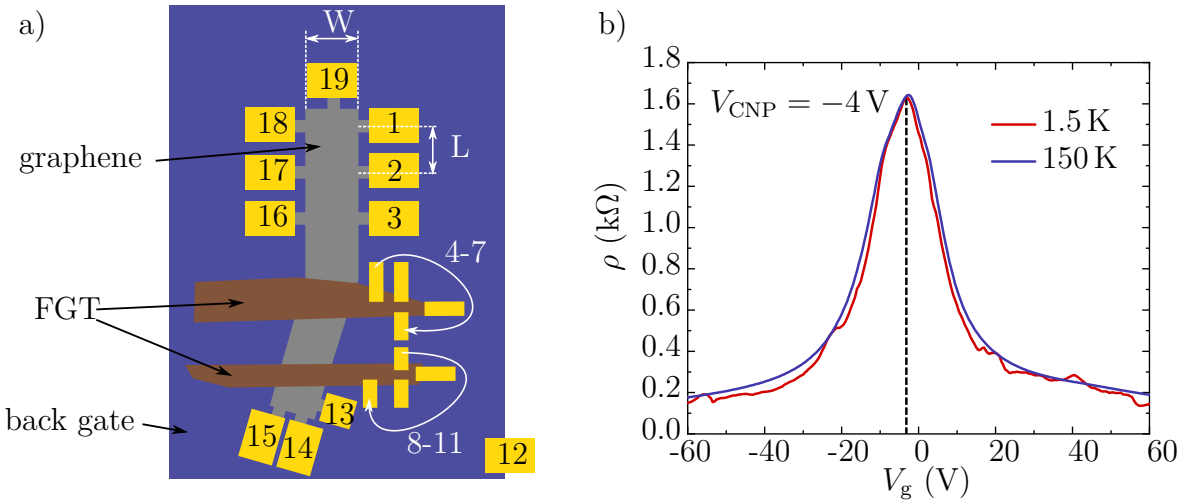

Fig. 6.1: a) Schematics of Sample A. The graphene (grey) is on top of a p^{++} Si/285 nm SiO_2 back gate (blue). FGT strips (purple) are placed on top of the graphene separated by a hBN tunnel barrier in-between. The hBN tunnel barrier is not shown for improved visualisation. The contacts (yellow) are numbered from 1 to 19, where the numbers on the FGT strips are counted clockwise. b) Back gate voltage dependence of the resistivity of Sample A at 1.5 K (red curve) and 150 K (blue curve). The resistivity shows almost no temperature dependence in the investigated temperature range. The charge neutrality point of the Dirac measurement is at $V_{CNP} = -4$ V indicating a n-type doping of the graphene.

in the linear regime, as illustrated in Fig. 6.2. A hole mobility of $\mu_{h,A} = 9930 \frac{cm^2}{Vs}$ and an electron mobility of $\mu_{e,\,A} = 9460 \frac{cm^2}{Vs}$ is determined for Sample A. For Sample B, similar mobilities are extracted resulting in a hole mobility $\mu_{h,\,B} = 10315 \frac{cm^2}{Vs}$ and an electron mobility of $\mu_{e,\,B} = 9005 \frac{cm^2}{Vs}$. The Dirac measurement and the conductivity of Sample B can be seen in the Appendix in Fig. A.4.

In addition, the mobility can also be extracted via the Hall effect. Here, the transverse resistivity ρ_{xy} depends on the external perpendicular magnetic field B as $\rho_{xy} = \frac{B}{ne}$ [91]. Therefore, the charge carrier density can be calculated as the inverse slope of the transverse Hall resistivity $n = \frac{1}{e}(\frac{d\rho_{xy}}{dB})^{-1}$. The mobility is then determined via Eq. (2.11), where $\sigma_{Hall} = (\rho_{xx}(0\,T))^{-1}$. The Hall measurements are described in the Appendix A.3.2. In Fig. 6.2 b) a Hall measurement for Sample A at various back gate voltages V_g at a temperature of 150 K is shown. The transverse resistance scales linearly with the external perpendicular magnetic field within the investigated magnetic field range. Linear fits are indicated by yellow lines. For Sample A, an average hole mobility of $\mu_{h,\,A,\,Hall} = 10882 \frac{cm^2}{Vs}$ and an electron mobility of $\mu_{e,\,A,\,Hall} = 7530 \frac{cm^2}{Vs}$ is obtained by these Hall measurements.

The results of both methods are in good agreement for Sample A. A possible explanation for the lower electron mobilities in the Hall measurements is that these measurements were

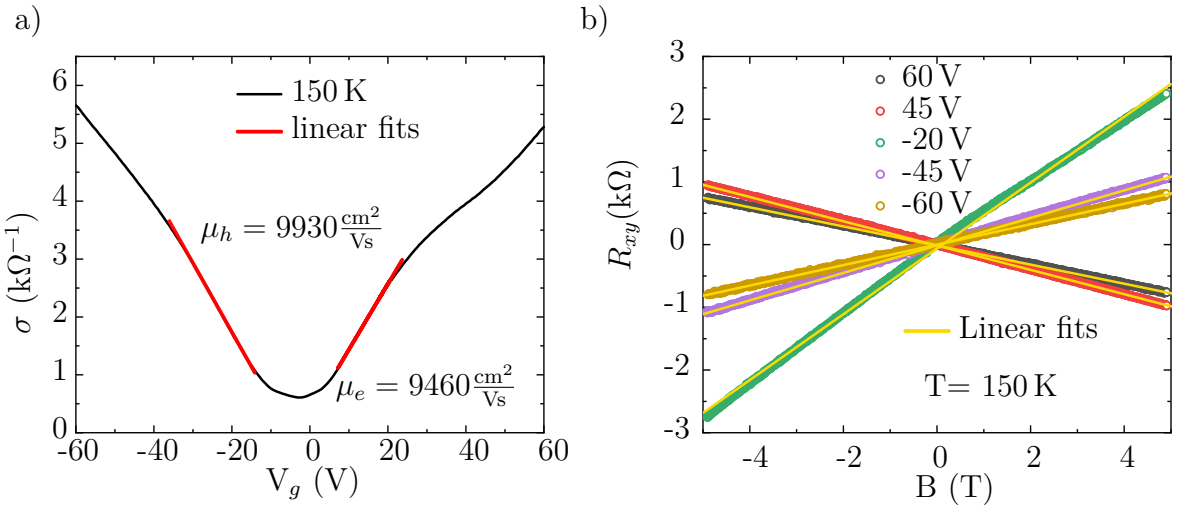

Fig. 6.2: a) Back gate voltage dependence of the corresponding conductivity from the same 150 K measurements as in Fig. 6.1 b). The electron and hole mobilities are determined by the slope of the linear fits (red). b) Hall measurements of Sample A at specific back gate voltages. The charge carrier density is determined by the inverse slope of the linear fits (yellow).

recorded after the sample had been taken out of the cryostat after the first measurements. Therefore, the sample got exposed to the environment and cooled down again. This can lead to small changes in the transport properties of the graphene, even though it is encapsulated. However, both analysis of the mobility show, that the mobilities are in the range from $\mu = 7500 - 10900 \frac{cm^2}{Vs}$ and $\mu_h > \mu_e$.

The carrier mobility is limited by various factors. At low temperatures, the mobility of graphene on SiO_2 is mainly limited by disorder effects [175–177]. Charged impurities, trapped at the SiO_2 or graphene surface [176], adsorbates on the graphene before encapsulation [136] or an induced surface roughness onto the graphene [178] introduce scattering and limit mobility of charge carriers. A sublinear back gate voltage dependence of $\sigma(V_g)$ can be explained by the induced corrugation of graphene [177, 179] and invasive contact probes [180]. At higher temperatures (T>200 K), remote interfacial phonon scattering from the polar optical phonons of the SiO_2 substrate also need to be considered [178, 181]. The observed asymmetry in the hole and electron mobility is characteristic for invasive metallic contacts to graphene [180]. However, the calculated mobilities are consistent with other graphene-on-SiO_2 samples [25, 178, 181].

6.1.2. Charge diffusion constant D_c

In non-local spin transport experiments, the spin diffusion constant D_s is an important parameter and is closely related to the spin diffusion length L_s and spin lifetime τ_s. The equivalent property in charge transport experiments is the charge diffusion constant D_c,

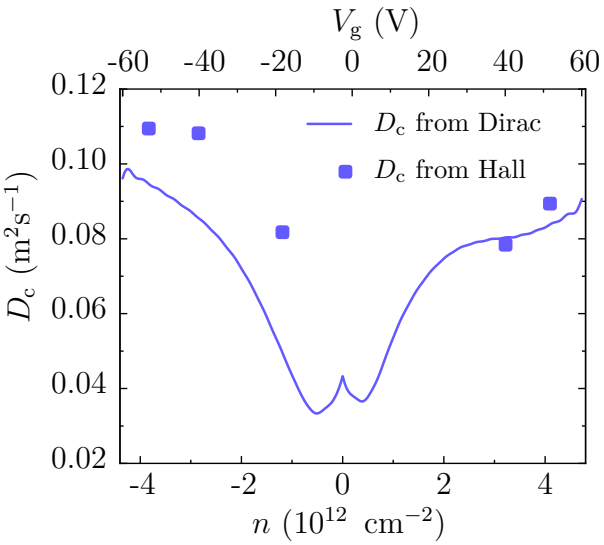

Fig. 6.3: Charge diffusion constant for Sample A calculated from Dirac (line) and Hall measurements (points) as a function of charge carrier density n and gate voltage V_g. The energy broadening was assumed to be $\xi = 75\,\text{meV}$. In the electron regime (positive n and V_g), D_c from Dirac and Hall measurements are in agreement, whereas in the hole regime (negative n and V_g) they differ showing a similar dependence on n.

which was found to be equal to the spin diffusion constant D_s in graphene [97, 182]. D_c can be experimentally obtained from the Dirac measurements in Fig. 6.1 b). For this, the Fermi energy is calculated from the charge carrier density n with Eq. (2.15). Eq. (2.18) then gives the broadened DOS g^*. For the energy broadening $\xi = 75\,\text{meV}$ was used. The charge diffusion constant D_c is then calculated with the broadened DOS g^* via Eq. (2.17) with σ being the measured conductivity, as in Fig. 6.2 a). The result is plotted as the solid line in Fig. 6.3. The charge diffusion constant D_c was also calculated from the Hall measurements in Fig. 6.2 b). The results are plotted in Fig. 6.3 as points. The calculated D_c varies within the range $D_{c,\,\text{Dirac, A}} = 0.033 - 0.1\,\text{m}^2\text{s}^{-1}$ for the Dirac and $D_{c,\,\text{Hall, A}} = 0.078 - 0.11\,\text{m}^2\text{s}^{-1}$ for the Hall measurements. The Hall measurements were carried out only at V_g sufficiently away from the charge neutrality point. The D_c for Sample B, shown in Fig. A.5, vary within the range $D_{c,\,\text{Dirac, B}} = 0.023 - 0.107\,\text{m}^2\text{s}^{-1}$, which is similar to the results of Sample A. Similar values for D_c were obtained for both samples, when calculating the charge diffusion constant from the mean-free path l_{mfp}. The obtained values, however, are larger compared to other reported charge diffusion constants for similar samples ranging from $D_{c,\,\text{literature}} = 0.015 - 0.03\,\text{m}^2\text{s}^{-1}$ [97, 182]. This discrepancy might be attributed to the low resistivity observed in the Dirac measurement in Fig. 6.1 b), particularly with a small resistivity at the charge neutrality point of $R_{\text{CNP}} \approx 1.65\,\text{k}\Omega$. Due to the inverse proportionality with respect to the resistivity (Eq. (2.17)), the resulting D_c gets large.

6.2. Characterization of the hBN tunnel barriers

As a next step, the exfoliated hBN tunnel barriers are characterized. The barriers are crucial in order to circumvent the conductivity mismatch problem and to ensure efficient spin injection, as discussed in Sec. 3.2. However, the thickness of the barriers is limited to

allow for tunnelling. The tunnel current decreases exponentially as the thickness increases [101]. The zero-bias resistance increases exponentially from 1 kΩμm^2 for a single layer of hBN to 0.1 GΩμm^2 for four layers. Therefore, the hBN thickness should be within this range for feasible tunnel barriers. Thicker barriers result in larger resistances and may even prevent charge carriers from tunnelling.

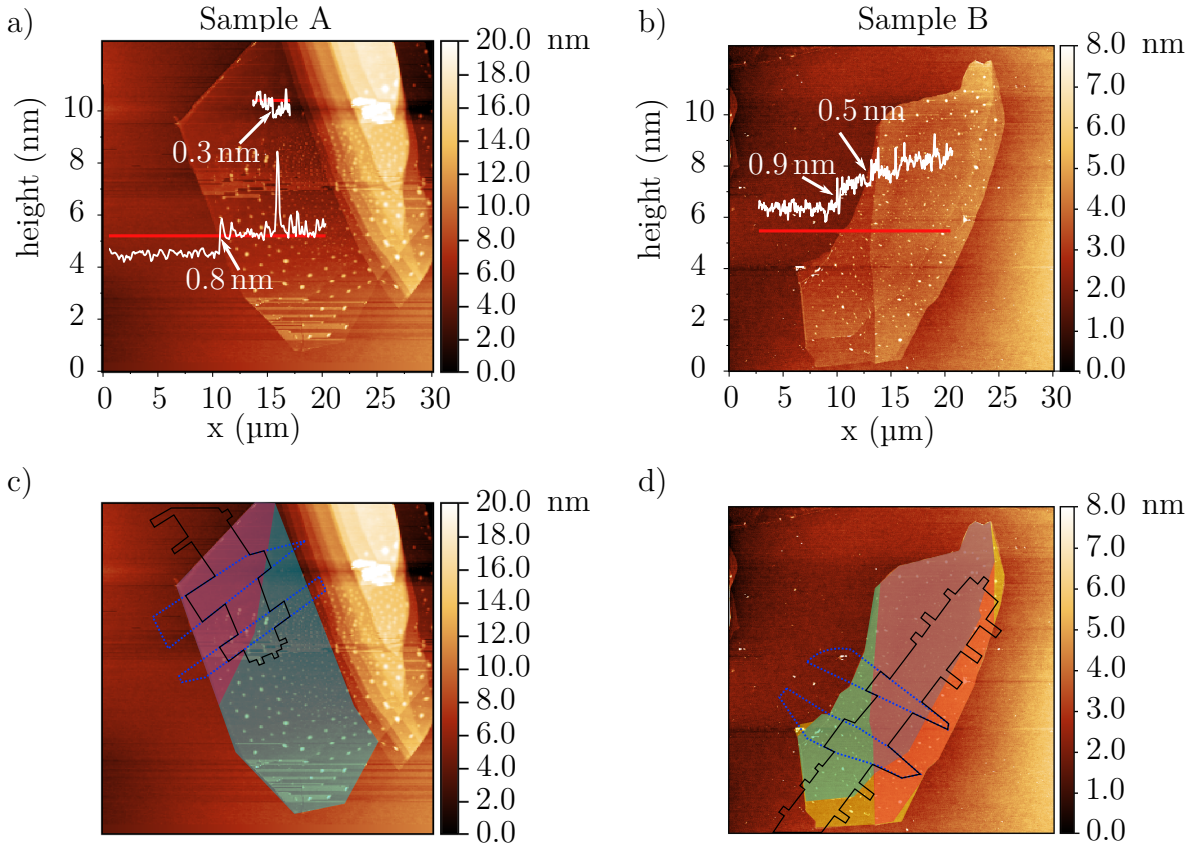

Fig. 6.4: Topography of the hBN tunnel barriers for Sample A in a) and c), and Sample B in b) and d) measured by non-contact mode AFM. The height profile is also plotted, with the extracted height of the hBN flakes. The scale bar corresponding to the height profile is on the left of each image. The red lines indicate the position of the AFM line scan, shown in the image. c) AFM image clearly distinguishing each individual hBN layer by colour. The green blue area corresponds to a two-layer thick hBN, while the purple area corresponds to a three-layer thick hBN. The etched graphene is outlined in black, and the FGT electrodes are shown as blue dashed lines. d) AFM image showing monolayer hBN in yellow. Green and red areas represent two-layer thick hBN, while the purple area in the middle represents three-layer thick hBN. The outlines of graphene and FGT are again illustrated as black solid and blue dashed lines, respectively.

6.2.1. AFM characterization

Fig. 6.4 a) and b) show the topography of the hBN flakes used as a tunnel barrier for Samples A and B, respectively, along with their corresponding height profiles. The reported monolayer hBN thickness of 0.333 nm [183] suggests non-uniform two- and three-layer thick tunnel barriers for both samples underneath the outlined FGT strips (see Fig. 6.4 c) and d)). However, the hBN thicknesses can be overestimated by the AFM due to adsorbates like e.g. water on the surface. Fig. 6.4 c) and d) clearly illustrate the individual hBN layers (colored areas) combined with the outlines of graphene and FGT. In Sample A, the upper FGT electrode was primarily utilized as the spin-injecting electrode, whereas in Sample B the bottom was employed for this purpose. As illustrated by the individual layers and outlines, the overlap of the FGT/2-layer-hBN/graphene contact is larger at the injector of Sample B compared to Sample A, where the injector is predominantly above a 3-layer hBN barrier.

6.2.2. Electrical characterization

To verify the accuracy of the AFM measurements in determining the number of layers, the comparison of the zero-bias resistances can also be used. The zero-bias resistance is determined by the current dependence of the three-terminal voltage $V_{3\mathrm{T}}$, which was measured during non-local spin injection experiments at the injector, as described in Sec. 4.3. Therefore, only statements regarding the hBN thickness beneath the injectors can be made in the following. In general, a tunnel current from a top to a bottom electrode depends on the density of states of both materials, the tunnel probability $T(E)$ and the number of unoccupied states of the bottom electrode in the energy interval from E to $E + dE$ and is given by [101, 184]

$$I(V) \propto \int_{-\infty}^{\infty} dE g_{\mathrm{T}}(E) g_{\mathrm{B}}(E + eV) T(E) \left[f(E) - f(E + eV) \right], \tag{6.1}$$

where $f(E)$ is the Fermi distribution, $g_{\mathrm{T(B)}}$ is the density of states of the top (bottom) electrode at the given energy and V is the applied voltage between top and bottom electrode. The tunnel probability $T(E)$ is directly influenced by the tunnel barrier thickness. Furthermore, it has to be noted that the density of states is material dependent which leads to different tunnel currents and, consequently, different zero-bias resistances depending on the used top and bottom electrode materials. Therefore, comparing $R_{3\mathrm{T},\,0V}$ measured from samples using different electrode materials, rather acts as a reference point for estimating the tunnel barrier thickness in the following.

Fig. 6.5 a) and b) show the applied current multiplied by the area of the FGT/hBN contact plotted against the measured three-terminal voltage at different back gate voltages V_{g} at a temperature of $T = 1.5\,\mathrm{K}$ for Sample A and B, respectively. For both samples, the

current densities are in the range of 1 to 20 $\frac{\mu A}{\mu m^2}$ which best fit the two-layer hBN curve in Fig. 6.5 c). The zero-bias resistances $R_{3T,\,0V}$ were calculated using the $I - V_{3T}$-curves, shown in Fig. 6.5 a) and b), and correspond to the inverse slope of the $I - V_{3T}$-curve at low three-terminal voltages. It is evident from both samples that $R_{3T,\,0V}$ at positive gate voltages (electron conduction in graphene) are approximately half that of those at negative gate voltages (hole conduction in graphene). A gate-dependence is expected, as the density of states of graphene is also gate dependent. However, as the charge neutrality point is only slightly shifted for both samples, one naively would expect the same tunnel current for the same positive and negative applied gate voltage, as this results in the same calculated charge carrier density and, thus density of states in graphene (see Eq. (2.16)). The density of states of the bottom graphene varies from $g_A^* = 1.87 - 2.07 \cdot 10^{32}\,(\mathrm{J{\cdot}cm})^{-2}$ in Sample A, when sweeping the gate voltage V_g from $-45\,\mathrm{V} \rightarrow 45\,\mathrm{V}$. In Sample B it varies from $g_B^* = 2.49 - 2.05 \cdot 10^{32}\,(\mathrm{J{\cdot}cm})^{-2}$, when sweeping the applied gate voltage V_g from $-60\,\mathrm{V}$ to $60\,\mathrm{V}$. As these values for negative and positive gate voltages are quite similar, one would also expect similar values for the tunnel currents and, thus, zero-bias resistances. Furthermore, these findings contradict the findings of Iqbal *et al.* [185], where they observed a monotonically decreasing current density as the back gate voltage was swept from -60 V to +60 V, with the dielectric thickness of 300 nm SiO_2 being similar. However, they do not show a Dirac measurement, which prevents the calculation of the charge carrier density and density of states, as the CNP could be highly shifted to large negative or positive values by doping from the environment. This makes a direct comparison impossible.

The original data of Britnell *et al.* , presented in Fig. 6.5 d) (white boxes), show both Au/hBN/Au and graphite/hBN/graphite samples, which both exhibit different characteristics. The extracted zero-bias resistances of Sample A and B are plotted in Fig. 6.5 d) alongside the original data of Britnell *et al.* [101]. Fig. 6.5 d) demonstrates that for Sample A, the zero-bias resistances are beneath the predicted value for three layers of hBN, based on the linear fit from Ref. [101]. This might be due to the small overlap of the FGT/2-layer-hBN/graphene contact which is reducing, the average zero-bias resistance. In contrast, for Sample B, the zero-bias resistances are in good agreement with the predicted fit. This is also consistent with the AFM data which clearly show the majority of the FGT/hBN/graphene injector contact being on top of two layers of hBN.

In conclusion, the data obtained from the AFM and electrical characterization are consistent with one another. The FGT electrodes in Samples A and B are on top of a two- to three-layer thick hBN tunnel barrier. For the spin injecting electrodes, the overlapping area with the three-layer hBN is more prevalent in Sample A, while for Sample B the two-layer hBN overlap predominates. For the spin detecting FGT electrodes it is vice versa.

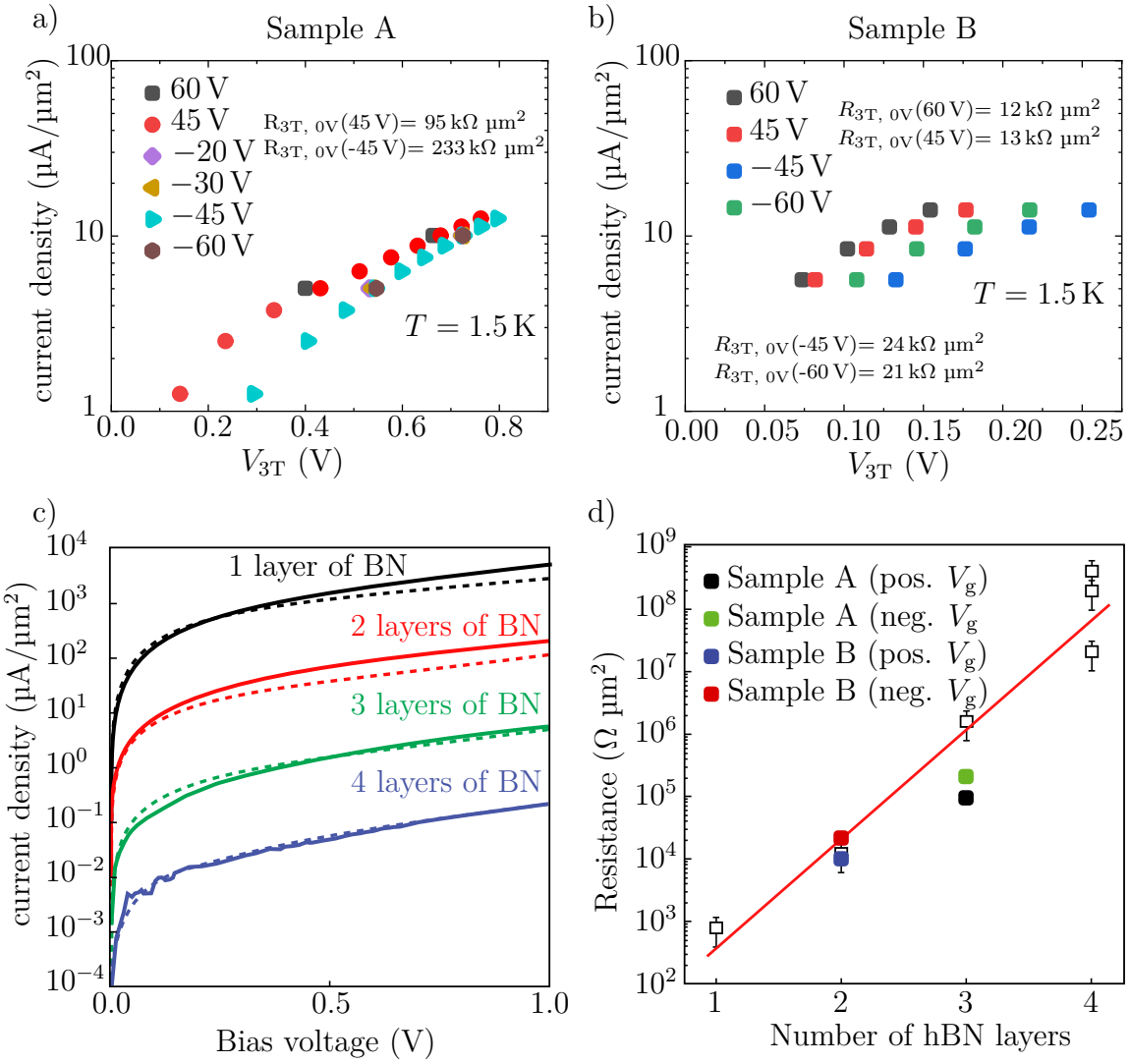

Fig. 6.5: a) and b) electrical characterization of the hBN tunnel barriers at the injector of Sample A and B, respectively. The measured three-terminal voltage V_{3T} is plotted against the applied current I divided by the FGT/hBN contact area A on a logarithmic scale for different back gate voltages V_g. From these measurements, the zero-bias resistances $R_{3T,\,0V}$ for each V_g was determined. c) $I-V$-curves for graphite/hBN/graphite devices for different hBN thicknesses. The applied current I was normalized by the overlapping area of the graphite/hBN/graphite. Solid lines are experimental data, while dashed lines are the theoretical prediction. Adapted from [101]. d) Exponential dependence of the zero-bias resistance for different numbers of hBN layers. Currents are normalized as in c). Additionally, the zero-bias resistances for Sample A and B for positive and negative V_g are plotted. Adapted from [101].

6.2.3. Temperature dependence of the three-terminal resistance

In order to confirm that the hBN barrier acts as a tunnel contact, it is necessary to confirm the Rowell criteria [186]. For non-superconducting ferromagnet-insulator-ferromagnet magnetic tunnel junctions (MTJs), three criteria must be fulfilled: the resistance must increase exponentially with thickness; the $I-V$-curves must be non-linear following Simmons' model [187]; and the resistance should exhibit a weak insulating-like temperature dependence, i.e. decreasing with increasing temperature. Nevertheless, only the latter remains a reliable criterion for tunnelling, as the other two can also be established by tunnel barriers with pinholes [188].

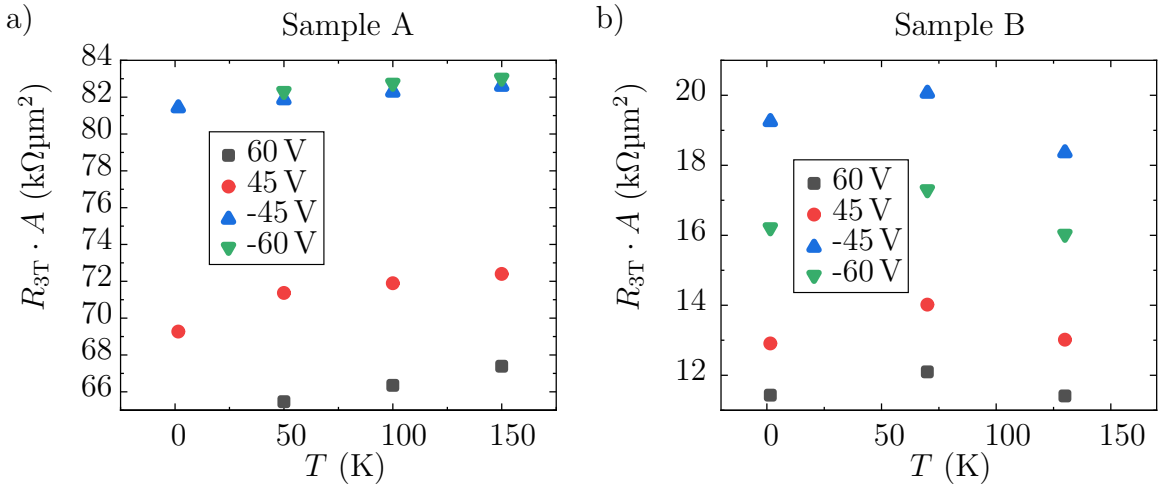

Fig. 6.6: Temperature dependence of the three-terminal resistances multiplied by the contact area A for a) Sample A and b) Sample B, at various applied back gate voltages. All measurements were carried out at a constant current of $I = -200\,\mu\text{A}$.

As the three-terminal voltage was only measured for selected currents, it is not possible to determine the zero-bias resistances for $T > 1.5\,\text{K}$. Consequently, only the three-terminal resistances multiplied by the contact area $R_{3T}A$ are shown in Fig. 6.6 a) and b) for Sample A and B, respectively. For Sample A, a monotonous increase in $R_{3T}A$ with temperature can be observed for all investigated back gate voltages, while for Sample B $R_{3T}A$ is larger at $T = 1.5\,\text{K}$ than for $T = 130\,\text{K}$. However, for Sample B $R_{3T}A(70\,\text{K})$ is largest for all applied gate voltages. In Ref. [188], an increasing zero-bias resistance with increasing temperature was only reported for samples with pinholes in the barriers, thus exhibiting a metallic-like temperature dependence. Consequently, it cannot be ruled out that both samples may have experienced the formation of pinholes in the tunnel barriers in the form of cracks that may have appeared during the stacking process.

7. Non-local spin transport experiments

This chapter presents the main experimental findings of this thesis, which demonstrate efficient non-local spin transport in all-2D van der Waals samples. This is verified through non-local spin valve measurements on both Samples A and B, presented in Sec. 7.1, which is a standard way of demonstrating a non-equilibrium spin accumulation. Moreover, the spin dynamics in both samples are investigated through Hanle measurements, presented in Sec. 7.2, thereby corroborating the existence of a non-equilibrium spin accumulation in graphene. This chapter begins with presenting the non-local spin valve measurements of Sample A and B in Sec. 7.1.1 and Sec. 7.1.2, respectively. Subsequently, Hanle measurements of both samples are presented in Sec. 7.2.1 and Sec. 7.2.2. By fitting the measurement data, spin transport parameters, such as the spin lifetime τ_s, the spin diffusion constant D_s, and the spin injection efficiency P are extracted. These results are then discussed with the aid of *COMSOL* finite-element simulations that model the spin dynamics in our system.

7.1. Non-local spin valve measurements

7.1.1. Sample A

In non-local spin valve measurements, the spin accumulation underneath the detecting FM electrode is probed as a function of the external magnetic field, which is applied along the easy-axis of the FM. In the case of FGT spin-aligning electrodes, the external magnetic field is swept out-of-plane. The measurement setup is depicted in Fig. 4.7. In the following, the non-local spin valve measurements of Sample A are discussed. The numbering of the contacts of this sample can be seen in Fig. 6.1 a). During the measurements, a constant current I is applied at the injector circuit from contacts 5 to 19, while the spin accumulation is measured as a non-local voltage V_{nl} between the contacts 11 and 14. By sweeping the magnetic field past the coercive fields of the injector and detector, which are at different field values due to their differing shapes and thicknesses, a parallel and anti-parallel magnetization configuration of both electrodes can be established. This is accompanied by corresponding steps in the measured non-local voltage V_{nl}, which is characteristic for spin valve measurements. In order to assign the change in V_{nl} to the

magnetic configuration, the anomalous Hall effect was measured simultaneously at the spin-injecting electrode, between contacts 6 and 4. The two signals were then compared, to determine whether they share the same switching behaviour. Since current is required, the anomalous Hall effect can only be measured at the injector.

Fig. 7.1 a) depicts the anomalous Hall loop of the injecting electrode of Sample A at a temperature of $T = 1.5\,\mathrm{K}$, a constant injecting current $I = -250\,\mu\mathrm{A}$, and an applied back gate voltage of $V_\mathrm{g} = 45\,\mathrm{V}$. A sharp switching of the injector's magnetization is observed at $B \approx \pm 0.5\,\mathrm{T}$. The corresponding spin valve trace, which was simultaneously measured, is shown in Fig. 7.1 b). In this figure, the non-local voltage V_nl is normalized by the injection current I, resulting in a non-local resistance $R_\mathrm{nl} = V_\mathrm{nl}/I$. The switching of the injector's magnetization illustrated in Fig. 7.1 a) coincides with R_nl switching back to a positive normalized voltage in Fig. 7.1 b). This leads to the conclusion that the initial switching of R_nl is due to the detecting electrode, which exhibits a smaller coercive field than that of the injecting electrode. During the measurement of the magnetic up-sweep, the magnetic field is swept from $B = -1\,\mathrm{T}$ to $1\,\mathrm{T}$. Initially, both FGT electrodes exhibit a parallel magnetization configuration. In this case, the detector senses the majority spin accumulation in the graphene channel as a large non-local signal R_nl. Sweeping the magnetic field towards larger field values, the applied magnetic field exceeds the coercive field of the detecting electrode. The detector's magnetization switches, which results in an anti-parallel magnetization configuration of both FM electrodes. The detector now probes a minority spin accumulation, which can be observed as a sudden change in the non-local signal R_nl, exhibiting a negative normalized voltage. Upon increasing the magnetic field above the coercive field of the injector, a parallel magnetization configuration is restored. In this configuration, the detector senses the majority spin accumulation, which results in a positive non-local signal. The typical non-local spin valve trace is obtained. The identical phenomenon can be observed in the magnetic down-sweep, displaying clear magnetic switching. This results in a symmetric spin valve signal around $B = 0\,\mathrm{T}$ for both up- and down-sweeps. Moreover, this switching can be ascribed to a change in the magnetization configuration of both electrodes via the anomalous Hall effect. It can therefore be confidently stated, that the spin-polarized current in the injection circuit establishes a non-equilibrium spin accumulation in the graphene channel, which is probed as a non-local voltage at the second detecting FGT electrode.

The amplitude of the non-local spin valve, defined as $\Delta R_\mathrm{nl} = R_{\mathrm{nl,\,P}} - R_{\mathrm{nl,\,AP}}$, as illustrated in Fig. 7.1 b), represents a measure of the spin accumulation beneath the detector, as described by Eq. (3.28). Here, $R_{\mathrm{nl,\,P\,(AP)}}$ denote the non-local signals in the parallel (anti-parallel) configuration. However, the value of ΔR_nl is not unambiguous. As can be seen in Fig. 7.1 b), the non-local signal $R_{\mathrm{nl,\,P}}$ is larger after changing the direction of the external magnetic field and before switching of the first electrode. Consequently, a mean value for $R_{\mathrm{nl,\,P}}$ is calculated from measurement points situated to the left and right of the spin valve signal. The calculated mean value of all measured points in the anti-parallel alignment calculates $R_{\mathrm{nl,\,AP}}$. The resulting ΔR_nl is then the mean value of the up- and down-sweep signal heights $\Delta R_{\mathrm{nl,\,up}}$ and $\Delta R_{\mathrm{nl,\,down}}$. This yields a spin valve

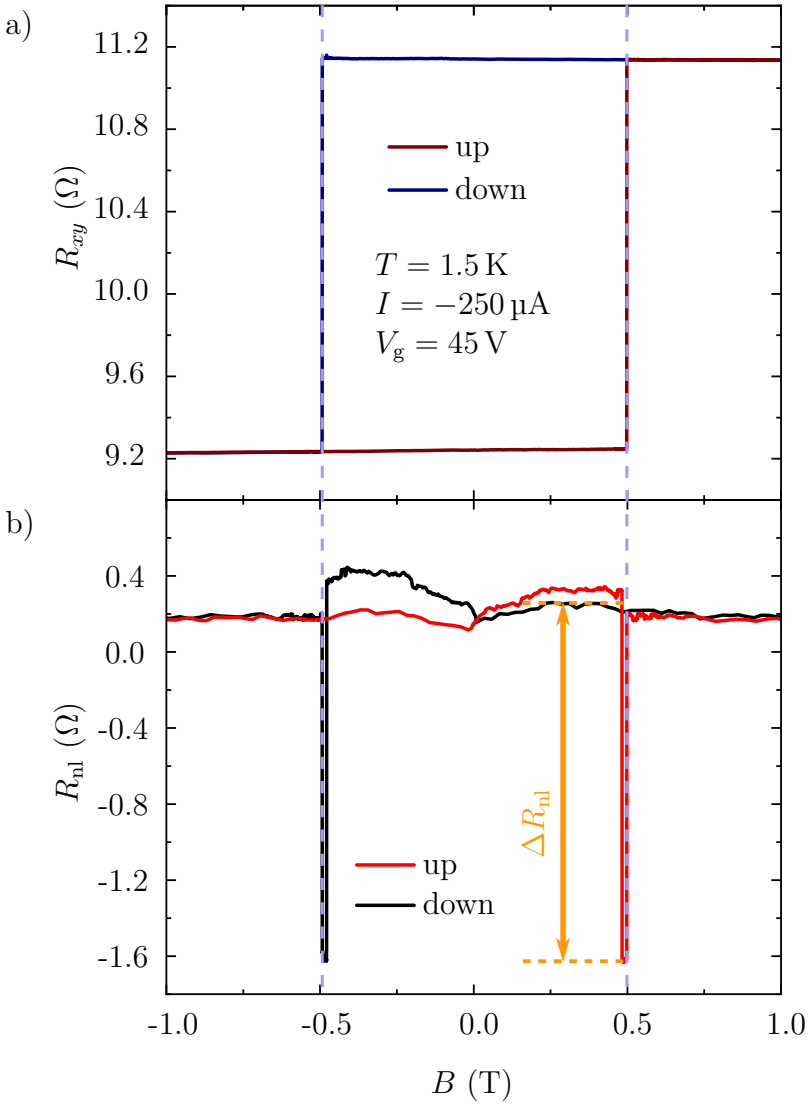

Fig. 7.1: a) Magnetization loops of the spin injecting electrode of Sample A at a temperature of $T = 1.5\,\mathrm{K}$, injection current $I = -250\,\mu\mathrm{A}$, and an applied back gate voltage of $V_\mathrm{g} = 45\,\mathrm{V}$. Clear single domain switching is observed. b) Magnetic up- (red) and down-sweeps (black) of the non-local signal R_nl. As indicated by the purple dashed lines, the magnetization switching of the injector coincides with the switching of R_nl. The height of the non-local signal ΔR_nl is evaluated as described in the text. Both measurements shown in a) and b) were recorded simultaneously.

height of $\Delta R_\mathrm{nl} = 1.88\,\Omega$ for the measurement illustrated in Fig. 7.1 b). This large value confirms efficient spin injection in our devices and is three orders of magnitude larger than for FGT/graphene based all-2D van der Waals non-local spin valve devices without a tunnel barrier, where a signal height of up to $1.5\,\mathrm{m}\Omega$ was reported [31]. Additionally, the spin valve signal was also measured in the switched injector-detector configuration at $T = 1.5\,\mathrm{K}$, as illustrated in the Appendix Fig. A.6. However, as the spin valve signals

were markedly lower in this configuration, with spin valve heights of up to $\Delta R_{\mathrm{nl}} = 0.12\,\Omega$, and not discernible at all applied currents and gate voltages, the spin valve signals in the configuration as illustrated in Fig. 4.7 are examined in more detail in the following.

Stability of the signal

Interestingly, the spin valve signal was observed to exhibit a certain degree of instability, as can be seen in Fig. 7.2. Fig. 7.2 a) illustrates how the non-local signal changes in the down- and up-sweeps for the same set of parameters of $I = -200\,\mu\mathrm{A}$, $V_{\mathrm{g}} = 45\,\mathrm{V}$ at $T = 1.5\,\mathrm{K}$. However, the measurements shown in Fig. 7.2 a) were not recorded directly one after another. In between the discussed measurements, other spin valve traces were recorded for other sets of parameters, while maintaining a constant temperature of $T = 1.5\,\mathrm{K}$. As previously discussed in Sec. 5.2, both the injecting and detecting FGT are subject to a varying exchange bias field. This is evidenced by the variation in their switching fields from one sweep to the next, as can be seen in Fig. 7.2 a). The corresponding extracted spin valve heights ΔR_{nl} are plotted in Fig. 7.2 b), demonstrating a decreasing tendency of the spin valve signal for each measurement iteration. However, as these curves were not recorded in a direct sequence and the current and gate voltages are varied in between these measurements, a small hysteresis with respect to these parameters cannot be excluded and could potentially result in a smaller signal.

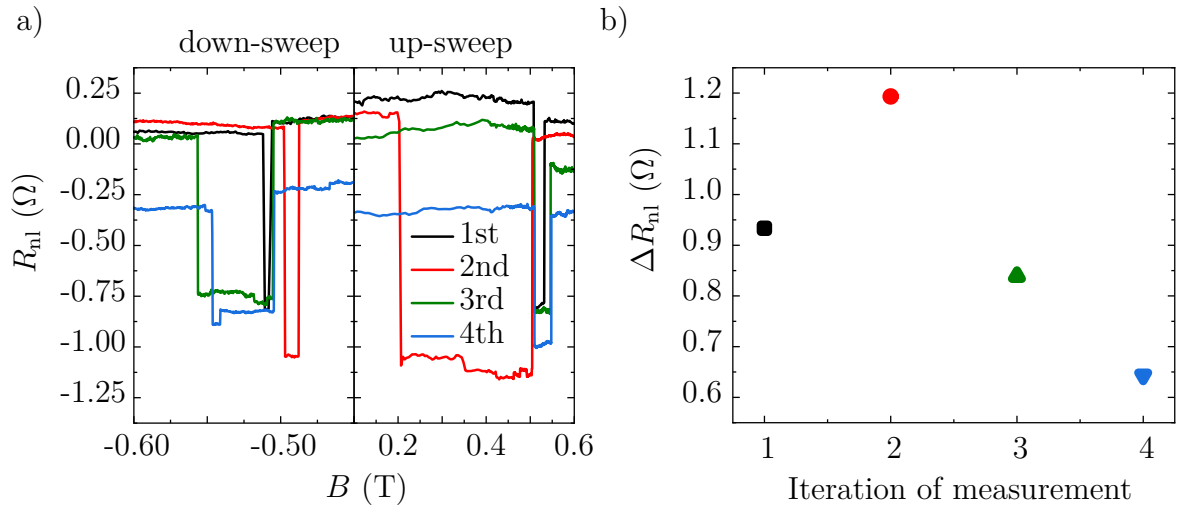

Fig. 7.2: a) Comparison of down- and up-sweeps of spin valve measurements carried out in the same measurement configuration at an applied bias of $I = -200\,\mu\mathrm{A}$, a back gate voltage of $V_{\mathrm{g}} = 45\,\mathrm{V}$ and a temperature of $T = 1.5\,\mathrm{K}$. Both FGT strips exhibit a varying exchange bias field in different sweeps. b) Extracted spin valve heights ΔR_{nl} of the measurements shown in a), observing a decreasing tendency for every measurement iteration.

Signatures of magnetic moments

The non-local signal exhibits a dip centred at zero magnetic field, as can already be seen in Fig. 7.1 b). This phenomenon was observed for all investigated temperatures, back gate voltages, and applied biases, both for up- and down-sweeps of the external magnetic field, being more pronounced in some curves than in others. This feature had been previously investigated in other graphene spin-valve devices and has been attributed to magnetic moments in the graphene channel. The randomly oriented localized magnetic moments can be introduced via lattice vacancies or hydrogenation of the graphene [132, 189]. Similar to the Dyakanov-Perel model, spin precession around these randomly fluctuating exchange fields in x- and y-direction leads to spin relaxation. Consequently, the spin signal is reduced. At high applied magnetic fields, the spin relaxation is suppressed due to the fact that the applied field defines the precession axis, effectively preventing the fluctuating fields from tilting this axis. Consequently, the peak in the spin relaxation at low magnetic fields is observed as a dip in the non-local signal R_{nl}.

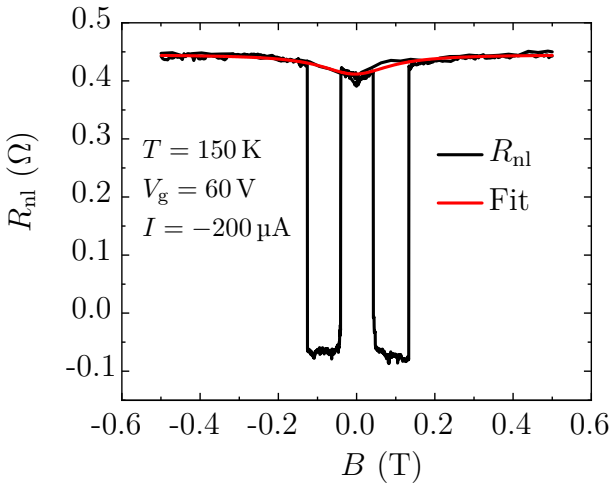

Fig. 7.3: Non-local signal R_{nl} (black) displaying a dip at low magnetic fields, which could possibly be attributed to magnetic moments. The fit (red) agrees well with both up- and down-sweeps.

The dip is best observed in the non-local spin valve measurements at an elevated temperature of $T = 150\,\mathrm{K}$ at $V_{\mathrm{g}} = 60\,\mathrm{V}$, and an applied current of $I = -200\,\mu\mathrm{A}$, as illustrated in Fig. 7.3. The dip is centred around zero applied field, exhibiting no hysteresis with respect to the applied magnetic field. Such a behaviour is characteristic for paramagnetic moments. In contrast, ferromagnetic moments would generate a hysteretic dip that is centred at a finite external field. The dip in the non-local signal can be fitted with Eq. (3.27), by introducing an additional spin relaxation mechanism due to a fluctuating field generated by the magnetic moments. The spin relaxation time due to a fluctuating field is given by [17, 132]

$$\frac{1}{\tau_{\mathrm{l}}^{\mathrm{ex}}} = \frac{(\Delta B)^2}{\tau_{\mathrm{c}}} \frac{1}{(B_{\mathrm{app},z} + B_{\mathrm{ex},z})^2 + (\frac{\hbar}{g_{\mathrm{L}}\mu_{\mathrm{B}}\tau_{\mathrm{c}}})^2}, \tag{7.1}$$

where ΔB is the rms fluctuation, τ_{c} is the correlation time, $B_{\mathrm{app},z}$ is the applied magnetic field, $B_{\mathrm{ex},z}$ the effective field generated by the exchange interaction and g_{L} corresponds to

the charge carrier's g-factor. The non-local voltage V_{nl} is given by Eq. (3.27), where the spin relaxation length is given by $L_{\mathrm{s}} = \sqrt{D_{\mathrm{s}} T_{\mathrm{l}}^{\mathrm{total}}}$. The total spin relaxation time $T_{\mathrm{l}}^{\mathrm{total}}$ depends on both the spin relaxation due to spin-orbit coupling τ_{so} and spin relaxation from the exchange field $\tau_{\mathrm{l}}^{\mathrm{ex}}$ as $(T_{\mathrm{l}}^{\mathrm{total}})^{-1} = (\tau_{\mathrm{l}}^{\mathrm{ex}})^{-1} + (\tau_{\mathrm{so}})^{-1}$. Fitting results in a rms fluctuation $\Delta B = 16.07\,\mathrm{mT}$, correlation time $\tau_{\mathrm{c}} = 509\,\mathrm{ps}$, a spin-orbit coupling induced spin relaxation time $\tau_{\mathrm{so}} = 495\,\mathrm{ps}$, and an exchange interaction field $B_{\mathrm{ex},z} = 3.95\,\mathrm{mT}$. These values are comparable to the results presented in Ref. [132], where a hydrogen concentration in the order of 0.1 % for a sample that was hydrogenated for 8 s was estimated. Given that the samples investigated in this thesis were stacked in an inert atmosphere, capped with hBN, and not subjected to any hydrogenation or annealing processes [132, 189], the origin of these magnetic moments remains unclear. However, it has to be noted that graphene was exfoliated under ambient conditions in the cleanroom and subsequently stored in a glove box, which may have resulted in an accumulation of adsorbates on its surface.

In order to investigate the influence of external parameters on the non-local signal, it was investigated for injecting currents ranging from $I = -250$ to $250\,\mu\mathrm{A}$, for various back gate voltages in the range of $V_{\mathrm{g}} = -60$,V to 60 V, at specific temperatures $T = 1.5\,\mathrm{K}$, 50 K, 100 K, and 150 K.

Current dependence

The non-local signal is not a direct function of the applied bias current, as it does not enter Eq. (3.28). Nevertheless, there is an implicit dependence on current in the spin injection efficiency P_{inj}, which in real devices depends on the injection current. The dependence of the non-local signal height ΔR_{nl} on the applied bias is shown in Fig. 7.4, where ΔR_{nl} is plotted against the applied current I at a temperature of $T = 1.5\,\mathrm{K}$, at $V_{\mathrm{g}} = \pm 45\,\mathrm{V}$. This corresponds to the electron (positive V_{g}) and hole (negative V_{g}) conduction regime of graphene, as the charge neutrality point of Sample A is centred at $V_{\mathrm{CNP}} = -4\,\mathrm{V}$. For both gate voltages, ΔR_{nl} decreases upon changing I to larger positive values. This even leads to an inversion of the non-local signal around $I = 200\,\mu\mathrm{A}$, as shown in Fig. 7.5.

This inversion of the spin signal is typically attributed to a change of sign of P_{inj} with applied bias, indicating an inversion of the spin polarization at the Fermi level of the injecting FGT electrode. This phenomenon has been previously observed in both, conventional graphene spin valve devices utilizing Co electrodes [190, 191] and also in III-V spin valve devices [20]. In graphene spin valve devices employing Co electrodes, this inversion was observed in a narrow range of bias voltages ranging from $-225\,\mathrm{mV}$ to $-75\,\mathrm{mV}$, when utilizing both MgO and hBN tunnel barriers. Consequently, this mechanism is also independent of the tunnel barrier material [191]. The voltage drop across the tunnel barrier tunes the band alignment of the FM electrode and graphene,

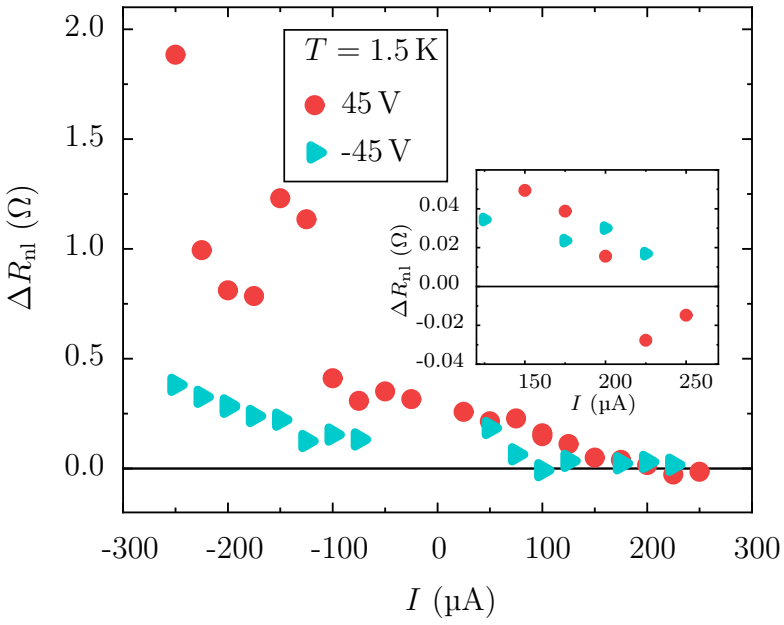

Fig. 7.4: Current dependence of the non-local signal height in the electron ($V_g = 45\,V$, red) and hole ($V_g = -45\,V$, blue) conduction regime of the graphene channel. Increasing the applied current towards positive values leads to a reduction of the spin valve signal. For the electron regime, even an inversion of the spin valve signal is observed at a current of $I = 200\,\mu A$. The region, where the non-local signal inverts, is shown as an inset.

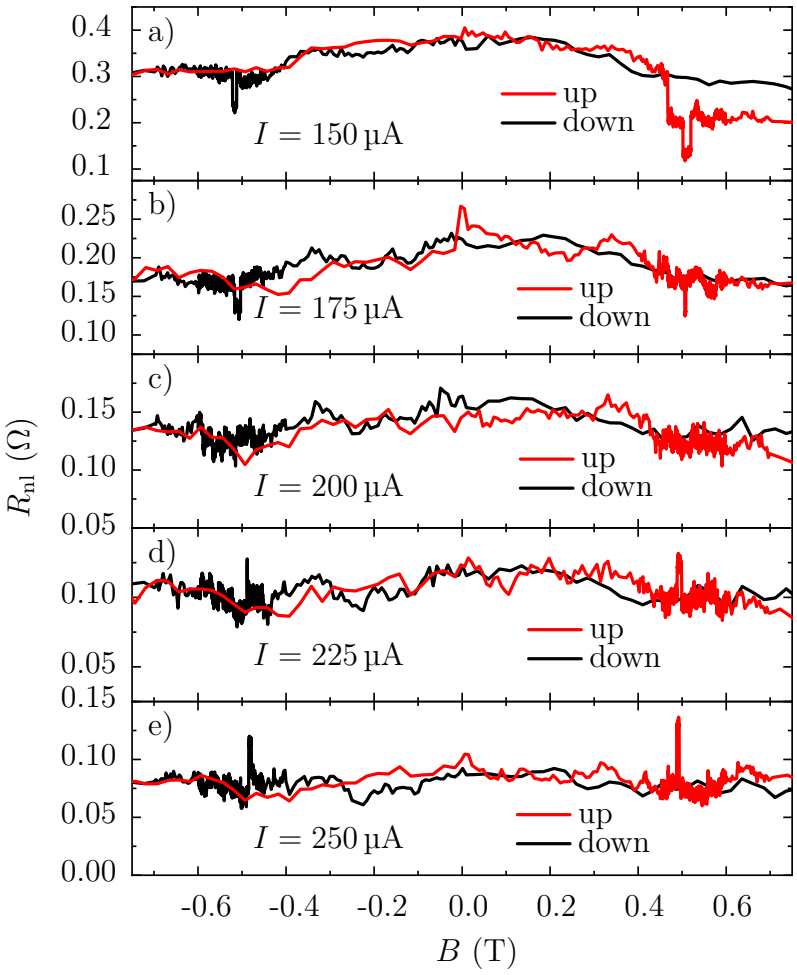

Fig. 7.5: Non-local spin valve signal R_{nl} at $V_g = 45\,V$, and $T = 1.5\,K$ in the current range of the inversion. The applied current increases from a) $I = 150\,\mu A$ to e) $I = 250\,\mu A$ in $25\,\mu A$ steps. While the non-local spin valve points downwards in a), it vanishes at a current of $I = 200\,\mu A$ in c). Increasing the current to $I = 225\,\mu A$ reverses the spin valve signal in d), pointing upwards.

thereby tuning the spin injection efficiency. However, for Sample A utilizing FGT electrodes, the large currents of up to $I = 250\,\mu\text{A}$ correspond to a much larger voltage drop of up to $V_{3\text{T}} = 0.8\,\text{V}$, as illustrated in Fig. 6.5 a). The ability to tune the spin polarization of injected spins via bias and back gate voltages has enabled the realization of spin field effect transistor action in Co/MgO/graphene spin valve devices [190].

Several mechanisms have been identified that give rise to non-linear bias-dependent spin signals, including electric field-induced spin drift and tunnel barrier spin filtering [33, 192–194]. In graphene spin valves it has been demonstrated that the measured non-local signal is affected by an electric field in the spin diffusion channel [33, 192]. This is due to the fact that the electric field induces a drift effect of the spin-polarized carriers. Additionally, a spin filtering effect in non-uniform hBN tunnel barriers was reported [193]. Here, an asymmetric bias dependence in spin polarization is then a result of the asymmetric junctions. Moreover, combining an AC and DC injecting current was reported to exhibit a DC bias dependent sign reversal of the differential spin signal for graphene based spin valve devices with a hBN tunnel barrier thickness of two layers [194].

Gate and temperature dependence

The non-local signal, according to Eq. (3.28), does not include a direct dependence on the gate voltage and temperature. Nevertheless, the sheet resistance of graphene R_s depends on the applied gate voltage. As can be already seen in the current dependence of the non-local signal, illustrated in Fig. 7.4, ΔR_nl is significantly larger in the electron than in the hole regime for all investigated bias currents. This is confirmed in Fig. 7.6 a) that presents ΔR_nl in dependence on the gate voltage at a constant bias of $I = -250\,\mu\text{A}$. Here, the x-axis is shifted by the position of the charge neutrality point V_CNP, with positive (negative) values corresponding to the electron (hole) conduction regime in graphene. Moreover, ΔR_nl increases with the absolute value of $V_\text{g} - V_\text{CNP}$. This trend is observed across all investigated temperatures.

The temperature dependence of ΔR_nl at $I = -250\,\mu\text{A}$ is shown in Fig. 7.6 b), displaying a general decreasing trend of the signal height with increasing temperature for both carrier types. While the bias dependence of ΔR_nl can be linked to a bias dependence of P_inj, the same cannot be claimed for the gate and temperature dependence of the signal. For this, also the gate and temperature dependence of the spin diffusion length L_s have to be considered. In order to evaluate L_s, distance dependent studies of ΔR_nl are conducted. However, this is not possible in the devices presented in this thesis, as both devices comprise only two FGT strips with a fixed distance. By conducting Hanle experiments, which will be presented later in Sec. 7.2, it is possible to determine the spin transport properties D_s and τ_s together with the spin injection efficiency P by fitting.

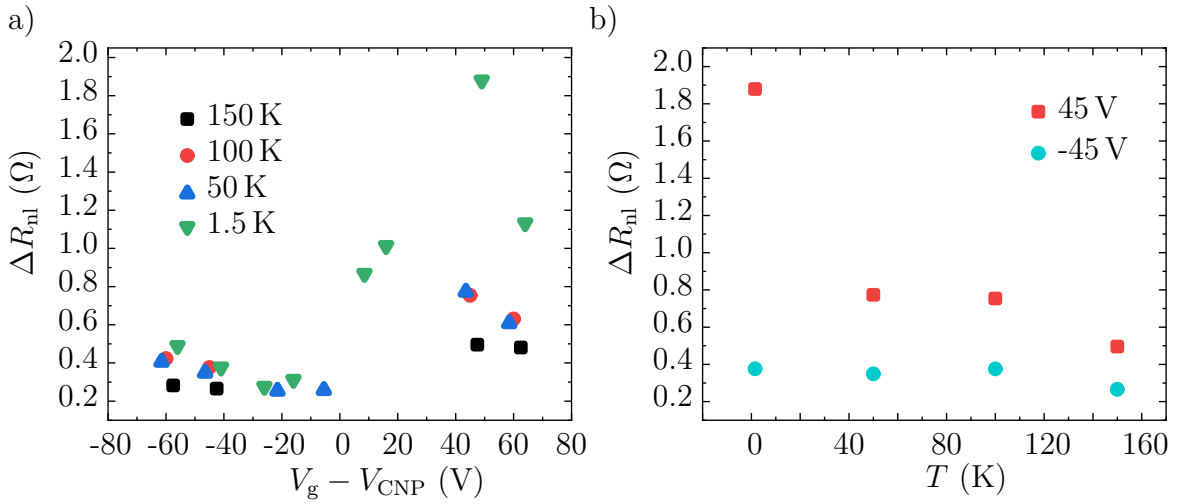

Fig. 7.6: a) Gate and b) temperature dependence of the non-local signal measured at an applied bias of $I = -250\,\mu A$.

Current and gate-sweeps

In addition to the non-local spin valve measurements, gate and current sweeps were performed in the parallel and anti-parallel configurations. This allows for obtaining the current and gate correlation of the non-local signal height ΔR_{nl} in a more straightforward way, requiring only two measurements, as opposed to the individual non-local spin valve measurements, where each point corresponds to two measurements. Furthermore, these sweeps could allow for a more detailed examination of the signal. In order to obtain the current and gate correlation, the difference in the signals from both sweeps is calculated and the result is normalized by the current. Fig. 7.7 a) presents the current sweeps of the non-local signal height ΔR_{nl} at $V_g = 45\,V$ and $T = 1.5\,K$, depicted as lines. The reproducibility of these sweeps is demonstrated by the presentation of several representative examples. Sweep 1 and 2 were recorded in succession, while sweep 3 was recorded subsequent to Hanle measurements that followed the sweep 2. It can be observed that sweep 1 and 2 match well, whereas sweep 3 is lower for negative currents. All sweeps diverge as they approach $I = 0\,\mu A$, which is an artefact of dividing by a small number. Consequently, the current sweeps align well with the heights extracted from the spin valve measurements for $|I| \geq 50\,\mu A$, as this divergence was not observed in the spin valve signals. At $I = -250\,\mu A$, the spin valve signal is significantly larger than that obtained from the current sweep. The current sweeps also indicate the inversion of the spin signal at the current of $I = 200\,\mu A$.

The non-local signal height ΔR_{nl} obtained from the gate sweep is illustrated in Fig. 7.7 b) exemplarily at $I = -250\,\mu A$ and $T = 1.5\,K$. The gate sweep shows a significantly higher level of noise compared to the current sweeps. However, the gate sweeps align well with the signal heights extracted from the spin valve measurements. Notably, no inversion

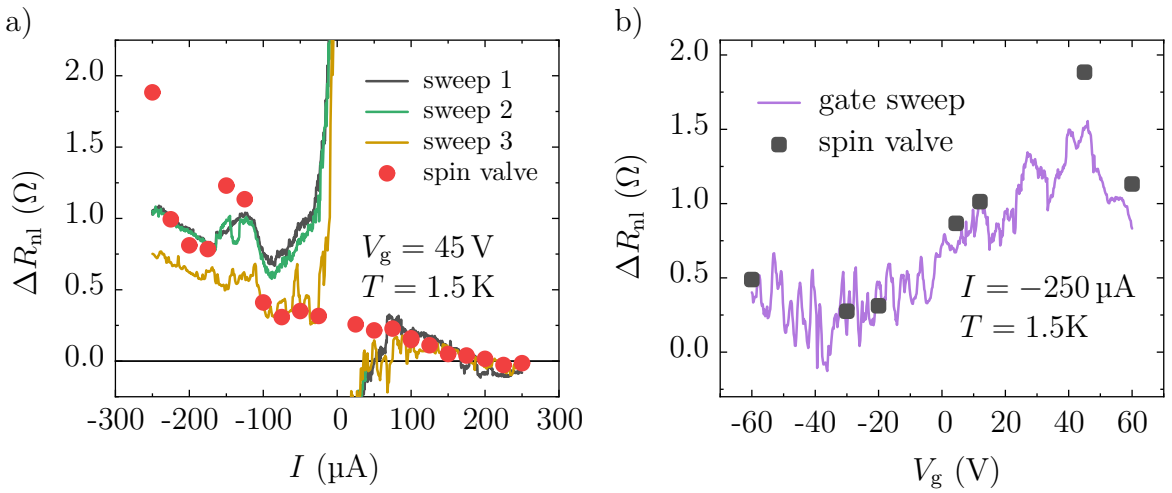

Fig. 7.7: a) Current and b) gate sweeps of the non-local signal ΔR_{nl}. Sweeps are indicated by lines, while the points show the extracted heights from the spin valve measurements.

of ΔR_{nl} was observed in the gate dependence as observed for example in Ref. [190]. However, it is consistent with the spin valve measurements. Gate sweeps conducted at other applied currents, which are not displayed, also agree well with the non-local spin valve signals. However, they become noisier with increasing positive currents.

7.1.2. Sample B

Non-local spin valve measurements were also conducted on Sample B. Its schematics are provided in Fig. 7.8. Fig. 7.9 a) to d) present the non-local signals at a constant current of $I = -250\,\mu A$ and $T = 1.5\,K$, in which the injector and detector electrodes were continuously interchanged. The contacts utilized for the injection and detection of the spin signal, as well as for the measurement of the anomalous Hall signal, are labelled

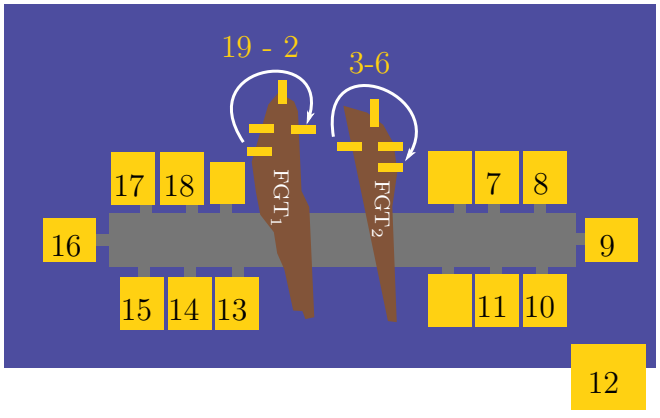

Fig. 7.8: Schematic of Sample B with contact numbers. The FGT electrodes are indicated by the brown shapes and are named FGT_1 and FGT_2. As the utilized chip carrier has a maximum amount of 20 contacts, the contacts on FGT_1 are numbered in a clockwise direction and counted as 19, 20, 1, and 2. Similarly, the contacts on FGT_2 are numbered in a clockwise direction as 3, 4, 5, and 6. Contact 12 is connected to the back gate.

above each figure. First, the spin signal V_{nl}, illustrated in Fig. 7.9 a), was detected on contacts 6 to 9. This was followed by other characterization steps, before measuring the non-local spin valve signal V_{nl} on electrodes 1 to 16 in Fig. 7.9 b). Subsequently, the injector and detector were interchanged on two further occasions, with intervening measurements. Fig. 7.9 c) and d) show the spin signal detected at contacts 2 and 16, and 6 and 9, respectively. In Fig. 7.9 a) and b), the anomalous Hall resistance R_{xy}, which was measured simultaneously, is shown as a dark blue and dark red line for the down- and up-sweep, respectively, with the corresponding y-axis to the right. Unfortunately, it was not possible to obtain this signal for Fig. 7.9 c) and d), as the contacts ceased to function. The anomalous Hall measurements in Fig. 7.9 a) and b) demonstrate that the switching of the injector's magnetization coincides with a sharp change in the non-local signal R_{nl}. Therefore, Fig. 7.9 proves spin injection in Sample B in both injector-detector configurations.

The spin signal in Sample B was generally smaller than that observed in Sample A. This may be attributed to the larger contact resistance of Sample A. This highlights the significance of the tunnel barrier that is necessary for efficient spin injection and detection. Furthermore, the data obtained from the spin valve measurements are less stable than that obtained from Sample A, and typically exhibit a lower signal-to-noise ratio with background signals of up to $10\,\Omega$. Consequently, it is not always possible to observe a clear spin valve signal for each magnetic field sweep. Peculiarly, interchanging the injecting and detecting electrode systematically inverts the measured signal. This is unexpected given that injected spins and their detection should be insensitive to the exact electrodes. The spin valve height changes from $\Delta R_{\mathrm{nl}} = -1.30\,\Omega$ detected at FGT_2 (Fig. 7.9 a)) to $\Delta R_{\mathrm{nl}} = 0.15\,\Omega$ and $\Delta R_{\mathrm{nl}} = 0.23\,\Omega$ measured at FGT_1 (Fig. 7.9 b) and c)) to $\Delta R_{\mathrm{nl}} = -0.52\,\Omega$ measured at FGT_2 again (Fig. 7.9 d)). Note, that the spin valve in Fig. 7.9 d) is shown for $V_{\mathrm{g}} = 60\,\mathrm{V}$, as the measurement for $V_{\mathrm{g}} = 32\,\mathrm{V}$ did not yield any signal. No reduction of the spin signal at low magnetic fields was observed in all measurements, indicating an absence of magnetic moments in the graphene channel.

In general, an inverted spin signal can be attributed to a spin filtering effect of the hBN tunnel barrier, which results in a negative spin polarization in graphene [193]. This effect has been observed in graphene spin valves with hBN tunnel barriers of different thicknesses at the injector and detector [193]. It was found that only an injector-detector combination of a high contact resistance with a low contact resistance at the electrodes resulted in a negative spin polarization. This effect was reproducibly observed in both non-local spin valve and Hanle experiments in several devices and was found to persist over a wide range of applied biases [193]. Therefore, a non-uniform tunnel barrier thickness can give rise to different spin polarizations. Given that the hBN thickness is not uniform in both of the presented samples, it may be reasonable to expect a spin valve inversion from Sample A to Sample B due to this spin filtering effect. In contrast to our findings, the spin signal inversion due to the spin filtering effect was observed to be independent of the interchanging of the injector and detector electrodes in Ref. [193]. Given that both electrodes are different in size and height, they might are subjected

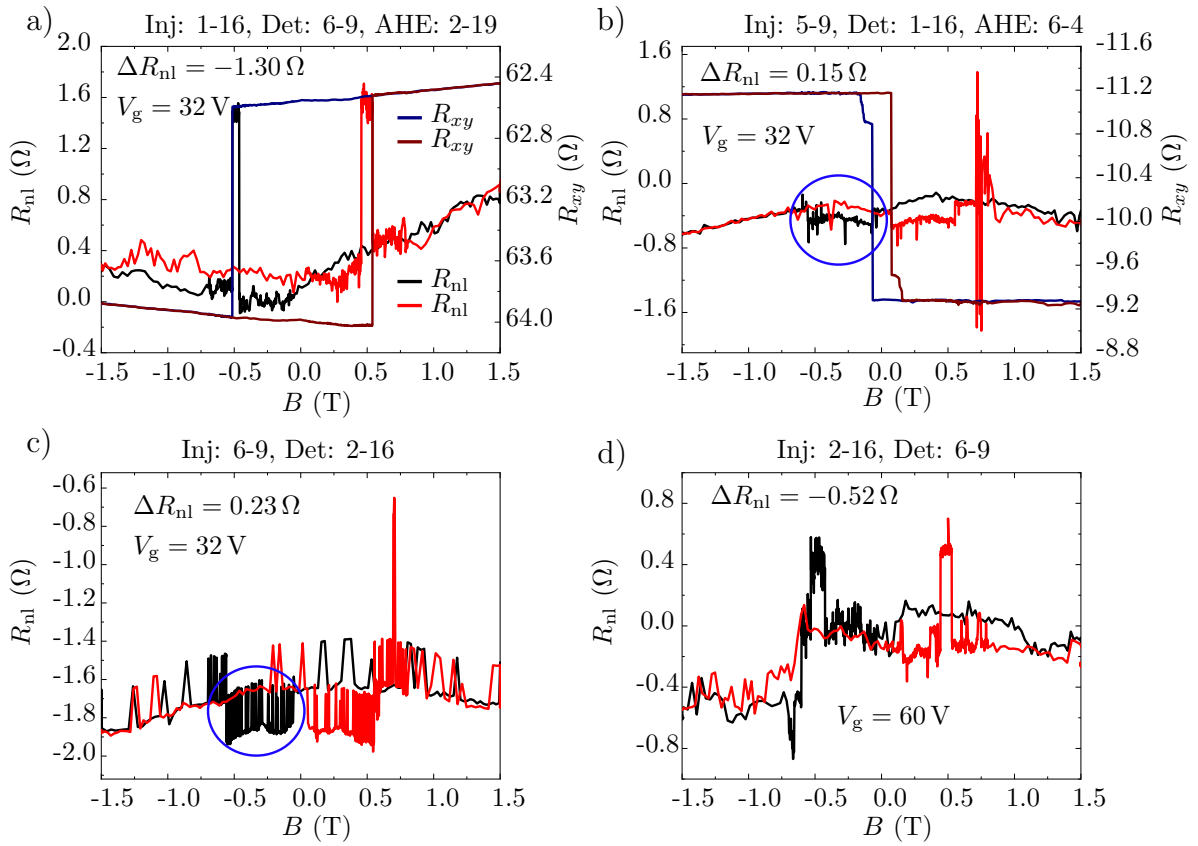

Fig. 7.9: Non-local spin valve measurements interchanging the injector and detector at an applied bias of $I = -250\,\mu A$ and $T = 1.5\,K$. Figures a) to d) present a series of non-local spin valve measurements with intervening measurements in between, where a) was measured first and d) was measured last. The spin valve measurements are shown as black and red curves for the down- and up-sweeps, respectively. For a) and b), anomalous Hall loops of the injecting electrodes are shown as dark blue and dark red lines, with the corresponding y-axis to the right. The non-local signal R_{nl} was detected at a) FGT_2, b) FGT_1, c) FGT_1, and d) FGT_2. The blue circles in b) and c) highlight the spin valve signal in the anti-parallel configuration. Furthermore, figure d) illustrates the spin valve measurement at $V_g = 60\,V$, as the measurement at $V_g = 32\,V$ did not yield any signal.

to a different bias-dependent spin injection efficiency P_{inj}. As suggested for Sample A in the previous section, the spin polarization at the Fermi level of the injector may potentially be inverted with increasing positive bias, resulting in an inversion of P_{inj} and, consequently, an inversion of the spin valve signal ΔR_{nl}. The observed inversion of the spin signal in Fig. 7.9, when the injector and detector electrodes are interchanged, could be explained by the reversal of the spin polarization of FGT_2, while that of FGT_1 remains unchanged, when the utilized currents are applied. The spin polarization of FGT_1 remains unaltered when no bias is applied, i.e., in the case of FGT_1 functioning as the detector. Consequently, a typical spin signal, as observed in Sample A, is recorded when injecting from FGT_2. Conversely, when injecting from FGT_1, the signal is reversed. However, only

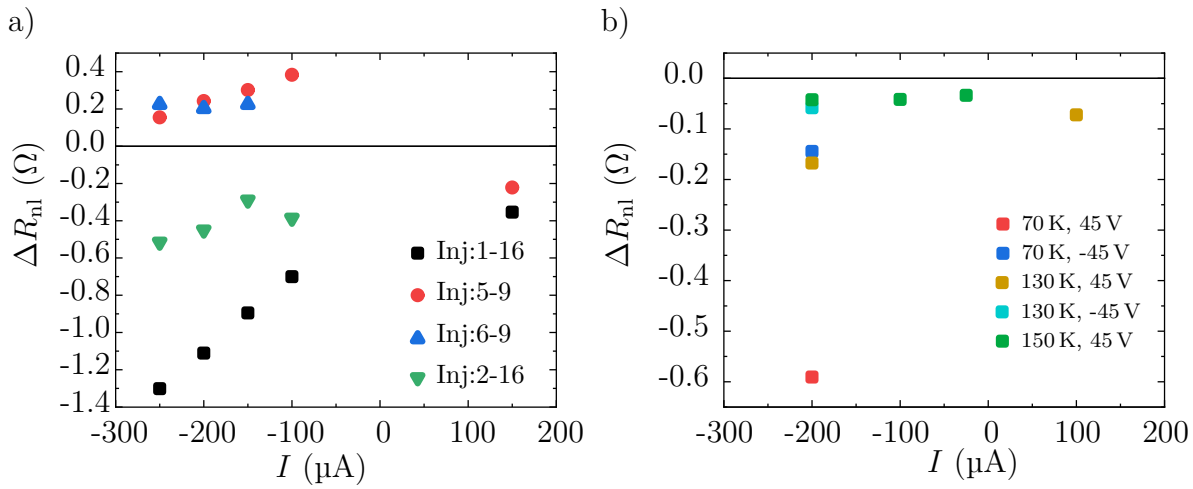

Fig. 7.10: a) Current dependence of the non-local signal ΔR_{nl} for the injector and detector configurations at $T = 1.5\,\mathrm{K}$ as in Fig. 7.9 a)-d), indicated by black, red, blue, and green dots, respectively. Note that ΔR_{nl} was measured at $V_g = 32\,\mathrm{V}$ except for the green triangles, where it was measured for $V_g = 60\,\mathrm{V}$. b) Current dependence of the non-local signal for the injector and detector configuration of Fig. 7.9 d), injecting from contacts 2-16 and detecting at contacts 6-9 at various temperatures and back gate voltages.

one bias-dependent inversion of the spin signal ΔR_{nl} is observed in Sample B, as will be presented in the following.

Current dependence

The sensitivity of the spin signal on the exact injector-detector configuration is also evident in the current dependence of the signal, as illustrated in Fig. 7.10 a). In this figure, ΔR_{nl} is plotted for the same configurations as presented in Fig. 7.9 at $T = 1.5\,\mathrm{K}$. Upon injecting spins at the FGT_1 electrode (injecting at 1-16 and 2-16), the extracted ΔR_{nl} is negative, exhibiting a decreasing tendency of the absolute height with increasing the current from negative to positive values, similar to Sample A. As both signals were measured at different gate voltages, their corresponding height differs from each other. When interchanging the injector and detector, such that spins are now detected at the FGT_1 electrode, the spin signal ΔR_{nl} is observed to be positive for negative currents. No clear correlation between ΔR_{nl} and bias current is observable when increasing the current from negative to positive values. However, an inversion of the spin signal is observed when injecting spins from contact 5-9. This was not observed by subsequent measurements with an injection current between contacts 6-9, as no spin valve signal was observed for positive currents. Nevertheless, the signal heights are comparable in both configurations, 5-9 and 6-9. Fig. 7.10 b) depicts the current dependence of the spin signal for temperatures of $T = 70\,\mathrm{K}$, $130\,\mathrm{K}$, and $150\,\mathrm{K}$ at various applied back gate voltages, with injection at FGT_2 and detection at FGT_1 (configuration of Fig. 7.9 d)). For all

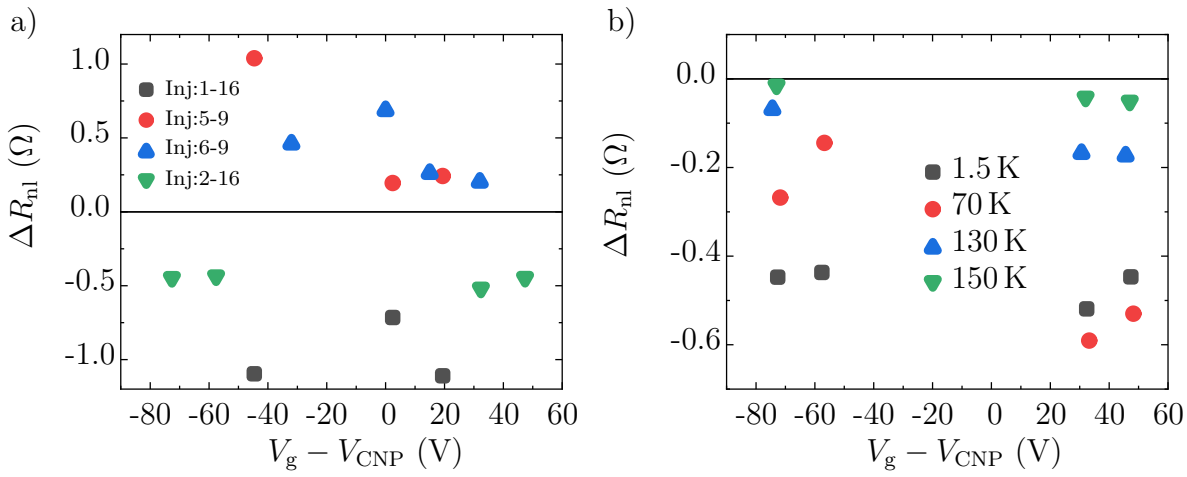

Fig. 7.11: a) Gate dependence of the non-local signal ΔR_{nl} for the injector and detector configurations at $T = 1.5\,\mathrm{K}$ and $I = -200\,\mu\mathrm{A}$ as presented in Fig. 7.9 a)-d), indicated by black, red, blue, and green dots, respectively. b) Gate dependence of the non-local signal for the injector and detector configuration of Fig. 7.9 d) at various temperatures at an applied bias $I = -200\,\mu\mathrm{A}$.

measurements, a decreasing trend of the spin valve signal, when increasing the applied bias from negative to positive currents, is observed without, an inversion of the signal.

Gate and temperature dependence

In Fig. 7.11 a) the gate dependence of the spin signal is presented for all the aforementioned configurations. A clear correlation with applied gate voltage is not evident. This however changes, when looking at the gate dependence when injecting at contacts 2-16 (FGT_1) at a bias of $I = -200\,\mu\mathrm{A}$ at various temperatures, as illustrated in Fig. 7.11 b). In this case, the absolute value of ΔR_{nl} is found to be larger for positive than for negative gate voltages, exhibiting a trend similar to that observed for Sample A. Finally, the temperature dependence of ΔR_{nl} at an applied bias of $I = -200\,\mu\mathrm{A}$ between contacts 2-16 (FGT_1) is illustrated in Fig. 7.12. A decreasing tendency of the absolute value with increasing temperature is observed for all investigated back gate voltages, which is in agreement with Sample A.

Current and gate sweeps

Additionally, current and gate sweeps were performed, injecting at contacts 1-16 (FGT_1), as illustrated in Fig. 7.13. In contrast to Sample A, the current sweeps were not reproducible. Sweep 1 and 2 are inverse to each other at positive current values, as

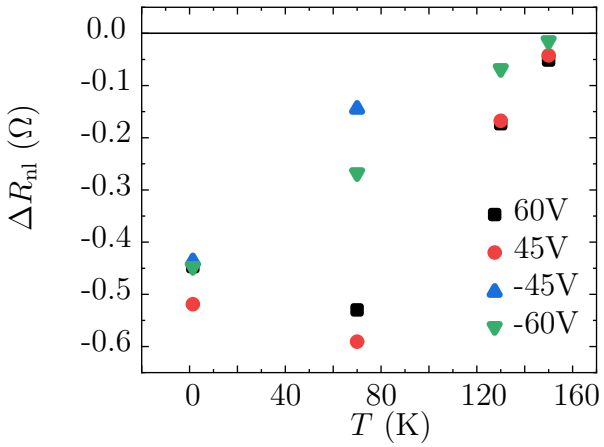

Fig. 7.12: Temperature dependence of the non-local signal for the injector and detector configuration of Fig. 7.9 d) at various back gate voltages at an applied bias $I = -200\,\mu A$. The decreasing tendency of the absolute value of ΔR_{nl} with increasing temperature is consistent with the temperature dependence of the spin valve signal observed in Sample A.

presented in Fig. 7.13 a). Furthermore, both sweeps diverge inversely. While sweep 1 diverges to negative ΔR_{nl} for small positive currents, sweep 2 diverges to positive values. Again, the observed divergence at $I = 0\,\mu A$ is an artefact of dividing by a small number. Sweep 1 aligns with the extracted spin valve heights at sufficiently large negative currents, whereas sweep 2 fails to align with the spin valve data. Nevertheless, the inversion of the spin signal at $I = -100\,\mu A$ of sweep 1 is not observed in the spin valve data. The gate sweep of ΔR_{nl} is illustrated in Fig. 7.13 b) and is subjected to a significant noise reaching up to $\approx 5\,\Omega$ close to the charge neutrality point. However, it is consistent with the spin valve heights at higher applied positive and negative gate voltages.

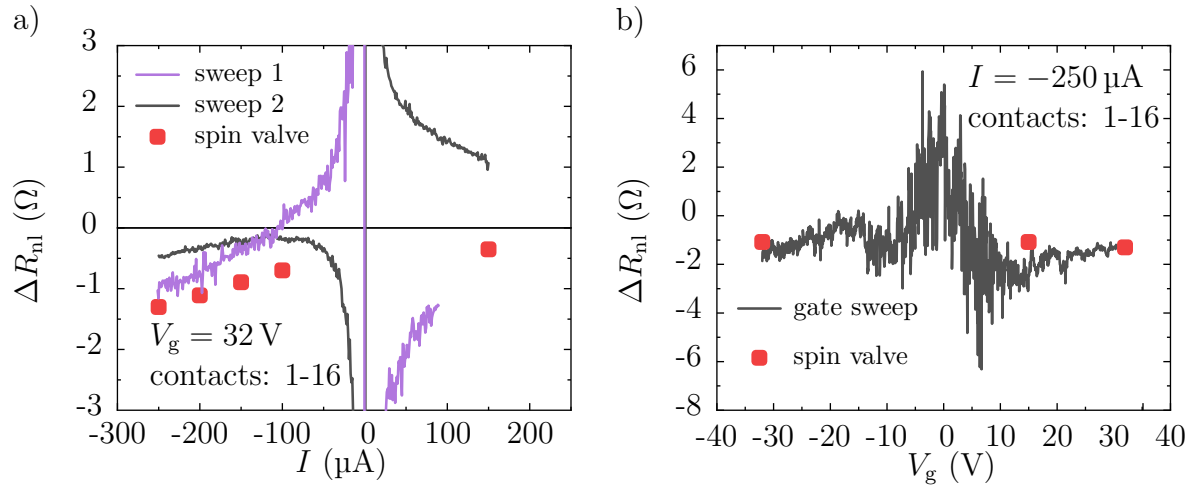

Fig. 7.13: a) Current and b) gate sweeps of the non-local signal height ΔR_{nl}. The sweeps are indicated as lines while the extracted heights from the spin valve measurements are indicated as red dots.

7.1.3. Summary

Successful non-local spin transport was demonstrated in two very similar all-2D van der Waals devices via non-local spin valve measurements with spin valve heights reaching up to $\Delta R_{\mathrm{nl}} = 1.88\,\Omega$. The non-local signal R_{nl} was successfully assigned to the magnetization configurations of the injecting and detecting electrodes via the anomalous Hall effect. It was observed that the spin valve height ΔR_{nl} is not stable for both samples. However, a hysteresis with respect to current or gate voltage cannot be ruled out. Moreover, the presence of magnetic moments is indicated by a dip in the non-local spin valve measurements at low magnetic fields in Sample A. In contrast, no such dip was observed in Sample B. Given that both samples were not subjected to any hydrogenation or annealing, the origin of these magnetic moments in Sample A remains unclear. However, as graphene was exfoliated under ambient conditions, adsorbates on the surface of graphene cannot be excluded. The current, back gate voltage, and temperature dependencies of both samples exhibit comparable characteristics. The current dependence demonstrates a decreasing tendency of ΔR_{nl} upon increasing the bias current I towards larger positive values, which can be attributed to a bias dependence of P_{inj}. This even results in an inversion of the spin valve signal at $I = 200\,\mu\mathrm{A}$ for Sample A, which is attributed to an inversion of the spin polarization at the Fermi level of the injecting FGT electrode. Nevertheless, alternative mechanisms may also give rise to non-linear current-dependent spin signals. Current inversion was also observed for Sample B. More peculiarly, the spin valve signal is inverted for Sample B when interchanging injector and detector electrodes. This phenomenon might be attributed to a current-dependent spin polarization which is different for both FGT electrodes of Sample B. The gate voltage dependence of the spin valve height ΔR_{nl} exhibits a larger signal at positive gate voltages (electron regime). Furthermore, an increase in temperature from $T = 1.5\,\mathrm{K}$ to $150\,\mathrm{K}$ results in a decrease of ΔR_{nl}. Additionally, current and gate sweeps were conducted, which align well with the extracted spin valve data for Sample A. However, for Sample B, they are not reliable as the current sweeps exhibited inconsistencies from one sweep to the next, and the gate sweep was subject to significant noise.

7.2. Non-local Hanle measurements

7.2.1. Sample A

Non-local Hanle measurements investigate the phase coherent precession of a spin ensemble when an external magnetic field is applied perpendicular to the spin orientation, as outlined in Sec. 3.4 and 4.4.2. Spins diffuse from the injector to the detector while the spin ensemble dephases and depolarizes, resulting in the characteristic Hanle curve. Spins injected from FGT are polarized out-of-plane. Thus, the external magnetic field is applied in-plane, perpendicular to the magnetic easy-axis and parallel to the long-axis of the FGT electrodes. Fig. 7.14 a) illustrates the Hanle signal at a temperature of $T = 1.5\,\mathrm{K}$, at an applied bias $I = -250\,\mu\mathrm{A}$, and a back gate voltage $V_\mathrm{g} = 60\,\mathrm{V}$ for the parallel (red) and anti-parallel (grey) magnetization configuration of the injector and detector. The observed oscillations of the signal clearly correspond to spin precession with a simultaneous decay as a result of spin dephasing. At large magnetic field values $B_\perp \gtrsim 0.2\,\mathrm{T}$, the spin signal vanishes and a constant offset $R_{\mathrm{nl,\,offset}}$ is measured. The parallel and anti-parallel sweeps yield Hanle curves of opposite polarity with an identical offset.

The difference between the Hanle curves of both magnetization configurations $\Delta R_{\mathrm{nl,\,Hanle}}$ at $B_\perp = 0\,\mathrm{T}$ corresponds to the difference between the majority and minority spin signal. It is expected to be of similar magnitude as the signal heights extracted from spin valve measurements. A signal height of $\Delta R_{\mathrm{nl,\,Hanle}} = 0.88\,\Omega$ was calculated, which is slightly lower than the corresponding spin valve signal $\Delta R_{\mathrm{nl,\,SV}} = 1.13\,\Omega$, as shown in Fig. 7.14 b). This discrepancy between the Hanle and spin valve signals may be attributed to magnetic moments previously mentioned, which have been reported to reduce the spin signal at low magnetic fields [132, 189]. Given that $\Delta R_{\mathrm{nl,\,Hanle}}$ is determined at $B_\perp = 0\,\mathrm{T}$, this results in a smaller extracted non-local signal height $\Delta R_{\mathrm{nl,\,Hanle}}$ compared to the spin valve measurements, which are observed at finite magnetic fields. However, this discrepancy could also be due to the measurement procedure. First, the spin valve measurements were recorded for all currents and back gate voltages. Subsequently, the Hanle measurements were performed. A small hysteresis with respect to the current or gate voltage cannot be excluded and could potentially lead to a smaller signal in the Hanle curves. Additionally, as the spin signal was observed to vary over time, this instability could also be the reason for the discrepancy in the measured signals.

The black lines in Fig. 7.14 a) correspond to fitting curves based on Eq. (3.30). Fitting was conducted using the *Origin* software. As the widths of the FGT electrodes of $2.6\,\mu\mathrm{m}$ and $1.6\,\mu\mathrm{m}$ cannot be neglected, Eq. (3.30) is also integrated over the size of the injector and detector. The resulting fitting function after integration is presented in the Appendix A.4.1 in Eq. (A.6). The fits yield values for the parameters D_s, τ_s, and P. The extracted value of P is $P = \sqrt{P_\mathrm{inj} P_\mathrm{det}}$. Assuming a homogeneous tunnel barrier,

leads to $P_{\mathrm{inj}} \approx P_{\mathrm{det}} = P$ at low applied currents. However, at higher applied biases, the current only affects the injector, leading to a change in the spin injection efficiency P_{inj}. Consequently, any changes in P with current are related to a change in P_{inj}. Henceforth, the spin injection efficiency will be referred to as P. The spin diffusion length can be calculated via $L_{\mathrm{s}} = \sqrt{D_{\mathrm{s}}\tau_{\mathrm{s}}}$. In order to minimize errors when fitting these three variables, the Hanle data were normalized first with $(R_{\mathrm{nl}}(B) - R_{\mathrm{nl,\,offset}})/(R_{\mathrm{nl}}(0\,\mathrm{T}) - R_{\mathrm{nl,\,offset}})$, which results in curves, which are independent of P. Subsequently, the normalized Hanle data were fitted to extract the values of τ_{s} and D_{s}. Afterwards, P was extracted by fitting the raw Hanle data with fixed values of τ_{s} and D_{s} obtained from the normalized fits. Accordingly, P was the only fitting variable in the second fit. As illustrated in Fig. 7.14 a), the fits match the experimental data well and result in $\tau_{\mathrm{s}} = 0.447\,\mathrm{ns}$, $D_{\mathrm{s}} = 0.0210\,\mathrm{m^2 s^{-1}}$, and $P = 18.4\,\%$ in the parallel configuration. In the anti-parallel configuration quite similar values of $\tau_{\mathrm{s}} = 0.415\,\mathrm{ns}$, $D_{\mathrm{s}} = 0.0199\,\mathrm{m^2 s^{-1}}$, and $P = 18.3\,\%$ are obtained. These results are in agreement to other graphene spin injection experiments reporting spin relaxation times ranging from $\tau_{\mathrm{s}} = 0.07\,\mathrm{ns}$ up to $1.1\,\mathrm{ns}$ and spin diffusion constants of $D_{\mathrm{s}} = 0.011\,\mathrm{m^2 s^{-1}}$ up to $0.032\,\mathrm{m^2 s^{-1}}$ [27, 30, 33].

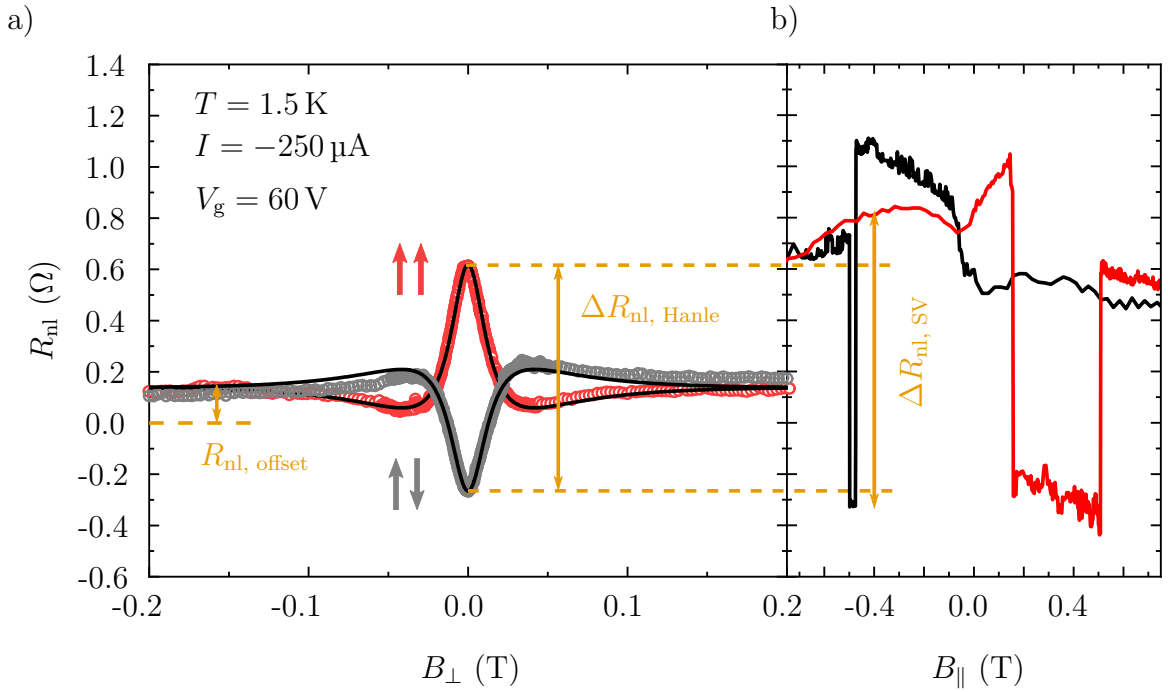

Fig. 7.14: a) Non-local Hanle measurements of Sample A at $T = 1.5\,\mathrm{K}$, $I = -250\,\mu\mathrm{A}$, and $V_{\mathrm{g}} = 60\,\mathrm{V}$ with a magnetic field sweep along the long-axis of the FGT electrodes. The Hanle curves are shown for (anti-)parallel magnetization alignment of the FGT electrodes in red (grey). Fits to the Hanle measurements are indicated by the black lines. b) The non-local spin valve measurement for the same set of parameters is shown for comparison. Note that the magnetic field is swept in different directions in a) and b).

Comparing parallel and anti-parallel Hanle curves

For Sample A, the Hanle curves were successfully measured in both parallel and anti-parallel magnetization configurations of the injector and detector at $T = 1.5\,\mathrm{K}$ at $V_\mathrm{g} = 45\,\mathrm{V}$ and $60\,\mathrm{V}$ for various bias currents. Fig. 7.15 a) illustrates the parallel and anti-parallel Hanle curves for $I = -250\,\mu\mathrm{A}$ and $V_\mathrm{g} = 45\,\mathrm{V}$ in red and grey, respectively. It is evident that the amplitudes of the signals differ between the two configurations. A comparison between the normalized curves of these two signals, as presented in Fig. 7.15 b), reveals that they are distinctively different. Consequently, different values for all three fitted parameters were obtained for parallel and anti-parallel configurations: $\tau_{\mathrm{s},\uparrow\uparrow} = 0.398\,\mathrm{ns}$ vs. $\tau_{\mathrm{s},\uparrow\downarrow} = 0.637\,\mathrm{ns}$, $D_{\mathrm{s},\uparrow\uparrow} = 0.0097\,\mathrm{m^2 s^{-1}}$ vs. $D_{\mathrm{s},\uparrow\downarrow} = 0.0393\,\mathrm{m^2 s^{-1}}$, and $P_{\uparrow\uparrow} = 25.2\,\%$ vs. $P_{\uparrow\downarrow} = 13.2\,\%$. The reason for this discrepancy is unclear, as it only appeared at $V_\mathrm{g} = 45\,\mathrm{V}$. At $V_\mathrm{g} = 60\,\mathrm{V}$, the Hanle curves are quite similar, as presented in Fig. 7.14 a), yielding similar fitting results. As with the non-local spin valve measurements, the Hanle curves were recorded for all back gate voltages and bias currents in the parallel configuration first. Subsequently, the Hanle curves were measured in the anti-parallel configuration. Consequently, a small hysteresis with respect to these parameters cannot be excluded.

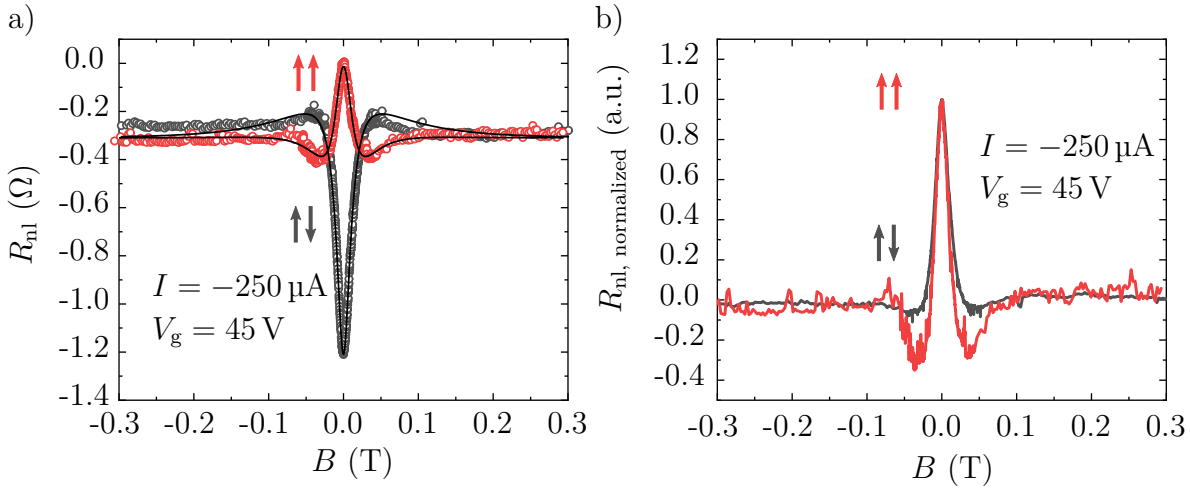

Fig. 7.15: a) Hanle curves in the (anti-)parallel configuration in red (grey) at $I = -250\mu\mathrm{A}$ and $V_\mathrm{g} = 45\,\mathrm{V}$ at $T = 1.5\,\mathrm{K}$. Fits to the curves are indicated by the black solid lines. b) The corresponding normalized Hanle curves are plotted in order to compare the shape of the signals in the anti-parallel and parallel configuration.

Comparison of non-local spin valve and Hanle measurements

As illustrated in Fig. 7.14, the extracted non-local signal heights from the Hanle measurement $\Delta R_{\mathrm{nl,\ Hanle}}$ can be compared to the extracted spin valve heights $\Delta R_{\mathrm{nl,\ SV}}$. This

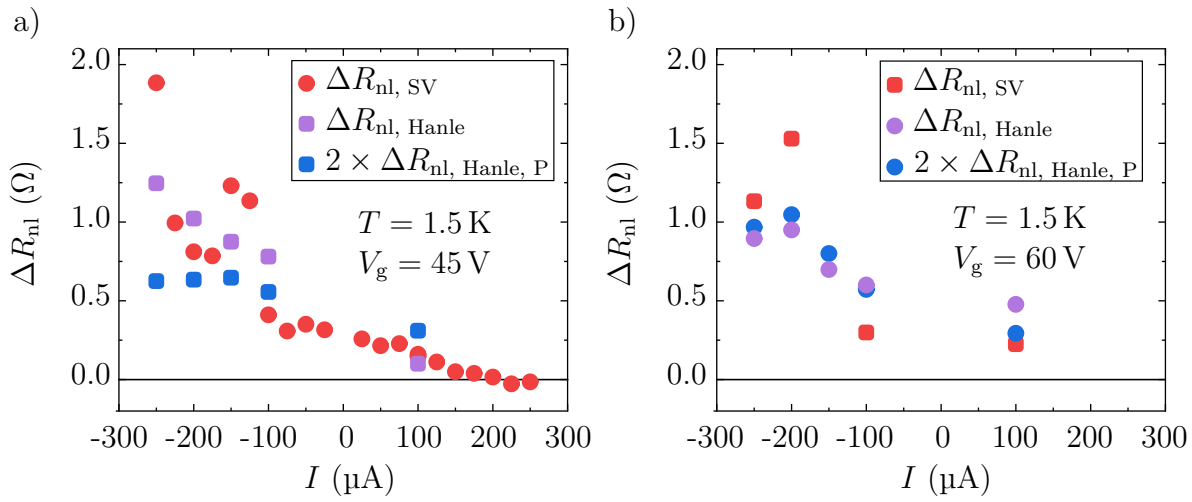

Fig. 7.16: Comparison of the non-local spin valve heights $\Delta R_{\mathrm{nl,\,SV}}$ and the Hanle heights $\Delta R_{\mathrm{nl,\,Hanle}}$ and $2 \times \Delta R_{\mathrm{nl,\,Hanle,\,P}}$, which corresponds to twice the height of the extracted parallel Hanle curve amplitudes. The extracted heights are plotted against the applied current at a temperature $T = 1.5\,\mathrm{K}$ at a) $V_{\mathrm{g}} = 45\,\mathrm{V}$ and b) $V_{\mathrm{g}} = 60\,\mathrm{V}$.

is illustrated in Fig. 7.16 a) and b), where the extracted heights are plotted against the applied bias at a temperature of $T = 1.5\,\mathrm{K}$ for $V_{\mathrm{g}} = 45\,\mathrm{V}$ and $60\,\mathrm{V}$, respectively. For these gate voltages the Hanle signal was measured in both parallel and anti-parallel configuration. In order to further investigate the discrepancy of the parallel and anti-parallel Hanle curves, additionally $2 \times \Delta R_{\mathrm{nl,\,Hanle,\,P}}$ is presented, which corresponds to the doubled Hanle amplitude in the parallel configuration. It is evident that the Hanle amplitudes $2 \times \Delta R_{\mathrm{nl,\,Hanle,\,P}}$ and $\Delta R_{\mathrm{nl,\,Hanle}}$ agree well with the spin valve heights $\Delta R_{\mathrm{nl,\,SV}}$. Furthermore, the decreasing trend of the signals with increasing positive current is also consistent. A comparison of the magnitudes of the extracted heights $2 \times \Delta R_{\mathrm{nl,\,Hanle,\,P}}$ and $\Delta R_{\mathrm{nl,\,Hanle}}$ reveals that they are notably different at $V_{\mathrm{g}} = 45\,\mathrm{V}$, as the points do not align. However, at $V_{\mathrm{g}} = 60\,\mathrm{V}$, they are in good agreement with each other. As previously stated, the reason for this discrepancy of the parallel and anti-parallel Hanle curves at $V_{\mathrm{g}} = 45\,\mathrm{V}$ remains unclear.

Tilting of the magnetization direction of the injector and detector

Fitting according to Eq. (A.6) assumes that the external magnetic field does not affect the magnetization direction of FGT. However, the transverse field exerts a torque on the magnetization of both FGT electrodes, which could potentially tilt its direction towards the external magnetic field. The in-plane magnetic fields applied for the Hanle measurements reach up to $B_{\perp} = \pm 0.3\,\mathrm{T}$. At low temperatures, with the coercive field of the injector electrode of $H_{\mathrm{c}}(1.5\,\mathrm{K}, -250\,\mu\mathrm{A}) = \pm 0.5\,\mathrm{T}$, it is reasonable to assume a fixed FGT magnetization. However, this cannot be assumed at high temperatures,

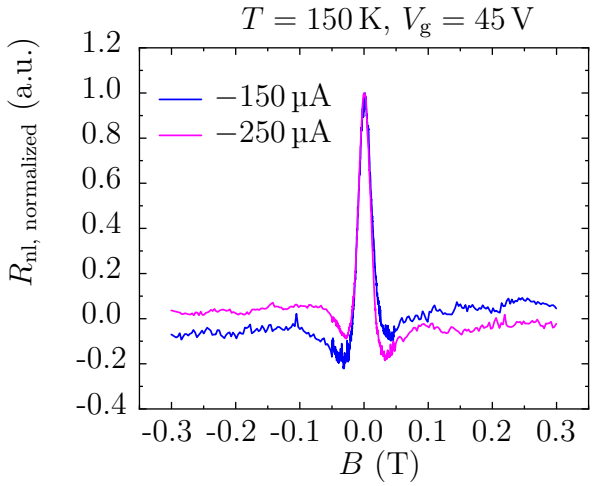

Fig. 7.17: Normalized Hanle curves for $I = -150\,\mu\mathrm{A}$ and $-250\,\mu\mathrm{A}$. Both signals are clearly non-symmetric around $B = 0\,\mathrm{T}$.

where the injector's coercive field H_c reduces down to $H_\mathrm{c}(150\,\mathrm{K}, -250\,\mu\mathrm{A}) = \pm 0.11\,\mathrm{T}$. When the magnetization directions of both electrodes are tilted towards the external applied field, the injected spins would no longer be injected perpendicular to the external field. Moreover, the angle between the injected spins and the external field would be dependent on the external field magnitude, and consequently change during the Hanle sweep. Assuming that the magnetization directions of both injector and detector remain parallel and get increasingly tilted towards the external field as the magnetic field magnitude increases, one would expect an increasing background signal as a result [27]. Furthermore, the Hanle signal would be broader, as the precession requires a transverse field. As a result of the decreased angle between the injected spins and the external field, the dephasing of the spins would necessitate larger magnetic field values compared to the perpendicular case. Consequently, in order to ensure that the magnetization directions of both FGT electrodes are not affected by the external magnetic field, it is necessary to ensure that all measured Hanle curves, even at elevated temperatures, exhibit a comparable shape and show a constant background signal $R_\mathrm{nl,\ offset}$.

In the curves shown in Fig. 7.14 a) and Fig. 7.15, the background signal at high magnetic field values remains constant. However, when examining the Hanle curves at $T = 150\,\mathrm{K}$, $V_\mathrm{g} = 45\,\mathrm{V}$ at bias currents $I = -250$ and $-150\,\mu\mathrm{A}$, as illustrated in Fig. 7.17, a clear asymmetry is revealed in the curves, with a shift in the background signal. Both measurements were obtained as a part of a series of current-dependent measurements, with a single Hanle measurement conducted at a current of $I = -200\,\mu\mathrm{A}$ in between, that did not show this background shift. All other parameters, including the temperature, back gate voltage, and sample orientation within the cryostat were maintained at a constant value. In these curves, the background signal for negative magnetic field values is shifted in relation to positive field values. At $I = -250\,\mu\mathrm{A}$, the background signal at negative magnetic field values is shifted towards higher values in comparison to the background signal at positive field values. Conversely, at $I = -150\,\mu\mathrm{A}$, the opposite is true. However, if the magnetization directions of the electrodes were tilted towards the external magnetic field, the shift in the background signal would be

expected to increase with increasing field strength, symmetric around $B = 0\,\mathrm{T}$ [27]. Furthermore, the extracted values of the spin diffusion constant and spin relaxation time, which determine the shape of the Hanle curve, are $D_\mathrm{s}(-150\,\mu\mathrm{A}) = 0.022\,\mathrm{m^2 s^{-1}}$ and $D_\mathrm{s}(-250\,\mu\mathrm{A}) = 0.019\,\mathrm{m^2 s^{-1}}$, and $\tau_\mathrm{s}(-150\,\mu\mathrm{A}) = 0.48\,\mathrm{ns}$ and $\tau_\mathrm{s}(-250\,\mu\mathrm{A}) = 0.51\,\mathrm{ns}$. These values are comparable to the extracted values of the symmetric Hanle curve at $I = -200\,\mu\mathrm{A}$ with $D_\mathrm{s}(-200\,\mu\mathrm{A}) = 0.018\,\mathrm{m^2 s^{-1}}$ and $\tau_\mathrm{s}(-200\,\mu\mathrm{A}) = 0.47\,\mathrm{ns}$. Consequently, a broadening of the curve due to a tilting of the magnetization direction is not observed. Furthermore, not only the background baselines $R_{\mathrm{nl,\,offset}}$ are shifted, but also the dips at small positive and negative fields. This cannot be explained by a tilting of the FGT magnetization directions towards the external field. Interestingly, the baselines are shifted by the same amount as the dips. Furthermore, this asymmetry was only observed occasionally. During the measurements at $V_\mathrm{g} = 45\,\mathrm{V}$ and $T = 150\,\mathrm{K}$, for instance, the asymmetry was observed at bias currents of $I = -250$ and $-150\,\mu\mathrm{A}$, yet it was not observed at other currents analysed. Furthermore, the asymmetry was observed at all investigated temperatures and gate voltages. Consequently, this asymmetry is potentially due to a shift in the background signal during the measurement sweep and not due to a tilting of the FGT magnetizations. Possible spurious signals in the non-local detection scheme are evaluated in Sec. 4.4.3. Therefore, in the following analysis, it is assumed that the FGT magnetizations are not tilted by the external magnetic field.

Hanle measurements were conducted for various injection currents, back gate voltages, and temperatures in the parallel configuration. In the following, the results of fitting of the Hanle curves are presented for all three fitting parameters P, τ_s, and D_s. While the spin relaxation time τ_s and the spin diffusion constant D_s were determined first through the fitting of the normalized Hanle curves, the spin injection efficiency P was the last parameter to be extracted from a fit to the raw Hanle curves. However, P is discussed first, as it reflects the behaviour of the non-local signal of the spin valve measurements.

Spin injection efficiency P

Fig. 7.18 a) illustrates the Hanle curves obtained at different bias currents I at $T = 100\,\mathrm{K}$ and $V_\mathrm{g} = 45\,\mathrm{V}$. The curves are shifted so that their offsets $R_{\mathrm{nl,\,offset}} = 0\,\Omega$ are aligned to allow for a direct comparison of the amplitudes. The spin injection efficiency P has a significant effect on the amplitude of the Hanle signal, as its square features in the pre-factor of the Hanle curve in Eq. (3.27). It can be seen that the amplitude is greater for negative than for positive currents, with a maximum amplitude at $I = -250\,\mu\mathrm{A}$. The fits to the Hanle curves, extracting the values of P, are not presented here for the sake of clarity.

In Sample A, the spin injection efficiency P ranges from $P(150\,\mathrm{K}$, -4 V, $200\,\mu\mathrm{A}) = 0.35\,\%$ to $P(1.5\,\mathrm{K}$, 45 V, -200 µA) = 39.7 %, verifying efficient spin injection. Values of up to $P \approx 40\,\%$ are significantly larger than that reported for FGT-graphene spin valve devices

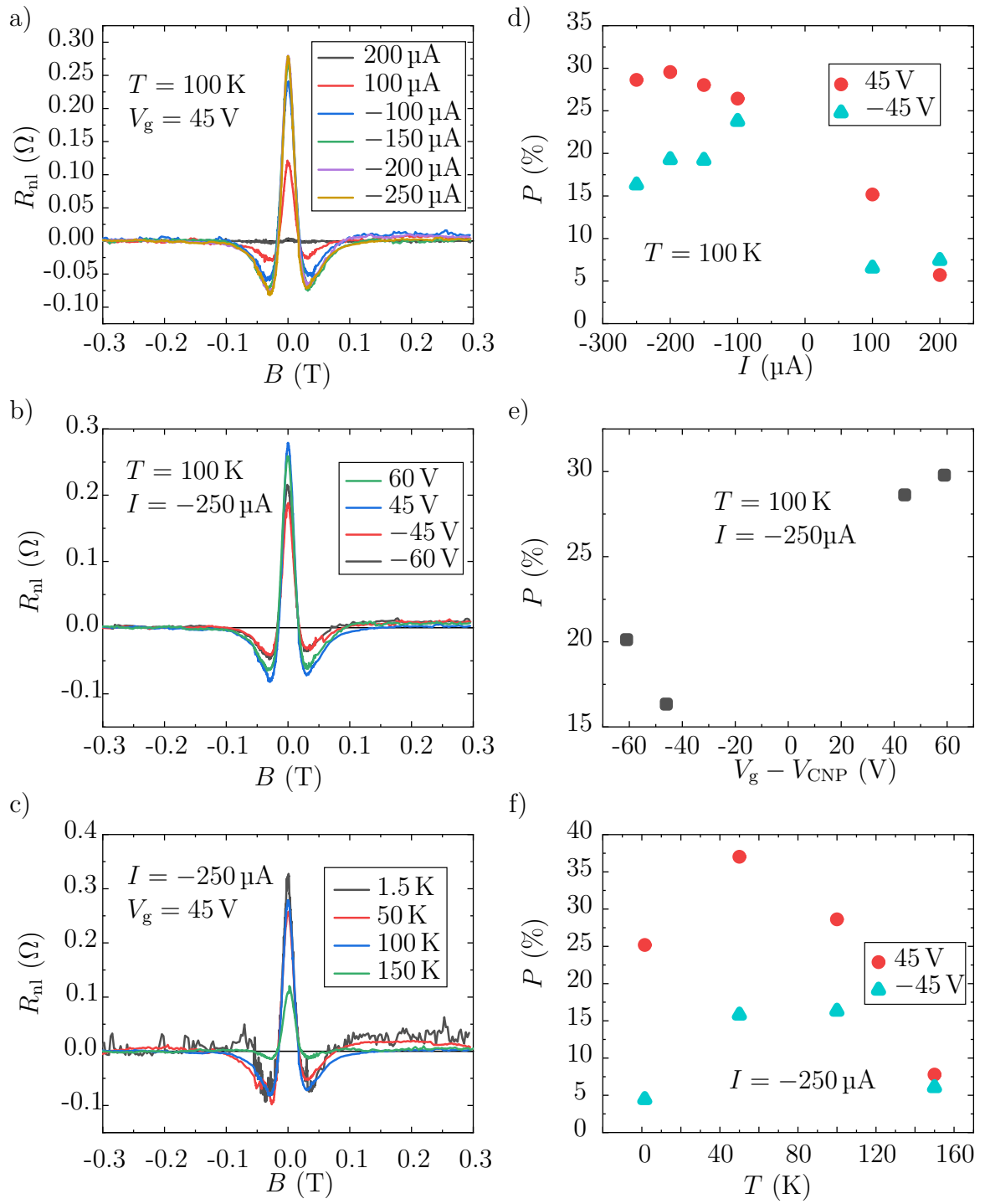

Fig. 7.18: Non-local Hanle curves in parallel magnetization configuration at a) constant temperature and back gate voltage at different currents, b) constant temperature and bias current at various back gate voltages, and c) constant bias current and gate voltage at various temperatures. All curves are shifted, so that their offset is zero. This allows for a direct comparison of the Hanle curves and their amplitudes. Fit results of P are plotted against d) the applied current for $V_\mathrm{g} = \pm 45\,\mathrm{V}$ at $T = 100\,\mathrm{K}$, e) $V_\mathrm{g} - V_\mathrm{CNP}$ at a constant current $I = -250\,\mu\mathrm{A}$ and $T = 100\,\mathrm{K}$, and f) temperature at a constant current of $I = -250\,\mu\mathrm{A}$ for $V_\mathrm{g} = \pm 45\,\mathrm{V}$. Error bars of P are obscured by the dots themselves.

without a tunnel barrier, where an injection efficiency of $P = 1\,\%$ was estimated [31]. However, as $P = \sqrt{P_{\mathrm{det}} P_{\mathrm{inj}}}$ this is a low estimate of P_{inj}. When linearly interpolating the spin detection efficiency at low currents from the current dependence of P at 1.5 K, a value of $P_{\mathrm{det}}(45\,\mathrm{V}, 1.5\,\mathrm{K}) = P(0\,\mu\mathrm{A},\, 45\,\mathrm{V},\, 1.5\,\mathrm{K}) = 17\,\%$ is obtained. From this, a spin injection efficiency of even $P_{\mathrm{inj}}(-200\,\mu\mathrm{A}, 45\,\mathrm{V}, 1.5\,\mathrm{K}) = 93\,\%$ can be estimated. However, in the following the conservative estimates of P are presented. The extracted values from the fits for P at $V_{\mathrm{g}} = \pm 45\,\mathrm{V}$, corresponding to the electron and hole regime of graphene, at a temperature of $T = 100\,\mathrm{K}$ are shown in Fig. 7.18 d). The obtained values reflect the behaviour of the amplitudes of the measured Hanle curves. The spin injection efficiency P is observed to be larger for negative than for positive currents at all observed back gate voltages. This indicates that in the electron regime (positive V_{g}), spin injection (negative currents) is more efficient than spin extraction (positive currents). Conversely, at negative V_{g}, i.e. in the hole regime, spin extraction (negative currents) is more efficient than spin injection (positive currents). Additionally, it is evident that the spin injection efficiency is larger in the electron than in the hole regime. This is also observed in the gate dependence of the Hanle curves, which is presented in Fig. 7.18 b). The Hanle amplitudes are smaller for negative back gate voltages. This is also reflected in the obtained values for P, which are illustrated in Fig. 7.18 e). As observed from the current dependency of the signal, injecting spins via electrons (positive V_{g}, negative I) results in highest values for P.

Until now, only Hanle curves at $T = 100\,\mathrm{K}$ have been discussed. Hanle curves measured at different temperatures are shown in Fig. 7.18 c), showing a decreasing trend in the Hanle amplitudes with increasing temperature. However, the measurement at $T = 100\,\mathrm{K}$ exhibits the best signal-to-noise ratio with the second highest amplitude of the measured curves at a current of $I = -250\,\mu\mathrm{A}$. The temperature dependence of the extracted values of P, as presented in Fig. 7.18 f), reveals a decreasing tendency of P with temperature for $T \geq 50\,\mathrm{K}$. Interestingly, values for P at 1.5 K are observed to be lower than at 50 K. The dependencies of P on these three external parameters are also reflected in the spin valve measurements. The current dependency of P is analogous to the current dependency of the spin valve height ΔR_{nl} in Sec. 7.1.1. Therefore, the reduction of ΔR_{nl} with larger positive currents can be confidently attributed to the current dependence of P. Furthermore, the gate voltage and temperature dependencies of P are also similar to those of ΔR_{nl}.

Spin relaxation time τ_{s}

The two important spin transport parameters, the spin relaxation time τ_{s} and the spin diffusion constant D_{s}, define the shape of the Hanle curves. Consequently, these two parameters were extracted from fits to the normalized Hanle curves and are the only two variables of the corresponding fitting function. First, the results of τ_{s} are investigated. The normalized Hanle curves are presented in Fig. 7.19 a), b), and c) at various currents, gate

voltages, and temperatures, respectively. When one of these three external parameters is modified, the other two are fixed at a constant value. Again, the fits to the normalized Hanle curves are not presented here for the sake of clarity.

An examination of the normalized Hanle curves at $T = 100\,\mathrm{K}$ and $V_\mathrm{g} = 45\,\mathrm{V}$ in Fig. 7.19 a) reveals that the shape of the Hanle curves remains unaltered when the current is varied, and all the curves lie on top of each other. Consequently, the obtained values for τ_s, as illustrated in Fig. 7.19 d), span from 0.315 ns to 0.383 ns at $V_\mathrm{g} = 45\,\mathrm{V}$ and from 0.314 ns to 0.423 ns at $V_\mathrm{g} = -45\,\mathrm{V}$, with no discernible correlation with the current. The error bars indicate the errors from the fits and are mostly obscured by the dots. As the spin signal decreases with increasingly more positive currents, the signal-to-noise ratio decreases, resulting in very noisy Hanle signals at $I = 200\,\mu\mathrm{A}$, which is presented in the Appendix in Fig. A.7. Consequently, the accuracy of the fit parameters is also reduced, resulting in large error bars for values at positive currents. Fig. 7.19 b) depicts the normalized Hanle curves at various back gate voltages. Once more, the shapes of the curves remain unaltered, exhibiting a uniform trace. Consequently, the derived values for τ_s are in a range from 0.270 ns to 0.440 ns with no discernible dependence on the gate voltage, as illustrated in Fig. 7.19 e). This indicates that the spin relaxation time τ_s is independent of the charge carrier type, and thus is identical in the electron and hole conduction regimes of graphene. As illustrated in Fig. 7.19 c), the temperature dependence reveals identical normalized Hanle curves except for $T = 150\,\mathrm{K}$. Here, the dips adjacent to the peaks are less pronounced than those observed at lower temperatures. The temperature dependence of τ_s is shown in Fig. 7.19 f). Interestingly, an increasing tendency of τ_s for temperatures $T \geq 50\,\mathrm{K}$ can be observed for both applied gate voltages. While the values at $T = 1.5\,\mathrm{K}$ are larger than at $T = 50\,\mathrm{K}$, the spin relaxation time increases from $\tau_\mathrm{s} = 0.3$ to 0.5 ns in the electron regime for $T \geq 50\,\mathrm{K}$.

Such a temperature dependence of τ_s is consistent with spin relaxation caused by resonant scattering at magnetic impurities, as discussed in detail in Sec. 3.5.3 [123]. In this scenario, a high spin relaxation rate $1/\tau_\mathrm{s}$ is calculated for 70 K, an intermediate rate for 4 K, and a low rate at 300 K. This results in a temperature dependence of τ_s as observed in Fig. 7.19 f). As signatures of magnetic moments have also been observed in the non-local spin valve measurements, this behaviour may be attributed to these moments. Nevertheless, as evidenced by the current and gate dependencies, curves with comparable shapes can yield a variation in τ_s varying from 0.27 ns to 0.44 ns. Therefore, the scattered values of $\tau_\mathrm{s} = 0.3\,\mathrm{ns}$ to 0.5 ns when increasing the temperature from $T = 50\,\mathrm{K}$ to 150 K may also be attributed to the significant variation in the fit results.

As FGT is magnetized out-of-plane, experiments to test for an anisotropy in the in- and out-of-plane spin relaxation time could not be conducted the way it has been done with Co-electrodes [27]. In order to achieve this, an in-plane tilting of the FGT-magnetization would be required, which would necessitate the application of magnetic fields of several Teslas [48]. However, the magnetization of FGT is reported to be in-plane, with T_C above room temperature, when doped with Co, substituting its outermost Fe-layer [195].

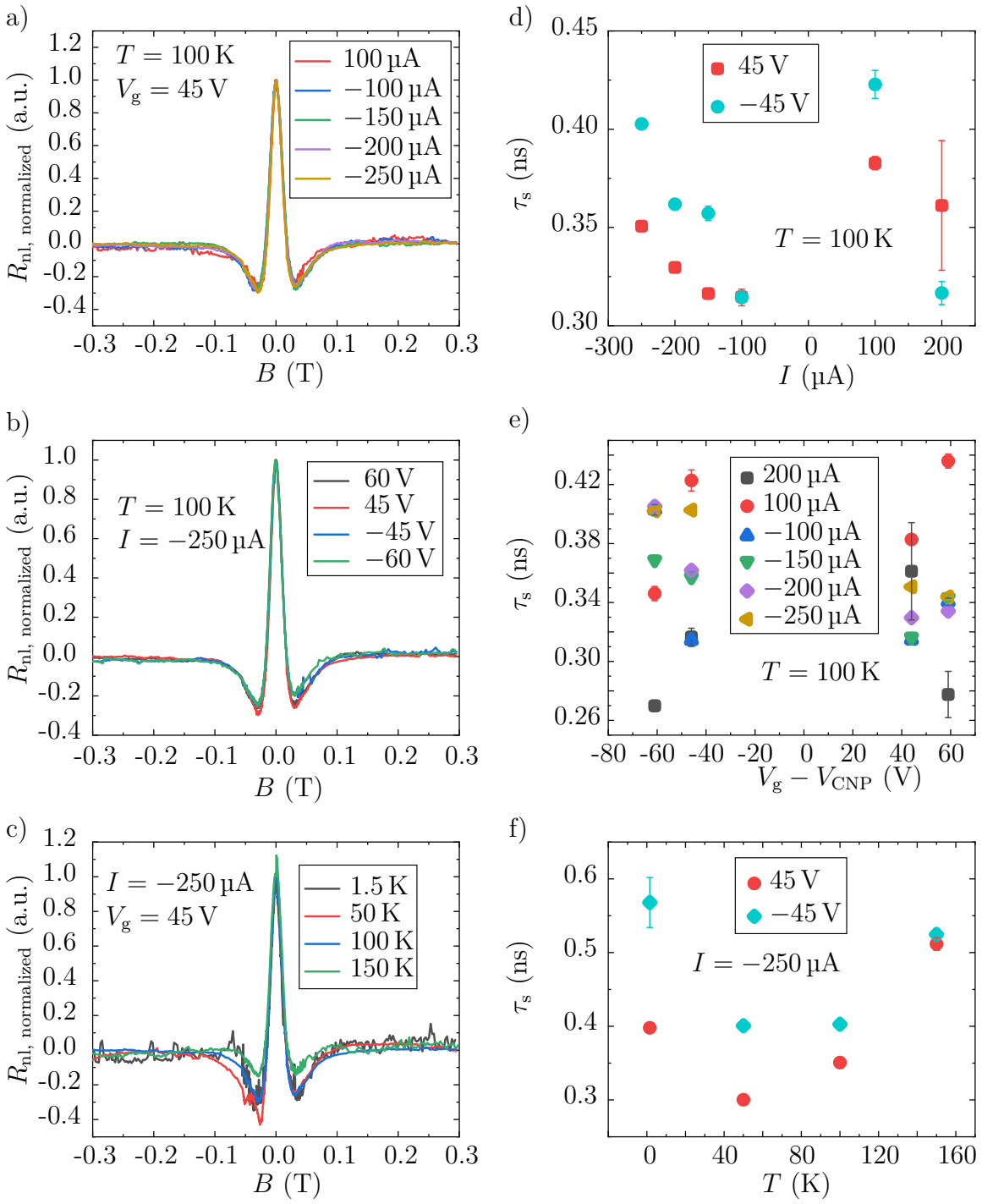

Fig. 7.19: Normalized non-local Hanle curves in parallel magnetization configuration shown at various a) currents, b) back gate voltages, and c) temperatures. While one parameter is changed, the other two variables are kept constant similar as in Fig. 7.18. The fit results of τ_s are shown as a function of current, back gate voltage, and temperature in d), e), and f), respectively. The current dependence is shown for the electron and hole regime at $V_\mathrm{g} = \pm 45\,\mathrm{V}$ at $T = 100\,\mathrm{K}$. The gate dependence is shown for various currents at the same temperature. The temperature dependence is presented at a constant bias current $I = -250\,\mu\mathrm{A}$ for the electron and hole regime at $V_\mathrm{g} = \pm 45\,\mathrm{V}$.

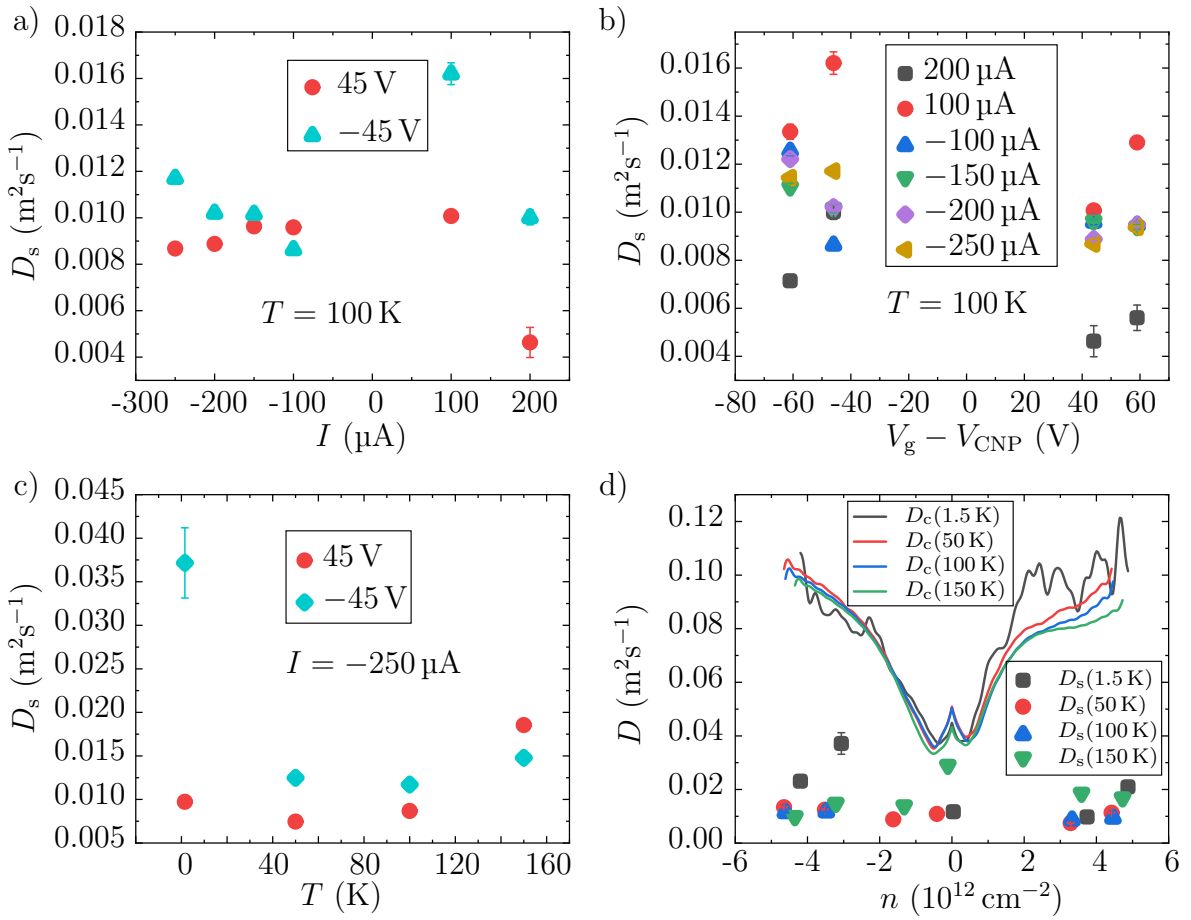

Fig. 7.20: The fit results of D_s shown as a function of current, back gate voltage, and temperature in a), b), and c), respectively. Both, a) and b) are presented at a constant temperature of $T = 100\,\mathrm{K}$. a) and c) present the data for the electron and hole regime, while b) plots the fit results for various currents. d) Comparison of the charge and spin diffusion constants, D_c and D_s, respectively. The charge diffusion constant D_c was calculated as described in Sec. 6.1.2. The spin diffusion constant D_s is extracted from Hanle fits at a constant current of $I = -250\,\mu\mathrm{A}$.

Spin diffusion constant D_s

The obtained values of the spin diffusion constant D_s are shown in Fig. 7.20. Fig. 7.20 a) depicts the current dependence at $T = 100\,\mathrm{K}$ in the electron and hole regime. The spin diffusion constant varies from $D_s = 0.0086$ to $0.012\,\mathrm{m^2s^{-1}}$ with two outliers at $D_s(200\,\mu\mathrm{A}, 45\,\mathrm{V}) = 0.0046\,\mathrm{m^2s^{-1}}$ and $D_s(100\,\mu\mathrm{A}, -45\,\mathrm{V}) = 0.0162\,\mathrm{m^2s^{-1}}$. As anticipated from similar shapes of the Hanle curves at various currents, the spin diffusion constant D_s does not show any systematic dependence on the current I. Upon investigating the gate dependence at $T = 100\,\mathrm{K}$, the spin diffusion constant was observed to vary from $D_s = 0.0043$ to $0.016\,\mathrm{m^2s^{-1}}$, exhibiting no discernible correlation, as illustrated in Fig. 7.20 b) for various currents. The temperature dependence of D_s is presented in

Fig. 7.20 c), which reveals an increasing tendency from $D_s = 0.0075\,m^2s^{-1}$ to $0.0185\,m^2s^{-1}$ for $T \geq 50\,K$, analogous to τ_s. It remains unclear whether this observed increase is due to the large variation in the fitting results obtained for curves of similar shapes, or if it is a genuine increase of D_s with temperature.

Spin diffusion length L_s

The spin diffusion length L_s is calculated from the extracted values of τ_s and D_s via $L_s = \sqrt{D_s \tau_s}$. The results vary from $L_s = 1.25\,\mu m$ to $2.62\,\mu m$ at a temperature of $T = 100\,K$ for all observed bias currents and back gate voltages. As a consequence of the observed increase in both τ_s and D_s with increasing temperature, the spin diffusion length L_s is found to double from $L_s(50\,K,\ 45\,V,\ -250\,\mu A) = 1.5\,\mu m$ to $L_s(150\,K,\ 45\,V,\ -250\,\mu A) = 3.1\,\mu m$. In the same temperature range, L_s only increases from 2.24 to 2.78 µm at $V_g = -45\,V$. The temperature dependence of L_s can be seen in the Appendix in Fig. A.8 a).

Discrepancy between D_s and D_c

The charge and spin diffusion constants, D_c and D_s, are compared as a function of the charge carrier density n in Fig. 7.20 d). The charge diffusion constants D_c (lines) are calculated as described in Sec. 6.1.2, while the spin diffusion constants D_s (dots) are obtained from the normalized fits to the Hanle curves at a constant current of $I = -250\,\mu A$. There is a significant discrepancy of both diffusion constants, with D_s being up to one order of magnitude smaller than D_c. This discrepancy is unexpected, given that similar values for D_s and D_c have been reported in graphene spin valve devices with conventional Co-electrodes, which suggest a weak Coulomb electron-electron interaction [97, 196].

In general, the discrepancy between D_c and D_s in our data may be attributed to a number of factors. As previously discussed in Sec. 3.5.4, the ratio of the contact resistance and the spin resistance of the channel $\mathcal{R}_c/R^s_{ch}$ influences the shape and the height of the Hanle curves. However, when calculating the ratio for Sample A the minimum value we obtain is $\mathcal{R}_c/R^s_{ch} = 13.9$. For values of $\mathcal{R}_c/R^s_{ch} > 10$, the fit values are reported to be in agreement with the simulated data in Ref. [124], irrespective of the factor d/L_s. Consequently, contact-induced spin relaxation can be ruled out as a potential explanation for the observed discrepancy between D_s and D_c. However, additional factors may contribute to this observed discrepancy in the diffusion constants. Firstly, the fitting function assumes an isotropic spin relaxation so that $\tau_{s,x} = \tau_{s,y} = \tau_{s,z}$. An anisotropy in the spin relaxation times may be introduced by SOC, as discussed in Sec. 3.5. This could result in an incorrect determination of τ_s when obtained by fits that assume an isotropic spin relaxation. Secondly, given that the hBN tunnel barrier is only two to three layers

thick, the graphene underneath may potentially be exposed to a proximity effect due to the FGT, affecting the spin transport properties underneath the electrodes. Thirdly, the presence of magnetic moments has been reported to narrow the Hanle curves [132]. Large D_s values result in wide Hanle curves. In presence of magnetic moments, the Hanle curve would get narrower, leading to lower extracted D_s by fitting. Additionally, stray fields from the FGT electrodes could potentially penetrate the graphene layer, increasing spin dephasing underneath the injector and detector. In the following, all of these possible factors are discussed in detail.

In order to investigate an anisotropy in τ_s, proximitized graphene underneath the FGT electrodes, and stray fields, *COMSOL* simulations were employed. The utilized geometry in the simulations was modelled after the sample geometry, injecting and detecting spins along a line separated by $d = 5\,\mu m$, as illustrated in Fig. 7.21. The mesh was automatically generated by dividing the modelled geometry into small triangles. To eliminate any discrepancies in the simulations resulting from the mesh, it was fixed for all simulations. The areas of the FGT injector and detector flakes are also indicated in red on the mesh, allowing for a separate definition of parameters in each area. It should be noted that although the FGT area is imprinted in the mesh, spin injection and detection is only simulated along the yellow lines in the center of these areas.

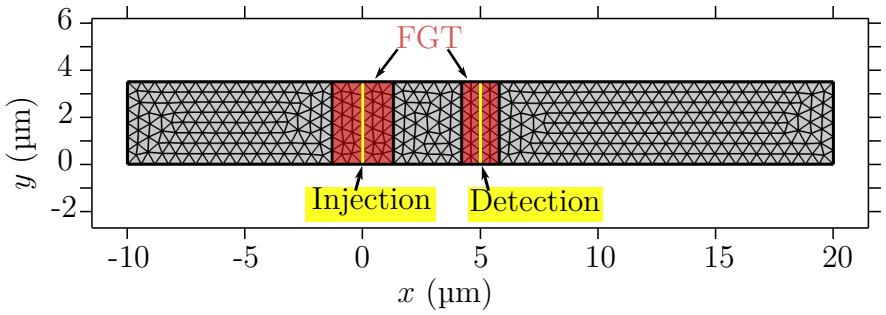

Fig. 7.21: Utilized mesh for the *COMSOL* simulations. The red areas indicate the positions of the FGT electrodes. The spins are injected and detected across the center yellow lines in these areas.

Anisotropy in the spin relaxation

As a first step, an anisotropy in τ_s is investigated. Given that the external magnetic field was applied along the long-axis of the FGT strips in y-direction, the spins would precess in the xz-plane. Accordingly, an anisotropy factor k was introduced as $\tau_{s,z} = k \cdot \tau_{s,x}$. In order to maintain a constant total spin relaxation time $\tau_s = \sqrt{\tau_{s,x} \cdot \tau_{s,z}} = \text{constant}$, both components of the spin relaxation time were calculated as $\tau_{s,x} = \sqrt{\frac{\tau_s^2}{k}}$ and $\tau_{s,z} = \sqrt{\tau_s^2 \cdot k}$. The simulations were compared to the measured Hanle curve at $T = 1.5\,K$, $I = -250\,\mu A$ and $V_g = 45\,V$. The *COMSOL* simulations were conducted at a constant $L_s = 1.96\,\mu m$, which was the value obtained from the *Origin* fits. Hanle curves were simulated for the obtained diffusion constants from transport and Hanle measurements, $D_c = 0.0991\,m^2s^{-1}$

and $D_s = 0.0097\,m^2s^{-1}$. The corresponding spin relaxation time τ_s were then calculated, as L_s and D_c or D_s are fixed. The anisotropy k was varied from $k = 0.2$ to 2. The results for both simulations compared to the measured Hanle curve are presented in Fig. 7.22 a) and b). Because of the discrepancy in the amplitudes observed between the two simulations, P was set to $P_{a)} = 0.11$ and $P_{b)} = 0.048$ in panel a) and b), respectively. The simulated curves based on D_c fail to fit the measured curve at any anisotropy value k. Even at large anisotropies (low or high k-values), the simulated curves did not match the measurement. The resulting curves were too wide, so that the dips next to the maximum were located at very large magnetic field values. In contrast, utilizing D_s provides an excellent fit for $k = 1$, meaning no anisotropy in τ_s. This also serves to validate the Hanle model within *COMSOL*. Higher or lower k-values over- and underestimate the height of the Hanle peak at zero magnetic field, respectively. Additionally, the positions of the dips next to the peak fit best for $k = 1$. Consequently, an anisotropy in τ_s is excluded as a potential cause for the discrepancy between D_s and D_c.

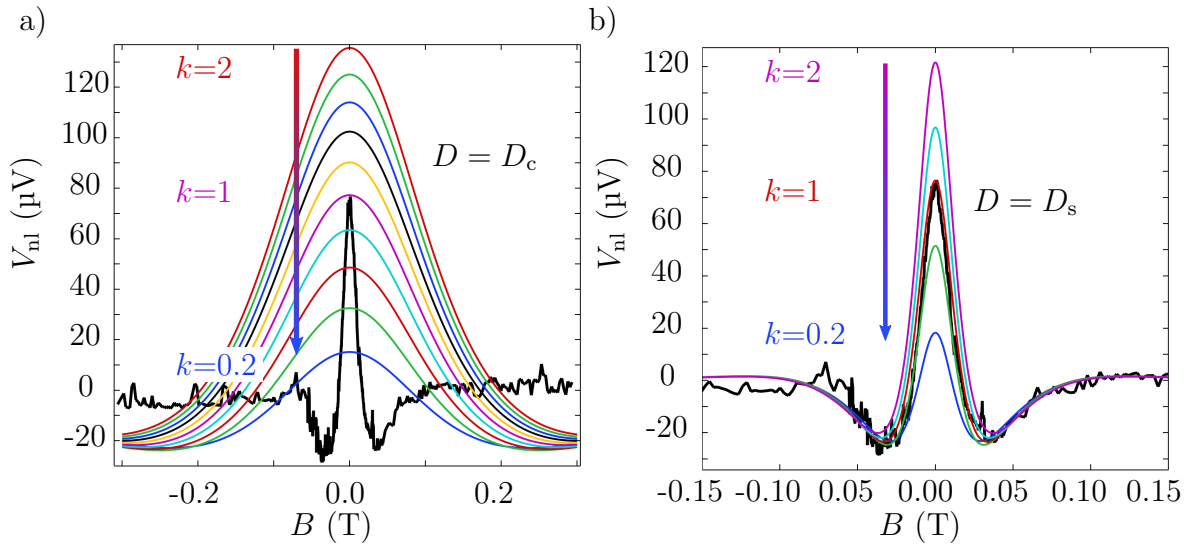

Fig. 7.22: Comparison of *COMSOL* simulations and the Hanle measurement with an employed diffusion constant a) $D = D_c$ and b) $D = D_s$ in the simulations. The measured Hanle curve is illustrated as a black solid line. Simulated curves are shown as colored lines. The anisotropy k is swept from 2 to 0.2 from top to bottom in steps of 0.2. In b), simulated curves for $k = 2, 1.6, 1, 0.6$, and 0.2 are shown from top to bottom, respectively.

Proximity effect in graphene

As a second step, *COMSOL* simulations were performed to test for a proximity effect underneath the FGT electrodes. This is phenomenologically simulated by separately defining the spin transport parameters D_s and τ_s in the area underneath the FGT (red areas in the mesh) and in the graphene transport channel (grey areas in the mesh). In the unproximitized areas, the diffusion constant and spin relaxation time were defined

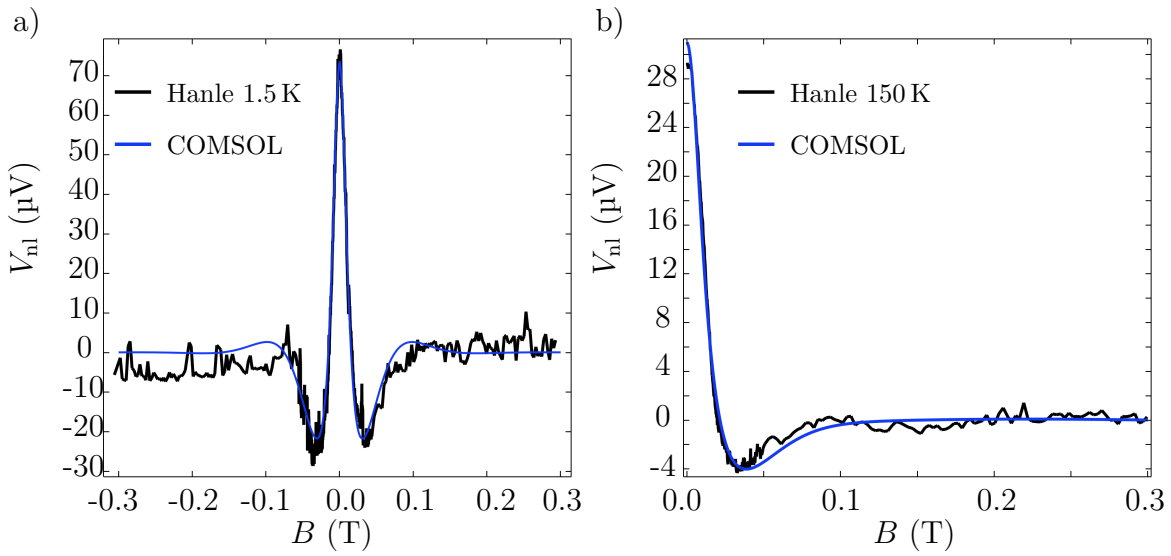

Fig. 7.23: *COMSOL* fit to the experimentally obtained Hanle curve at a) 1.5 K and b) 150 K. The *COMSOL* simulations are in good agreement with the measured data, when fitting for P, τ_s, and f_{proxy}. The extracted values are $P_{1.5\,K} = 69\,\%$, $\tau_{s,\,1.5\,K} = 7.43\,ns$, and $f_{proxy,\,1.5\,K} = 0.00973$, and $P_{150\,K} = 696\,\%$, $\tau_{s,\,150\,K} = 7.64\,ns$, and $f_{proxy,\,150\,K} = 0.00553$. As the Hanle curve at $T = 150\,K$ is not perfectly symmetric, only the experimental data for positive fields was fitted.

as D_c and τ_s. In contrast, in the red areas the diffusion constant and spin relaxation time was set to $D_{s,\,proximitized} = f_{proxy} \cdot D_c$ and $\tau_{s,\,proximitized} = f_{proxy} \cdot \tau_s$. Here, f_{proxy} is an additional factor, which phenomenologically introduces the proximity in the graphene layer. For the sake of simplicity, the same proximity factor was assumed for both the diffusion constants and the spin relaxation times.

The *COMSOL* simulations fit the Hanle measurement via a least-square optimization. However, when τ_s was set to the extracted values from the *Origin* fits and the fitting in *COMSOL* was carried out for P and f_{proxy}, the *COMSOL* fit did not agree with the experimental data. This is to be expected, given the drastic difference of the spin diffusion constants D_s compared to D_c in the graphene within both models. When fitting for P, f_{proxy}, and τ_s in *COMSOL*, a good fit of the simulation with the measured curve was achieved, as illustrated in Fig. 7.23 a) and b). This shows, that assuming different τ_s and D_s underneath the FGT electrodes could explain the discrepancy between D_s and D_c. The spin relaxation time $\tau_s = 7.43\,ns$ obtained from the *COMSOL* fitting process in Fig. 7.23 a) is one order of magnitude larger than the value from the *Origin* fits. The resulting proximity factor of $f_{proxy} = 0.00973$ corresponds to a drastic change of D_s and τ_s underneath the electrodes. Given that FGT is not in direct contact with graphene, separated by a two to three layer thick hBN tunnel barrier, such a large proximity effect is not anticipated.

Moreover, the measured Hanle curve at $T = 150\,K$ was fitted with *COMSOL*, at the same back gate voltage of $V_g = 45\,V$ and applied bias $I = -250\,\mu A$, as presented in Fig. 7.23 b).

As the experimental data were subject to a shift in the background signal, as previously discussed and presented in Fig. 7.17, the Hanle curve was fitted for positive magnetic fields. The *COMSOL* fitting resulted in an unrealistically high value of $P_{150\,\mathrm{K}} = 696\,\%$. The spin relaxation time was found to be $\tau_{\mathrm{s},\,150\,\mathrm{K}} = 7.64\,\mathrm{ns}$, comparable to the value obtained at 1.5 K. The proximity factor $f_{\mathrm{proxy},\,150\,\mathrm{K}} = 0.00553$ is found to be lower than at 1.5 K, indicating an increase in the proximity effect with increasing temperature. This is contrary to the expectation that a reduction in magnetization would result in a decrease in proximity effect.

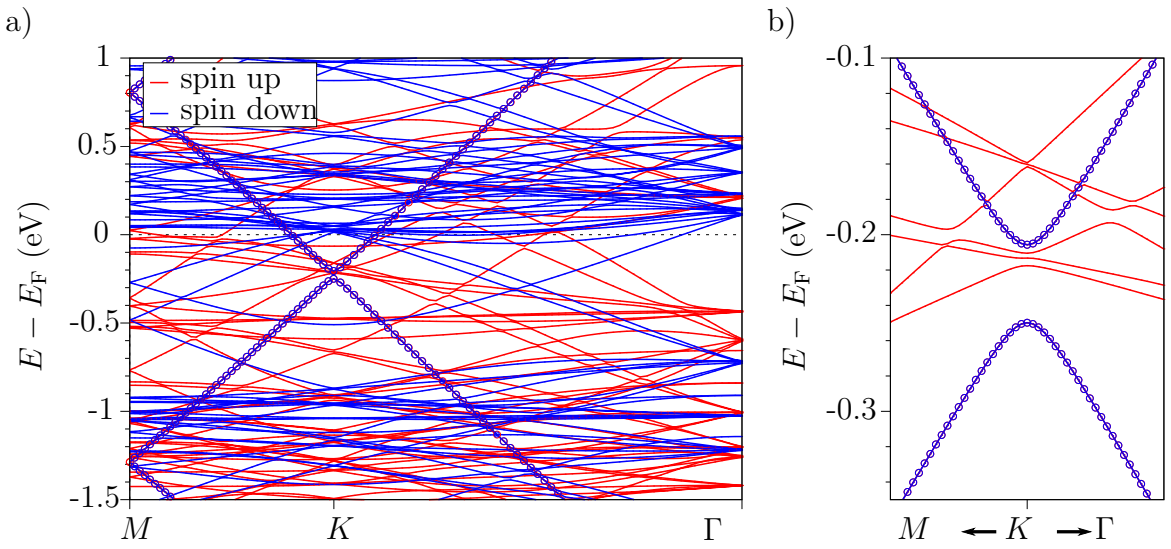

Fig. 7.24: a) DFT-calculated band structure of the FGT/hBN/hBN/graphene heterostructure. Spin up and down states are illustrated by red and blue lines, respectively. The graphene states are indicated by open circles. b) Zoom to the Dirac states at K. The two hBN layers prevent a proximity exchange splitting of the Dirac bands. These DFT-calculations were provided by Dr. Klaus Zollner.

To gain further insights into a potential proximity effect, Dr. Klaus Zollner has conducted density functional theory (DFT) calculations for a two-layer hBN tunnel barrier. Details on the configuration of these simulations can be found in the Appendix A.6. The calculated band structure of the heterostructure is presented in Fig. 7.24 a) and b). The two layers of hBN are observed to preserve the Dirac states of graphene within the heterostructure. However, the Dirac point is shifted by approximately 215 meV below the Fermi level, indicating charge transfer between the individual layers. No evidence of proximity-induced exchange coupling in the graphene layer was observed. The Dirac bands remain spin degenerate and no magnetic moments are induced. The hBN layers introduce a sublattice asymmetry and a staggered potential gap, which opens an orbital gap. Consequently, a proximity effect in graphene due to the FGT can be ruled out and cannot explain the discrepancy of D_{c} and D_{s}.

Stray fields

Stray fields could potentially influence the spins in the graphene and are simulated phenomenologically by adding an extra constant magnetic field term $\vec{B}_{\mathrm{sf}}$ to the external magnetic field in the absorption coefficient A in the *COMSOL* simulations, as introduced in Sec. 3.6. Given that a stray field $\vec{B}_{\mathrm{sf}}$ at the edge of an FGT flake would lie in the xz-plane, the y-component of $\vec{B}_{\mathrm{sf}}$ is set to be zero [197]. To simulate, whether stray fields could account for the discrepancy in the diffusion constants, the *COMSOL* simulation was fitted to the experimental data by fitting the x- and z-component of $\vec{B}_{\mathrm{sf}}$, P, and τ_{s}. A global diffusion constant of $D_{\mathrm{c}} = 0.0991\,\mathrm{m^2 s^{-1}}$, obtained from the charge transport measurements, was assumed throughout the simulations.

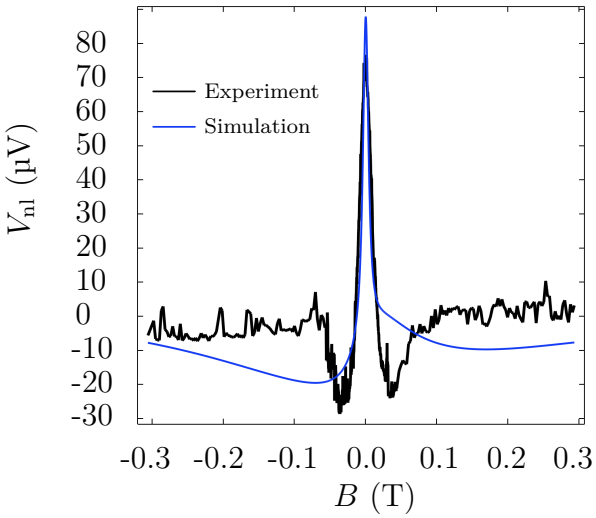

Fig. 7.25: Hanle simulation fitted for an introduced stray field in xz-direction in *COMSOL*. The simulation did not result in satisfactory fits to the experimental data.

As illustrated in Fig. 7.25, the *COMSOL* fits did not yield a satisfactory agreement to the experimental data. Stray fields of up to 5 mT have been reported for FGT flakes [197]. However, inserting stray fields with a magnitude of 5 mT did not result in matching simulations. When considered alongside the poor fit quality, it can be concluded that stray fields from the FGT flakes are unlikely to be the cause of the discrepancy in the diffusion constants.

Magnetic moments

Fig. 7.22 a) clearly demonstrates that the Hanle curves exhibit a considerably broader profile than the experimentally measured curve when setting $D = D_{\mathrm{c}}$. The observed dips in vicinity of the maximum occur at magnetic fields that are significantly higher. In the presence of magnetic moments within the graphene channel itself, a sharpening of the Hanle curve can result from an exchange field $\vec{B}_{\mathrm{ex}}$ of these moments [132, 189]. In this context, the spins precess around a total field $\vec{B}_{\mathrm{total}} = \vec{B}_{\mathrm{app},y} + \vec{B}_{\mathrm{ex}}$, where $\vec{B}_{\mathrm{app},y}$

is the applied magnetic field in y-direction. Assuming that the magnetic moments are paramagnetic, their magnetization scales with the external applied field $\vec{B}_{\mathrm{ex}} = k_{\mathrm{para}}\vec{B}_{\mathrm{app},y}$, with k_{para} being the proportionality constant. As a result, the Larmor frequency is recalculated as [132]

$$\vec{\omega}_0 = \frac{g_{\mathrm{L}}\mu_{\mathrm{B}}}{\hbar}\vec{B}_{\mathrm{total}} = \frac{g_{\mathrm{L}}\mu_{\mathrm{B}}}{\hbar}(1+k_{\mathrm{para}})\vec{B}_{\mathrm{app},y} = \frac{g_{\mathrm{L,\,para}}\mu_{\mathrm{B}}}{\hbar}\vec{B}_{\mathrm{app},y}, \tag{7.2}$$

with $g_{\mathrm{L,\,para}} = g_{\mathrm{L}}(1+k_{\mathrm{para}})$ being the modified enhanced g-factor. Thus, the presence of magnetic moments can be verified by Hanle fits that fit for $g_{\mathrm{L,\,para}}$. An increased $g_{\mathrm{L,\,para}} > 2$ is then a result of the increased spin precession frequency due to the exchange field from the magnetic moments.

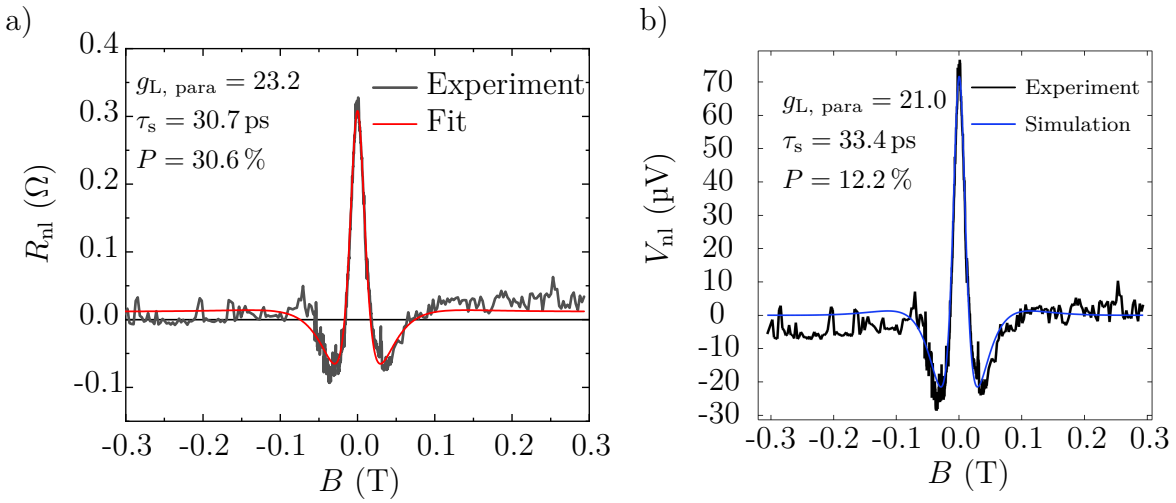

Fig. 7.26: a) *Origin* and b) *COMSOL* fit to the Hanle curve at $T = 1.5\,\mathrm{K}$, $V_{\mathrm{g}} = 45\,\mathrm{V}$, and $I = -250\,\mu\mathrm{A}$. A diffusion constant of $D = D_{\mathrm{c}}$ was assumed while fitting for the parameters $g_{\mathrm{L,\,para}}$, τ_{s}, and P. The obtained values for $g_{\mathrm{L,\,para}}$ and τ_{s} from both fits agree well with each other.

The Hanle curves were fitted with the *Origin* fitting function Eq. (A.6) and via *COMSOL* simulations. The results of these fits are shown in Fig. 7.26 a) and b), respectively. The diffusion constant was set to the large $D = D_{\mathrm{c}}$ obtained from the charge transport measurements. The results derived from the *Origin* and *COMSOL* fits are in good agreement. With spin relaxation times of $\tau_{\mathrm{s,\,Origin}} = 30.7\,\mathrm{ps}$ compared to $\tau_{\mathrm{s,\,COMSOL}} = 33.4\,\mathrm{ps}$ and large effective g-factors of $g_{\mathrm{L,\,para,\,Origin}} = 23.2$ and $g_{\mathrm{L,\,para,\,COMSOL}} = 21.0$, the Hanle curve is subjected to a significant narrowing. However, the discrepancy between the obtained value of $g_{\mathrm{L,\,para}}$ and the unaffected value of $g_{\mathrm{L}} = 2$ is unexpected, as the origin of these paramagnetic moments remains unclear.

Accordingly, the temperature dependence of $g_{\mathrm{L,\,para}}$ for the Hanle curves measured at $V_{\mathrm{g}} = 45\,\mathrm{V}$ and $I = -250\,\mu\mathrm{A}$ is investigated, as presented in Fig. 7.27 (grey dots). It is evident that the temperature dependence of $g_{\mathrm{L,\,para}}$ does not follow a $1/T$ dependence, which is expected for paramagnetic moments [132, 189]. Instead, the data indicates

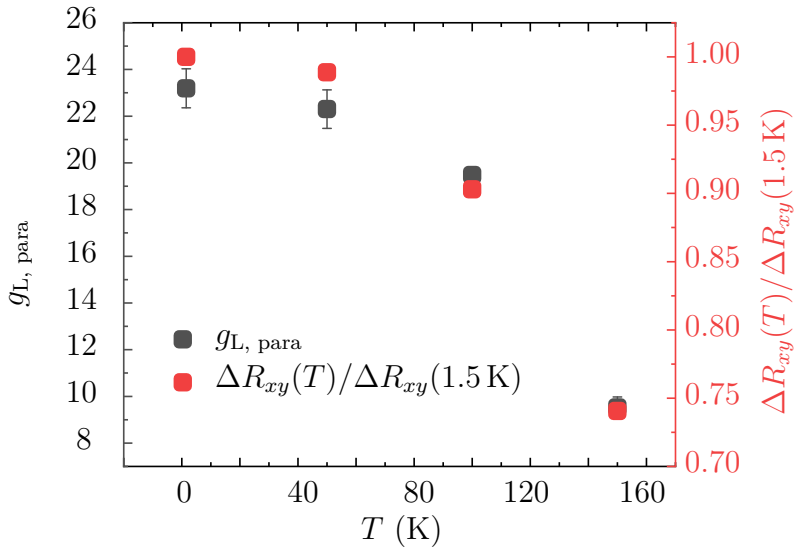

Fig. 7.27: Temperature dependence of $g_{\mathrm{L,\,para}}$ obtained from *Origin* fits (grey dots) and of the FGT injector's magnetization of Sample A (red dots). The temperature dependence correlates for both values.

that the temperature dependence of $g_{\mathrm{L,\,para}}$ is similar to that of FGT's magnetization, as represented by $\Delta R_{xy}(T)/\Delta R_{xy}(1.5\,\mathrm{K})$ (red dots in Fig. 7.27). This could be a sign that the magnetic moments may originate from spurious FGT residues on top of the graphene spin diffusion channel, resulting in an increased g-factor. However, in the case of ferromagnetic moments, a dip in the non-local spin valve measurement is expected, which exhibits a hysteretic behaviour, centred at non-zero magnetic field values. This, however, was not observed in the non-local spin valve measurements. Consequently, ferromagnetic moments, such as spurious FGT residues, are excluded as a possible origin.

Summary Hanle Sample A

Non-local Hanle measurements demonstrated efficient spin injection, with spin injection efficiencies reaching up to $P \approx 40\,\%$. Dissimilar Hanle curves were shown for $V_{\mathrm{g}} = 45\,\mathrm{V}$ in the anti-parallel and parallel configuration. The reason for this discrepancy remains unclear. However, at $V_{\mathrm{g}} = 60\,\mathrm{V}$ the Hanle curves are comparable in both magnetization configurations, resulting in similar obtained values for τ_{s}, D_{s}, and P. Occasionally, a shift in the background signal was observed. Other possible mechanisms for asymmetric Hanle curves, e.g. a tilting of the magnetization direction of the injector and detector electrode towards the external magnetic field, were excluded. The extracted values for P and the spin valve heights $\Delta R_{\mathrm{nl,\,SV}}$ display a correlation with respect to the gate, current, and temperature dependence, indicating that the change in the spin-valve signal corresponds to a change in the spin injection efficiency P. Spin injection in the electron regime is more efficient than other spin injection or extraction mechanisms. No correlation with the

current or back gate voltage was observed for the spin relaxation time τ_s and constant D_s. However, both parameters appear to increase with $T \geq 50\,\mathrm{K}$. This results in a doubling of the spin diffusion length L_s in the temperature range from 50 K to 150 K at $V_g = 45\,\mathrm{V}$. The extracted spin diffusion constants D_s are approximately one order of magnitude lower than the extracted D_c obtained from the charge transport measurements. The lower extracted $\Delta R_{\mathrm{nl,\,Hanle}}$ compared to $\Delta R_{\mathrm{nl,\,sv}}$, in combination with the temperature dependence of τ_s and the increased g-factor indicate the presence of magnetic moments in the graphene channel. These moments could explain the drastic difference observed between D_s and D_c. However, the origin of these moments remains unclear, as graphene was not subjected to any hydrogenation or other processes that could induce lattice vacancies. Furthermore, spurious FGT residues are also excluded as the source of these magnetic moments as the dip in the non-local spin valve measurements did not exhibit a hysteresis, expected in presence of ferromagnetic moments.

7.2.2. Sample B

Hanle signals have also been measured in Sample B, as shown in Fig. 7.28 a), injecting spins at the contacts 2-16. The external magnetic field was applied perpendicular to the easy-axis of the FGT electrodes, along the graphene channel in x-direction. As was previously observed in the non-local spin valve measurements, the Hanle curves exhibit a reversed polarity in this measurement configuration with respect to Sample A, as illustrated in Fig. 7.28. The height of the non-local Hanle signal $\Delta R_{\text{nl, Hanle}} = -0.57\,\Omega$ is in agreement with the spin valve measurement $\Delta R_{\text{nl, SV}} = -0.52\,\Omega$, shown in Fig. 7.28 b). All measurements presented in Fig. 7.28 are shifted, so that the Hanle measurements have zero offset. The Hanle measurements in Sample B exhibit a lower signal-to-noise ratio compared to Sample A, which results in a less precise fitting. Nevertheless, the fits align well with the measurements, yielding $\tau_s = 0.529\,\text{ns}$, $D_s = 0.971\,\text{m}^2\text{s}^{-1}$, and $P = 2.8\,\%$ in the parallel configuration. In the anti-parallel configuration, comparable values of $\tau_s = 0.428\,\text{ns}$ are obtained. Both, the spin injection efficiency P and the diffusion

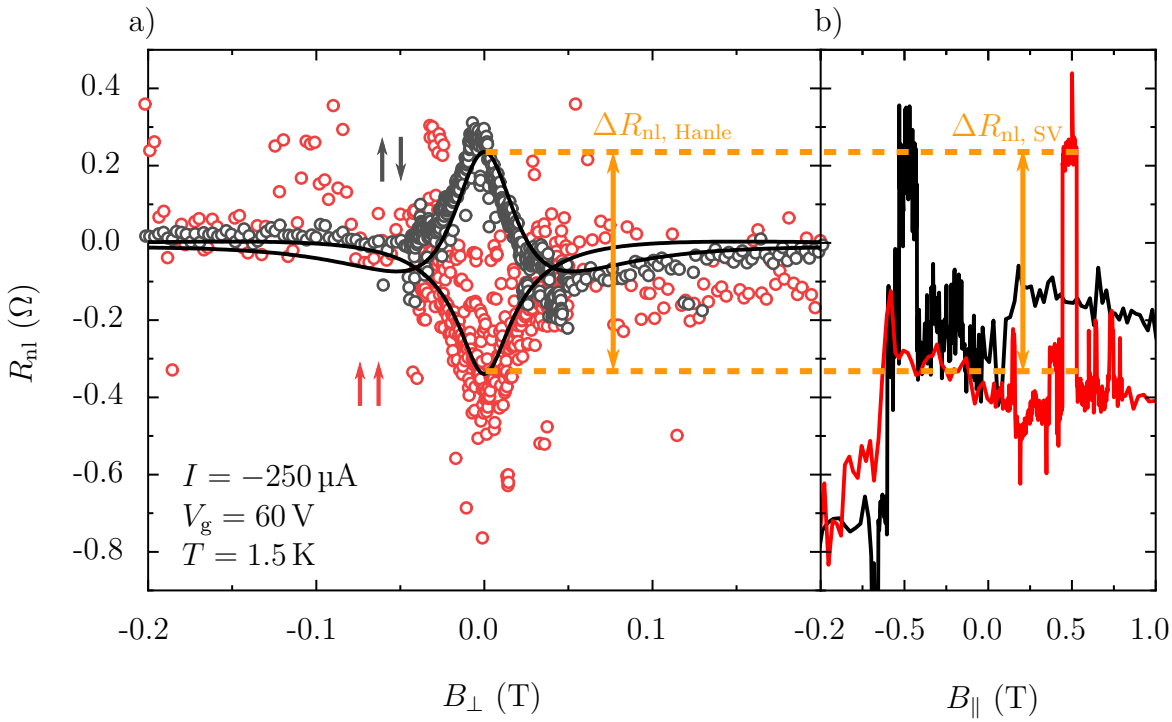

Fig. 7.28: a) Non-local Hanle measurements of Sample B at $T = 1.5\,\text{K}$, $I = -250\,\mu\text{A}$, and $V_g = 60\,\text{V}$ with a magnetic field sweep along the graphene channel in x-direction. The Hanle curves are shown for (anti-)parallel magnetization alignment of the FGT electrodes in red (grey). Fits to the Hanle measurements are indicated by the black lines. b) The non-local spin valve measurement for the same set of parameters is shown for comparison. Note that the magnetic field is swept in different directions in a) and b). The spins were injected at contacts 2-16 for both measurements.

constant D_s vary considerably with $P = 8.8\,\%$ and $D_s = 0.050\,m^2s^{-1}$. However, the fitting error of the diffusion constant is considerable in the parallel configuration. The parallel curve can also be fitted well with spin diffusion constants down to $D_s = 0.08\,m^2s^{-1}$ with corresponding $\tau_s = 0.267\,ns$, due to the large noise in the measurements. As a consequence, the extracted values of the Hanle fits of Sample B can only be considered as estimates. In the following, the best fits to the experimental Hanle curves will be discussed. The extracted values for τ_s are comparable to those of Sample A, however, the obtained values for P are significantly lower.

Comparison of non-local spin valve and Hanle measurements

In order to compare the non-local spin valve and the Hanle signals, $\Delta R_{nl,\,SV}$, $\Delta R_{nl,\,Hanle}$, and $2 \times \Delta R_{nl,\,Hanle,P}$ are plotted against the applied currents at $V_g = 45\,V$ and $60\,V$ in Fig. 7.29 a) and b), respectively. At both gate voltages, there is a good agreement between $\Delta R_{nl,\,Hanle}$ and the extracted spin valve heights $\Delta R_{nl,\,SV}$, exhibiting the decreasing tendency with increasing positive currents. Nevertheless, the discrepancy between the parallel and anti-parallel Hanle amplitudes is observed at both gate voltages, as can be seen from the different values of $\Delta R_{nl,\,Hanle}$ and $2 \times \Delta R_{nl,\,Hanle,P}$. Given the significant noise present in the Hanle curves with a difference of approximately $0.1\,\Omega$ between the two values, it cannot be excluded that this discrepancy is due to the noise in the Hanle data. In the following, the current, gate and temperature dependence of the best fits of P, τ_s, and D_s are evaluated for Sample B.

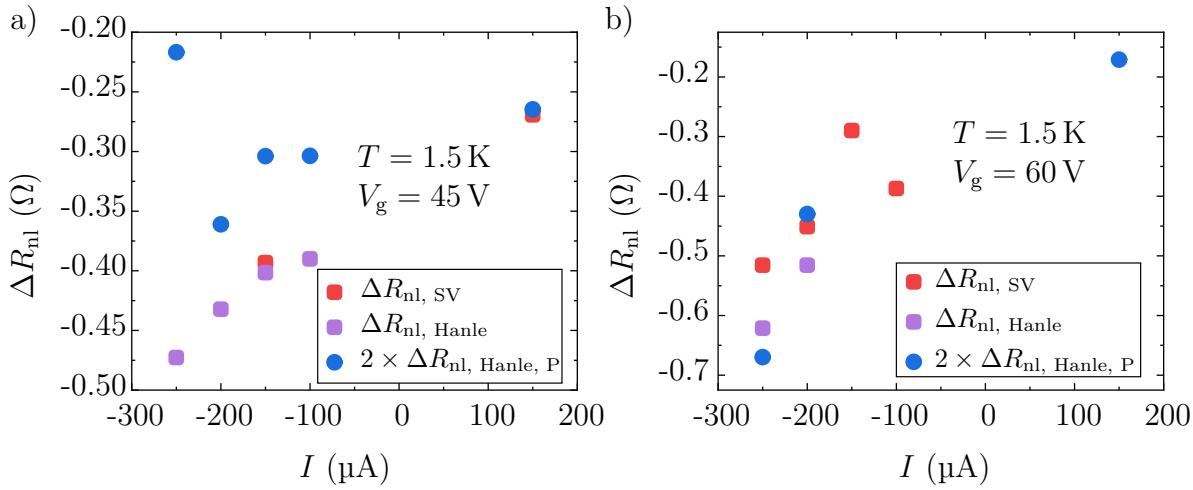

Fig. 7.29: Comparison of the non-local spin valve heights $\Delta R_{nl,\,SV}$ and the Hanle amplitudes $\Delta R_{nl,\,Hanle}$ and $2 \times \Delta R_{nl,\,Hanle,P}$ at a) $V_g = 45\,V$ and b) $V_g = 60\,V$. The non-local signal heights are plotted against the current.

Spin injection efficiency P

The Hanle curves for various currents at $T = 1.5\,\mathrm{K}$ and $V_\mathrm{g} = 45\,\mathrm{V}$ are illustrated in Fig. 7.30 a). As a consequence of the considerable noise present in the data, the shapes and the amplitudes of the curves cannot be compared directly from the measurements anymore. For Sample B, all Hanle measurements were conducted in both parallel and anti-parallel magnetization configurations. However, not all of the measurements yielded a clear Hanle curve. Consequently, some parameters are only extracted in the parallel or anti-parallel alignment. The current dependence of P at $V_\mathrm{g} = \pm 45\,\mathrm{V}$ at $T = 1.5\,\mathrm{K}$ is shown in Fig. 7.30 d) for the parallel (P, filled boxes) and anti-parallel (AP, open boxes) magnetization alignment. The extracted values exhibit considerable scattering, ranging from 1.7 % (AP, -45 V, -150 µA) up to 87.8 % (P, 45 V, -250 µA). However, the two values exceeding $P > 80\,\%$ are regarded as outliers due to the considerable noise in the data. A discernible correlation between P and current is challenging to ascertain. Nevertheless, it appears that the extracted values decrease with increasing the current from negative to positive values, consistent with the observations reported in Sample A. Hanle curves in the parallel magnetization configuration for various gate voltages are shown in Fig. 7.30 b). The yellow curve of $V_\mathrm{g} = -60\,\mathrm{V}$ exhibits the previously reported shift in the background signal, as the signal at large negative and large positive magnetic field values is shifted in opposite direction. The extracted values indicate a more efficient spin injection the further from the charge neutrality point, as presented in Fig. 7.30 e). However, a clear correlation cannot be identified due to the considerable scattering of the extracted values. The parallel Hanle measurements are presented at two temperatures, 1.5 K and 130 K, in Fig. 7.30 c). A clear decrease in signal height is observed with increasing temperature. This is also reflected in the decreasing tendency of P when plotted against temperature, as illustrated in Fig. 7.30 f). This behaviour is consistent with that observed in Sample A.

Spin relaxation time τ_s

Again, the normalized Hanle curves were fitted to extract the spin diffusion constant D_s and spin relaxation time τ_s, identically to Sample A. Consequently, normalized parallel measurements are presented in Fig. 7.31 a) for various applied bias currents at a fixed gate voltage of $V_\mathrm{g} = 45\,\mathrm{V}$ and a constant temperature of $T = 1.5\,\mathrm{K}$. However, due to the large noise, the shapes cannot be compared quite well to each other, as the noise obscures the majority of the shape. The extracted values for τ_s are plotted against the applied current in Fig. 7.31 d) for both anti-parallel and parallel magnetization configurations in the electron and hole regime. Once more, the values exhibit considerable scattering, ranging from τ_s(AP, 45 V, -200 µA) = 0.123 ns to τ_s(AP, -45 V, -150 µA) = 1.30 ns. No clear correlation with current is discernible. Fig. 7.31 b) illustrates the normalized parallel curves at a constant temperature and current of $T = 1.5\,\mathrm{K}$ and $I = -250\,\mu\mathrm{A}$

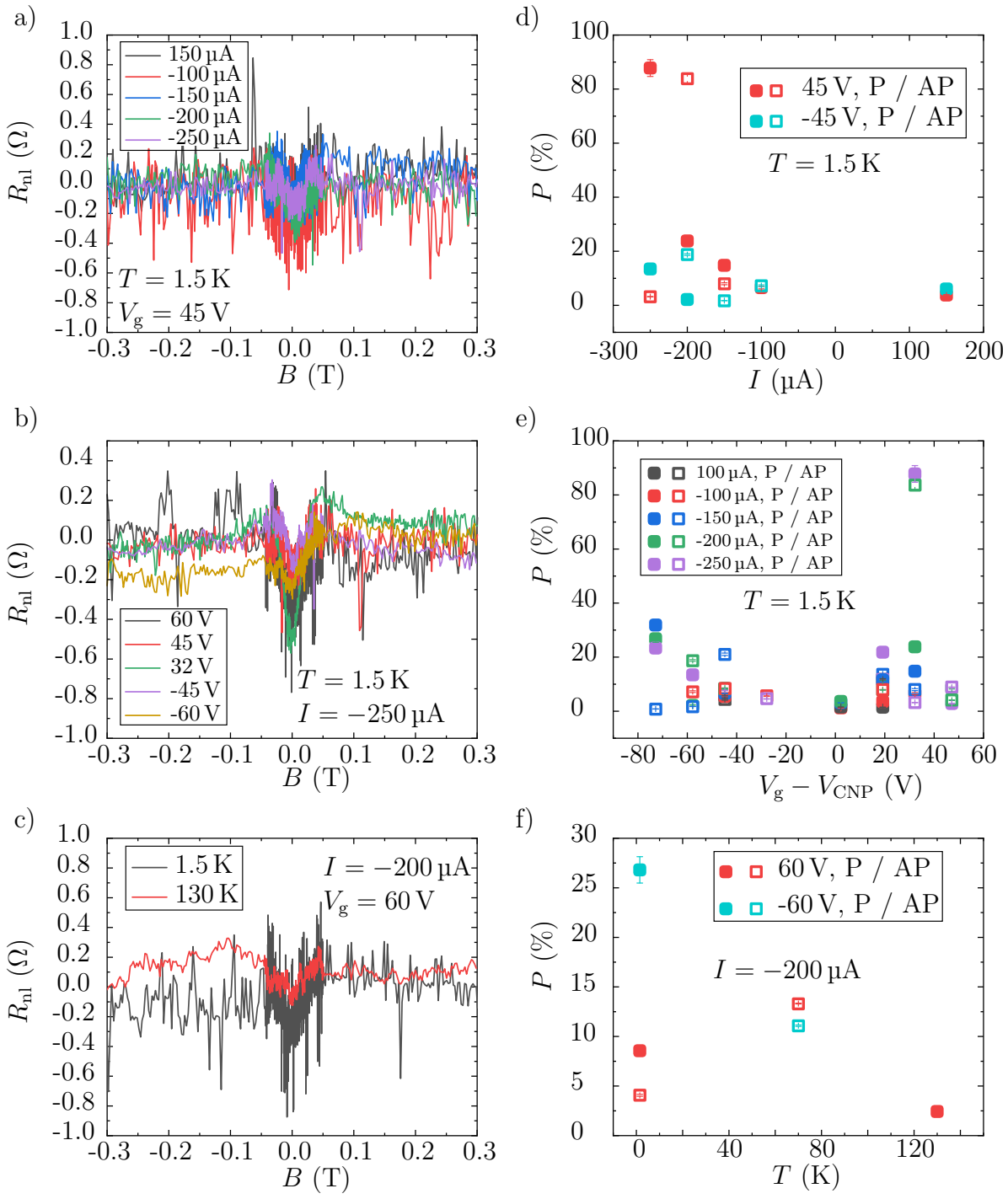

Fig. 7.30: Non-local Hanle curves in parallel magnetization configuration at a) constant temperature and back gate voltage at varying currents, b) constant temperature and bias current at various back gate voltages, and c) constant bias current and gate voltage at various temperatures. All curves are shifted, so that their offset is zero. A direct comparison of the measured Hanle curves is difficult due to the small signal-to-noise ratio. Fit results of P in the parallel (P, filled boxes) and anti-parallel (AP, open boxes) alignment are plotted against d) the applied current for $V_g = \pm 45\,\mathrm{V}$ at $T = 1.5\,\mathrm{K}$, e) $V_g - V_{CNP}$ at constant temperature $T = 1.5\,\mathrm{K}$ at various currents, and f) temperature at a constant current of $I = -200\,\mu\mathrm{A}$ for $V_g = \pm 60\,\mathrm{V}$. Error bars of P are mostly obscured by the dots themselves.

for various gate voltages. In Fig. 7.31 e) the extracted values of τ_s are presented for the same temperature at various currents plotted against the gate voltage in both parallel and anti-parallel magnetization configurations. The scattered results indicate an increasing tendency of τ_s towards gate voltages close to the charge neutrality point. The normalized parallel Hanle curves for 1.5 K and 130 K are presented in Fig. 7.31 c), with the corresponding fit results for τ_s plotted against temperature in Fig. 7.31 f). A decreasing tendency of τ_s with increasing temperature can be observed. However, the situation is less clear in the hole regime, as no Hanle signal was observed in the parallel or anti-parallel magnetization configuration at $T = 130$ K. This behaviour differs from that observed in Sample A, where an increasing tendency with increasing temperature was observed. However, no indications of magnetic moments were observed for Sample B. Neither the non-local spin valve measurements showed a characteristic dip at low magnetic fields, nor was the extracted height $\Delta R_{\text{nl, Hanle}}$ different from the spin valve height $\Delta R_{\text{nl, SV}}$.

Spin diffusion constant D_s

The values of D_s obtained by fitting the normalized Hanle curves are shown in Fig. 7.32. The results for the spin diffusion constant range from $D_s = 0.0041$ to $0.252\,\text{m}^2\text{s}^{-1}$, with outliers of even higher implausible values of $D_{\text{s, AP}}$(1.5 K, -45 V, -150 µA)$= 0.65\,\text{m}^2\text{s}^{-1}$ and $D_{\text{s, P}}$(1.5 K, 60 V, -250 µA)$= 0.97\,\text{m}^2\text{s}^{-1}$ that are not included in Fig. 7.32. Fig. 7.32 a), b), and c) present the spin diffusion constant plotted against applied bias currents, gate voltage and temperature, respectively. While one of these parameters is varied, the other two are fixed. The spin diffusion constant appears to increase with increasing applied bias from negative to positive values in both hole and electron regimes. Plotted against the gate voltage, D_s exhibits a similar correlation with gate voltage as τ_s, increasing towards the charge neutrality point. Furthermore, D_s seems to increase with temperature. As previously mentioned, the fits align with the experimental Hanle curves for a wide range of D_s-values. Consequently, the variation of D_s may also be attributed to a significant variation in the fit results.

A comparison of the extracted spin diffusion constant values D_s with the calculated charge diffusion constant D_c in Fig. 7.32 d) reveals that the two values do not correspond to each other, with the exception of a few cases at $T = 1.5$ K. Again, contact-induced spin relaxation can be ruled out as a potential explanation, given that the ratio of the contact resistance and spin resistance of the channel and the ratio of the channel length and extracted L_s calculate to $\mathcal{R}_c/R^s_{ch} = 2.7 > 1$ and $d/L_s > 1$. It is difficult to ascertain whether this discrepancy in D_s and D_c is attributable to the inferior fit quality resulting from the considerable noise in the data, or if it could be attributed to magnetic moments, as suspected for Sample A. However, no signatures of magnetic moments were observed in the non-local spin valve measurements. When comparing the height of the Hanle to the spin valve signal, only a small discrepancy between the parallel and anti-parallel Hanle

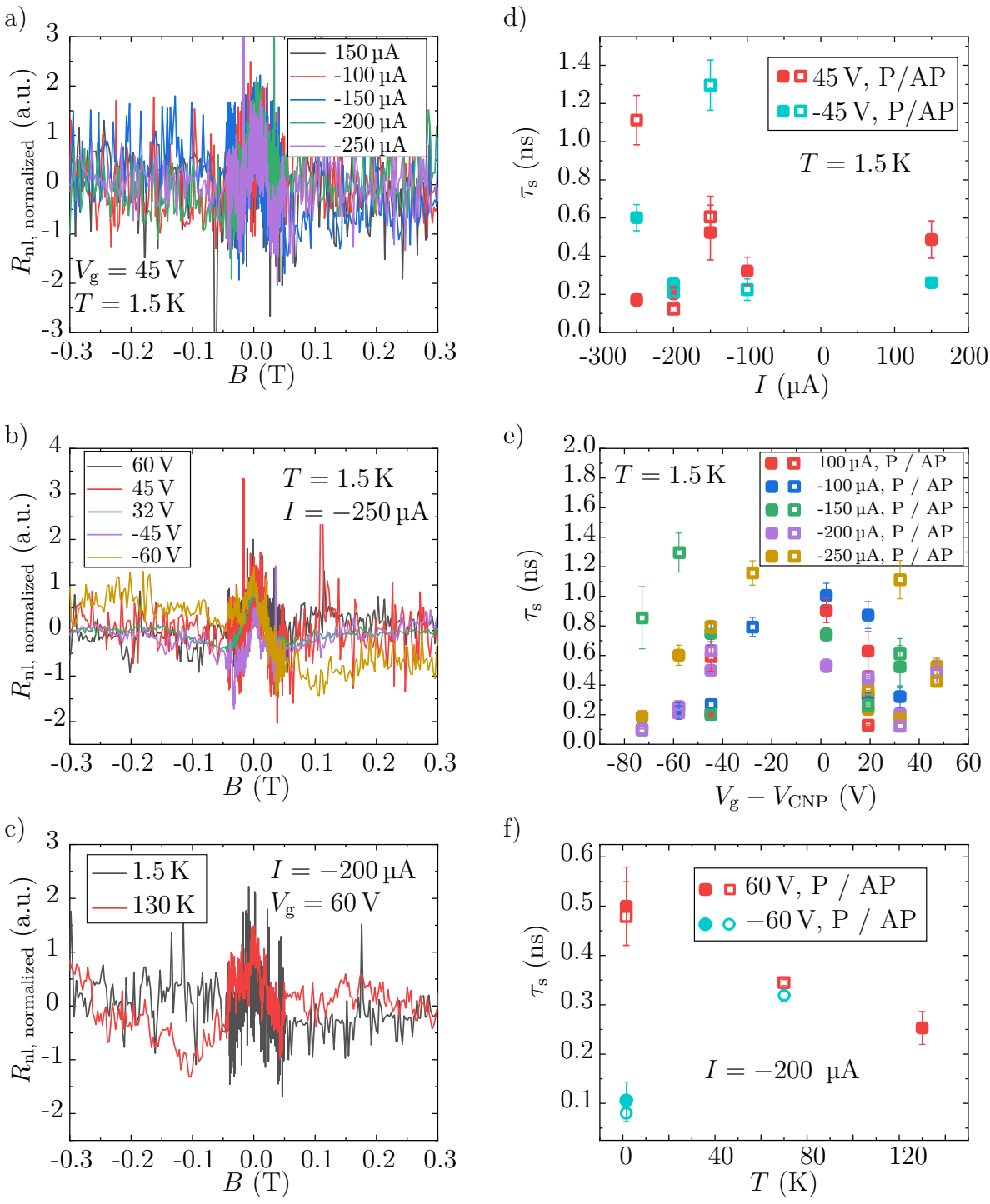

Fig. 7.31: Normalized parallel non-local Hanle curves shown at various a) currents, b) back gate voltages, and c) temperatures. While one parameter is changed, the other two variables are fixed. The fit results of τ_s are shown for the parallel (P, filled boxes) and anti-parallel (AP, open boxes) configuration as a function of current, back gate voltage, and temperature in d), e), and f), respectively. The current dependence is shown for the electron and hole regime at $V_g = \pm 45$ V at $T = 1.5$ K. The gate dependence is shown for various currents at the same temperature. The temperature dependence is presented at a constant bias current $I = -200$ µA for the electron and hole regime.

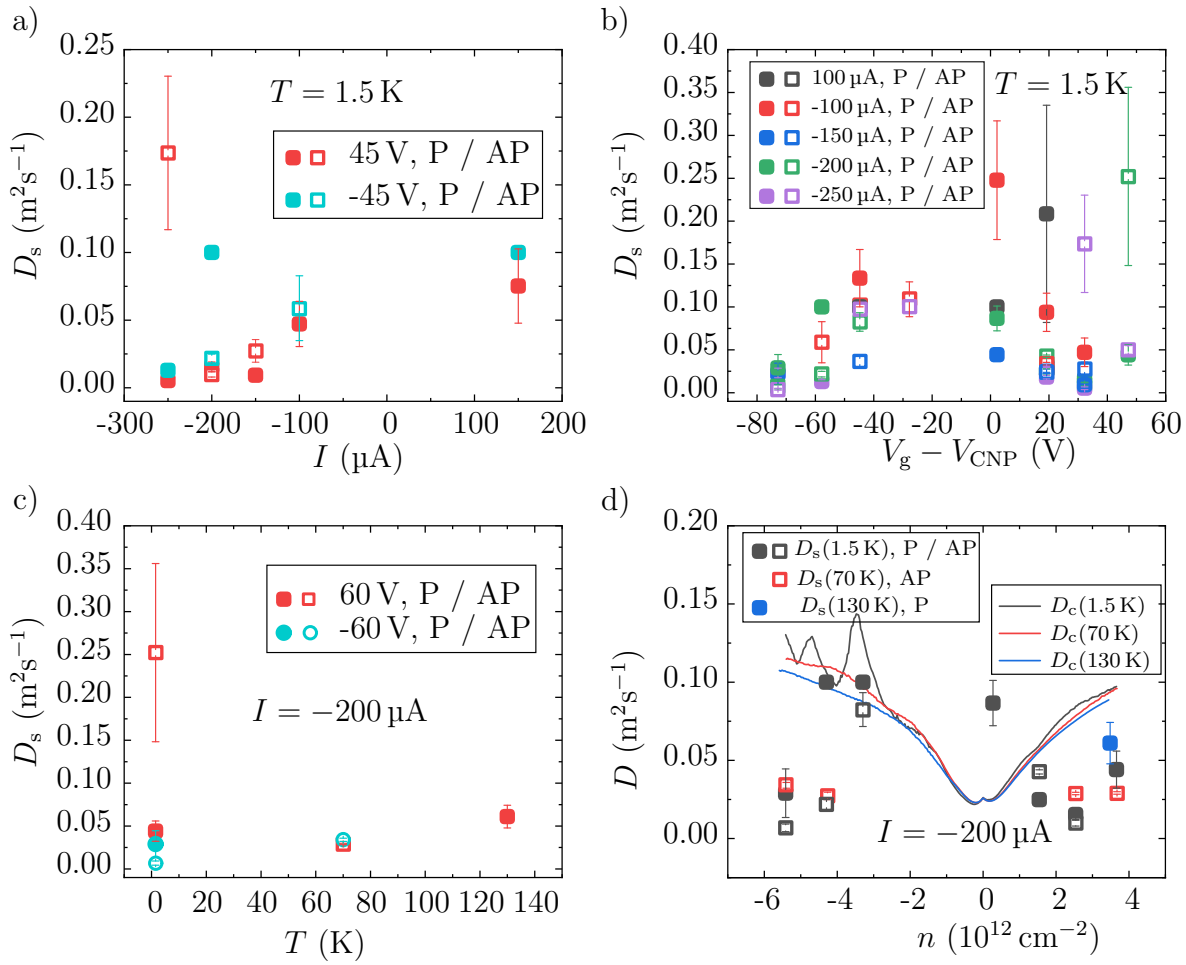

Fig. 7.32: The fit results of D_s shown as a function of current, back gate voltage and temperature in a), b), and c), respectively. Both, a) and b) are presented at a constant temperature of $T = 1.5\,\mathrm{K}$. a) and c) present the data for the electron and hole regime, while b) plots the fit results for various currents. d) Comparison of the charge and spin diffusion constants, D_c and D_s, respectively. The charge diffusion constant D_c is calculated as described in Sec. 6.1.2. The spin diffusion constant D_s is extracted from Hanle fits at a constant current of $I = -200\,\mu\mathrm{A}$.

measurements was observed, which could potentially be attributed to the significant noise in these measurements. Given that τ_s and D_s are subjected to large variations, the same also applies to the calculated spin diffusion length L_s. The temperature dependence of L_s is shown in the Appendix in Fig. A.8 b).

Magnetic moments

To investigate, whether magnetic moments can be attributed to the discrepancy in D_s and D_c, the obtained Hanle curves are fitted for P, τ_s, and $g_{L,\,para}$ in *Origin*. For all fits, the

diffusion constant was set to $D = D_c$ obtained from the charge transport measurements. The extracted values for $g_{L,\,para}$ are plotted against temperature at $V_g = \pm 60\,V$ and $I = -200\,\mu A$ in Fig. 7.33. Despite the absence of signatures of magnetic moments in the non-local signals, fitting for the g-factor yields increased g-factors $g_{L,\,para} > 2$. In the case of the anti-parallel configuration at $V_g = 60\,V$ and $T = 130\,K$, a g-factor of $g_{L,\,para} = 2.06$ was extracted, which would indicate the absence of magnetic moments. Moreover, the anti-parallel configuration at $V_g = \pm 60\,V$ and $T = 1.5\,K$ yielded values of $g_{L,\,para} \approx 1$, a result that cannot be explained by the model. Furthermore, Hanle signals could not be observed at certain temperatures and magnetic configurations, which considerably reduces the number of data points in Fig. 7.33. As a result, it is challenging to identify a correlation between the extracted values of $g_{L,\,para}$ and temperature, due to the significant errors associated with fitting to the noisy curves and the limited number of data points.

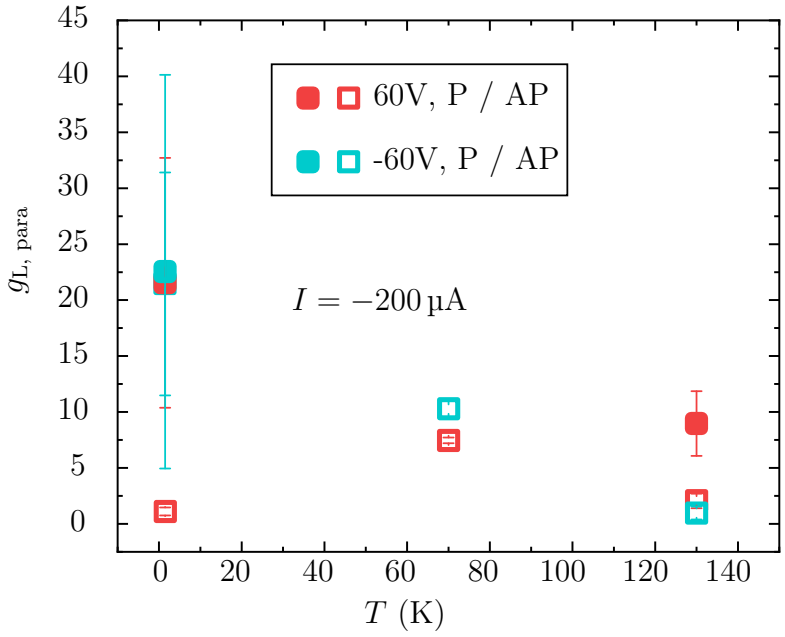

Fig. 7.33: Extracted values for $g_{L,\,para}$ plotted against the temperature at $V_g = \pm 60\,V$ and $I = -200\,\mu A$. $g_{L,\,para}$ is illustrated for both parallel and anti-parallel configurations as filled and open boxes, respectively.

Summary Hanle Sample B

In conclusion, the Hanle effect was also demonstrated in Sample B, with curves showing opposite polarity in the parallel and anti-parallel magnetization alignment. As observed in the non-local spin valve measurements, the polarity is reversed with respect to the Hanle curves of Sample A. However, the presence of significant noise in the Hanle curves hinders the precise determination of the fitting values for P, τ_s, and D_s. The spin diffusion constant D_s is particularly sensitive to the exact shape of the curve. As a consequence of the substantial noise, satisfactory fits are achieved for a range of D_s values. Nevertheless, best fits to the measured Hanle data were presented, as the fit results still provide estimate values. With a varying spin injection efficiency ranging from $P = 1\,\%$ to $31\,\%$

with some outliers and a spin relaxation time from $\tau_s = 0.08\,\text{ns}$ up to $1.3\,\text{ns}$, the fit results are comparable to those from Sample A. The extracted values for the spin diffusion constant D_s exhibit a considerable scattering, with the majority of values falling within the range of $D_s = 0.004\,\text{m}^2\text{s}^{-1}$ to $0.13\,\text{m}^2\text{s}^{-1}$. Given the considerable noise, no statements about correlations of the fit parameters with applied bias, gate voltage or temperature can be made. Yet, also for Sample B the extracted D_s do not fit the calculated D_c for the majority of the values. However, it is challenging to ascertain whether this discrepancy is attributable to the imprecise fitting of the noisy curves or to potential magnetic moments, as postulated for Sample A. Even though fitting for an effective g-factor $g_{\text{L, para}}$ results in values $g_{\text{L, para}} > 2$, no signatures of magnetic moments were observed in the non-local spin valve measurements. Furthermore, the height of the Hanle curve $\Delta R_{\text{nl, Hanle}}$ matches the spin valve height $\Delta R_{\text{nl, SV}}$ perfectly. Both observations are incompatible with the hypothesis of the presence of magnetic moments and suggest a clean Sample B.

8. Summary

This thesis demonstrates spin injection, transport and detection in all-2D van der Waals heterostructures comprising of monolayer graphene, hBN, and FGT. Non-local spin valve and Hanle measurements were performed on two very similar samples, designated as A and B. Prior to the spin transport experiments, an in-depth characterization of each building block of the samples was conducted. The spin-injecting electrodes of both samples exhibited a rectangular anomalous Hall loop, demonstrating sharp magnetization switching in one domain. As a consequence of significant Joule heating at large applied currents, a minimum Curie temperature of $T_\mathrm{C} = 188\,\mathrm{K}$ was extracted for Sample A. For both samples, the mobility of graphene was determined to be $\mu_\mathrm{m} \approx 10000\,\frac{\mathrm{cm}^2}{\mathrm{Vs}}$. Furthermore, the hBN tunnel barrier was characterized using AFM and electrical measurements, which revealed a two- to three-layer thick hBN in both samples, enabling efficient tunnelling.

Non-local spin valve signals of up to $\Delta R_\mathrm{nl} = 1.88\,\Omega$ clearly demonstrate efficient spin injection, transport, and detection. Clear phase coherent spin precession was observed in the non-local Hanle measurements. This enabled the extraction of the spin injection efficiency P together with the spin transport parameters τ_s and D_s. The spin signals ΔR_nl, together with the extracted spin injection efficiencies of up to $P \approx 40\,\%$ reported in this thesis, are significantly larger than those reported for FGT/graphene spin valve devices without tunnel barriers [31]. The current, back gate voltage, and temperature dependencies of the non-local spin valve signals of both samples exhibit comparable characteristics. It was observed that the spin valve signals decrease as the current increases from negative to positive values. The current dependence of P correlates with the signal height ΔR_nl. Consequently, the current dependency of the non-local signal ΔR_nl can be attributed to a current dependent spin injection efficiency P. The current dependency of ΔR_nl even leads to an inversion of the signal at high positive currents. Furthermore, the spin valve signal of Sample B is systematically inverted when interchanging the injector and detector electrode. The inversion of the spin signals in both cases may be attributed to a current-dependent inversion of the spin polarization at the Fermi level of the respective injecting FGT electrode. Furthermore, the spin valve height ΔR_nl is larger for positive gate voltages in the electron conduction regime and decreases with increasing temperature. The spin relaxation time was observed to be in the range of $\tau_\mathrm{s} = 0.1\,\mathrm{ns}$ to $1.3\,\mathrm{ns}$, while the spin diffusion constants are in the range of $D_\mathrm{s} = 0.0046\,\mathrm{m}^2\mathrm{s}^{-1}$ to $0.037\,\mathrm{m}^2\mathrm{s}^{-1}$. This is consistent with previous Hanle experiments in graphene-based devices utilizing conventional ferromagnets as spin-aligning electrodes [27,

30, 33]. However, no discernible current, temperature, or gate dependent behaviour of τ_s was observed, making any conclusions about the dominating spin relaxation mechanism elusive. Furthermore, the obtained spin diffusion constants D_s do not align with the charge diffusion constants D_c extracted from transport measurements in both samples. In order to elucidate this discrepancy, a number of potential mechanisms were considered and discussed via *COMSOL* simulations, including contact-induced spin relaxation, an anisotropy in the spin relaxation time, proximity effects, stray fields, and resonant scattering at magnetic moments. However, only resonant scattering at magnetic moments agrees with the experimental data. Magnetic moments, when present in the sample, introduce an additional exchange field, which in turn results in an increased spin precession. This results in a narrowing of the Hanle curve, which might account for the discrepancy between D_s and D_c. The presence of magnetic moments is consistent with the observation of a dip in the non-local spin signal ΔR_{nl} at low applied magnetic fields in the spin valve measurements, the discrepancy between the extracted non-local signal heights $\Delta R_{nl,\,SV}$ and $\Delta R_{nl,\,Hanle}$ of the spin valve and Hanle measurements, respectively, and an increasing temperature dependence of τ_s. Moreover, fitting for an effective g-factor results in $g_{L,\,para} > 2$, which is also characteristic of magnetic moments. The origin of these moments remains unclear but may be attributed to adsorbates on the graphene surface.

Outlook

In conclusion, the successful demonstration of efficient spin injection, transport, and detection in two all-van der Waals devices paves the way for future spin transport experiments in van der Waals heterostructures. Given that the Curie temperature of FGT is $T_C \approx 230\,K$, the experiments presented in this thesis were conducted at cryogenic temperatures. Nevertheless, the ever-growing family of 2D magnets, which includes Co-doped FGT, Fe_5GeTe_2, and Fe_3GaTe_2, already includes above-room-temperature ferromagnets [162, 195, 198]. The observation of spin valve signals at room-temperature in devices utilizing Co-doped FGT and Fe_5GeTe_2 in combination with conventional Co-electrodes [162, 195], indicates that 2D ferromagnets have the potential to be employed in future all-van der Waals spintronic applications. In conjunction with tunable spin-orbit coupling in graphene heterostructures [24, 135], spins can be controlled electrically. A spin transistor effect has recently been observed in a bilayer graphene/WSe_2 device with conventional Co/TiO_x contacts [199]. Here, the spin signal was observed to reverse as a function of a back gate voltage and drain current, due to spin precession in spin-orbit fields of the WSe_2. This could potentially facilitate the realization of an all-2D spin-orbit valve device, which would represent a Datta-Das-spin-FET consisting of only van der Waals materials [16, 200, 201]. The extensive versatility of the van der Waals materials makes them an optimal selection for future applications. The range of heterostructures that can be produced from these materials has yet to be fully exploited, making it a particularly promising avenue of future research.

A. Appendix

A.1. Characterization of the spin injecting electrode of Sample B

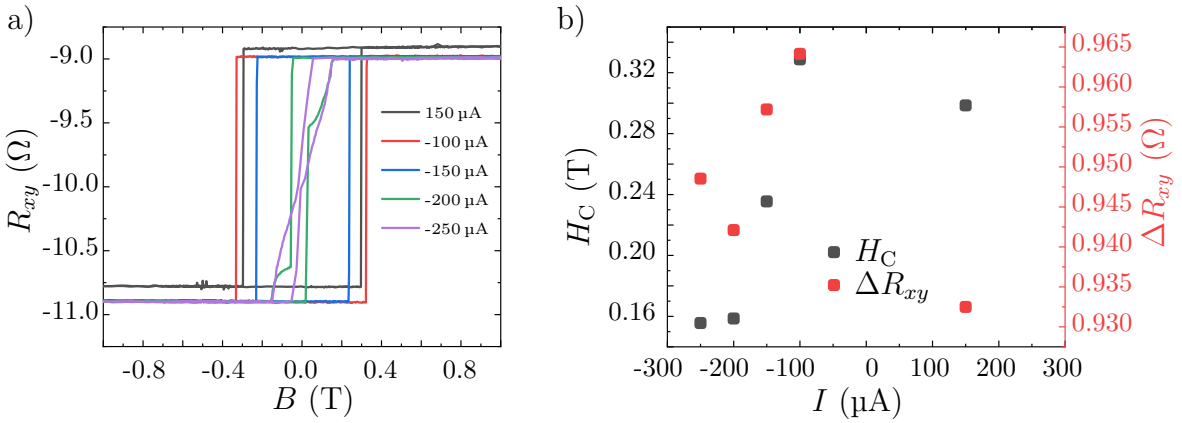

Fig. A.1: a) Magnetic hysteresis loops for the spin injecting electrode FGT_1 of Sample B at a temperature of $T = 1.5\,\mathrm{K}$ b) Current dependence of the coercive field and of the height of the hysteresis loops ΔR_{xy}.

The anomalous Hall effect has also been measured for the spin injecting electrode FGT_1 of Sample B. The magnetic hysteresis loops at a temperature of $T = 1.5\,\mathrm{K}$ at various applied currents can be seen in Fig. A.1 a). The hysteresis curves demonstrate a sharp one-domain switching of the magnetization for currents with absolute values below $|I| < 200\,\mu\mathrm{A}$. For a current of $I = -200\,\mu\mathrm{A}$, FGT is in an intermediate regime, exhibiting two-domain switching. One domain switches sharply, while the other exhibits a gradual alignment of its magnetization along the external field. At $I = -250\,\mu\mathrm{A}$, the magnetization only gradually aligns along the external field. This current-dependent behaviour can be well understood by considering Joule heating, that leads to heating of the FGT, thereby reducing its Curie temperature. The increase in the FGT temperature is accompanied by a reduction of the coercive fields and the height of the hysteresis loops. The coercive field exhibits a significant monotonic reduction, from 0.33 to 0.16 T, corresponding to a 51.5% reduction when increasing the negative currents from -100 to -250 µA. In the same current range, the height of the hysteresis loops ΔR_{xy} only reduces slightly, from 0.96 to 0.94 Ω. However, this reduction is not monotonic, with ΔR_{xy} being larger for

-250 µA than for -200 µA. As the hysteresis loops are quite symmetric, the exchange bias H_E is small, ranging from -3.75 to 4.85 mT. Unfortunately, the contacts to the FGT ceased to function after the measurements at $T = 1.5$ K, preventing the measurement of a temperature dependence of the anomalous Hall effect. Consequently, the determination of the Curie temperature is not possible for any of the FGT electrodes of Sample B.

A.2. FGT/FGT Homojunctions

An optical micrograph of the second FGT/FGT homojunction sample can be seen in Fig. A.2 a). Blue and pink lines show contours of the top and bottom FGT flakes, respectively. During the lift-off process some contacts were destroyed. Fig. A.2 b) shows the absolute value of $|\Delta R_{\mathrm{L,\ low/high}}|$ at different temperatures. Since the low resistance state height is negative, the absolute values are compared. It can be seen, that the low resistance state is always smaller than the high resistance state by 0.5 to 2 Ω. The reason for this asymmetry in the low and high resistance states is the asymmetry of the slopes in the up- and down-sweeps of the ↑↑ and ↓↓ configurations, as can be seen in Fig. 5.8 b) for instance. This leads to a slight overestimation of $\Delta R_{\mathrm{L,\ high}}$.

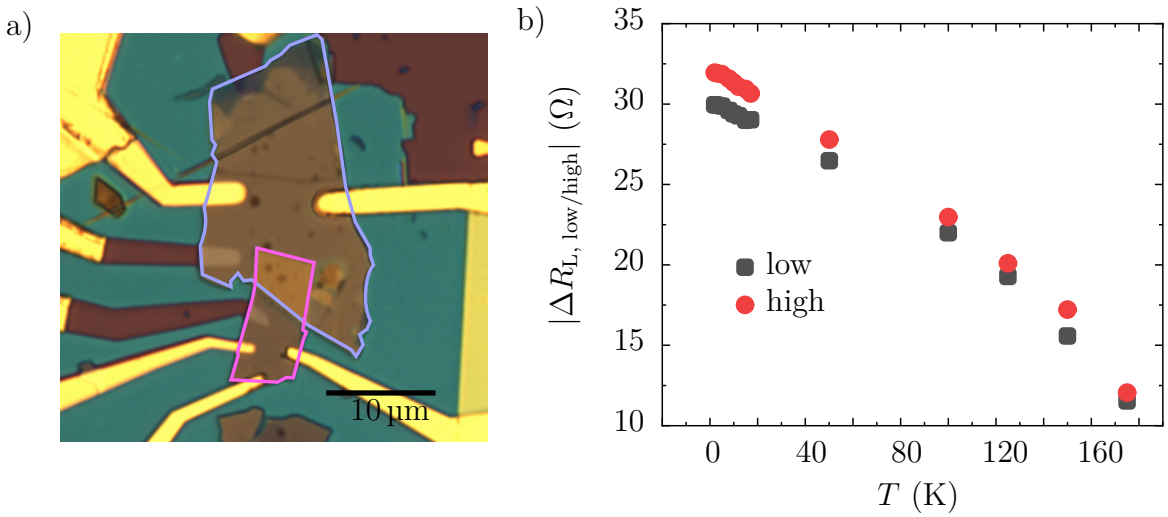

Fig. A.2: a) Optical image of the second FGT/FGT homojunction. Here, the top FGT (blue) with a thickness of 21 nm has a higher coercive field than the bottom FGT (pink) with a thickness of 22.4 nm. During the lift-off process some contacts ripped off. The black bar indicates 10 µm. b) Comparison of the low and high resistance state heights at different temperatures at a current of $I = 100$ µA of the sample illustrated in Fig. 5.8 a).

Fig. A.3 a) and b) show the magnetic field sweeps of the longitudinal two-terminal resistances of the top and bottom FGT flake, respectively, of the FGT/FGT homojunction sample shown in Fig. A.2 a), resulting in the butterfly-shaped hysteresis. The signal increases linearly with a constant slope up to the coercive field. At the coercive fields of

each FGT flake, the longitudinal resistances abruptly decrease. At magnetic fields larger than the coercive field, the signal decreases with a reversed slope. This has also been observed in Ref. [173] and is expected for most ferromagnetic systems [143].

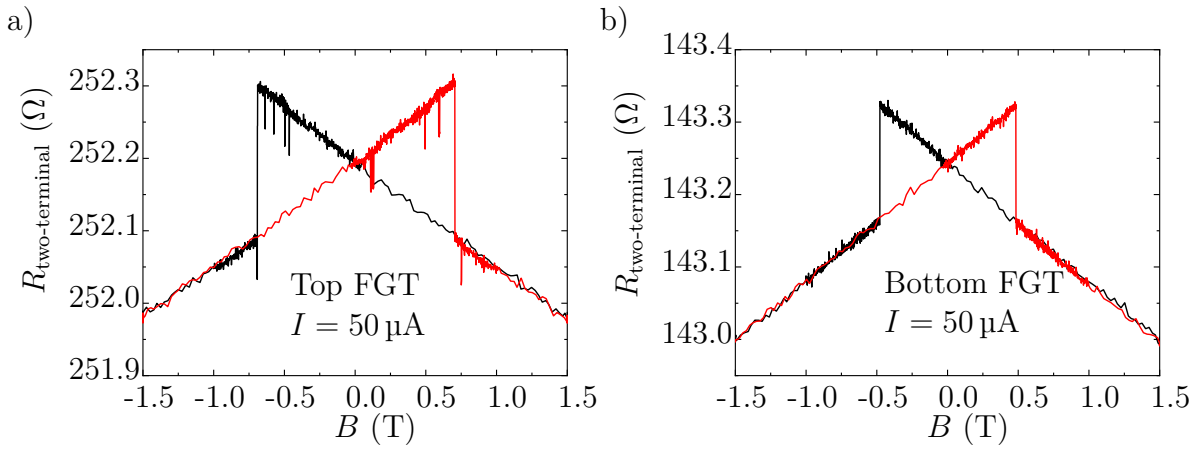

Fig. A.3: Up (red) and down (black) magnetic field sweeps of the two-terminal longitudinal resistance of a) the top and b) the bottom FGT flake of the second sample, that can be seen in Fig. A.2 a). At the corresponding coercive fields the resistances abruptly decrease. Afterwards, the slope of the signal is reversed.

It should be noted that only a few fabricated FGT/FGT homojunctions exhibited decoupled magnetizations in both FGT flakes. Although all samples were fabricated in the same way, interface contaminations cannot be ruled out as a possible cause of this phenomenon. Bubbles are visible at the overlapping areas of both homojunction samples, as shown in Fig. 5.8 a) and Fig. A.2 a). A very clean FGT/FGT interface could lead to a coupling of the magnetizations. Furthermore, a twisting angle between both FGT flakes could potentially lead to decoupled magnetizations.

A.3. Graphene characterization

A.3.1. Graphene characterization of Sample B

Sample B was characterized analogously to Sample A. In Fig. A.4 a) the Dirac measurement can be seen. The charge neutrality point fluctuates by 3 V, from $V_{\text{CNP}}(1.5\,\text{K}) = 11\,\text{V}$ to $V_{\text{CNP}}(130\,\text{K}) = 14\,\text{V}$. The charge neutrality point is centered at positive gate voltages, indicating a p-type doping. The shift of the charge neutrality point might be attributed to a temperature dependent adsorbate concentration on the graphene. Other than that, the resistivity is not temperature independent in the examined temperature range. Fig. A.4 b) shows the conductivity of Sample B with the corresponding linear fits leading to hole

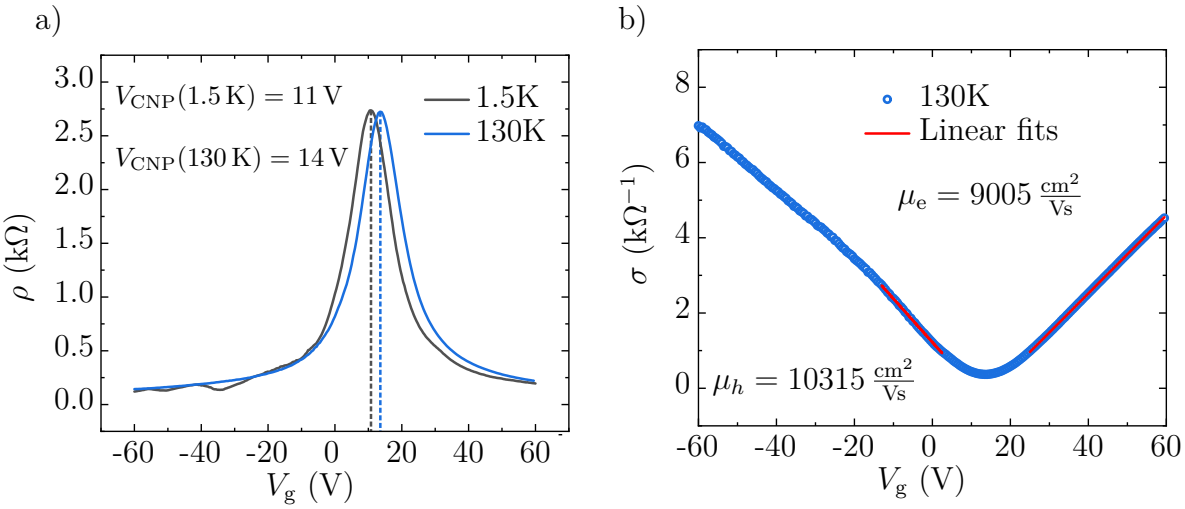

Fig. A.4: a) Back gate voltage dependence of the resistivity of Sample B at 1.5 K (grey curve) and 130 K (blue curve). The resistivity shows a slight shift of the charge neutrality point from $V_{CNP} = 11\,V$ at 1.5 K to $V_{CNP} = 14\,V$ at 130 K, indicating a p-type doping of the graphene. b) Conductivity of Sample B as a function of the applied back gate voltage at $T = 130\,K$. Mobilities were calculated from the linear fits (red).

and electron mobilities of $\mu_h = 10315\,\frac{cm^2}{Vs}$ and $\mu_e = 9005\,\frac{cm^2}{Vs}$, which is quite similar to Sample A. In Fig. A.5 the calculated charge diffusion constant D_c can be seen as a function of n and V_g. For Sample B, no Hall measurements were conducted. D_c varies from $D_{c,\,Dirac} = 0.023 - 0.107\,m^2s^{-1}$ which is similar to Sample A. As mentioned in the main text in Sec. 6.1.2, the charge diffusion constant D_c can also be determined from the mean-free-path $l_{mfp} = \mu_e \frac{h}{e}(\frac{\pi}{n})^{-\frac{1}{2}}$ with $D_C = \frac{1}{2} l_{mfp} v_F$, where h is the Planck's constant, e is the elementary charge, and v_F is the Fermi velocity, resulting in similar values.

A.3.2. Hall measurements of Sample A

For the Hall measurements presented in Fig. 6.2 b), Sample A was cooled down for a third time. The Hall measurements were conducted on different contacts than the Dirac measurements discussed in Sec. 6.1. This was due to some contacts failing during the non-local spin valve and Hanle measurements. A constant AC voltage bias $V_{ds} = 0.5\,V$ was applied at a pre-resistance of $R_{PRE} = 1\,M\Omega$, using one channel of the Synktek MCL1-540 multi-channel Lock-In. This ensures a constant AC current through the sample. This current is applied from contact 19 to contact 4. All measurements were taken at an AC frequency of $f = 13\,Hz$. The longitudinal voltage was measured from contact 17 to 16 (just like in the Dirac measurements) and the transversal voltage was measured from contact 2 to 17. These voltages were measured using two separate Lock-In channels of the Synktek system. The magnetic field was applied perpendicular to the graphene plane. Sweeping the external magnetic field at a constant back gate voltage V_g

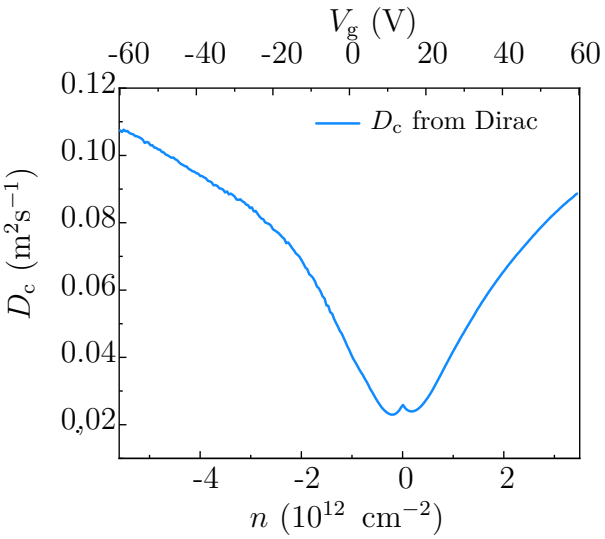

Fig. A.5: Charge diffusion constant for Sample B calculated from Dirac measurements as a function of charge carrier density n and gate voltage V_g. An energy broadening $\xi = 75\,\text{meV}$ was used in the calculations.

and a constant current while measuring the transversal voltage resulted in the curves shown in Fig. 6.2 b).

A.4. Hanle fitting function

The following section presents the Hanle fitting function, which was employed in the *Origin* software. The Hanle curves are described in accordance with the depicted geometry in Fig. 3.5, wherein the external magnetic field is oriented in y-direction, while spins diffuse in the x-direction and the ferromagnetic electrodes are magnetized in z-direction. The solution to the steady-state spin drift-diffusion equation Eq. (3.29) can be obtained by solving for each spin component, s_x, s_y, and s_z, with the boundary conditions of a vanishing spin density at the far end of the NM ($s_x(\infty) = s_y(\infty) = s_z(\infty) = 0$). Moreover, only spins in z-direction are injected into the NM, given that the FGT magnetization is out-of-plane so that

$$\begin{aligned} -v_\mathrm{d} s_x'(0) + D_\mathrm{s} s_x'(0) &= 0, \\ -v_\mathrm{d} s_y'(0) + D_\mathrm{s} s_y'(0) &= 0, \\ -v_\mathrm{d} s_z'(0) + D_\mathrm{s} s_z'(0) &= j_{s0}/e, \end{aligned} \tag{A.1}$$

where v_d is the drift velocity. As we are interested in the steady-state solution of the spin drift-diffusion equation, time derivatives are zero. Solving for the z-component with an exponential ansatz results in the following solution [17]

$$s_z(d) = -\frac{j_{s0} L_\mathrm{s}}{e D_\mathrm{s}} \exp^{-\alpha_1 d/L_\mathrm{s}} \left[\frac{2\kappa + \alpha_1}{(2\kappa+\alpha_1)^2 + \alpha_2^2} \cos\left(\frac{\alpha_2}{L_\mathrm{s}} d\right) - \frac{\alpha_2}{(2\kappa+\alpha_1)^2 + \alpha_2^2} \sin\left(\frac{\alpha_2}{L_\mathrm{s}} d\right) \right]. \tag{A.2}$$

Here, the dimensionless parameter $\kappa = \frac{v_\mathrm{d}\tau_\mathrm{s}}{2L_\mathrm{s}}$ describes the ratio of drift and diffusion. In the diffusion regime $\kappa \ll 1$, and is assumed to be zero in the presented fits. The parameters α_1 and α_2 take the effective spin relaxation and the effective spin precession into account, respectively, and are defined as

$$\begin{aligned}\alpha_1 &= \frac{1}{\sqrt{2}}\sqrt{1+\kappa^2+\sqrt{(1+\kappa^2)^2+(\omega_0\tau_\mathrm{s})^2}} - \kappa \\ \alpha_2 &= \frac{1}{\sqrt{2}}\sqrt{-1-\kappa^2+\sqrt{(1+\kappa^2)^2+(\omega_0\tau_\mathrm{s})^2}}.\end{aligned} \tag{A.3}$$

As the measured voltage is fitted, the spin density must be converted into a voltage following Eq. (3.43). Given that only half of the spins diffuse to the detector, the result must be divided by two. The pre-factor of Eq. (A.2), when multiplied by the conversion factor, yields

$$V_0 = \frac{P_\mathrm{inj}P_\mathrm{det}IR_\mathrm{s}L_\mathrm{s}}{2w} \tag{A.4}$$

A.4.1. Fitting function with finite injector and detector width

In order to account for the finite width of the injector and detector, it is necessary to substitute the distance d with $d = x_2 - x_1$ in Eq. (A.2), where x_2 and x_1 mark the position of spin detection and injection, respectively. Subsequently, an integration of x_2 and x_1 is performed over the detector and injector width, w_det and w_inj, respectively. This results in

$$\begin{aligned}V_z(x_2-x_1) = \int_{d-w_\mathrm{det}}^{d+w_\mathrm{det}} \int_{\frac{-w_\mathrm{inj}}{2}}^{\frac{w_\mathrm{inj}}{2}} V_0 \exp^{\frac{-\alpha_1(x_2-x_1)}{L_\mathrm{s}}} \Big[A_A \cos\Big(\frac{\alpha_2}{L_\mathrm{s}}(x_2-x_1)\Big) \\ -B_B \sin\Big(\frac{\alpha_2}{L_\mathrm{s}}(x_2-x_1)\Big)\Big]\, dx_1 dx_2.\end{aligned} \tag{A.5}$$

The pre-factors of the cosine and sine functions are identical to those in Eq. (A.2), and are represented as A_A and B_B, respectively. The calculation of the two integrals yields in the final fitting function

$$
\begin{aligned}
V_z(d, w_{\mathrm{inj}}, w_{\mathrm{det}}) =& \frac{V_0 F_1^2}{w_{\mathrm{inj}} w_{\mathrm{det}}} \Bigg[\Big(A_A - B_B \cdot r \Big) \cdot \\
& \cdot \Bigg[\exp(-a(m-l))[\cos(b(m-l)) - r\sin(b(m-l))] \\
& - \exp\left(-a(n-l)\right)\left[\cos\left(b(n-l)\right) - r\sin\left(b(n-l)\right)\right] \\
& - \exp\left(-a(m-k)\right)\left[\cos\left((b(m-k)\right) - r\sin\left(b(m-k)\right)\right] \\
& + \exp(-a(n-k))[\cos(b(n-k)) - r\sin(b(n-k))] \Bigg] \\
& + \Big(B_B + A_A \cdot r \Big) \Bigg[\exp(-a(n-l))[\sin(b(n-l)) + r\cos(b(n-l))] \\
& - \exp(-a(m-l))[\sin(b(m-l)) + r\cos(b(m-l))] \\
& - \exp(-a(n-k))[\sin(b(n-k)) + r\cos(b(n-k))] \\
& + \exp(-a(m-k))[\sin(b(m-k)) + r\cos(b(m-k))] \Bigg] \Bigg],
\end{aligned}
\tag{A.6}
$$

where the following abbreviations where used:

$$
\begin{aligned}
A_A =& \frac{2\kappa + \alpha_1}{(2\kappa + \alpha_1)^2 + \alpha_2^2} \\
B_B =& \frac{\alpha_2}{(2\kappa + \alpha_1)^2 + \alpha_2^2} \\
a =& \frac{\alpha_1}{L_{\mathrm{s}}} \\
b =& \frac{\alpha_2}{L_{\mathrm{s}}} \\
r =& \frac{b}{a} \\
F_1 =& -\frac{1}{a(1+r^2)} \\
k =& -\frac{w_{\mathrm{inj}}}{2} \\
l =& \frac{w_{\mathrm{inj}}}{2} \\
m =& \frac{d - w_{\mathrm{det}}}{2} \\
n =& \frac{d + w_{\mathrm{det}}}{2}
\end{aligned}
\tag{A.7}
$$

A.5. Non-local spin transport experiments

A.5.1. Sample A: Non-local spin valve measurements with switched injector and detector

Additionally, non-local spin valve signals were also measured in the switched configuration at $T = 1.5\,\mathrm{K}$, as illustrated in Fig. A.6. In this switched configuration, the spin valve signals were markedly lower than in the other configuration and not discernible at all gate and currents applied. The spin valve height of the measurement shown in Fig. A.6 calculates to $\Delta R_{\mathrm{nl,\,switched}} = 0.12\,\Omega$ at $I = -250\,\mu\mathrm{A}$, $V_\mathrm{g} = 45\,\mathrm{V}$, and $T = 1.5\,\mathrm{K}$. In comparison, the normal configuration exhibited a spin valve signal of $\Delta R_\mathrm{nl} = 1.88\,\Omega$ for the same set of parameters, which simultaneously was the largest spin valve signal measured. Consequently, the non-local spin valve signal was fully characterized in the configuration as illustrated in Fig. 4.7.

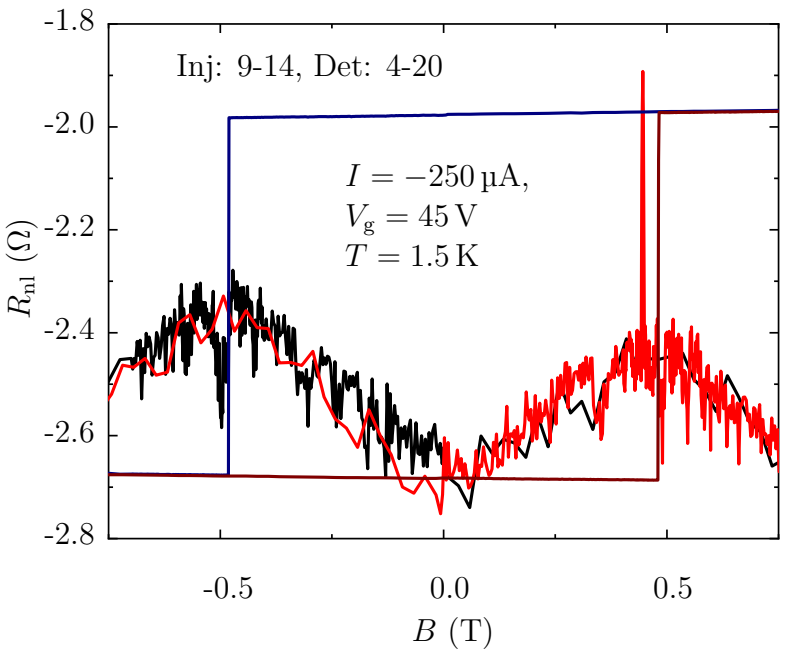

Fig. A.6: Non-local spin valve measurement of Sample A with switched injector and detector. The spins are injected from contact 9 to 14 and the non-local voltage is measured at contacts 4 to 19.

A.5.2. Sample A: Hanle measurements at 200 µA

The Hanle curve at $T = 100\,\mathrm{K}$, $V_\mathrm{g} = 45\,\mathrm{V}$, and $I = 200\,\mu\mathrm{A}$ for Sample A is presented in Fig. A.7 as a grey line. The signal-to-noise ratio of this curve is significantly lower than that of Hanle curves measured at other currents at the same gate voltage and temperature. Consequently, it is not shown in Fig. 7.31 a) for improved visual clarity.

The fit to the Hanle curve is illustrated as a red line, which shows good agreement with the experimental data.

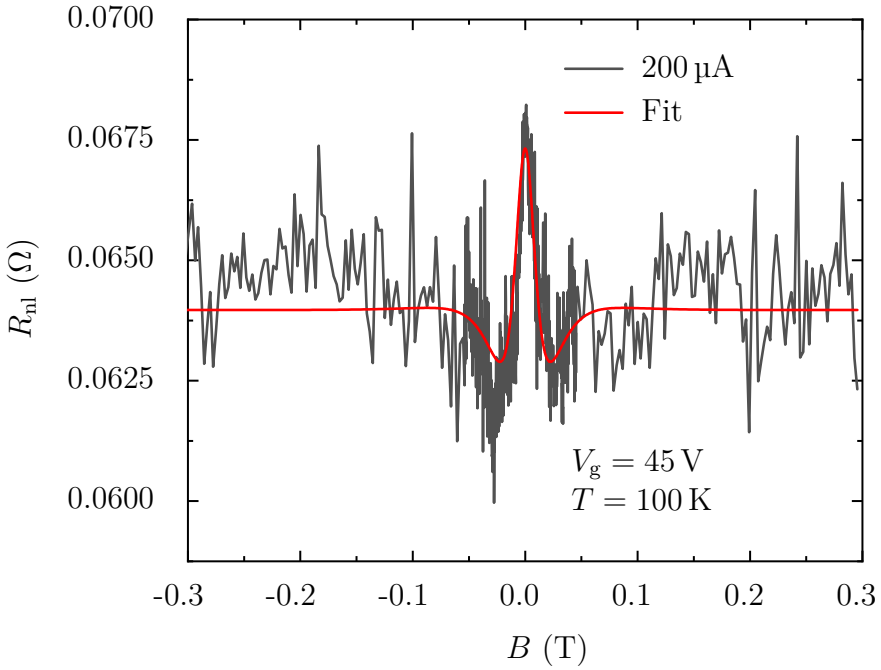

Fig. A.7: Hanle measurement of Sample A at $T = 100\,\mathrm{K}$, $V_g = 45\,\mathrm{V}$, and $I = 200\,\mu\mathrm{A}$ in grey, with the corresponding fit in red. The Hanle curve exhibits a significant lower signal-to-noise ratio and is therefore not shown in the comparison of the Hanle curves in Fig. 7.31 a)

A.5.3. Spin diffusion length L_s

The spin diffusion length is plotted against the temperature for Sample A and Sample B in Fig. A.8 a) and b), respectively. It is plotted for the same set of parameters as in Fig. 7.19 f) and Fig. 7.31 f). In Fig. A.8 a) the increasing trend of L_s with respect to temperature for temperatures larger than 50 K is observed for both the hole and electron conduction regime. For Sample B, L_s varies significantly which can be attributed to the large variation in D_s as a result of fitting to the noisy Hanle curves.

A.6. DFT calculations

The following details on the DFT calculations were provided by Dr. Klaus Zollner. The FGT/hBN/hBN/graphene supercell was set-up with the *atomic simulation environment*

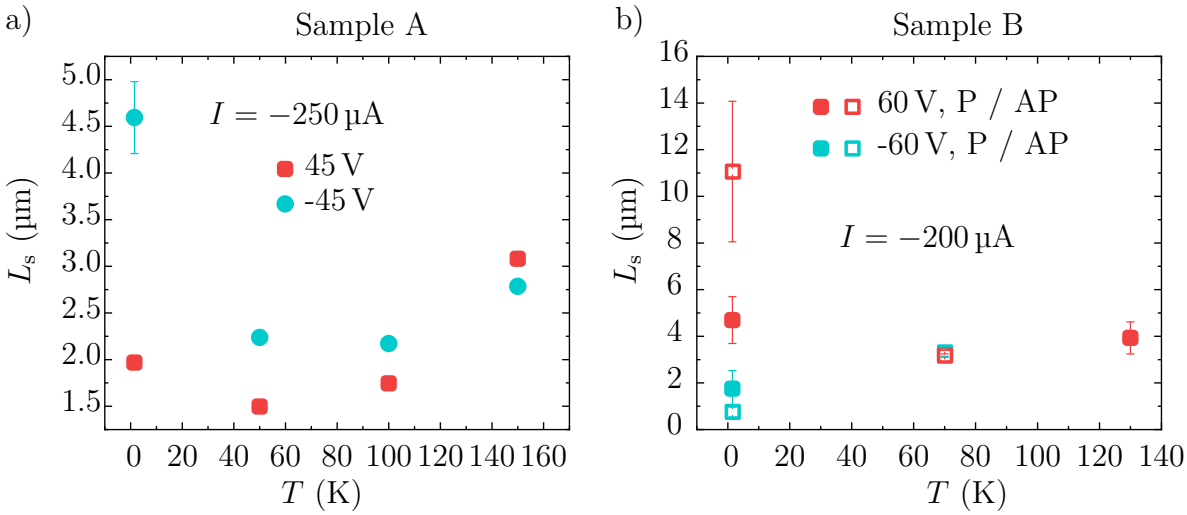

Fig. A.8: The spin diffusion length of a) Sample A and b) Sample B is plotted against the temperature.

(ASE) [202] and the *CellMatch* code [203], implementing the coincidence lattice method [204, 205]. The lattice constant of FGT within the heterostructure was defined as 3.991 Å [61], while the graphene and hBN layers are exposed to a biaxially strain, resulting in a lattice constant of 2.423 Å. Therefore, the individual monolayers are barely strained in the simulated heterostructure, enabling a reliable extraction of band offsets as well as proximity exchange effects on Dirac states. In order to prevent interactions between periodic images in the utilized slab geometry, a vacuum of about 20 Å was added to simulate this quasi-2D system.

The electronic structure calculations and structural relaxations of the heterostructure were performed by DFT [206] with *Quantum ESPRESSO* [207]. For self-consistent calculations a k-point sampling of $24 \times 24 \times 1$ was utilized. The spin-polarized ground state of the FGT monolayer was calculated utilizing open shell calculations. For this, an energy cut-off for charge density of 1400 Ry and a kinetic energy cut-off for wavefunctions of 130 Ry was applied for the scalar relativistic pseudopotentials with the projector augmented wave method with the Perdew-Zunger local density approximation (LDA). Using the LDA results in calculated magnetic moments close to experimental values [64]. For example, 1.69 μ_B/Fe was calculated, while experiments find 1.625 μ_B/Fe [208]. The relaxation of the heterostructures was performed adding DFT-D2 vdW corrections [209–212] and a quasi-Newton algorithm based on the trust radius procedure. During relaxation, FGT atoms are allowed to move freely within the heterostructure geometry, while graphene and hBN atoms are fixed. The heterostructure is fully relaxed when every component of each force is below $1 \cdot 10^{-3}$ [Ry/a_0], with a_0 being the Bohr radius.

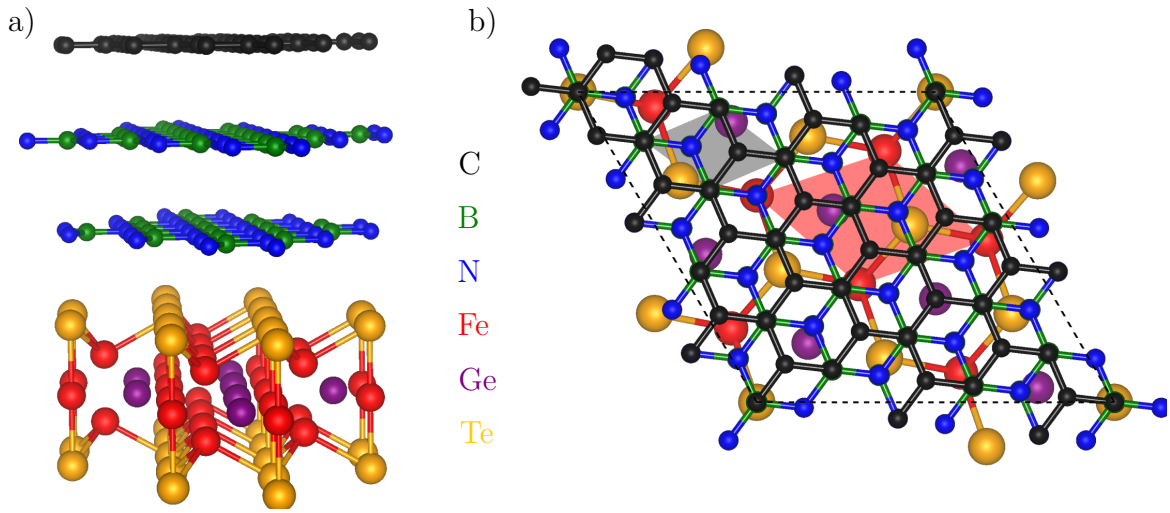

Fig. A.9: a) Top and b) side view of the FGT/hBN/hBN heterostructure. The supercell consists of 156 atoms and a lattice constant of 10.559 Å. The relaxed interlayer distance between the lower hBN layer and the adjacent Te layer of the FGT is $d_{\text{inter}} = 3.161$ Å. The remaining interlayer distances are fixed to 3.3 Å. The hBN is stacked as AA' and the graphene/hBN (FGT) unit cell are indicated by the grey (red) shaded area. This figure was provided by Dr. Klaus Zollner.

A.7. Samples after measurements

During the measurement of the non-local spin valve and Hanle measurements, large currents of up to $I = -250\,\mu\text{A}$ were applied. In the case of small contact areas of the Ti/Au wiring with graphene and FGT, this results in significant local current densities. This can result in damage to the wiring and even the flakes themselves, as illustrated in Fig. A.10 a) and b), which present micrographs of Sample A and B after the measurements, respectively. In these images, it can be seen that the wiring has been severely damaged, with entire pieces missing, and that parts of the FGT flakes have also been lost. In order to avoid this, it is necessary to maximize the contact areas, in order to reduce the current densities.

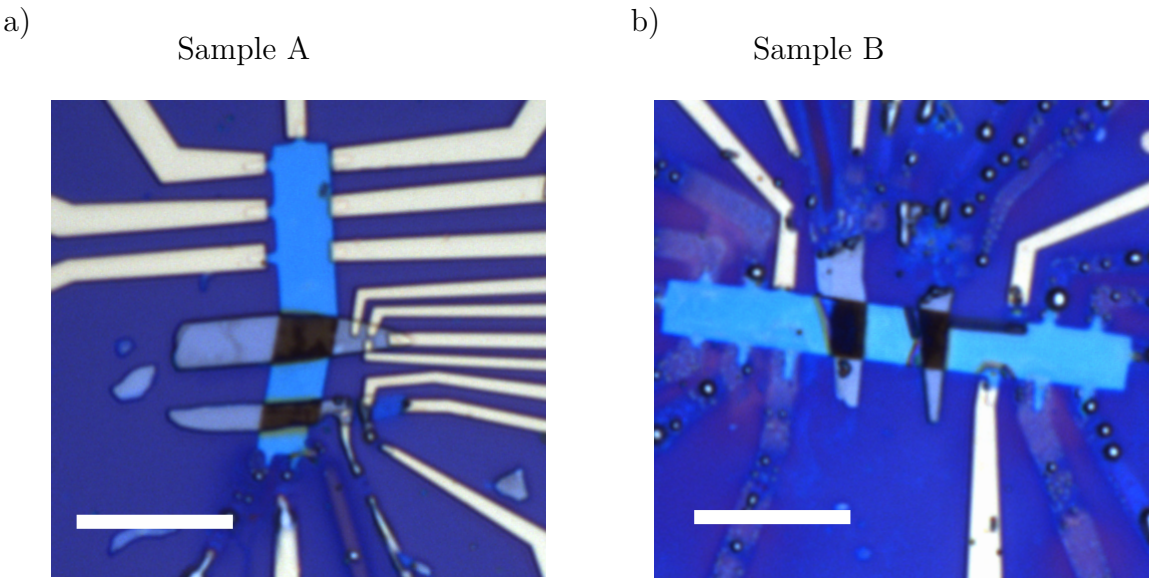

Fig. A.10: Micrographs of a) Sample A and b) Sample B after the measurements. In both samples the wiring is damaged and even some parts of the FGT flakes are missing. The white bar indicates 10 µm.

Bibliography

[1]W. Demtröder, *Experimentalphysik 4: Kern-, Teilchen- und Astrophysik* (Springer Berlin, Berlin, 2017).

[2]P. Y. Bruice, *Organische Chemie*, 8., aktualisierte Auflage (Pearson, München, 2022).

[3]H. Riebeek, *The Carbon Cycle*, edited by NASA Earth Observatory, (2011) `https://earthobservatory.nasa.gov/features/CarbonCycle` (visited on 09/10/2024).

[4]G. P. Bulanova, "The formation of diamond", Journal of Geochemical Exploration **53**, 1–23 (1995).

[5]M. Razeghi, *The mystery of carbon* (IOP Publishing, 2020).

[6]N. Savage, "Materials science: Super carbon", Nature **483**, S30–1 (2012).

[7]K. S. Novoselov, A. K. Geim, S. V. Morozov, D. Jiang, Y. Zhang, S. V. Dubonos, I. V. Grigorieva, and A. A. Firsov, "Electric field effect in atomically thin carbon films", Science (New York, N.Y.) **306**, 666–669 (2004).

[8]M. I. Katsnelson, *Graphene: Carbon in two dimensions* (Cambridge University Press, Cambridge and New York, 2012).

[9]G. E. Moore, "Cramming more components onto integrated circuits, Reprinted from Electronics, volume 38, number 8, April 19, 1965, pp.114 ff", IEEE Solid-State Circuits Society Newsletter **11**, 33–35 (2006).

[10]D. A. Padua, *Encyclopedia of parallel computing*, Vol. n4 (Springer, New York, N.Y., 2011).

[11]S. M. Thompson, "The discovery, development and future of GMR: The Nobel Prize 2007", Journal of Physics D: Applied Physics **41**, 093001 (2008).

[12]M. Julliere, "Tunneling between ferromagnetic films", Physics Letters A **54**, 225–226 (1975).

[13]G. Binasch, P. Grünberg, F. Saurenbach, and W. Zinn, "Enhanced magnetoresistance in layered magnetic structures with antiferromagnetic interlayer exchange", Phys. Rev. B **39**, 4828–4830 (1989).

[14]M. N. Baibich, J. M. Broto, A. Fert, D. F. van Nguyen, F. Petroff, P. Etienne, G. Creuzet, A. Friederich, and J. Chazelas, "Giant magnetoresistance of (001)Fe/(001)Cr magnetic superlattices", Physical Review Letters **61**, 2472–2475 (1988).

[15]T. Schäpers, *Semiconductor spintronics*, De Gruyter Graduate (De Gruyter, Berlin and Boston, 2016).

[16]S. Datta and B. Das, "Electronic analog of the electro-optic modulator", Applied Physics Letters **56**, 665–667 (1990).

[17]J. Fabian, A. Matos-Abiague, C. Ertler, P. Stano, and I. Žutić, "Semiconductor spintronics", Acta Physica Slovaca. Reviews and Tutorials **57**, 75313 (2007).

[18]P. R. Hammar and M. Johnson, "Spin-dependent current transmission across a ferromagnet–insulator– two–dimensional electron gas junction", Applied Physics Letters **79**, 2591–2593 (2001).

[19]O. M. J. van 't Erve, A. T. Hanbicki, M. Holub, C. H. Li, C. Awo-Affouda, P. E. Thompson, and B. T. Jonker, "Electrical injection and detection of spin-polarized carriers in silicon in a lateral transport geometry", Applied Physics Letters **91**, 212109 (2007).

[20]X. Lou, C. Adelmann, S. A. Crooker, E. S. Garlid, J. Zhang, K. S. M. Reddy, S. D. Flexner, C. J. Palmstrøm, and P. A. Crowell, "Electrical detection of spin transport in lateral ferromagnet–semiconductor devices", Nature Physics **3**, 197–202 (2007).

[21]K. S. Novoselov, A. Mishchenko, A. Carvalho, and A. H. Castro Neto, "2D materials and van der Waals heterostructures", Science (New York, N.Y.) **353**, aac9439 (2016).

[22]A. Jorio, "Twistronics and the small-angle magic", Nature Materials **21**, 844–845 (2022).

[23]W. Han, R. K. Kawakami, M. Gmitra, and J. Fabian, "Graphene spintronics", Nature Nanotechnology **9**, 794–807 (2014).

[24]K. Zollner, S. M. João, B. K. Nikolić, and J. Fabian, "Twist- and gate-tunable proximity spin-orbit coupling, spin relaxation anisotropy, and charge-to-spin conversion in heterostructures of graphene and transition metal dichalcogenides", Phys. Rev. B **108**, 235166 (2023).

[25]T. Völkl, "Spin-Orbit Coupling in Functionalized Graphene", PhD thesis (Universität Regensburg, 2021).

[26]A. W. Cummings, J. H. Garcia, J. Fabian, and S. Roche, "Giant Spin Lifetime Anisotropy in Graphene Induced by Proximity Effects", Physical Review Letters **119**, 206601 (2017).

[27]S. Ringer, S. Hartl, M. Rosenauer, T. Völkl, M. Kadur, F. Hopperdietzel, D. Weiss, and J. Eroms, "Measuring anisotropic spin relaxation in graphene", Phys. Rev. B **97**, 205439 (2018).

[28]W. Yan, O. Txoperena, R. Llopis, H. Dery, L. E. Hueso, and F. Casanova, "A two-dimensional spin field-effect switch", Nature Communications **7**, 13372 (2016).

[29]A. Dankert and S. P. Dash, "Electrical gate control of spin current in van der Waals heterostructures at room temperature", Nature Communications **8**, 16093 (2017).

[30]N. Tombros, C. Jozsa, M. Popinciuc, H. T. Jonkman, and B. J. van Wees, "Electronic spin transport and spin precession in single graphene layers at room temperature", Nature **448**, 571–574 (2007).

[31]X. He, C. Zhang, D. Zheng, P. Li, J. Q. Xiao, and X. Zhang, "Nonlocal Spin Valves Based on Graphene/Fe_3GeTe_2 van der Waals Heterostructures", ACS Applied Materials & Interfaces **15**, 9649–9655 (2023).

[32]W. Han, K. Pi, K. M. McCreary, Y. Li, J. J. I. Wong, A. G. Swartz, and R. K. Kawakami, "Tunneling spin injection into single layer graphene", Physical Review Letters **105**, 167202 (2010).

[33]C. Józsa, T. Maassen, M. Popinciuc, P. J. Zomer, A. Veligura, H. T. Jonkman, and B. J. van Wees, "Linear scaling between momentum and spin scattering in graphene", Phys. Rev. B **80**, 241403 (2009).

[34]M. Drögeler, C. Franzen, F. Volmer, T. Pohlmann, L. Banszerus, M. Wolter, K. Watanabe, T. Taniguchi, C. Stampfer, and B. Beschoten, "Spin Lifetimes Exceeding 12 ns in Graphene Nonlocal Spin Valve Devices", Nano Letters **16**, 3533–3539 (2016).

[35]Q. H. Wang, A. Bedoya-Pinto, M. Blei, A. H. Dismukes, A. Hamo, S. Jenkins, M. Koperski, Y. Liu, Q.-C. Sun, E. J. Telford, H. H. Kim, M. Augustin, U. Vool, J.-X. Yin, L. H. Li, A. Falin, C. R. Dean, F. Casanova, R. F. L. Evans, M. Chshiev, A. Mishchenko, C. Petrovic, R. He, L. Zhao, A. W. Tsen, B. D. Gerardot, M. Brotons-Gisbert, Z. Guguchia, X. Roy, S. Tongay, Z. Wang, M. Z. Hasan, J. Wrachtrup, A. Yacoby, A. Fert, S. Parkin, K. S. Novoselov, P. Dai, L. Balicas, and E. J. G. Santos, "The Magnetic Genome of Two-Dimensional van der Waals Materials", ACS Nano **16**, 6960–7079 (2022).

[36]N. D. Mermin and H. Wagner, "Absence of Ferromagnetism or Antiferromagnetism in One- or Two-Dimensional Isotropic Heisenberg Models", Physical Review Letters **17**, 1133–1136 (1966).

[37]F. Huang, M. T. Kief, G. J. Mankey, and R. F. Willis, "Magnetism in the few-monolayers limit: A surface magneto-optic Kerr-effect study of the magnetic behavior of ultrathin films of Co, Ni, and Co-Ni alloys on Cu(100) and Cu(111)", Phys. rev. B **49**, 3962–3971 (1994).

[38]K. H. J. Buschow, *Magnetic materials: a handbook on the properties of magnetically ordered substances* (North-Holland Pub. Co. and Sole distributors for the U.S.A. and Canada, Elsevier North-Holland, Amsterdam and New York, 1993).

[39]P. Poulopoulos and K. Baberschke, "Magnetism in thin films", Journal of Physics: Condensed Matter **11**, 9495–9515 (1999).

[40]C. Gong, L. Li, Z. Li, H. Ji, A. Stern, Y. Xia, T. Cao, W. Bao, C. Wang, Y. Wang, Z. Q. Qiu, R. J. Cava, S. G. Louie, J. Xia, and X. Zhang, "Discovery of intrinsic ferromagnetism in two-dimensional van der Waals crystals", Nature **546**, 265–269 (2017).

[41]B. Huang, G. Clark, E. Navarro-Moratalla, D. R. Klein, R. Cheng, K. L. Seyler, D. Zhong, E. Schmidgall, M. A. McGuire, D. H. Cobden, W. Yao, Di Xiao, P. Jarillo-Herrero, and X. Xu, "Layer-dependent ferromagnetism in a van der Waals crystal down to the monolayer limit", Nature **546**, 270–273 (2017).

[42]M.-W. Lin, H. L. Zhuang, J. Yan, T. Z. Ward, A. A. Puretzky, C. M. Rouleau, Z. Gai, L. Liang, V. Meunier, B. G. Sumpter, P. Ganesh, P. R. C. Kent, D. B. Geohegan, D. G. Mandrus, and K. Xiao, "Ultrathin nanosheets of $CrSiTe_3$: a semiconducting two-dimensional ferromagnetic material", Journal of Materials Chemistry C **4**, 315–322 (2016).

[43]J.-U. Lee, S. Lee, J. H. Ryoo, S. Kang, T. Y. Kim, P. Kim, C.-H. Park, J.-G. Park, and H. Cheong, "Ising-Type Magnetic Ordering in Atomically Thin $FePS_3$", Nano Letters **16**, 7433–7438 (2016).

[44]D. J. O'Hara, T. Zhu, A. H. Trout, A. S. Ahmed, Y. K. Luo, C. H. Lee, M. R. Brenner, S. Rajan, J. A. Gupta, D. W. McComb, and R. K. Kawakami, "Room Temperature Intrinsic Ferromagnetism in Epitaxial Manganese Selenide Films in the Monolayer Limit", Nano Letters **18**, 3125–3131 (2018).

[45]M. Bonilla, S. Kolekar, Y. Ma, H. C. Diaz, V. Kalappattil, R. Das, T. Eggers, H. R. Gutierrez, M.-H. Phan, and M. Batzill, "Strong room-temperature ferromagnetism in VSe_2 monolayers on van der Waals substrates", Nature Nanotechnology **13**, 289–293 (2018).

[46]C. Huang, J. Feng, F. Wu, D. Ahmed, B. Huang, H. Xiang, K. Deng, and E. Kan, "Toward Intrinsic Room-Temperature Ferromagnetism in Two-Dimensional Semiconductors", Journal of the American Chemical Society **140**, 11519–11525 (2018).

[47]W. Chen, Z. Sun, Z. Wang, L. Gu, X. Xu, S. Wu, and C. Gao, "Direct observation of van der Waals stacking-dependent interlayer magnetism", Science (New York, N.Y.) **366**, 983–987 (2019).

[48]C. Tan, J. Lee, S.-G. Jung, T. Park, S. Albarakati, J. Partridge, M. R. Field, D. G. McCulloch, L. Wang, and C. Lee, "Hard magnetic properties in nanoflake van der Waals Fe_3GeTe_2", Nature Communications **9**, 1554 (2018).

[49]D. Torelli and T. Olsen, "First principles Heisenberg models of 2D magnetic materials: the importance of quantum corrections to the exchange coupling", Journal of Physics: Condensed Matter **32**, 335802 (2020).

[50]M. Gibertini, M. Koperski, A. F. Morpurgo, and K. S. Novoselov, "Magnetic 2D materials and heterostructures", Nature Nanotechnology **14**, 408–419 (2019).

[51]S. Blundell, *Magnetism in condensed matter*, Oxford Master Series in Condensed Matter Physics 4 (OUP Oxford, 2001).

[52]R. Peierls, "On Ising's model of ferromagnetism", Mathematical Proceedings of the Cambridge Philosophical Society **32**, 477–481 (1936).

[53]L. Onsager, "Crystal Statistics. I. A Two-Dimensional Model with an Order-Disorder Transition", Physical Review **65**, 117–149 (1944).

[54]J. M. Kosterlitz and D. J. Thouless, "Ordering, metastability and phase transitions in two-dimensional systems", Journal of Physics C: Solid State Physics **6**, 1181–1203 (1973).

[55]V. L. Berezinskii, "Destruction of long-range order in one-dimensional and Destruction of long-range order in one-dimensional and two-dimensional systems having a continuous symmetry group 1. Classical systems.", Sov. Phys. JETP-USSR, 493–500 (1971).

[56]H. Kurebayashi, J. H. Garcia, S. Khan, J. Sinova, and S. Roche, "Magnetism, symmetry and spin transport in van der Waals layered systems", Nature Reviews Physics **4**, 150–166 (2022).

[57]Z. Fei, B. Huang, P. Malinowski, W. Wang, T. Song, J. Sanchez, W. Yao, Di Xiao, X. Zhu, A. F. May, W. Wu, D. H. Cobden, J.-H. Chu, and X. Xu, "Two-dimensional itinerant ferromagnetism in atomically thin Fe_3GeTe_2", Nature Materials **17**, 778–782 (2018).

[58]R. F. L. Evans, U. Atxitia, and R. W. Chantrell, "Quantitative simulation of temperature dependent magnetization dynamics and equilibrium properties of elemental ferromagnets", Physical Review B **91**, 144425 (2015).

[59]B. Liu, Y. Zou, S. Zhou, L. Zhang, Z. Wang, H. Li, Z. Qu, and Y. Zhang, "Critical behavior of the van der Waals bonded high T_C ferromagnet Fe_3GeTe_2", Scientific Reports **7**, 6184 (2017).

[60]J. M. D. Coey, *Magnetism and magnetic materials* (Cambridge University Press, Cambridge, 2010).

[61]H.-J. Deiseroth, K. Aleksandrov, C. Reiner, L. Kienle, and R. K. Kremer, "Fe_3GeTe_2 and Ni_3GeTe_2 – Two New Layered Transition–Metal Compounds: Crystal Structures, HRTEM Investigations, and Magnetic and Electrical Properties", European Journal of Inorganic Chemistry **2006**, 1561–1567 (2006).

[62]Y. Wu, Y. Hu, C. Wang, X. Zhou, X. Hou, W. Xia, Y. Zhang, J. Wang, Y. Ding, J. He, P. Dong, S. Bao, J. Wen, Y. Guo, K. Watanabe, T. Taniguchi, W. Ji, Z.-J. Wang, and J. Li, "Fe-Intercalation Dominated Ferromagnetism of van der Waals Fe_3GeTe_2", Advanced Materials **35**, 2302568 (2023).

[63]X. Xu, Y. W. Li, S. R. Duan, S. L. Zhang, Y. J. Chen, L. Kang, A. J. Liang, C. Chen, W. Xia, Y. Xu, P. Malinowski, X. D. Xu, J.-H. Chu, G. Li, Y. F. Guo, Z. K. Liu, L. X. Yang, and Y. L. Chen, "Signature for non-Stoner ferromagnetism in the van der Waals ferromagnet Fe_3GeTe_2", Physical Review B **101**, 201104 (2020).

[64]H. L. Zhuang, P. R. C. Kent, and R. G. Hennig, "Strong anisotropy and magnetostriction in the two-dimensional Stoner ferromagnet Fe_3GeTe_2", Physical Review B **93**, 134407 (2016).

[65]W. Xie, J. Zhang, Y. Bai, Y. Liu, H. Wang, P. Yu, J. Li, H. Chang, Z. Wang, F. Gao, G. Wei, W. Zhao, and T. Nie, "Air stability and composition evolution in van der Waals Fe_3GeTe_2", APL Materials **12**, 031102 (2024).

[66]Y. Li, X. Hu, A. Fereidouni, R. Basnet, K. Pandey, J. Wen, Y. Liu, H. Zheng, H. O. H. Churchill, J. Hu, A. K. Petford-Long, and C. Phatak, "Visualizing the Effect of Oxidation on Magnetic Domain Behavior of Nanoscale Fe_3GeTe_2 for Applications in Spintronics", ACS Applied Nano Materials **6**, 4390–4397 (2023).

[67]D. Kim, S. Park, J. Lee, J. Yoon, S. Joo, T. Kim, K.-J. Min, S.-Y. Park, C. Kim, K.-W. Moon, C. Lee, J. Hong, and C. Hwang, "Antiferromagnetic coupling of van der Waals ferromagnetic Fe_3GeTe_2", Nanotechnology **30**, 245701 (2019).

[68]J. Holler, L. Bauriedl, T. Korn, A. Seitz, F. Özyigit, M. Eichinger, C. Schüller, K. Watanabe, T. Taniguchi, C. Strunk, and N. Paradiso, "Air tightness of hBN encapsulation and its impact on Raman spectroscopy of van der Waals materials", 2D Materials **7**, 015012 (2020).

[69]K. Kim, J. Seo, E. Lee, K.-T. Ko, B. S. Kim, B. G. Jang, J. M. Ok, J. Lee, Y. J. Jo, W. Kang, J. H. Shim, C. Kim, H. W. Yeom, B. Il Min, B.-J. Yang, and J. S. Kim, "Large anomalous Hall current induced by topological nodal lines in a ferromagnetic van der Waals semimetal", Nature Materials **17**, 794–799 (2018).

[70]Y. Deng, Y. Yu, Y. Song, J. Zhang, N. Z. Wang, Z. Sun, Y. Yi, Y. Z. Wu, S. Wu, J. Zhu, J. Wang, X. H. Chen, and Y. Zhang, "Gate-tunable room-temperature ferromagnetism in two-dimensional Fe_3GeTe_2", Nature **563**, 94–99 (2018).

[71]X. Wang, J. Tang, X. Xia, C. He, J. Zhang, Y. Liu, C. Wan, C. Fang, C. Guo, W. Yang, Y. Guang, X. Zhang, H. Xu, J. Wei, M. Liao, X. Lu, J. Feng, X. Li, Y. Peng, H. Wei, R. Yang, D. Shi, X. Zhang, Z. Han, Z. Zhang, G. Zhang, G. Yu, and X. Han, "Current-driven magnetization switching in a van der Waals ferromagnet Fe_3GeTe_2", Science Advances **5**, eaaw8904 (2019).

[72]S. N. Kajale, T. Nguyen, C. A. Chao, D. C. Bono, A. Boonkird, M. Li, and D. Sarkar, "Current-induced switching of a van der Waals ferromagnet at room temperature", Nature Communications **15**, 1485 (2024).

[73]R. Fujimura, R. Yoshimi, M. Mogi, A. Tsukazaki, M. Kawamura, K. S. Takahashi, M. Kawasaki, and Y. Tokura, "Current-induced magnetization switching at charge-transferred interface between topological insulator $(Bi,Sb)_2Te_3$ and van der Waals ferromagnet Fe_3GeTe_2", Applied Physics Letters **119**, 032402 (2021).

[74]Z. Wang, D. Sapkota, T. Taniguchi, K. Watanabe, D. Mandrus, and A. F. Morpurgo, "Tunneling Spin Valves Based on Fe_3GeTe_2/hBN/Fe_3GeTe_2 van der Waals Heterostructures", Nano Letters **18**, 4303–4308 (2018).

[75]M. Piquemal-Banci, R. Galceran, S. Caneva, M.-B. Martin, R. S. Weatherup, P. R. Kidambi, K. Bouzehouane, S. Xavier, A. Anane, F. Petroff, A. Fert, J. Robertson, S. Hofmann, B. Dlubak, and P. Seneor, "Magnetic tunnel junctions with monolayer hexagonal boron nitride tunnel barriers", Applied Physics Letters **108**, 102404 (2016).

[76]M. Piquemal-Banci, R. Galceran, M.-B. Martin, F. Godel, A. Anane, F. Petroff, B. Dlubak, and P. Seneor, "2D-MTJs: introducing 2D materials in magnetic tunnel junctions", Journal of Physics D: Applied Physics **50**, 203002 (2017).

[77]A. Dankert, M. Venkata Kamalakar, A. Wajid, R. S. Patel, and S. P. Dash, "Tunnel magnetoresistance with atomically thin two-dimensional hexagonal boron nitride barriers", Nano Research **8**, 1357–1364 (2015).

[78]W. Wang, A. Narayan, L. Tang, K. Dolui, Y. Liu, X. Yuan, Y. Jin, Y. Wu, I. Rungger, S. Sanvito, and F. Xiu, "Spin-Valve Effect in NiFe/MoS_2/NiFe Junctions", Nano Letters **15**, 5261–5267 (2015).

[79]H.-C. Wu, C. Ó. Coileáin, M. Abid, O. Mauit, A. Syrlybekov, A. Khalid, H. Xu, R. Gatensby, J. Jing Wang, H. Liu, L. Yang, G. S. Duesberg, H.-Z. Zhang, M. Abid, and I. V. Shvets, "Spin-dependent transport properties of Fe_3O_4/MoS_2/Fe_3O_4 junctions", Scientific Reports **5**, 15984 (2015).

[80]M. Z. Iqbal, M. W. Iqbal, S. Siddique, M. F. Khan, and S. M. Ramay, "Room temperature spin valve effect in NiFe/WS_2/Co junctions", Scientific Reports **6**, 21038 (2016).

[81]L. Zhou, J. Huang, M. Tang, C. Qiu, F. Qin, C. Zhang, Z. Li, Di Wu, and H. Yuan, "Gate–tunable spin valve effect in Fe_3GeTe_2 –based van der Waals heterostructures", InfoMat **5**, e12371 (2023).

[82]H. Lin, F. Yan, C. Hu, Q. Lv, W. Zhu, Z. Wang, Z. Wei, K. Chang, and K. Wang, "Spin-Valve Effect in Fe_3GeTe_2/MoS_2/Fe_3GeTe_2 van der Waals Heterostructures", ACS Applied Materials & Interfaces **12**, 43921–43926 (2020).

[83]C. Hu, D. Zhang, F. Yan, Y. Li, Q. Lv, W. Zhu, Z. Wei, K. Chang, and K. Wang, "From two- to multi-state vertical spin valves without spacer layer based on Fe_3GeTe_2 van der Waals homo-junctions", Science Bulletin **65**, 1072–1077 (2020).

[84]S. Albarakati, C. Tan, Z.-J. Chen, J. G. Partridge, G. Zheng, L. Farrar, E. L. H. Mayes, M. R. Field, C. Lee, Y. Wang, Y. Xiong, M. Tian, F. Xiang, A. R. Hamilton, O. A. Tretiakov, D. Culcer, Y.-J. Zhao, and L. Wang, "Antisymmetric magnetoresistance in van der Waals Fe_3GeTe_2/graphite/Fe_3GeTe_2 trilayer heterostructures", Science Advances **5**, eaaw0409 (2019).

[85]W. Niu, Z. Cao, Y. Wang, Z. Wu, X. Zhang, W. Han, L. Wei, L. Wang, Y. Xu, Y. Zou, L. He, and Y. Pu, "Antisymmetric magnetoresistance in Fe_3GeTe_2 nanodevices of inhomogeneous thickness", Physical Review B **104**, 125429 (2021).

[86]A. H. Castro Neto, F. Guinea, N. M. R. Peres, K. S. Novoselov, and A. K. Geim, "The electronic properties of graphene", Reviews of Modern Physics **81**, 109–162 (2009).

[87]P. R. Wallace, "The Band Theory of Graphite", Physical Review **71**, 622–634 (1947).

[88]M. C. Lemme, "Current Status of Graphene Transistors", Solid State Phenomena **156-158**, 499–509 (2009).

[89]N. M. R. Peres, "Colloquium: The transport properties of graphene: An introduction", Reviews of Modern Physics **82**, 2673–2700 (2010).

[90]D. W. Boukhvalov, M. I. Katsnelson, and A. I. Lichtenstein, "Hydrogen on graphene: Electronic structure, total energy, structural distortions and magnetism from first-principles calculations", Physical Review B **77**, 035427 (2008).

[91]S. Hunklinger, *Festkörperphysik*, 4., aktualisierte Auflage, De Gruyter Studium (Oldenbourg Wissenschaftsverlag, München, 2014).

[92]K. S. Novoselov, A. K. Geim, S. V. Morozov, D. Jiang, M. I. Katsnelson, I. V. Grigorieva, S. V. Dubonos, and A. A. Firsov, "Two-dimensional gas of massless Dirac fermions in graphene", Nature **438**, 197–200 (2005).

[93]A. K. Geim and K. S. Novoselov, "The rise of graphene", Nature Materials **6**, 183–191 (2007).

[94]B. El-Kareh, *Fundamentals of Semiconductor Processing Technology* (Springer US, Boston, MA, 1995).

[95]J. Martin, N. Akerman, G. Ulbricht, T. Lohmann, J. H. Smet, K. von Klitzing, and A. Yacoby, "Observation of electron–hole puddles in graphene using a scanning single-electron transistor", Nature Physics **4**, 144–148 (2008).

[96]M. Gibertini, A. Tomadin, F. Guinea, M. I. Katsnelson, and M. Polini, "Electron-hole puddles in the absence of charged impurities", Physical Review B **85**, 201405 (2012).

[97]C. Józsa, M. Popinciuc, N. Tombros, H. T. Jonkman, and B. J. van Wees, "Controlling the efficiency of spin injection into graphene by carrier drift", Physical Review B **79**, 081402 (2009).

[98]C. R. Dean, A. F. Young, I. Meric, C. Lee, L. Wang, S. Sorgenfrei, K. Watanabe, T. Taniguchi, P. Kim, K. L. Shepard, and J. Hone, "Boron nitride substrates for high-quality graphene electronics", Nature Nanotechnology **5**, 722–726 (2010).

[99]J. Xue, J. Sanchez-Yamagishi, D. Bulmash, P. Jacquod, A. Deshpande, K. Watanabe, T. Taniguchi, P. Jarillo-Herrero, and B. J. LeRoy, "Scanning tunnelling microscopy and spectroscopy of ultra-flat graphene on hexagonal boron nitride", Nature Materials **10**, 282–285 (2011).

[100]L. Wang, I. Meric, P. Y. Huang, Q. Gao, Y. Gao, H. Tran, T. Taniguchi, K. Watanabe, L. M. Campos, D. A. Muller, J. Guo, P. Kim, J. Hone, K. L. Shepard, and C. R. Dean, "One-dimensional electrical contact to a two-dimensional material", Science (New York, N.Y.) **342**, 614–617 (2013).

[101]L. Britnell, R. V. Gorbachev, R. Jalil, B. D. Belle, F. Schedin, M. I. Katsnelson, L. Eaves, S. V. Morozov, A. S. Mayorov, N. M. R. Peres, A. H. C. Neto, J. Leist, A. K. Geim, L. A. Ponomarenko, and K. S. Novoselov, "Electron tunneling through ultrathin boron nitride crystalline barriers", Nano Letters **12**, 1707–1710 (2012).

[102]P. Miró, M. Audiffred, and T. Heine, "An atlas of two-dimensional materials", Chemical Society Reviews **43**, 6537–6554 (2014).

[103]G. Cassabois, P. Valvin, and B. Gil, "Hexagonal boron nitride is an indirect bandgap semiconductor", Nature Photonics **10**, 262–266 (2016).

[104]N. Alem, R. Erni, C. Kisielowski, M. D. Rossell, W. Gannett, and A. Zettl, "Atomically thin hexagonal boron nitride probed by ultrahigh-resolution transmission electron microscopy", Physical Review B **80**, 155425 (2009).

[105]A. Pakdel, C. Zhi, Y. Bando, and D. Golberg, "Low-dimensional boron nitride nanomaterials", Materials Today **15**, 256–265 (2012).

[106]T. Q. P. Vuong, S. Liu, A. van der Lee, R. Cuscó, L. Artús, T. Michel, P. Valvin, J. H. Edgar, G. Cassabois, and B. Gil, "Isotope engineering of van der Waals interactions in hexagonal boron nitride", Nature Materials **17**, 152–158 (2018).

[107]C. Elias, P. Valvin, T. Pelini, A. Summerfield, C. J. Mellor, T. S. Cheng, L. Eaves, C. T. Foxon, P. H. Beton, S. V. Novikov, B. Gil, and G. Cassabois, "Direct band-gap crossover in epitaxial monolayer boron nitride", Nature Communications **10**, 2639 (2019).

[108]R. V. Gorbachev, I. Riaz, R. R. Nair, R. Jalil, L. Britnell, B. D. Belle, E. W. Hill, K. S. Novoselov, K. Watanabe, T. Taniguchi, A. K. Geim, and P. Blake, "Hunting for monolayer boron nitride: optical and Raman signatures", Small **7**, 465–468 (2011).

[109]I. Žutić, J. Fabian, and S. Das Sarma, "Spintronics: Fundamentals and applications", Reviews of Modern Physics **76**, 323–410 (2004).

[110]J. Fabian and I. Zutic, "The standard model of spin injection", arXiv preprint, arXiv:0903.2500 (2009).

[111]N. F. Mott, "Electrons in transition metals", Advances in Physics **13**, 325–422 (1964).

[112]R. H. Silsbee, "Novel method for the study of spin transport in conductors", Bulletin of Magnetic Resonance, 284–285 (1980).

[113]M. Johnson and R. H. Silsbee, "Interfacial charge-spin coupling: Injection and detection of spin magnetization in metals", Physical Review Letters **55**, 1790–1793 (1985).

[114]F. Volmer, T. Bisswanger, A. Schmidt, C. Stampfer, and B. Beschoten, "Charge-Induced Artifacts in Nonlocal Spin-Transport Measurements: How to Prevent Spurious Voltage Signals", Physical Review Applied **18**, 014028 (2022).

[115]M. Oltscher, M. Ciorga, M. Utz, D. Schuh, D. Bougeard, and D. Weiss, "Electrical spin injection into high mobility 2D systems", Physical Review Letters **113**, 236602 (2014).

[116]P. Zhang and M. W. Wu, "Electron spin relaxation in graphene with random Rashba field: comparison of the D'yakonov–Perel' and Elliott–Yafet-like mechanisms", New Journal of Physics **14**, 033015 (2012).

[117]L. A. Benítez, J. F. Sierra, W. Savero Torres, A. Arrighi, F. Bonell, M. V. Costache, and S. O. Valenzuela, "Strongly anisotropic spin relaxation in graphene–transition metal dichalcogenide heterostructures at room temperature", Nature Physics **14**, 303–308 (2018).

[118]F. Volmer, M. Drögeler, E. Maynicke, N. von den Driesch, M. L. Boschen, G. Güntherodt, and B. Beschoten, "Role of MgO barriers for spin and charge transport in Co/MgO/graphene nonlocal spin-valve devices", Physical Review B **88**, 161405 (2013).

[119]W. Han and R. K. Kawakami, "Spin relaxation in single-layer and bilayer graphene", Physical Review Letters **107**, 047207 (2011).

[120]H. Ochoa, A. H. Castro Neto, and F. Guinea, "Elliot-Yafet mechanism in graphene", Physical Review Letters **108**, 206808 (2012).

[121]D. Pesin and A. H. MacDonald, "Spintronics and pseudospintronics in graphene and topological insulators", Nature Materials **11**, 409–416 (2012).

[122]D. van Tuan, F. Ortmann, D. Soriano, S. O. Valenzuela, and S. Roche, "Pseudospin-driven spin relaxation mechanism in graphene", Nature Physics **10**, 857–863 (2014).

[123]D. Kochan, M. Gmitra, and J. Fabian, "Spin relaxation mechanism in graphene: resonant scattering by magnetic impurities", Physical Review Letters **112**, 116602 (2014).

[124]T. Maassen, I. J. Vera-Marun, M. H. D. Guimarães, and B. J. van Wees, "Contact-induced spin relaxation in Hanle spin precession measurements", Physical Review B **86**, 235408 (2012).

[125]R. J. Elliott, "Theory of the Effect of Spin-Orbit Coupling on Magnetic Resonance in Some Semiconductors", Physical Review **96**, 266–279 (1954).

[126]Y. Yafet, "G factors and spin-lattice relaxation of conduction electrons", Journal of Physics C: Solid State Physics **14**, 1–98 (1963).

[127]M. I. Dyakonov and Perel V.I., "Spin relaxation of conduction electrons in noncentrosymmetric semiconductors", Soviet Physics Solid State, 3023–3026 (1972).

[128]Y. Yao, F. Ye, X.-L. Qi, S.-C. Zhang, and Z. Fang, "Spin-orbit gap of graphene: First-principles calculations", Physical Review B **75**, 041401 (2007).

[129]M. Gmitra, S. Konschuh, C. Ertler, C. Ambrosch-Draxl, and J. Fabian, "Band-structure topologies of graphene: Spin-orbit coupling effects from first principles", Physical Review B **80**, 235431 (2009).

[130]D. Huertas-Hernando, F. Guinea, and A. Brataas, "Spin-orbit-mediated spin relaxation in graphene", Physical Review Letters **103**, 146801 (2009).

[131]D. van Tuan, F. Ortmann, A. W. Cummings, D. Soriano, and S. Roche, "Spin dynamics and relaxation in graphene dictated by electron-hole puddles", Scientific Reports **6**, 21046 (2016).

[132]K. M. McCreary, A. G. Swartz, W. Han, J. Fabian, and R. K. Kawakami, "Magnetic moment formation in graphene detected by scattering of pure spin currents", Physical Review Letters **109**, 186604 (2012).

[133]O. V. Yazyev, "Emergence of magnetism in graphene materials and nanostructures", Reports on Progress in Physics **73**, 056501 (2010).

[134]M. Wojtaszek, I. J. Vera-Marun, T. Maassen, and B. J. van Wees, "Enhancement of spin relaxation time in hydrogenated graphene spin-valve devices", Physical Review B **87**, 081402 (2013).

[135]J. Amann, T. Völkl, T. Rockinger, D. Kochan, K. Watanabe, T. Taniguchi, J. Fabian, D. Weiss, and J. Eroms, "Counterintuitive gate dependence of weak antilocalization in bilayer graphene/WSe_2 heterostructures", Physical Review B **105**, 115425 (2022).

[136]H. Li, X. Han, A. S. Childress, A. M. Rao, and G. Koley, "Investigation of carrier density and mobility variations in graphene caused by surface adsorbates", Physica E: Low-dimensional Systems and Nanostructures **107**, 96–100 (2019).

[137]T. Naimer, K. Zollner, M. Gmitra, and J. Fabian, "Twist-angle dependent proximity induced spin-orbit coupling in graphene/transition metal dichalcogenide heterostructures", Physical Review B **104**, 195156 (2021).

[138]N. Tombros, S. Tanabe, A. Veligura, C. Jozsa, M. Popinciuc, H. T. Jonkman, and B. J. van Wees, "Anisotropic spin relaxation in graphene", Physical Review Letters **101**, 046601 (2008).

[139]J. Balakrishnan, G. Kok Wai Koon, M. Jaiswal, A. H. Castro Neto, and B. Özyilmaz, "Colossal enhancement of spin–orbit coupling in weakly hydrogenated graphene", Nature Physics **9**, 284–287 (2013).

[140]G. Dhatt, G. Touzot, and E. Lefrançois, *Finite element method*, Numerical methods series (ISTE and Wiley, London and Hoboken, N.J., 2013).

[141]T. Völkl, D. Kochan, T. Ebnet, S. Ringer, D. Schiermeier, P. Nagler, T. Korn, C. Schüller, J. Fabian, D. Weiss, and J. Eroms, "Absence of a giant spin Hall effect in plasma-hydrogenated graphene", Physical Review B **99**, 085401 (2019).

[142]F. Eberle, "Control of spin relaxation and spin precession in diffusive 2DEG channels", PhD thesis (Universität Regensburg, 2023).

[143]P. Li, L. T. Zhang, W. B. Mi, E. Y. Jiang, and H. L. Bai, "Origin of the butterfly-shaped magnetoresistance in reactive sputtered epitaxial Fe_3O_4 films", Journal of Applied Physics **106**, 033908 (2009).

[144]Da Luo, M. Wang, Y. Li, C. Kim, K. M. Yu, Y. Kim, H. Han, M. Biswal, M. Huang, Y. Kwon, M. Goo, D. C. Camacho-Mojica, H. Shi, W. J. Yoo, M. S. Altman, H.-J. Shin, and R. S. Ruoff, "Adlayer-Free Large-Area Single Crystal Graphene Grown on a Cu(111) Foil", Advanced Materials **31**, e1903615 (2019).

[145]M. Wang, M. Huang, Da Luo, Y. Li, M. Choe, W. K. Seong, M. Kim, S. Jin, M. Wang, S. Chatterjee, Y. Kwon, Z. Lee, and R. S. Ruoff, "Single-crystal, large-area, fold-free monolayer graphene", Nature **596**, 519–524 (2021).

[146]J. Li, M. Chen, A. Samad, H. Dong, A. Ray, J. Zhang, X. Jiang, U. Schwingenschlögl, J. Domke, C. Chen, Y. Han, T. Fritz, R. S. Ruoff, B. Tian, and X. Zhang, "Wafer-scale single-crystal monolayer graphene grown on sapphire substrate", Nature Materials **21**, 740–747 (2022).

[147]A. Jain, P. Bharadwaj, S. Heeg, M. Parzefall, T. Taniguchi, K. Watanabe, and L. Novotny, "Minimizing residues and strain in 2D materials transferred from PDMS", Nanotechnology **29**, 265203 (2018).

[148]M. J. Allen, V. C. Tung, L. Gomez, Z. Xu, L.-M. Chen, K. S. Nelson, C. Zhou, R. B. Kaner, and Y. Yang, "Soft Transfer Printing of Chemically Converted Graphene", Advanced Materials **21**, 2098–2102 (2009).

[149]J. N. Lee, C. Park, and G. M. Whitesides, "Solvent compatibility of poly- (dimethylsiloxane) based microfluidic devices", Analytical Chemistry **75**, 6544–6554 (2003).

[150]J. Kim, S. Son, M. J. Coak, I. Hwang, Y. Lee, K. Zhang, and J.-G. Park, "Observation of plateau-like magnetoresistance in twisted Fe_3GeTe_2/Fe_3GeTe_2 junction", Journal of Applied Physics **128**, 093901 (2020).

[151]A. M. Goossens, V. E. Calado, A. Barreiro, K. Watanabe, T. Taniguchi, and L. M. K. Vandersypen, "Mechanical cleaning of graphene", Applied Physics Letters **100**, 073110 (2012).

[152]N. Lindvall, A. Kalabukhov, and A. Yurgens, "Cleaning graphene using atomic force microscope", Journal of Applied Physics **111**, 064904 (2012).

[153]F. Pizzocchero, L. Gammelgaard, B. S. Jessen, J. M. Caridad, L. Wang, J. Hone, P. Bøggild, and T. J. Booth, "The hot pick-up technique for batch assembly of van der Waals heterostructures", Nature Communications **7**, 11894 (2016).

[154]A. Olzierski, "Development and molecular-weight issues on the lithographic performance of poly-(methyl methacrylate)", Microelectronic Engineering **73-74**, 244–251 (2004).

[155]S. Yasin, D. G. Hasko, and H. Ahmed, "Comparison of MIBK/IPA and water/IPA as PMMA developers for electron beam nanolithography", Microelectronic Engineering **61-62**, 745–753 (2002).

[156]J. Manjkow, J. S. Papanu, D. S. Soong, D. W. Hess, and A. T. Bell, "An in situ study of dissolution and swelling behavior of poly-(methyl methacrylate) thin films in solvent/nonsolvent binary mixtures", Journal of Applied Physics **62**, 682–688 (1987).

[157]J. S. Papanu, D. W. Hess, D. S. Soane, and A. T. Bell, "Swelling of poly(methyl methacrylate) thin films in low molecular weight alcohols", Journal of Applied Polymer Science **39**, 803–823 (1990).

[158]A. Felten, C. Bittencourt, J. J. Pireaux, G. van Lier, and J. C. Charlier, "Radio-frequency plasma functionalization of carbon nanotubes surface O_2, NH_3, and CF_4 treatments", Journal of Applied Physics **98**, 074308 (2005).

[159]C. Bittencourt, C. Navio, A. Nicolay, B. Ruelle, T. Godfroid, R. Snyders, J.-F. Colomer, M. J. Lagos, X. Ke, G. van Tendeloo, I. Suarez-Martinez, and C. P. Ewels, "Atomic Oxygen Functionalization of Vertically Aligned Carbon Nanotubes", The Journal of Physical Chemistry C **115**, 20412–20418 (2011).

[160]R. Huber, M.-H. Liu, S.-C. Chen, M. Drienovsky, A. Sandner, K. Watanabe, T. Taniguchi, K. Richter, D. Weiss, and J. Eroms, "Gate-Tunable Two-Dimensional Superlattices in Graphene", Nano Letters **20**, 8046–8052 (2020).

[161]A. Nachtnebel, "Optimierung verschiedener Prozessschritte zur Herstellung von CGT-Heterostrukturen", Bachelor's thesis (Universität Regensburg, Regensburg, 2021).

[162]B. Zhao, R. Ngaloy, S. Ghosh, S. Ershadrad, R. Gupta, K. Ali, A. M. Hoque, B. Karpiak, D. Khokhriakov, C. Polley, B. Thiagarajan, A. Kalaboukhov, P. Svedlindh, B. Sanyal, and S. P. Dash, "A Room-Temperature Spin-Valve with van der Waals Ferromagnet Fe_5GeTe_2/Graphene Heterostructure", Advanced Materials **35**, 2209113 (2023).

[163]F. L. Bakker, A. Slachter, J.-P. Adam, and B. J. van Wees, "Interplay of Peltier and Seebeck effects in nanoscale nonlocal spin valves", Physical Review Letters **105**, 136601 (2010).

[164]K. S. Das, F. K. Dejene, B. J. van Wees, and I. J. Vera-Marun, "Anisotropic Hanle line shape via magnetothermoelectric phenomena", Physical Review B **94**, 180403 (2016).

[165]R. K. Bennet, A. Hojem, and B. L. Zink, "Thermal gradients and anomalous Nernst effects in membrane-supported nonlocal spin valves", Physical Review B **100**, 104404 (2019).

[166]P. R. Gray and R. G. Meyer, "MOS operational amplifier design-a tutorial overview", IEEE Journal of Solid-State Circuits **17**, 969–982 (1982).

[167]P. R. Kinget, "Device mismatch and tradeoffs in the design of analog circuits", IEEE Journal of Solid-State Circuits **40**, 1212–1224 (2005).

[168]N. Nagaosa, J. Sinova, S. Onoda, A. H. MacDonald, and N. P. Ong, "Anomalous Hall effect", Reviews of Modern Physics **82**, 1539–1592 (2010).

[169]M. Alghamdi, P. R. Jothi, W.-C. Liao, S. Coh, X. Lin, B. P. T. Fokwa, and J. Shi, "Layer-dependence study of two-dimensional ferromagnets: Fe_3GeTe_2 and Fe_5GeTe_2", Applied Physics Letters **124**, 192404 (2024).

[170]J. Nogués and I. K. Schuller, "Exchange bias", Journal of Magnetism and Magnetic Materials **192**, 203–232 (1999).

[171]H. K. Gweon, S. Y. Lee, H. Y. Kwon, J. Jeong, H. J. Chang, K.-W. Kim, Z. Q. Qiu, H. Ryu, C. Jang, and J. W. Choi, "Exchange Bias in Weakly Interlayer-Coupled van der Waals Magnet Fe_3GeTe_2", Nano Letters **21**, 1672–1678 (2021).

[172]Y. Shao, W. Lv, J. Guo, B. Qi, W. Lv, S. Li, G. Guo, and Z. Zeng, "The current modulation of anomalous Hall effect in van der Waals Fe_3GeTe_2/WTe_2 heterostructures", Applied Physics Letters **116**, 092401 (2020).

[173]P. Liu, C. Liu, Z. Wang, M. Huang, G. Hu, J. Xiang, C. Feng, C. Chen, Z. Ma, X. Cui, H. Zeng, Z. Sheng, Y. Lu, G. Yin, G. Chen, K. Liu, and B. Xiang, "Planar-symmetry-breaking induced antisymmetric magnetoresistance in van der Waals ferromagnet Fe_3GeTe_2", Nano Research **15**, 2531–2536 (2022).

[174]X. M. Cheng, S. Urazhdin, O. Tchernyshyov, C. L. Chien, V. I. Nikitenko, A. J. Shapiro, and R. D. Shull, "Antisymmetric magnetoresistance in magnetic multilayers with perpendicular anisotropy", Physical Review Letters **94**, 017203 (2005).

[175]M. S. Fuhrer, C. N. Lau, and A. H. MacDonald, "Graphene: Materially Better Carbon", MRS Bulletin **35**, 289–295 (2010).

[176]J.-H. Chen, C. Jang, S. Adam, M. S. Fuhrer, E. D. Williams, and M. Ishigami, "Charged-impurity scattering in graphene", Nature Physics **4**, 377–381 (2008).

[177]J.-H. Chen, C. Jang, M. Ishigami, S. Xiao, W. G. Cullen, E. D. Williams, and M. S. Fuhrer, "Diffusive charge transport in graphene on SiO_2", Solid State Communications **149**, 1080–1086 (2009).

[178]S. V. Morozov, K. S. Novoselov, M. I. Katsnelson, F. Schedin, D. C. Elias, J. A. Jaszczak, and A. K. Geim, "Giant intrinsic carrier mobilities in graphene and its bilayer", Physical Review Letters **100**, 016602 (2008).

[179]M. I. Katsnelson and A. K. Geim, "Electron scattering on microscopic corrugations in graphene", Philosophical transactions. Series A, Mathematical, physical, and engineering sciences **366**, 195–204 (2008).

[180]B. Huard, N. Stander, J. A. Sulpizio, and D. Goldhaber-Gordon, "Evidence of the role of contacts on the observed electron-hole asymmetry in graphene", Physical Review B **78**, 121402 (2008).

[181]J.-H. Chen, C. Jang, S. Xiao, M. Ishigami, and M. S. Fuhrer, "Intrinsic and extrinsic performance limits of graphene devices on SiO_2", Nature Nanotechnology **3**, 206–209 (2008).

[182]T. Maassen, F. K. Dejene, M. H. D. Guimarães, C. Józsa, and B. J. van Wees, "Comparison between charge and spin transport in few-layer graphene", Physical Review B **83**, 115410 (2011).

[183]Y. Hattori, T. Taniguchi, K. Watanabe, and M. Kitamura, "Identification of the monolayer thickness difference in a mechanically exfoliated thick flake of hexagonal boron nitride and graphite for van der Waals heterostructures", Nanotechnology **34**, 295701 (2023).

[184]W. Demtröder, *Experimentalphysik 3* (Springer Berlin Heidelberg, Berlin, Heidelberg, 2016).

[185]M. Z. Iqbal, S. Siddique, M. F. Khan, A. u. Rehman, A. Rehman, and J. Eom, "Gate–Dependent Tunnelling Current Modulation of Graphene/hBN Vertical Heterostructures", Advanced Engineering Materials **20**, 1800159 (2018).

[186]E. Burstein and S. Lundqvist, *Tunneling Phenomena in Solids: Lectures presented at the 1967/NATO Advanced Study Institute at Risö, Denmark* (Springer, Boston, MA, 1969).

[187]J. G. Simmons, "Electric Tunnel Effect between Dissimilar Electrodes Separated by a Thin Insulating Film", Journal of Applied Physics **34**, 2581–2590 (1963).

[188]J. J. Åkerman, R. Escudero, C. Leighton, S. Kim, D. A. Rabson, R. W. Dave, J. M. Slaughter, and I. K. Schuller, "Criteria for ferromagnetic–insulator–ferromagnetic tunneling", Journal of Magnetism and Magnetic Materials **240**, 86–91 (2002).

[189]B. Birkner, D. Pachniowski, A. Sandner, M. Ostler, T. Seyller, J. Fabian, M. Ciorga, D. Weiss, and J. Eroms, "Annealing-induced magnetic moments detected by spin precession measurements in epitaxial graphene on SiC", Physical Review B **87**, 081405 (2013).

[190]S. Ringer, M. Rosenauer, T. Völkl, M. Kadur, F. Hopperdietzel, D. Weiss, and J. Eroms, "Spin field-effect transistor action via tunable polarization of the spin injection in a Co/MgO/graphene contact", Applied Physics Letters **113**, 132403 (2018).

[191]T. Zhu, S. Singh, J. Katoch, H. Wen, K. Belashchenko, I. Žutić, and R. K. Kawakami, "Probing tunneling spin injection into graphene via bias dependence", Physical Review B **98**, 054412 (2018).

[192]C. Józsa, M. Popinciuc, N. Tombros, H. T. Jonkman, and B. J. van Wees, "Electronic spin drift in graphene field-effect transistors", Physical Review Letters **100**, 236603 (2008).

[193]M. V. Kamalakar, A. Dankert, P. J. Kelly, and S. P. Dash, "Inversion of Spin Signal and Spin Filtering in Ferromagnet|Hexagonal Boron Nitride-Graphene van der Waals Heterostructures", Scientific Reports **6**, 21168 (2016).

[194]M. Gurram, S. Omar, and B. J. van Wees, "Bias induced up to 100% spin-injection and detection polarizations in ferromagnet/bilayer-hBN/graphene/hBN heterostructures", Nature Communications **8**, 248 (2017).

[195]R. Ngaloy, B. Zhao, S. Ershadrad, R. Gupta, M. Davoudiniya, L. Bainsla, L. Sjöström, M. A. Hoque, A. Kalaboukhov, P. Svedlindh, B. Sanyal, and S. P. Dash, "Strong In-Plane Magnetization and Spin Polarization in $(Co_{0.15}Fe_{0.85})_5GeTe_2$/Graphene van der Waals Heterostructure Spin-Valve at Room Temperature", ACS Nano **18**, 5240–5248 (2024).

[196]C. P. Weber, N. Gedik, J. E. Moore, J. Orenstein, J. Stephens, and D. D. Awschalom, "Observation of spin Coulomb drag in a two-dimensional electron gas", Nature **437**, 1330–1333 (2005).

[197]M. Huang, J. Zhou, Di Chen, H. Lu, N. J. McLaughlin, S. Li, M. Alghamdi, D. Djugba, J. Shi, H. Wang, and C. R. Du, "Wide field imaging of van der Waals ferromagnet Fe_3GeTe_2 by spin defects in hexagonal boron nitride", Nature Communications **13**, 5369 (2022).

[198]G. Zhang, F. Guo, H. Wu, X. Wen, L. Yang, W. Jin, W. Zhang, and H. Chang, "Above-room-temperature strong intrinsic ferromagnetism in 2D van der Waals Fe_3GaTe_2 with large perpendicular magnetic anisotropy", Nature Communications **13**, 5067 (2022).

[199]J. Ingla-Aynés, F. Herling, J. Fabian, L. E. Hueso, and F. Casanova, "Electrical control of valley-zeeman spin-orbit-coupling–induced spin precession at room temperature", Phys. Rev. Lett. **127**, 047202 (2021).

[200]M. Gmitra and J. Fabian, "Proximity effects in bilayer graphene on monolayer WSe_2: field-effect spin valley locking, spin-orbit valve, and spin transistor", Phys. Rev. Lett. **119**, 146401 (2017).

[201]M. Ciorga, "Perspective on the spin field-effect transistor", Journal of Physics D: Applied Physics **58**, 012001 (2024).

[202]S. R. Bahn and K. W. Jacobsen, "An object-oriented scripting interface to a legacy electronic structure code", Computing in Science & Engineering **4**, 56–66 (2002).

[203]P. Lazić, "CellMatch: Combining two unit cells into a common supercell with minimal strain", Computer Physics Communications **197**, 324–334 (2015).

[204]D. S. Koda, F. Bechstedt, M. Marques, and L. K. Teles, "Coincidence Lattices of 2D Crystals: Heterostructure Predictions and Applications", The Journal of Physical Chemistry C **120**, 10895–10908 (2016).

[205]S. Carr, S. Fang, and E. Kaxiras, "Electronic-structure methods for twisted moiré layers", Nature Reviews Materials **5**, 748–763 (2020).

[206]P. Hohenberg and W. Kohn, "Inhomogeneous Electron Gas", Physical Review **136**, B864–B871 (1964).

[207]P. Giannozzi, S. Baroni, N. Bonini, M. Calandra, R. Car, C. Cavazzoni, D. Ceresoli, G. L. Chiarotti, M. Cococcioni, I. Dabo, A. Dal Corso, S. de Gironcoli, S. Fabris, G. Fratesi, R. Gebauer, U. Gerstmann, C. Gougoussis, A. Kokalj, M. Lazzeri, L. Martin-Samos, N. Marzari, F. Mauri, R. Mazzarello, S. Paolini, A. Pasquarello, L. Paulatto, C. Sbraccia, S. Scandolo, G. Sclauzero, A. P. Seitsonen, A. Smogunov, P. Umari, and R. M. Wentzcovitch, "QUANTUM ESPRESSO: a modular and open-source software project for quantum simulations of materials", Journal of Physics: Condensed Matter **21**, 395502 (2009).

[208]B. Chen, J. Yang, H. Wang, M. Imai, H. Ohta, C. Michioka, K. Yoshimura, and M. Fang, "Magnetic Properties of Layered Itinerant Electron Ferromagnet Fe_3GeTe_2", Journal of the Physical Society of Japan **82**, 124711 (2013).

[209]S. Grimme, "Semiempirical GGA-type density functional constructed with a long-range dispersion correction", Journal of Computational Chemistry **27**, 1787–1799 (2006).

[210]S. Grimme, J. Antony, S. Ehrlich, and H. Krieg, "A consistent and accurate ab initio parametrization of density functional dispersion correction (DFT-D) for the 94 elements H-Pu", The Journal of Chemical Physics **132**, 154104 (2010).

[211]V. Barone, M. Casarin, D. Forrer, M. Pavone, M. Sambi, and A. Vittadini, "Role and effective treatment of dispersive forces in materials: Polyethylene and graphite crystals as test cases", Journal of Computational Chemistry **30**, 934–939 (2009).

[212]K. Zollner, M. Gmitra, and J. Fabian, "Heterostructures of graphene and hBN: Electronic, spin-orbit, and spin relaxation properties from first principles", Physical Review B **99**, 125151 (2019).

Acknowledgments

Abschließend möchte ich allen Personen, die mich bei der Fertigstellung dieser Arbeit unterstützt haben, meinen Dank aussprechen.

Zunächst möchte ich mich bei Herrn **Prof. Dr. Dieter Weiss** für die Gelegenheit bedanken, an seinem Lehrstuhl zu diesem faszinierenden Thema zu forschen. Er verfügte stets über das richtige Gespür mich in die richtigen Bahnen zu lenken, wenn ich einmal auf dem Holzweg war. Der Umgang an seinem Lehrstuhl war arbeitsgruppenübergreifend durch eine freundliche und produktive Arbeitsatmosphäre gekennzeichnet, bei der man sich bei Problemen jederzeit an ihn wenden konnte. Diese Unterstützung war für mich von großem Wert.

Besonderer Dank gilt auch **Prof. Dr. Mariusz Ciorga** für die Bereitstellung des Themas meiner Promotion sowie die exzellente Betreuung. Seine offene Tür für jede physikalische oder laborbezogene Frage schätzte ich an seiner Betreuung außerordentlich. Die Diskussionen über meine Daten und Messungen waren für mich jederzeit von großem Nutzen.

Darüber hinaus möchte ich mich bei **Prof. Dr. Jaroslav Fabian** und **Dr. Klaus Zollner** für die zahlreichen und aufschlussreichen Meetings und Diskussionen, sowie für die Durchführung und Bereitstellung der DFT-Berechnungen bedanken.

Des Weiteren möchte ich mich bei **Prof. Dr. Jaroslav Fabian**, **Prof. Dr. Dominique Bougeard** und **Prof. Dr. Milena Grifoni** für die Bereitschaft, meine Arbeit zu prüfen und zu bewerten, bedanken.

Ein besonderer Dank gilt **PD Dr. Jonathan Eroms** und seiner Graphen-Arbeitsgruppe, für die Einarbeitung und Hilfestellung bezüglich aller Aspekte von van-der-Waals-Materialien.

Meinen Bachelorstudentinnen **Michaela Zoth** und **Miriam Waldner** möchte ich für ihr Engagement an meinem Thema danken. Die Weitergabe meines Wissens und meiner Erfahrungen, die Betreuung eurer Arbeiten, sowie die daraus resultierenden Lernprozesse haben mir große Freude bereitet.

Besonderer Dank gilt **Dr. Franz Eberle** für die Unterstützung im Magnetlabor. Die

zahlreichen fachlichen Diskussionen zum Thema Spintransport waren für mich stets eine wertvolle Quelle des Lernens.

Des Weiteren möchte ich mich bei **Dr. Vanessa Junk**, **Dr. Tobias Völkl**, **Dr. Robin Huber**, **PD Dr. Jonathan Eroms**, **Dr. Benedikt Grünewald**, **Dr. Stefan Hartl**, **Julia Amann**, **Pauline Drexler** und **Jaydean Schmidt** für das Korrekturlesen dieser Arbeit bedanken. Insbesondere möchte ich mich bei Vanessa, Stefan und Benedikt für die gemeinsame Zeit und den zahlreichen Kaffee- und Mittagspausen während des Studiums und der Promotion bedanken. Ohne euch wäre diese Reise nur halb so schön gewesen.

Des Weiteren möchte ich mich bei allen Kolleginnen und Kollegen, sowie Mitarbeiterinnen und Mitarbeitern des Lehrstuhls für die freundliche, entspannte und stets produktive Arbeitsatmosphäre bedanken. Ein besonderer Dank hierbei gilt den beiden Sekretärinnen **Elke Haushalter** und **Claudia Moser**, die sich über das übliche Maß hinaus um organisatorische und bürokratische Aufgaben gekümmert haben.

Für die emotionale Unterstützung während meiner Promotionszeit möchte ich mich bei meinen Freunden und insbesondere meiner Freundin **Janine Richter** bedanken. Deine Bereitschaft, sich meinen Problemen anzunehmen, hat mir stets neue Kraft verliehen.

Abschließend möchte ich mich bei **meinen Eltern** und **meiner Familie** bedanken, die mich stets ermutigt und mein Studium und gesamten Werdegang ermöglicht haben.